
UNIVERSITY OF
LINCOLN

# Investigation into Balancing of High-Speed Flexible Shafts by Compensating Balancing Sleeves

James Grahame Knowles

A thesis submitted in fulfilment of the requirements of the University of Lincoln for the degree of Doctor of Philosophy

2017

## ABSTRACT

Engineers have been designing machines with long, flexible shafts and dealing with consequential vibration problems, caused by shaft imbalance since the beginning of the industrial revolution in the mid 1800's. Modern machines still employ balancing techniques based on the Influence Coefficient or Modal Balancing methodologies, that were introduced in the 1930's and 1950's, respectively.

The research presented in this thesis explores fundamental deficiencies of current trim balancing techniques and investigates novel methods of flexible attachment to provide a component of lateral compliance. Further, a new balancing methodology is established which utilizes trim balance induced bending moments to reduce shaft deflection by the application of compensating balancing sleeves. This methodology aims to create encastre simulation by closely matching the said balancing moments to the fixing moments of an equivalent, encastre mounted shaft. It is therefore significantly different to traditional methods which aim to counter-balance points of residual eccentricity by applying trim balance correction, usually at pre-set points, along a shaft.

Potential benefits of this methodology are initially determined by analysis of a high-speed, simply supported, plain flexible shaft, with uniform eccentricity which shows that near elimination of the 1$^{st}$ lateral critical speed, (LCS) is possible, thereby allowing safe operation with much reduced LCS margins.

Further study of concentrated, residual imbalances provides several new insights into the behaviour of the balancing sleeve concept: 1) a series of concentrated imbalances can be regarded simply as an equivalent level of uniform eccentricity, and balance sleeve compensation is equally applicable to a generalised unbalanced distribution consisting of any number of

concentrated imbalances, 2) compensation depends on the sum of the applied balancing sleeve moments and can therefore be achieved using a single balancing sleeve (thereby simulating a single encastre shaft), 3) compensation of the 2nd critical speed, and to a lesser extent higher orders, is possible by use of two balancing sleeves, positioned at shaft ends, 4) the concept facilitates on-site commissioning of trim balance which requires a means of adjustment at only one end of the shaft, thereby reducing commissioning time, 5) the Reaction Ratio, *RR* (simply supported/ encastre) is independent of residual eccentricity, so that the implied benefits resulting from the ratio (possible reductions in the equivalent level of eccentricity) are additional to any balancing procedures undertaken prior to encastre simulation. The analysis shows that equivalent reductions of the order of 1/25th are possible.

Experimental measurements from a scaled model of a typical drive coupling employed on an industrial gas turbine package, loaded asymmetrically with a concentrated point of imbalance, support this analysis and confirms the operating mechanism of balancing sleeve compensation and also it's potential to vastly reduce shaft deflections/ reaction loads.

## List of publications

## Publications resulting from research presented in this thesis

1. Mathematical development and modelling of a counter balance compensating sleeve for the suppression of lateral vibrations in high speed flexible couplings. ASME Turbo Expo San Antonio, TX, 3-7 June 2013; Paper number GT2013-95634. New York: ASME. Kirk A, Knowles G, Stewart J, Bingham C, [117]

**2.** Theoretical investigation into balancing high-speed flexible-shafts, by the use of a novel compensating balancing sleeve. IMechE Part C: Journal of Mechanical Engineering Science 2013; Article No. 517376. Knowles G, Kirk A, Stewart J, Bingham C, Bickerton R, [118]

**3.** Generalised analysis of compensating balancing sleeves with experimental results from a scaled industrial turbine coupling shaft. IMechE Part C: Journal of Mechanical Engineering Science - submitted March 2017; Knowles G, Kirk A, Bingham C, Bickerton R, [119] - PENDING

## Patents

4. An apparatus comprising a shaft and a balancing device for balancing the shaft. European Patent EP2703689A1. 2014. Knowles G, [123]

5. An apparatus comprising a shaft and a compensator balancing sleeve for balancing the shaft. European Patent EP2806186A1. 2014. Knowles G, [124]

## Acknowledgements

I would like to thank Siemens Industrial Turbomachinery Limited, Lincoln, for past employment and their faith in funding this research.

A general thanks is due to my many friends and colleagues, too numerous for individual acknowledgement, who helped me gain valuable experience in all aspects of drive train dynamics and package design; but special mention is due to: Mr. Steve Middlebrough, Mr. Herman Ruijsenaars, Dr. Gordon Beesley, Mr. Alan Coppin, and in particular my friend and co-worker Mr. Steve Atkinson, without whose help this germ of an idea would never have flourished.

I am grateful to Professors Paul and Jill Stewart for their early implementation and encouragement, Professor Ron Bickerton for his role of Chief Engineer and listening post and a special thanks to my supervisor Professor Chris Bingham for his very valuable advice and concise editorial work.

I am also indebted to my work colleagues at the University of Lincoln, School of Engineering, Technical Department and especially to my co-researcher Mr. Antony Kirk, for his invaluable help during the rig build and validation testing phases of this project.

Deserved thanks is also due to Mr. Dave Pemberton for his enduring interest and stimulating many thought provoking discussions of my work over many years.

Finally, but most importantly, sincere thanks is due to my wife Sally for providing much needed support and encouragement.

## Contents



## Chapter 1



## Chapter 2

## Chapter 3



## Chapter 4

## Chapter 5



## Chapter 6



## Chapter 7



## Chapter 8

## Nomenclature

### *General Analysis*

$A_{0i}$ ,$A_i$, $B_{0i}$ , $C_i$,$D_i$,$G$,$H$,$M$,$N$,$P$,$Q$,$b$ = Parameters substitutions

Parameter Suffixes: *e* = encastre shaft

*un* = uniform eccentricity

con = concentrated imbalance

*ss* = simply supported

*en* = encastre mounted

*a*,*f* = Eccentric zone end positions (m)

$BM$ = Shaft bending moment at point $x$

$c_i$ = Eccentricity of balance sleeve mass ( m)

$CF$ = Centrifugal force (N)

$CF_{disc}$ = Disc centrifugal Force (N)

$CF_{bal}$ = Balance centrifugal Force (N)

$e$ = Eccentricity of shaft (m)

$\hat{e}$ = Euler's number

$e_{disc}$ Disc eccentricity (m)

$e_{bal}$ Balance eccentricity (m)

$E$ = Young's Modulus (N/m^2)

$I$ = 2nd Moment of area in bending (m^4)

*k* = Concentrated imbalance coefficient

$K_i$ = Balance sleeve stiffness (N/m)

$\ell, \ell_i$ = Shaft length (m)

$L_i$ = Balance sleeve length (m)

$\overline{L}$ = Non-dimensional sleeve length

$m_i$ = Balance sleeve mass (kg)

$M_{fi}$ = Encastre system fixing moment (Nm)

$M_{0i}$ = Balance sleeve moment applied to shaft (Nm)

$M_x$ = Balance sleeve moment applied to shaft at point *x* (Nm)

$M_s$ = Shaft mass (kg)

$M_{disc}$ = Disc mass (kg)

$M_{bal}$ = Balance mass (kg)

$Mp$ = Concentrated zone mass (kg)

$Mu$ = Equivalent additional mass (kg)

$r$ = Shaft radial deflection (m)

$R_i$ = Parameters of shaft radial deflection (m)

$\dot{R}_{il}$ = Parameter derivatives of shaft radial deflection

$r_i, \bar{r}, \overline{R}_i$ = Laplace displacement derivatives

*R* = Radius of rotation of equivalent additional mass $Mu$ (m)

$R_{ei}$ = Reaction load at shaft ends (N)

$\overline{R}_e$ = Non dimensional reaction load

$s$ = Laplace Transform operator

*SFv* = Vertical Shear Force

$S_{bal}$ = Balance stiffness (N/m)

$S_{shaft}$ = Shaft stiffness (N/m)

$S_{bal}$ = Balance Stiffness (N/m)

*W* = Lateral load applied to a beam/ shaft

$x$ = Reference point position from shaft end (m)

$y_i$ = Balance mass displacement from rotation axis (m)

$Y_i$ = Balance sleeve deflection (m)

$\omega$ = Rotational speed (rad/s)

$\omega_{bal\_crit}$ = Balance critical speed (rad/s)

$\omega_{shaft\_crit}$ = Shaft critical speed (rad/s)

$\omega_{crit}$ = Critical speed (rad/s)

***Compensating Sleeve Design***

$A$ = Spar cross sectional area (m^2)

$BM\_bow$ = Spar radial bending moment (Nm)

$BM\_defl$ = Spar vertical bending moment (Nm)

$BM\_res$ = Spar resultant bending moment (Nm)

$f\_\max$ = Maximum bending stress (N/m^2)

$h$ = Height of spar centroid above X – X (m)

$I_{cc}$ = Spar moment of inertia through centroid (m^4)

$I_{xx}$ = Spar moment of inertia about X - X (m^4)

$I_{sleeve}$ = Sleeve bending moment of inertia (m^4)

$M$ = Fixing moment of double encastre beam (m)

$M_1$ = Spar 1st moment of area about X - X (m^3)

$M_2$ = Spar 2nd moment of area about X - X (m^4)

$R_i$ = Spar sectional radius (m)

$R$ = Reaction load of double encastre beam (m)

$u$ = Displacement of double encastre beam (m)

$\theta_i$ = Spar angular position (rad)

$y_{fibre}$ = Distance of extreme fibre in bending (m)

## Glossary

| | |
|---|---|
| ABB | Automatic Ball Balancer |
| API | American Petroleum Institute |
| AGMA | American Gear manufacturers Association |
| BW | Backward Whirl |
| CF | Centrifugal Force |
| CR | Compensation Ratio |
| DAVC | Direct Active Vibration Control |
| DOF | Degree of Freedom |
| FEA | Finite Element Analysis |
| FW | Forward Whirl |
| ISO | Institutional Organisation for Standardisation |
| GE | General Electric |
| LCS | Lateral Critical Speed |
| LHS | Left Hand Side |
| N | Number of modal balance planes |
| N + 2 | Number of modal + rigid body balancing planes |
| pk – pk | Peak to Peak |
| PT | Power Take-Off |
| RHS | Right Hand Side |
| RR | Reaction Ratio |
| SR | Simulation Ratio |
| TDC | Top Dead Centre |
| TP | Test Procedure |

| | |
|---|---|
| 2-D, 2.5-D, 3-D | Number of analysis planes considered in FEA |

# Chapter 1

## 1.1 Introduction

The investigation presented in this thesis was initiated by the need for controlling shaft vibration issues encountered in Gas Turbine (GT) driven Mechanical Drive Packages for the Oil and Gas market. Such units are usually required to pump liquid or gas, for utility purposes, over 100's of kilometres and must be able to operate over a wide speed range in order to provide the necessary performance flexibility to maintain a high overall operating efficiency.

However, it has been observed that in some instances it has been extremely difficult, and often impossible to dynamically balance the GT shafts across the required operating speed range because the phase vector of the bearing load was changing with respect to operating speed. Specifically, drive trains could be readily balanced at relatively low operating speeds, but with a new angular position of the load vector it was incorrectly balanced at higher operating frequencies, or vice versa.

In some cases the vector change is seen to approach 180°, indicating that the drive train would have traversed a critical speed, between the low and high speed operating points. However, dynamic analysis showed this not to be the case.

It is notable that such problems appear more acute on packages where the drive coupling, between the driver and driven units, was longer than standard, or had torque spacers incorporated as part of the assembly. In both cases the shaft flexibility is increased and this led to a hypothesis that shaft deflection could be an alternative cause of angular change of the vector. In turn, this has led to the proposition of an improved balancing mechanism, the compensated balancing sleeve [120,121,122,123,124],

with the potential to substantially reduce reaction loads applied to the driver and driven bearings.

The aim of this thesis is to investigate the fundamental causes of the balancing problems associated with high-speed flexible shafts and to assess the practical application of the proposed new balancing sleeve.

## 1.2 Background

The general evolutionary path of most dynamic machines is one of making components/ sub-assemblies bigger, more complex and operating at ever greater speeds in order to increase their production output and/ or obtain greater efficiency. Nevertheless, a substantial limiting factor in this development is often an accompanying increase in vibration, creating increased noise, output quality variation and instability in production machines, or problems with other important functions such as speed control, steering, braking etc. in vehicles – together with higher stresses, more frequent breakdowns and in some cases catastrophic failure.

### 1.2.1 Historical Perspective

The history of analysing and balancing shafts is now quite protracted, with the first serious study performed by Rankine [3] in 1869, who analysed an unloaded shaft resting freely in narrow bearings positioned at each end, thereby being analogous to a simply supported beam. The term ‘whirling’ was used to describe the circular motion of the central axis of the shaft, viewed in any lateral plane, when subjected to bending by centrifugal forces acting on the shaft during rotation and he equated these forces to the restraining stiffness forces of an equivalent beam, to obtain an equation for the critical speed. Beyond this speed the centrifugal forces exceeded the restraining forces and it was reasoned that shaft failure would result.

However, by not being aware that phase rotation of the mass centroid occurs about the geometric centre of the shaft, during transition through a critical speed, see Figure 1.1, [85], it was erroneously concluded at the time that operating beyond this speed was impossible.

Nevertheless, following this study a steam turbines was developed that could operate above the 1st critical speed, by De Laval in 1883 and by Parsons in 1884, [5], and hence some empirical engineering knowledge about self-balancing mechanisms existed whereby at super-critical speeds the “shaft again runs true”. In 1895, an analysis of an undamped rotor by Foppl [103] showed that the heavy side, or heavy spot, of an unbalanced disc migrates outwards when rotation is below the critical speed and that it migrates inwards, thus lessening the imbalance, when operated above the critical speed. Moreover, Dunkerley [1] in 1894 published experimental results of the critical speeds of numerous slender shafts, loaded with a variety of differently positioned pulley wheels, as was in common use in the cotton mills at the time, which further supported the above theories.

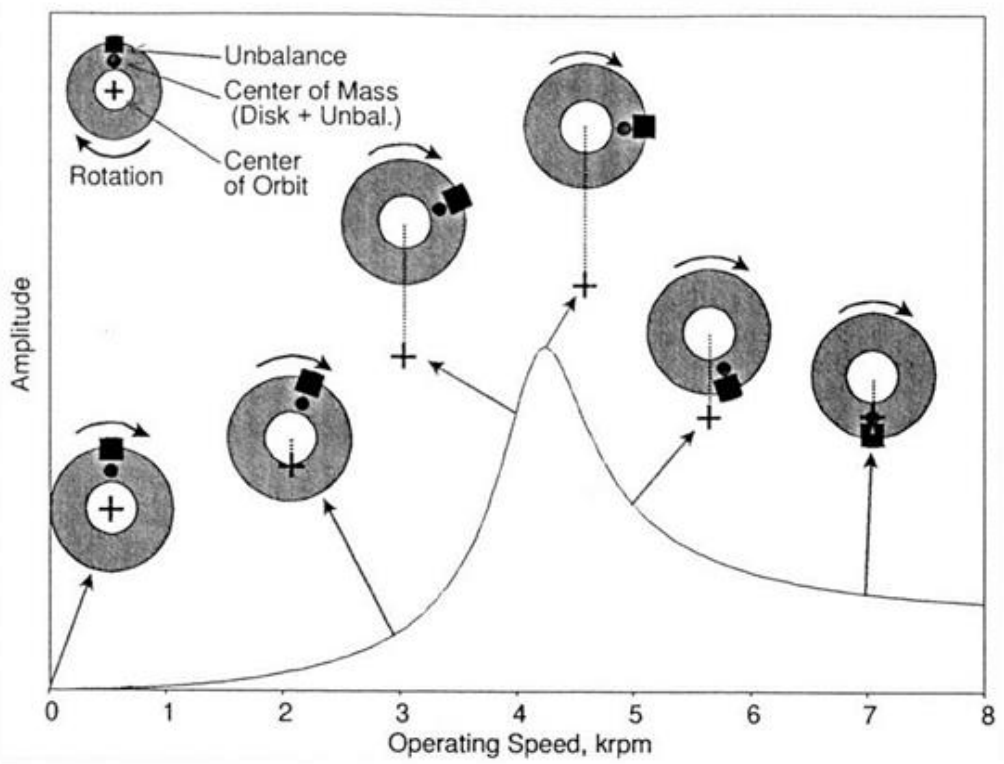


**Figure 1.1, [85],** Phase Rotation of Mass Centroid

To resolve the conflict between Rankine's theory and experimental observation, the Royal Society of London commissioned Jeffcott to further research the subject. The study [2] reported results from the analysis of a slender, massless shaft with a centrally mounted single disc and included external damping, as shown in Figure 1.2, [2a]. It confirmed the previous predictions given by Foppl [103] in which supercritical operation was considered stable and also showed that due to damping, the angular position of the heavy spot rotates continuously during transition of the critical speed. The report also asserted that since all rotors contain some imbalance eccentricity, due to imperfect machining and/ or material density non-uniformity, then a source of forced excitation must always exist, at a frequency equal to the speed of rotation. This fundamentally differentiates the dynamics of a rotating system from a structural beam, which may have the same natural frequency as a shaft's critical speed, but will only vibrate when an external excitation force is applied. The resulting paper by Jeffcott [2] is now regarded as seminal for an understanding of single degree of

freedom rotor/shafts, i.e. a single spring/ mass dynamic system, which are often now termed as Jeffcott or in some instances Laval/ Foppl rotors.

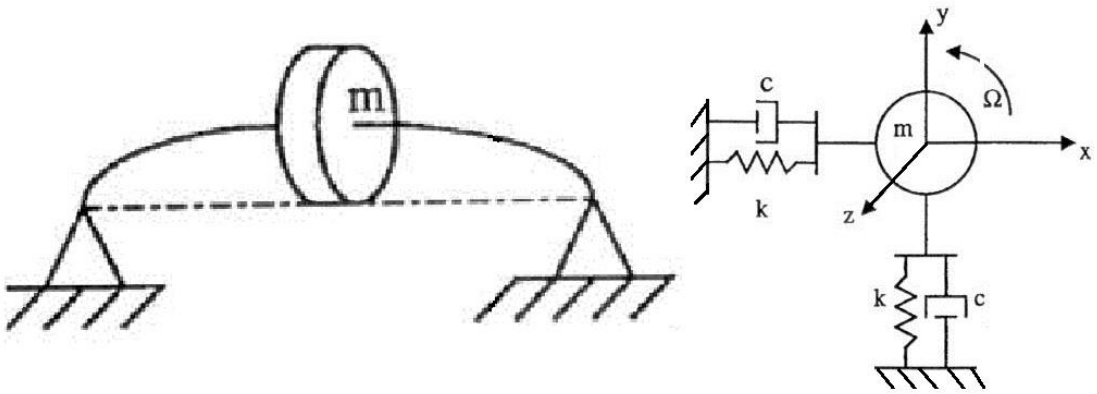


**Figure 1.2, [2a],** Jeffcott Rotor

As development of supercritical rotors in steam turbines continued, resulting in yet higher operating speeds, manufacturers sometimes experienced severe vibration problems. These were originally blamed on rotor imbalance, but correction difficulties led to some to consider the possibility that internal damping forces, acting tangentially to aid precession, might be inducing a form of self-exciting instability. It was reasoned that gravity effects could induce alternating internal bending moments/stresses, which in turn, if of sufficient magnitude could produce internal friction within the crystalline structure of a shaft (as per the hysteresis loop) which is commonly seen in outputs from tensile test machines, the area of which represents the energy loss known as hysteretic damping. Newkirk [8] and Kimball [7] first recognised that these forces could cause an unstable whirling motion during supercritical operation. Their work led to further research, by Stodola [5] et al, (1927), into other sources of frictional forces that may impart similar effects, such as oil whip within bearings, general peripheral rubbing against seals or stator casings and also localised rubs, which can cause local hot spots resulting in deformation of say discs and/ or shaft bending. Hot spot instability subsequently became known as the Newkirk Effect.

Campbell [6], (1924), investigated vibrations resulting currently from General Electric, GE, steam turbines and developed a method for plotting critical speeds and lines of synchronous excitations against operating speed, with their intersections highlighting points of whirling resonance—now widely known as Campbell Diagrams. During this period of rapid analytical development many accompanying bench tests were performed to measure the internal friction characteristic of various materials. Kimball, Lovell et al, [7] employed cantilever shafts with over-hung masses suspended from shaft end bearings, so that vertical gravity forces induced sinusoidal, once per revolution, bending stresses as the shaft rotated. The results showed that the hanging mass was always deflected to one side by a tangential damping force and its angular displacement was independent of the shafts rotational speed, but proportional to its vertical deflection. From bending stress/ strain relationships, the authors were able to relate the damping energy/ work done per cycle and hence a material/ damping loss factor to the angular off-set.

In 1933 Smith [14] analysed a rotor system with internal viscous damping and proved that without any external damping the system became unstable at the 1$^{st}$ critical speed. This point is called the instability threshold as the internal viscous damping had a stabilising effect up to this point, i.e. at subcritical speeds. Further, the presented formulae predicted that the threshold spin speed varied with the ratio of the internal to external damping. Other researchers [10-12] later confirmed these conclusions by differing methods and also showed that by including external damping the threshold of instability can be increased beyond the critical speed. By analysing the system using rotational coordinates and assuming isotropic supports, i.e. orthogonal coordinates fixed to the shaft, so that shaft forces/ moments seen from this perspective are independent of rotational speed and only the stationary environment is seen to rotate, reduces the mathematical complexity and simplifies the solution. This concept enhanced the understanding of forward and backward whirl, where a rotor spins about its

geometric centre due to the machine's driving torque, but also rotates, positively or negatively, about its bearing centres, (usually offset from the geometric centre by shaft deflection), to produce a whirl velocity. It was shown that the tangential direction of the internal damping force is proportional to the difference in these speeds and changes direction at the critical speed when they are equal. Instability results at supercritical speeds when the tangential force due to internal damping exceeds the equivalent external damping force.

It was also recognised that one of the main causes of internal damping came from interface friction within rotor joints due to flexing as cyclic bending occurred. Special test rotors were made to investigate shrink fits, in particular, as these were commonly used in turbine and compressor design. Robertson [13] et al concluded that axial fits should be short and as tight as possible, without exceeding the yield strength of the material and that if a long fit was required, it should be relieved in its centre to reduce the contact area. He also asserted that any friction which tends to limit a shaft's deflection will add to internal damping, e.g. as occurs between the teeth of gear couplings or the flexible laminations within disc couplings. But note must be made of the fact that different mechanisms cause different damping effects; for instance, mechanical rub produces a 'stick-slip' motion resulting in Coulomb damping, whereas hydrodynamic forces produce the classical viscous damping [58].

### 1.2.2 Balancing Machines

Separately to this fundamental research, manufacturers and engineers developed various methods of reducing the residual imbalance in rotating components and assemblies by attempting to correct the centre of mass eccentricity. In the late 1800's and early 1900's this was largely by trial and error, by placing a rotor horizontally on knife edges, using the 'roll-off' method. Mass was either added, or removed, in appropriate places, until

there was no tendency for the rotor to rock backwards or forwards or for an induced force to produce a cyclic rolling motion. This important work was performed by skilled fitters, but it could take 3 to 4 weeks, using a step by step approach, to balance a large steam turbine rotor assembly. Consequently, balancing machines were being developed to provide more accuracy and to speed up the process. Carl Schenck [21] commissioned such a machine in 1908 and later concluded a worldwide licensing agreement, in 1915, for a much improved, pendulum mounted machine, patented by Franz Lawaczeck, publication number, US1457629A.

The 1940's began to see electronic systems/sensors incorporated into balancing machine designs to measure both the magnitude and vector position of centrifugal forces imposed by unbalance, usually in two planes of the shaft axis. Special purpose machines were designed to meet the varying requirements of different industries [48,62], for example machine tool spindles required a very high degree of balance – equivalent eccentricity, *e,* of less than 0.000002 in, whereas motor car wheels only require an eccentricity, *e,* of less than 0.01 in. The designs either required the mounting of the test rotor in flexible/ soft or rigid/ hard bearing pedestals, so that the balancing speed of the rotor had a 4 to 5 times separation margin with the natural frequency of the supporting structure; this minimised response changes due to speed and ensured proportionality between the measured rotor response and its imbalance. For soft bearing designs, the test speed is usually well above the pedestal natural frequency, therefore stiffness and damping forces are small compared with the excitation and inertia forces and can be neglected so that shaft unbalance is directly proportional to pedestal displacement. In the case of hard bearing machines, the test speed is well below the pedestal natural frequency, so that damping and inertia forces are neglected and shaft unbalance is directly proportional to the pedestal reaction force. The choice of pedestal design and its test running speed was therefore often, by practical necessity, determined by the size/ mass of the rotor. Measurements were generally

made using electro-mechanical, moving coil transducers fitted to the bearing pedestals. Two types of systems were commonly used to measure or indicate the phase angle of the unbalance vector; either a stroboscopic light, triggered by the sinusoidal transducer outputs was used to light up the high point on a series of index numbers fastened on to the circumference of the rotor shaft, or the wattmeter method. In this case the output from a sine/ cosine wave generator, (2 electrical pick-up brushes at right angles, contacting a shaft mounted, circular resistance element), is fed into one side of a wattmeter and the vibration transducer output is fed into the other. Since a wattmeter only produces an output deflection when the two input coils have signals of the same frequency, both the unbalance magnitude and phase angle can be determined mathematically from the two outputs corresponding first to the sine and second the cosine generated inputs.

The 1950's saw balancing times and costs further reduced by the integration of metal removal accessories to high volume balancing machines, so that mass correction could be made during the measuring procedure, without the need to transfer the rotor to a separate machine.

### 1.2.3 Balancing Standards

However, even after undergoing a good balancing procedure, a perfect balance could never be achieved and the necessity to determine an appropriate level of balance quality, dependant on the type of application, became apparent and led to the introduction of several international standards whose aims was not only to produce a set of balance grades/ levels that would be economically functional, but also to standardise on terminology, measuring procedures and units of measurements etc. in order to minimise disputes between operators and venders.

A commonly employed standard is The International Organisation for Standardisation, ISO 1940/1, Balancing Quality Requirements of Rigid

Rotors [17,18], which reflects usage principally in metric systems and has been adopted by British, German and American National Standards; it categorises rotors, based on world wide experience, according to their type, mass, and maximum service speed, into a quality grade, G. Its corresponding number relates to the allowable level of vibration, mm/sec, measured on the bearing housing at the service speed and is the product of specific unbalance, (unbalance, g,mm/ rotor mass, kg) and the maximum angular velocity, rad/sec. Consequently, G is related to permissible residual unbalance measured in g.mm and allowable mass centre displacement, i.e. eccentricity, measured in microns, μm. This standard is based primarily on single components—for assemblies, it requires that the unbalances of component parts shall be added vectorially, taking account of expected unbalances resulting from assembly inaccuracies whilst also noting that further assembling positions may be different. ISO 5406-1980, The Mechanical Balancing of Flexible Rotors [22], classified flexible rotors into groups according to their balance requirements, established assessment methods for final unbalance and provided guidance on the establishment of balance grades. Rotors are classified to indicate which can be balanced by normal, modified rigid balancing techniques or which require some method of high-speed balancing. The standard is not an acceptance specification, but an aid to avoiding gross deficiencies, exaggerated or unattainable requirements.

The American Gear Manufacturers Association, AGMA 515 and 9000, Flexible Couplings – Potential Unbalance Classification [16], reflects usage principally in inch systems and is based on similar principles to ISO, but its method relates directly to flexible coupling assemblies. It specifies the unbalance in terms of a Balance Class Number, according to operating speed and coupling weight, representing the maximum displacement of the principal inertia axis, at specified balance planes, in micro-inches, μ-in.

More specifically, for the petroleum, chemical and gas industries, the American Petroleum Institute, API, which is of particular importance for the application sector of this thesis, has issued a number of design standards and recommended practices [15,19,20], which specify methods/ vibration limits for lateral dynamic analysis and very detailed balancing methods for couplings. These apply both to components and assemblies, with repeatability checks and specify unbalance limits, in inch and metric units, dependent on the proportionate mass at a balance plane and its maximum operating speed.

As an acknowledgement of the importance and difficulty of obtaining/ maintaining conditions of good balance, standards were also introduced that specify means of evaluating shaft and casing vibration, for monitoring, warning and shutting down machines, before serious damage occurred. ISO 7919-4 2nd Edition 2009-10-01 Mechanical Vibration – Evaluation of machine vibration by measurements on rotating shafts: Part 4 Gas turbines sets with fluid-film bearings [23] and ISO 10816-4 2nd Edition 2009-10-01 Mechanical Vibration – Evaluation of machine vibration by measurements on non-rotating shafts : Part 4 Gas turbines sets with fluid-film bearings [24], are two such examples.

### 1.2.4 Balancing Methods

Concurrent to the introduction of balancing standards were advancements in dynamic analysis and balancing methodology. All balancing techniques rely on making mass corrections in various axial positions along a shaft, but since it is unlikely that addition or reduction of mass can take place directly in the same plane as the inherent unbalance, special balancing planes are usually employed for this purpose, but their position is dependent on the rotor type. Rotors are generally classified for balancing purposes as being either rigid or flexible. Since all rotors are known to be flexible if operated at a high enough speed, the rigid definition determines that no significant

bending deformation must occur and that shafts rotate about their centre lines, which shall remain straight, although bearing pedestals may deflect. This generally limits the maximum operating speed to be less than 75% of its lowest flexural critical speed [32]. Rigid types are by far the easiest to balance since, even if mounted on flexible pedestals, there are no more than two modes of vibration/ critical speeds. Translator/bounce, where both ends of the rotor appear to go up and down together in a circular or elliptical orbit, resulting from a unidirectional, imbalance distribution, and a conical/ tilt mode, where motion of the ends are in anti-phase, resulting from an unbalance moment—caused by non-directional uniformity of the unbalance force vectors or gyroscopic effects. Hence, only two balancing planes are required to accomplish a state of good balance when operating near either of the critical speeds and these are generally positioned close to the pedestals for maximum effect.

Due to the greater difficulty of balancing flexible rotors they have generated much more research and produced two primary categorisations of methods for balancing them; known as the influence coefficient method and modal balancing.

The influence coefficient method was proposed by Thearle [50] in 1934, primarily for large electrical alternators weighing over 100 tons, and hence far too big for balancing machines. The technique considers single and two plane balancing of rotors at a given speed by individually placing trial weights at either end of the machine and measuring the response at each end relative to the prior response due solely to the rotor's residual unbalance. Assuming a linear system, vector algebra is used to determine vector operators or influence coefficients that are considered fundamental characteristics of the machine, from the measured change in vibration amplitude and phase angle due to the additional trial weights. These are then used to calculate the required magnitude and angular position of the correcting masses needed to balance the rotor. The complexity of the

method is increased when applied to multi-mass rotors, which typically require N trial runs for N balance planes—where response measurement is needed at each of the balance planes. More recently the use of matrix analysis and specialised computer programmes to determine the influence coefficients/ final trim balance corrections [48] are used. For instance, Goodman [55] in 1964 developed a weighted least squares calculation procedure to optimise the test data from multiple speeds and measuring locations. However, the use of trial weights does not accommodate other possible causes of unbalance, such as moment unbalance, caused by skewed discs, or shaft bow – caused by internal stresses induced during manufacture; hence it is possible that a good balance condition only applies at speeds close to the test speed and the shaft is unbalanced at other speeds.

The second method, modal balancing, is based on a detailed mathematical model of the system from which a relationship between the shaft displacement and the forcing function, for each of the critical speeds within the operating range of interest can be estimated. For analysis purposes two models have generally been employed: one where the rotor is considered as a series of point masses and the second where the shaft is treated as a continuous elastic body. The latter method, pioneered by Bishop [26], Gladwell [25,29] and Parkinson [32,33] developed a general unbalance distribution in terms of modal unbalance eccentricities. Using classical vibration theory and assuming simple supports, the critical speeds correspond to flexural natural frequencies of equivalent non-rotating beams with distinct deflexion shapes corresponding to particular modes of vibration—a simple bow for the 1$^{st}$ mode and a horizontal 'S' for the 2$^{nd}$ etc. Consequently, the components of each vibration mode are dependent on the particular parameters relating to that mode and the concept of orthogonality applies so that the differential equations of motion are independent of any cross-coupled forces or moments that may be present in other planes. It was claimed [32,48] that the unbalance distribution along

a shaft is not confined to any one axial plane, but that a modal unbalance distribution does lie in such a plane, which may vary from mode to mode. Hence, eccentricity is represented as a shaft distribution that includes parameter coefficients dependent on the mode/ natural frequency index number, $1^{st}$, $2^{nd}$ $3^{rd}$ etc. and presented as a mathematical series formulation that is integrated over the shaft length to establish the resultant unbalance for the mode.

With increasing computing power, the modelling of rotors as a series of elements/ point masses, gained prominence, allowing detailed analysis of much greater complexity, but producing systems with very large numbers of natural frequencies/ degrees of freedom, DOF's. Numerical solutions for this type of modelling are generally obtained by finite element analysis, (FEA), and such programs are today capable of solving extremely large matrix equations containing many thousands of elements. With the availability of such tools the desire for greater accuracy ensued and modifications to the method of modal balancing were reported. Kellenberger's [52] 1972 contribution studied the N modal planes of balancing proposed by Bishop et al, and also an N+2 method, which balanced the rigid body modes first, followed by the N flexible modes. The paper reported that the second method produced a greater degree of balancing accuracy. Racic and Hidalgo [45] in their 2007 review of practical balancing concluded that "there is no better or worse balancing method, only the more or less economical".

Nevertheless, in many cases the balancing process can be costly and time consuming, requiring several start-ups of the machine etc., which prompted researchers to investigate methods of balancing without trial weights [99]. It was reasoned that trial runs could be numerically simulated providing that the modelling of the rotor system is sufficiently accurate. An initial methodology, without damping, was proposed by Hundal and Harker [53] and later refined using more generalised analysis by Morton [31] and others, in the mid 1980's, to include damping, that also made allowance for different

bearing characteristics from the vibration data obtained during normal operation runs.

Due to readily available computing power and sensors, high speed/ response machine control software was frequently being installed on machines to protect bearings. This required the use of bearing proximity probes which were typically installed in bearing casings to measure shaft radial displacement, at any two coplanar positions, phased 90° apart, together with a shaft position sensor, (key phaser), which allowed the shaft orbit, within the bearing clearance to be monitored. Software then provided initial warnings and then if necessary initiated unit shut downs if the percentage of bearing clearance was considered dangerously low. This new facility also helps during site commissioning, by enabling production of frequency response curves, bode diagrams and polar plots to be made, during run-up and down tests. Hence, checks on actual critical speeds, damping ratios and bearing loads can be made so as to feed direct measurements to balancing processes.

Some researchers [44] made use of this additional data and incorporated complex algebra into their analysis and subsequent balancing programmes to present the x and y vector information as single modal parameter components, of eccentricity, unbalance mass/ centrifugal force, shaft deflection and bearing reaction load, etc. This real data allowed calibration of FEA models and provided increased analytical accuracy. As a result there followed several publications [34,41,43,51,54] of time saving methodologies, to enable balancing, for example, with a single trial weight test, or a single vibration transducer, or balancing without any trial runs at all. Further, Garvey [28] et al proposed utilising knowledge of the expected machine characteristics to introduce cost functions, based on the probability distribution of certain parameter variability or uncertainty, such as support stiffness. The authors reported, for example, elastomer supports whose characteristics change with temperature and age; and also noted that some

vibration, say at bearing pedestals, might be more tolerable than other synchronous vibration, at positions where stator/ rotor clearances are very low. By analysing the cost functions applicable to the machine in question, the authors were able to combine them to produce a weighted sum factor, which is then used to determine the required unbalance correction by minimising the worst possible cost.

The design of modern gas turbines requires faster, lighter engines utilising the very latest manufacturing techniques to produce longer, thinner and more flexible shafts. This has led to an increasing number of machines required to operate super critically and has spawned the requirement for economic procedures of obtaining good balance at these speeds. A practical procedure, suggested by Hylton [30] in 2008, demonstrated that by sharing the required balance correction between 3 balance planes, a good compromised state of balance can be achieved using only low speed balancing, which enabled machine operation at both sub- and super-critical speeds. The analysis of an assumed sinusoidal unbalance distribution and shaft deflection concluded that for a first balancing run, half of the resulting balance correction should be made at a central balance plane, with the remaining correction shared between the shaft end planes. A second balancing run is then made and the resulting balance correction shared solely by the end planes. The shaft is then considered balanced. This procedure proved successful on a number of engines used in the aerospace industry [30]. FEA analysis of other unbalance/ shaft geometric distributions produced other shape functions, which required a slightly different position for the 3$^{rd}$ balancing plane, but the same procedure remains applicable.

A good overview of well known balancing methods, including case histories of difficult balancing problems, is provided by Feese [67] and Grazier, 2004.

### 1.2.5 Lateral Critical Speed Margins

The above balancing procedures came about due to industry's ability to dynamically analyse very complex rotor shafts, usually by the use of FEA software; initially 2 dimensional, (2D), then 2.5D and now 3D. However, the use of such tools requires a greater level of engineering expertise than is traditionally available, i.e. rotor dynamic specialists. Hence, it remains common practice for lateral analysis to be simplified by being confined to individual driver and driven machines, as opposed to modelling the full drive train; since the flexible coupling between them is assumed to have 'moment release' and to act as a lateral hinge. However, this simplification makes assessing the critical speeds less accurate and therefore requires large margins between the maximum operating speed and the lateral critical speed, (LCS), for safe operation; typically 150%, as required by most API's [15,19,20]. This requirement is particularly problematic for manufacturers/users of high speed couplings (as highlighted by Corcoran [27] in 2003), since although the critical speed of a coupling is calculated as an individual item, based solely upon its bending stiffness, in reality its true value also depends on the neighbouring stiffness's of the driver and driven units. It is suggested that the 150% margin is only suitable where such stiffness's are extremely high, and a two times or higher margin should generally be used in the absence of a full train FEA analysis.

### 1.2.6 Gyroscopic Action

The importance of gyroscopic action on large discs and its contribution to critical speeds was well known and the general problem of free vibration of a single rotor on a light shaft had been considered by Timoshenko [61], Stodola [5], Green [56]. It was shown that gyroscopic action produced moments were proportional to the rate of change of the angle of tilt, known as the precession velocity, and acted orthogonally at 90$^{o}$ to the lateral displacement of the shaft, thereby resulting in moments that made positive

and negative contributions to the bending of the shaft, in the horizontal and vertical planes. This made the natural frequencies dependent on rotor speed and whirl direction, which in turn split the critical speed into two components and doubled their number, per bending mode shape. Forward Whirl, (FW) – which rotated in the same direction as the shaft rotation, resulted from the shaft stiffening moment and therefore increased the critical speed, while Backward Whirl, (BW), resulted from the lowering stiffening moment and produced a reduced critical speed. Figure 1.3, [85], illustrates the difference between these two whirling motions; it can be seen that in the case of FW whirl, the orbit of the heavy spot/ mass centroid is circular and that BW whirl produces an elliptical orbit—see Swanson [85] et al, and Sinou [72] et al, for detailed treatments.

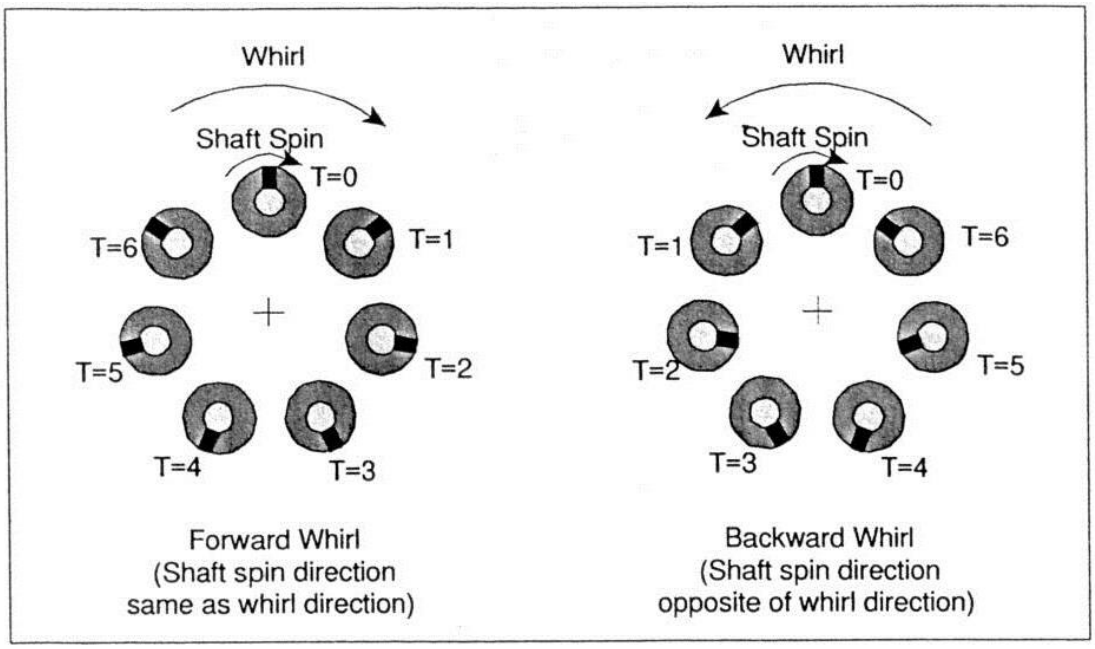


**Figure 1.3, [85],** FW and BW Whirl directions

Hence, gyroscopic moments are imparted when a disc's axis of rotation is made to change direction, and these can be positive or negative, depending on a machine's operating environment. With regard to balancing problems, since their action is to raise the speed at which a critical response occurs,

i.e. when shaft rotation coincides with a natural frequency having FW whirl, then knowledge of their contribution means the safe operating margins can often be increased.

Several studies made use of differing analytical techniques to solve the added complexity of gyroscopic action. Aleyaasin [82] et al made use of advanced computer capability to manipulate large matrix equations, a transfer matrix approach, as used in control theory, in which a series of flexible, distributed elements, connected together by rigid discs, forming lumped elements, were used to create a matrix model of a rotor. Laplace transforms are then applied to the differential equations of motion and the resulting damped natural frequencies solved by applying computer search/ optimisation algorithms, to establish a minimum value of the complex roots, thereby determining the natural frequencies. Whalley [84] et al reported, however, that the large number of natural frequencies derived from models of distributed parameters did not align with measured results, as practically they tend to vibrate at a single, dominant damped natural frequency. The authors therefore proposed that since the changes in deflection, slope, etc. are generally small when subjected to a load disturbance, the application of perturbation techniques, as used in wave mechanics, should provide results that were closer to reality. Laplace transformations were employed to determine a matrix output-parameter function, consisting of circular and hyperbolic terms and in-order to reduce the calculation overhead they were represented by a truncated power series.

An alternative technique is reported by Dutt [71] et al, who applied Lagrange's mechanics to obtain generalised equations of energy, and by equating the virtual work within the system to zero determined the equations of motion. This method was applied to a simple asymmetrically-placed disc on a flexible shaft, mounted on elastic supports with viscous damping, to determine the unbalanced response. The results confirmed that only the FW whirl natural frequencies were excited and also that the gyroscopic effects

caused the rotational speed, at which the unbalance peak response occurred, to increase.

### 1.2.7 Instability Problems

During the 1960's progress was made on the much more difficult analysis of general vibration, which included free and non-synchronous vibrations, and was applied to multi-disc systems, by Black [40] and other researchers. This was applicable to instability problems, which although less common, appeared in some self-exciting conditions, often associated with hydrodynamic action within bearings or seals. The general analysis produced four natural frequencies per whirling mode, in the orthogonal frame of reference – vertical and horizontal, both with FW and BW whirls, with only the synchronous modes being excited by unbalance. However, whilst most of the other natural frequencies might be excited by a sudden disturbing force, the majority are subjected to positive/ conservative re-storing forces and as a result perturbations decay back to a reference state and are deemed to be stable. The remaining unstable natural frequencies have negative/ non-conservative tangential forces that result from non-symmetric parameter matrices in the equations of motion, such as stiffness and damping. It is theoretically possible to excite all such cases by the external application of non-synchronous, alternating forces, or for self-excitation to occur if certain cross coupling conditions arise, such as between lateral, torsional and gravitational forces and/ or hydrodynamic fluid forces within bearings or between rotor and stator blades, seals etc. The analysis determines states of possible instability and equations governing their thresholds. Nelson [38] reported a good physical understanding of rotor dynamics and conditions affecting instability and claimed that the quality of rotor dynamic prediction depends as much on engineering insight as on the efficacy of the particular software used.

### 1.2.8 Rotating Coordinates

Classically, simple systems are analysed using a stationary or inertial coordinate frame of reference, which follows naturally from Newton's laws of motion relating accelerations to forces. However, for systems employing asymmetric rotors, where the lateral stiffness of the shaft varies from one angular plane to another, it is often very difficult to directly solve the fundamental equations of motion since the asymmetry causes the mathematical coefficients of the differential equations to be sinusoids instead of constants. In such circumstances, it is often found to be beneficial to employ a rotating coordinate system, i.e. one which is fixed to the shaft. Then, when viewed from this reference frame the sinusoidal nature of the coefficients disappears, since the rotating forces appear stationary, allowing the equations of motion to be more readily solved. However, such analysis fixes all points on a given cross section of the shaft relative to the rotating coordinates and is akin to defining their position in polar coordinates of length, $r$ and angle, $\omega.t$ , (angular velocity x time), which give rise to radial and transverse accelerations of the form:

$\frac{d^2r}{dt^2} - r.\omega^2$ and $2.\frac{dr}{dt}.\omega$ , respectively.

The latter term is the Coriolis Acceleration acting tangentially at right angles to the radial acceleration, i.e. the former term of which $-r.\omega^2$ produces a proportional force, (when multiplied by its mass), that opposes the spring force, inherent in the bending of the shaft and is subsequently known as, spin softening or centripetal softening. Such terms appear in the equations of motion to create natural frequencies, but since they are only produced in the rotating frame, the results from their inclusion have given rise to much debate, especially since spin softening can theoretically produce very low values of natural frequencies, often within the operating speed range of a machine. This phenomenon eloquently described in "Dynamics of Rotating

Machines", by Friswell [59] et al in 2010, where they concluded the following points:

- a stationary observer would view the shaft motion differently to a rotating observer
- it must be possible to make parameter transformations from the stationary frame to the rotating frame and vice-versa
- transformations doubles the number of frequencies creating pseudo-natural frequencies that are not real natural frequencies in the normal sense
- an excitable response in the stationary frame only occurs at pseudo-natural frequencies that are derived by adding the shaft speed to a FW whirl natural frequency or, by subtracting the shaft speed from a BW whirl natural frequency.

Other researchers have also cast some doubt on the spin softening phenomenon; Genta [37] and Silvagni, compared 1-D, 1 ½-D and 3-D FEA codes to investigate the effect on a rotating ring and a twin-spooled turbine rotor, without finding any evidence of a strong centrifugal softening effect on the critical speeds within the operating speed range of their models. A study by Chattoraj [78] et al, of a very flexible over-hung rotor, using rotating coordinates, produced a ½ critical speed response and an instability at 2.5 times critical. It is known that rotating coordinate analysis, although not generally excited by unbalance, does provide natural frequencies that can lead to instability under some conditions—such as cross coupling between lateral and torsional modes, Muszynska, 1984 [107]. It was therefore considered that the deflection at the end of the over-hung disc in the Chattoraj model could be large enough so that the internal damping effects contributed to the excitement of the ½ critical speed.

### 1.2.9 Complex Vibration Analysis

The benefits of 3-D FEA over a simpler analysis with fewer dimensions, is that as well as allowing warping of cross sections, as above, it also allows the actual rotor to be modelled including complicated geometry, flanges, fasteners etc. This encompasses shafts with non-circular cross sections and allows investigation of defects such as the formation of cracks. Nandi [39] and Neogy showed the benefits of such analysis using two examples; first analysing a uniform, simply supported shaft, with varying slenderness ratios and second, a tapered, cantilevered shaft with an edge crack. Of note is that the first example showed the convergence of FW and BW whirls, as the shaft diameter/ length ratio decreased, intuitively as a consequence of the reduction in the gyroscope moments acting on the individual discs that comprised the shaft. It is noted that divergence only became appreciable, (greater than 2%), as the ratio exceeded 0.3. This is also seen in example contributions reported elsewhere [59,115].

Additional interest that has spawned research study is the possible excitation of BW whirling modes, as proposed by Greenhill [96], after an FEA analysis of a large generator with fluid-film bearings predicted such a possibility. Their analysis of an off-centre, Jeffcott rotor, mounted on asymmetric supports, with damping, gave a lateral response to synchronous unbalance, at the BW whirling, conical/ tilting critical speed. This did not occur when supports were symmetric, i.e. had the same horizontal and vertical stiffness's. The difference being that unbalance produces a circular orbit when the supports are symmetric, coinciding with a FW mode and an elliptical orbit, coinciding with a BW mode, when they are asymmetric. It is apparent that it is necessary, for the orbit produced by unbalance, to match the orbit of the mode shape in order for the system to be dynamically excited. The fluid-film bearings used by the generator were significantly asymmetric and their experimental results showed signs of BW whirl excitation of a critical speed, but definite confirmation wasn't forthcoming

because the critical speed was just beyond the operating speed range. However, it was shown that external damping also reduces the peak amplitude of BW mode resonance, so that even though fluid-film bearings can be highly asymmetric, they also tend to over-damp this mode.

A similar effect is reported by Werner [73], who analysed the dynamics of elliptical shaft journals operating in fluid film sleeve bearings of electric motors. The varying displacement of the shaft on the oil film within the bearings represents a forced excitation with an elliptical orbit, which for a higher order mode with low damping is shown to excite a BW whirl mode.

Nevertheless, the use of 3-D FEA can still be problematic when presented with some practical, highly complex dynamic systems, as reported by Weimeng [70], for instance, who studied an asymmetric rotor supported on anisotropic bearings. Problems arise because the orthogonal stiffness/ damping forces of the rotor and bearing produce periodic coefficients, when viewed either in the inertia frame or the rotating frame, respectively, and the transformation of the governing equations between the two frames are too complex for accurate solution. Weimeng's proposed solution is to apply ANSYS, 3-D FEA in the rotating frame to the rotor, thereby fixing its coefficients and making that part of the solution possible and then determining the resulting time dependent, stiffness/ damping bearing matrices, as viewed from the rotor coordinates from a separate power series analysis, truncated for expediency, using the solving procedures available in MATLAB software. This is ongoing and further work is required to reduce the complexity.

Other specialised formulations have been made to FEA programs that assume discs are rigid and therefore treatable as lumped masses in order to allow for disc flexibility. Greenhill [74] et al use an axisymmetric harmonic finite element to analyse a disc as a series of annular rings, and for non-symmetric loading and deflection a Fourier series was used, which by use

of superposition, the total response was given by the sum of each harmonic contribution. The study showed that disc flexibility can produce some significant reduction in natural frequencies, even in some cases at the synchronous crossing points of critical speeds, but these were generally of the higher orders. In 2013 Varun Kumar [87] provided a good generic over-view of the command capabilities available in ANSYS, FEA, but again, due to the complexities of this type of analysis the importance of first establishing the “soundness of the basic model”, is stressed.

The general fundamentals of rotor vibration from basic concepts to self-exciting instability and the effects of cross-coupling, are well documented by Adams [89], in his book: Rotating Machinery Vibration – from analysis to trouble shooting, 2001. A more detailed study of instability, showing the effect of lateral and torsional cross-coupling, was reported by Gosiewski [97] in his 2008 paper. As with earlier studies, the analysis was simplified by considering a rigid disc mounted centrally on a massless flexible shaft, i.e. a Jeffcott rotor, but complicated by the introduction of torsional and gravity forces. As previously stated, rotating coordinates are generally used in stability analysis since they make constant the time dependent, cross coupling coefficients, to allow solution to the differential equations of motion and they produce the extra free natural frequencies, some of which lead to instability. Plotting these on a Campbell diagram produces several intersections between neighbouring natural frequencies and unstable speeds can occur in the vicinity of these intersections. However, not all of these intersections produce unstable behaviour of free vibrations. To distinguish them Gosiewski separately analysed the lateral and torsional vibrations applying cross-coupled, self-excitation feedback from the opposing mode as per standard control theory [104], to assess the likelihood of instability. He showed that for practical levels of unbalance, his model only produced significant instability at approximately 2.5 times the 1$^{st}$ critical speed.

Many instability problems are a result of non-linear mechanisms and their effect is described by Genta [35] who reports that the concept of a critical speed has been defined with reference to linear systems and it is not possible to define critical speeds in the case of non-linear rotors. However, a more general definition, which is often used for these systems, refers to the spin speed at which strong vibrations are encountered, but this is somewhat arbitrary as the amplitude of vibration is dependent on, among other things, the strength of excitation. Thus, the existence of a critical speed is not absolute - unlike the case for linear systems where the critical speeds are a characteristic of the system and are independent from any excitation.

One example that imparts significant nonlinearity is that of a breathing crack, which opens and closes periodically, due to say the force of gravity acting on a heavy rotor. Wu and Meagher [77] analysed a cracked, two disc, extended Jeffcott rotor and studied the vibrational differences between a cracked and an asymmetric shaft, to make problem identification easier. Sawicki and Kulesza [94] investigated the stability of a cracked rotor subjected to parametric excitation, i.e. excitation generated by the changing lateral stiffness of a breathing crack. As in the case of Wu and Meagher's contribution, the gravity force was assumed to be much greater than the unbalance force, thus ensuring flexing of the crack, and the crack stiffness was approximated by a cosine steering function. Their analysis produced stability maps which showed that the areas of instability reduced as the depth of crack increased, within reasonable limits, because of an increase in hysteretic damping within the crack.

Zhang [69] et al, 2014, used a non-linear FEA model to study the loss of stiffness in spline joints, which are often employed in the drive trains of large machines. They showed that for such assemblies, both lateral and torsional stiffness is lowered as a function of spline clearance compared with an integral model, and that they can be unstable at low loads, becoming stable

as the load increases. In their parametric model of a low pressure turbine rotor, the Young's modulus, for the joint material, was set to 70% of normal, to allow for this reduction and springs were also built on the main centring surface to simulate contact stiffness. The overall effect was to reduce the 1st and 4th critical speeds by up to 4% with little change for the 2nd and 3rd critical.

Further mechanisms containing non-linearity have been investigated, such as stiffness loss of bolted joints, Wang [81] et al, 2014; destabilizing effects within annular gas seals, Childs [68] and Vance [108], 1997; intermittent rotor/ stator annular rub, Zilli [80] et al, 2014; rub impact caused by oil rupture within squeeze film damper bearings, Shiau [79] et al, 2014, and the added effect of torsion to rotor/ stator contact, Edwards [75] et al, 1999. Differential heating radially across a bearing journal, particularly those subjected to large bending moments as in the case of over-hung rotors, has been studied by De Jongh [63,83] and Morton, 1996-98, and show that if of sufficient magnitude, shaft bending can occur, i.e. a thermal bow, particularly at the outboard bearing, thereby increasing the rotor imbalance. Supplementary studies by Marin [65], looked at the hysteretic behaviour of such rotors – the difference between run-up and run-down vibrational amplitudes versus speed. Nevertheless, such studies have been primarily of academic interest only and the vibrational problems caused by any of these effects have ultimately been overcome by improvements in component or system design, such as increasing the number of bolt fasteners at flange interfaces, the introduction of swirl brakes or pocket dampers within seals, or applying a heat shield to prevent thermal bow, etc.

A highly non-linear system of recent interest is one in which the driving force is influenced by the system's response, as in the case of a direct current d.c. electric motor, where the motor torque is a function of its speed. These "non-ideal" sources of supply energy can produce speed jumps characterised by an inability to realise certain speeds, typically near the

resonance frequency of a shared dynamic mechanism, such as the main system's foundation. Termed Sommerfeld effects, they result when an increase in supply energy that would normally develop an increase in speed, is instead absorbed by the vibration of the shared mechanism. If sufficient power is available to accelerate across the resonance, then a jump phenomenon can occur, or, depending on the level of system damping, either the system will fail or be stuck in resonance. Samantary [92] 2009 also reported these effects by modelling a simple Jeffcott rotor, driven by a d.c. electric motor to determine stability threshold speeds.

Another mechanism of general interest to researchers is the severe vibration that can result from the misalignment of coupling shafts between the driver and driven units of a transmission assembly. In order to investigate this phenomenon it is necessary to be able to accurately model the inherent stiffness and damping properties that exists generally within couplings. Tadeo [86] et al, endeavoured to do this by comparing FEA predictions of four coupling models, ranging from a simple massless, rigid rod, to a fully dynamic system with stiffness and damping in both angular and lateral directions, against the measured frequency response obtained from an instrumented, test rig, comprising two representative drive shafts connected by a commonly used, commercial coupling. They concluded that while the fully dynamic model produced the best representation, the most important parameters were its rotational/ angular stiffness and damping.

Further studies of coupling shafts, by Prabhakar [4] et al, investigated the start-up and run down characteristics of models with frictionless joints and also with stiffness and damping characteristics. The transient response for different angular accelerations were analysed using a finite element model, with both parallel and angular misalignment, in the time domain, to give vibration data as the operating speed passed through the critical speed. Signal processing was applied using a continuous wavelet transformation to obtain time scale information. The results produced sub-harmonic

resonant peaks when the coupling was misaligned, corresponding to one-half, one-third and one-fourth of the critical speed, which were not evident without misalignment. Although of small amplitude when compared with most problems of unbalance, it was suggested that this type of analysis could be of use when trying to detect coupling misalignment, at the early stages of machine operation before reaching steady state.

The effects caused by residual shaft bow or bent shafts, can produce interesting cases of apparent self-balancing and phase jumps, as well as balancing difficulties. These are usually caused when the angle between the residual bow vector and that of initial unbalance, is approaching 180º, with magnitudes such that at low speeds the resultant vector of imbalance is governed mainly by the shaft bow and at higher speeds by the unbalance. An intermediate speed usually exists whereby the two can cancel each other out, resulting in near zero shaft deflection and reaction load. Such cases have been studied by Nicholas [46] et al. and later by Rao [90].

### 1.2.10 Estimating Residual Imbalance

Knowledge that rotor imbalance can be derived directly from the measured vibrations taken from a machine's bearing pedestals, providing that an analytical model of sufficient accuracy is available, has recently prompted a further area of study. Research has been conducted into various methodologies, together with the required level of model efficiency, needed for the accurate evaluation of rotor imbalance. Lees [42] et al showed that useful estimates for imbalance may be derived from a good numerical model of a rotor that required only an approximate model of the bearings and its supporting structure. The modal parameters of the rotor model were determined either experimentally, with the rotor suspended by slings, or computationally via FEA. The supporting structure mass and stiffness matrices were determined from pedestal vibration measurements of displacement and frequency. The system model was found to be suitable

as long as the bearing oil film stiffness was greater than, or in the limit equal to, that of the supports, which is applicable to most turbo-machinery installations. Further studies followed, which were based on the whole frequency range of pedestal vibration, taken solely during machine run-down. However, the study assumed that the number of modes were equal to the number of bearings, leading to some inaccuracies in cases where large flexible foundations had many modes of natural frequencies. Lees [113,49] et al overcame this problem by splitting the frequency range of the foundation model into sections, thereby producing different mass and stiffness parameters for each frequency mode. The robustness of this methodology was checked by performing a sensitivity analysis, by introducing perturbation errors into the rotor and bearing models and determining the resulting change in the calculated imbalance. The conclusions were that the enhance model gave generally good results which were particularly robust in terms of its phase estimation. Whereas previous studies assumed the rotor bearings to have linear characteristics, Sergio [36] analysed an aircraft engine rotor, running on squeeze film damper bearings that were highly non-linear. This added complication was solved using a “Receptive Harmonic Balance Method”, i.e. one in which the equations of motion are expressed in the frequency domain, relating displacements to corresponding excitation forces and determined through Fourier analysis of their time histories, using a process of iteration.

### 1.2.11 Fault Diagnosis

Together with the ever increasing performance and reliability demands placed on today’s rotating machinery, the need for reliable control monitoring and fault diagnosis capability has increased. Moreover, since occurrences of mass unbalance, bowed and cracked shafts are among the most common of rotor dynamic faults, procedures for identifying and correcting such faults have received much attention. Consequently, over a period of time, these processes have moved away from human

interpretation of changes in parameters, such as noise, vibration and temperature, to fully computerised monitoring and control, often remotely over great distances. To be successful these methods rely on a detailed mathematical model-based diagnostic programme to predict a system's normal dynamic behaviour such that monitored changes in characteristic parameters can be analysed to determine the cause and the possible severity of a fault. Edwards [47] et al, produced a good, state of the art, review on the subject of fault diagnosis of rotating machinery, in 1998. Madden [76] et al introduced uncertainty in the form of additive noise and plant perturbations and established bounds to differentiate between the mathematical model and data received from the actual system. This system of model validation, coupled with model reconciliation – a method of model correction, provided a robust technique that better enabled the identification of damaged dynamics.

### 1.2.12 Active Balancing

In addition to work into control monitoring and fault diagnosis, a large amount of complementary research has been carried out into real-time balance correction techniques. Zhou [98] and Shi produced a good review in their 2001 paper, "active balancing and vibration control: a survey". Acknowledging that active control systems are more complicated and costly to install, it is claimed that this is usually offset by increases in flexibility to adjust for a range of vibration modes, which might be encountered during operation, especially in very high speed application. Typically, there are two major control techniques that make use of auxiliary actuators to reduce vibration; 1) a Direct Active Vibration Control, (DAVC), which applies a lateral load to the shaft from an external force actuator, such as a magnetic bearing and 2) a shaft mounted, mass redistribution actuator, which re-positions one or more trim balance masses to align the mass centroid of the shaft with its axis of rotation. Both are used in conjunction with feedback

sensors and system modelling software, as part of an integrated vibration control system.

As reported by Zhou [98] and Shi the first control technique, DAVC, can be achieved using many variants of actuator, including electromagnetic, hydraulic, piezoelectric etc. but the most common is the active magnetic bearing. The latter produces controlled levitation and hence reduces friction and mechanical wear, but also has the high speed response necessary to deliver a fast-changing lateral force, capable of suppressing both synchronous and transient vibrations. However, Burrows [114] et al reported that their limitation is the maximum force available in a given design envelope, since typically the load capacity of a magnetic bearing is only one-tenth of that of an equivalent sized hydraulic bearing. Moreover, for support and layout design purposes, the bearings are usually positioned at, or close to, shaft ends, but for balancing correction purposes they are more effective at a third or half span positions, hence some installations utilise multiple bearings to accommodate both functions, but at the detriment of increased complexity and cost. Further, Burrows [114] et al, considered the total system integration of controllable bearings/ actuators, vibration feedback sensors, on-line adaptive controllers and control algorithms etc., necessary to achieve good performance, together with re-configuration requirements in the case of faults. Mushi [88,91] et al, furthered this work with analysis and test of active magnetic bearings, used to control rotor-dynamic instability, often seen in turbo-compressor sets resulting from aerodynamic, cross-coupling stiffness, effects. However, both studies concluded that the evolution of smart systems, of self-adapting vibration control, represents a work in progress and that further development is still necessary.

An example of the second control methodology used in active balancing employs a mass redistribution actuator for use on large shaft lines and was investigated by Alauze [100] et al. A combination of balance correction masses were positioned by an actuator assembly, consisting of two electric

stepper motors, running in a circular, pinioned track and each driving a “satellite mass”, so that the magnitude and angular position of the resultant vector sum of combined balance correction, could be adjusted remotely, in real time. Control software was used to continually monitor the shaft vibration and determine the required movement of the satellite masses to achieve the required balance correction. Results, from large scale, single actuator testing, showed vibratory amplitudes to be reduced by 60% and overall control was reported to be excellent. In addition, this type of actuator is smaller and uses less power owing to the relatively small moveable masses, than DAVC magnetic bearing variants which act to control the entire rotor mass.

A similar technique, as reported by Horst [95] and Wolfel, utilises the high stiffness and fast dynamic response characteristics of surface bonded piezoceramic actuator patches. These are generally attached to the outside diameter of a rotor shaft in two orthogonal sets of diametrically opposite pairs that are energised out of phase with one another, so that as one is applying tension whilst the other is applying compression. Hence, the actuator assembly has the capability of creating two, orthogonal bending moments, at each actuator locality, so that multiple assemblies can be controlled to oppose any shaft bending resulting from residual imbalance, or other dynamic forces. They investigated suppression of lateral bending vibrations of an elastic shaft by such means and developed mathematical models for actuator implementation with theoretical simulations which demonstrated the potential of achieving good active vibration control and produced test rig validation of frequency response to noise excitation, but noted that further work is still required. Sloetjes [64] and De Boer’s considered stability problems resulting from shaft mounted piezoceramic sheets working in conjunction with rotor and stator mounted feedback strain sensors. They produced several different algorithms to add/ modify control functions such as: low-pass noise filtering; position, derivative and integral sensor feedback, etc., to cope with various stability scenarios. In addition to

studying piezoelectric actuators for control purposes, their work also analysed the possibilities of extracting electric power from such devices to function as an internal power source, to produce a self-energising system. Electrical generation results from periodic straining that occurs when a flexible rotor bends under its own weight during rotation. The general conclusions were that, to date, the proven effectiveness of piezoceramics for both, vibration control and power generation, justified further research to produce practical devices.

As an alternative to actuator control systems, self-balancing methods can be employed for rotors that operate at supercritical speeds. Concentric multi mass devices are clamped onto the rotor and make use of the fact that when the geometric centre of a shaft is displaced away from its axis of rotation, due to rotor imbalance, then centrifugal forces acting radially out from this axis, on the concentric balancing masses, tend to move them radially away from the geometric centre. At subcritical speeds, the shaft centroid, i.e. the heavy spot, lies beyond the geometric centre, further away from the axis of rotation, so that this movement adds to and increases the shaft residual imbalance. However, at supercritical speeds, due to the phase rotation of the mass centroid approaching 180º, the movement of the balancing masses away from the geometric centre is in the opposite direction to the mass centroid, so that overall imbalance is reduced. An Automatic Ball Balancer [93,101,102], (ABB), for example, is a device consisting of a series of balls that are free to travel around a bearing race, attached to the shaft at predetermined balancing planes. During supercritical operation centrifugal forces on the balls produce rotation which automatically re-positions them such that the principal axis of inertia is moved closer to the rotational axis and hence reduces shaft vibration. Because imbalance does not need to be determined beforehand, ABB's are ideally suited to applications where the level or position of imbalance varies during operation, e.g. optical disc drives, machine tools and washing machines

[112]. The later works on the same principle, but employs an annular mass of fluid, as opposed to balls, to achieve balance correction.

### 1.2.13 Vibration Absorbers

A further method of reducing machine vibration is by the application of vibration absorbers. Devices such as the Lanchester Torsional Damper [106] and the Stockbridge Damper [105] have been in use and subjected to much in-depth analysis since the 1920's. In essence, if the main system of a vibrating structure is modelled as a single spring/ mass system with just one degree of freedom, (DOF), producing one natural frequency, then by the introduction of an auxiliary spring/ mass system, so as to produce a two DOF system; the first natural frequency of the host system, is replaced by two new natural frequencies, one above and one below the first, as shown in Figure 1.4, [105]. Therefore, it is possible to avoid a resonant condition by ensuring that the two new natural frequencies are sufficiently separated from a source excitation frequency. Hence, if the vibration of the host system is caused by resonance, this can be suppressed by tuning the second, "vibration absorber" system to reduced or completely neutralise it, providing the dynamic characteristics and frequency of excitation are known with sufficient accuracy and are not subjected to drift. However, there are still two natural frequencies that can be excited if they coincide with the operating frequency of the machine. In order to overcome this problem, damping is usually added to the design of the absorber [109]. Also, deviation from the tuned condition, i.e. mis-tuning of some vibration absorbers or neutralisers can lead to an actual increase in the host system vibration. To avoid this possibility, smart or adaptively tunable, vibration absorbers have been developed – as reported in Bonello's [116] review of design principles, concepts and physical implementation. Nevertheless, this technique of vibration attenuation is usually applied to machine housings or foundations and is not suitable for correcting source excitations, such as rotor imbalance.

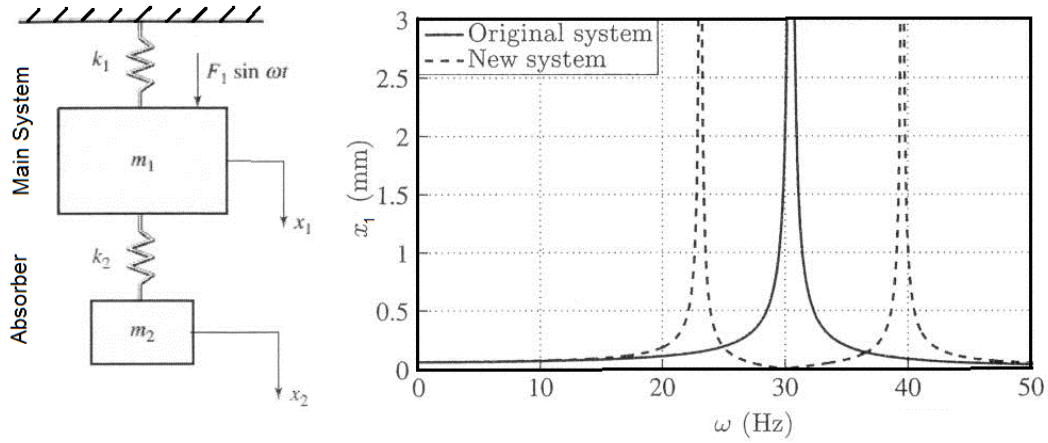


**Figure 1.4, [105],** Model of a Vibration Absorber and its Frequency Response

## 1.3 Problem statement

Siemens Industrial Turbomachinery have several Mechanical Drive contracts that have consistently, over a long period of time, been extremely difficult to dynamically balance across the required operating speed range. This in turn leads to unacceptably high vibration at the bearings and subsequent engine shut down. Generally, this problem has been associated with long coupling shafts operating at high speed. It should be noted that for a given length, the coupling design is often a compromise between the coupling lateral flexibility, (i.e. maintaining a suitable lateral critical speed margin), its maximum diameter, (in order to limit the heat generated by "churning" effects) and the need to meet dynamic ½ weight requirements of the driven unit. The consequence can be that from a balancing point of view, the coupling is more flexible than would be preferred.

A typical example of the balancing problems, often seen at site, is shown in Figure 1.5, an actual polar plot of bearing displacement, taken during site commissioning, whereby it is seen that the displacement, (a measure of

reaction load), varies angularly through 85 degree as the speed increases from 7200 rpm to 8940 rpm.

Trim balancing is given at predetermined balancing planes along a shaft so as to produce local changes in mass, positive or negative, in order to correct residual unbalance. But, since a trim balance adjustment can only be applied at a fixed angular position, the imbalance can only corrected for one particular “compromised” speed and not across the whole operating speed range.

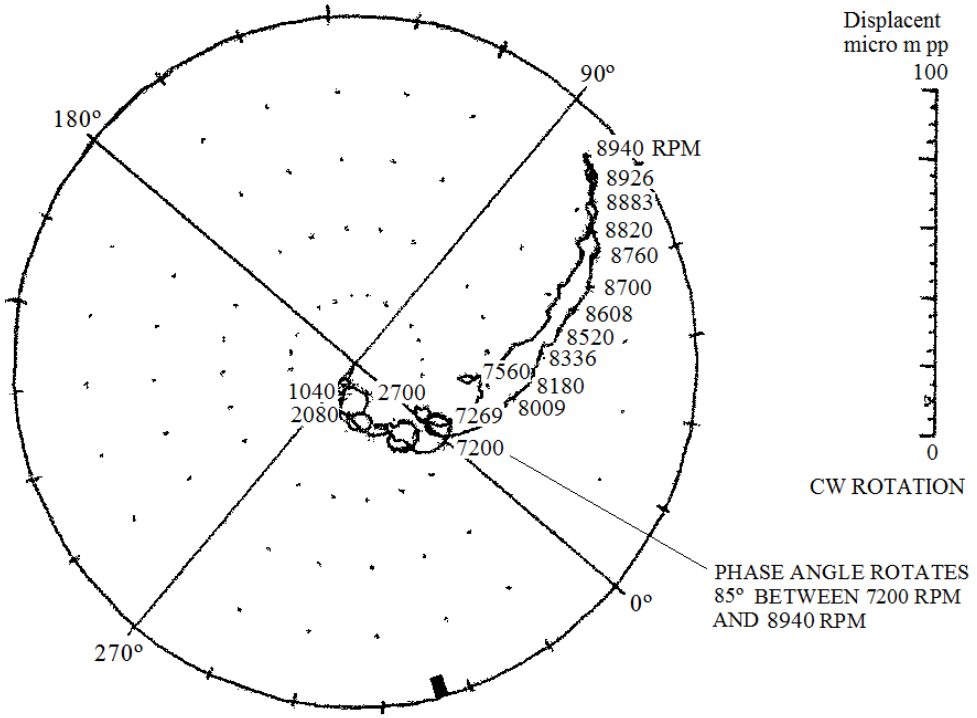


Polar Plot of PT 1X Vibration at PT Rear Bearing

**Figure 1.5,** Polar Plot showing a typical balancing problem often encountered with high-speed flexible coupling shafts

An alternative theory of the cause of this bearing reaction load vector change, to the usual cause of the operating speed passing through a lateral

critical speed, is demonstrated in Figure 1.6, and its analysis led to a proposed solution and ultimately to a new balancing methodology.

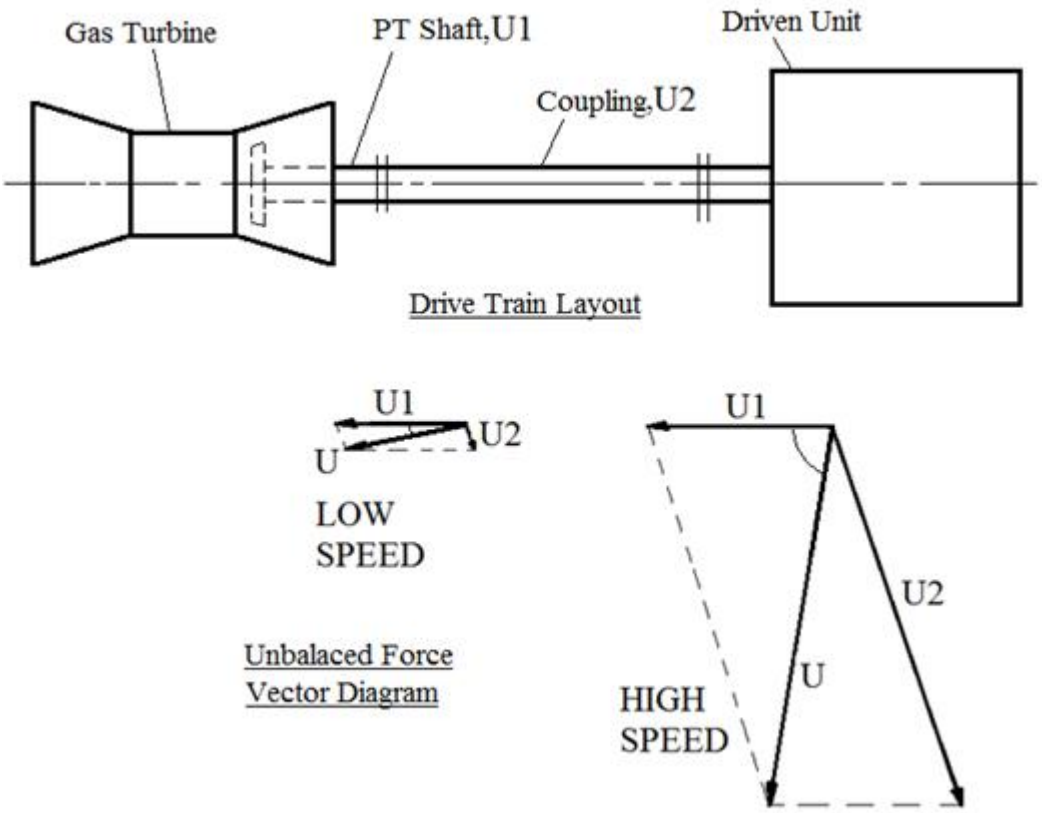


**Figure 1.6,** Schematic of PT and Coupling Residual Unbalance Vectors

It was noted that if the coupling shaft, between the engine power turbine shaft, PT shaft, and the driven unit is sufficiently flexible then, as the operating speed increases, the magnitude of its unbalance vector can increase significantly due to its deflection such that it would tend to become dominant with respect to the neighbouring PT shaft unbalance vector. Then, the phase angle of the resultant vector, i.e. the bearing reaction load, would appear to change with speed.

This is shown by the schematic representation in Figure 1.6, where U1 is the PT residual unbalance vector and U2 is the coupling residual unbalance vector. Vector U is the resultant of U1 and U2. It can be observed that if U2

were to increase in magnitude by a greater amount than that expected due only to rotational speed, (that is, due to flexing of the coupling shaft), then the resultant phase angle change with speed can be significant. A worked example of this is given in chapter 2, section 2.6.

## 1.4 Aims of this Research

Section 1.2 confirmed that the problems of machine balance and their subsequent methods of balance reduction stem back more than a century. However, there remain significant problems with techniques currently being used. The main techniques for balancing flexible rotors, i.e. Influence Coefficient and Modal Balancing were introduced in the 1930's and 1950's respectively. Since then improvements in overall balancing methodology have been largely the result of two distinct changes; 1) a reduction in the residual eccentricity of the rotating assembly, by advances in machining capability, (providing tighter tolerances on geometric features, such as roundness and straightness etc.), plus better control of material properties, (density, expansion/ contraction, creep etc.) and 2) greater analytical capability, due to the vast improvement in computing power, thereby allowing shafts to be analysed to greater depth, into evermore complex elemental sections. Nevertheless, the basic balancing techniques, although now producing more accurate results, often in greater detail and in shorter/ less costly time spans, have remained largely unchanged. They still aim to counter-balance residual eccentricity by making, often multiple, corrections of trim balance, at various locations along the length of the shaft.

Despite advancements, costly problems remain for industry, as highlighted in the previous section, thus warranting further investigation. It is the aim of this research to assess the fundamental deficiencies of current methods of applying trim balance correction and subsequently to investigate the application of an improvement, which emanated from this assessment, by

way of a novel methodology of balance sleeve compensation [120,121,122,123,124], as shown schematically in Figure 1.7.

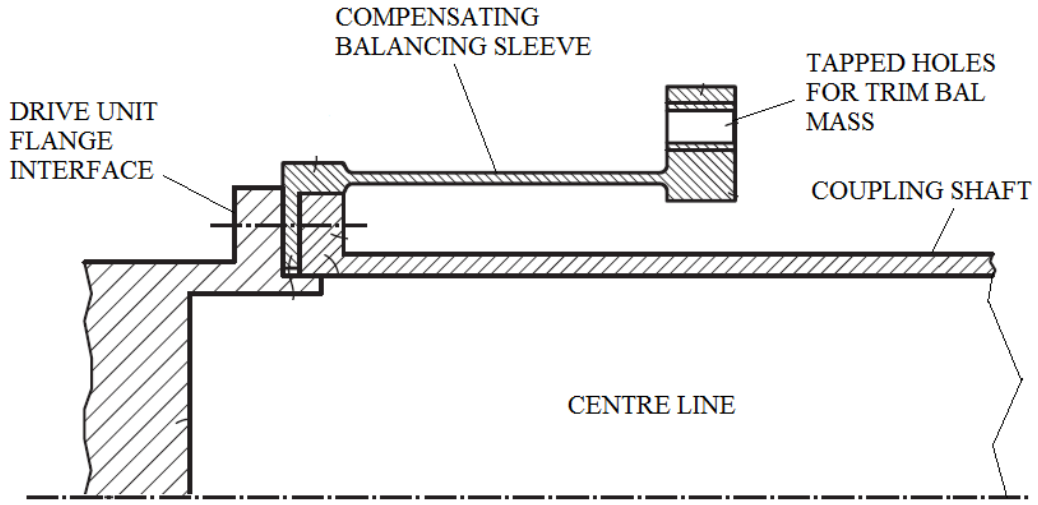


**Figure 1.7** Schematic of a Compensating Balancing Sleeve

## 1.5 Main contributions

The following chapters are deemed to offer the most revealing new insights into improving current methods of balancing high-speed, flexible shafts.

**Chapter 2:** this chapter investigated deficiencies of current methods of trim balance correction and the cause of imbalance vector change, seen at some problem industrial sites with very flexible couplings. This investigation led to the invention of a novel method of applying trim balance and further analysis of a specialised case of uniform eccentricity determined the fundamental mechanics of balance sleeve compensation.

**Chapter 4:** this chapter expands the analysis to a generalised case of any number of concentrated imbalances and determined that conversion to an equivalent encastre shaft depends on the equalisation of the sum of the balancing moments to the sum of the encastre fixing moments. This realisation ultimately leads to simulation being achieved by a single balancing sleeve at one end only, and subsequently to the ability to additionally eliminate/nullify the $2^{nd}$ critical speed.

**Chapter 5:** this chapter introduces a shear force reaction ratio, *RR,* which shows that the proposed methodology has the effect of further reducing the equivalent level of eccentricity achieved by prior balancing procedures, by as much as 25x and determines its application to most practical shafting. It further demonstrates its suitability to higher critical speeds by definition of a Simulation Ratio, *SR,* which determines the shaft stiffening effect and the reaction load reduction benefits to be gained from applying compensation to shaft ends only.

**Chapter 8:** presents laboratory test results of a scaled industrial turbine coupling shaft which supports the analysis determined in the previous

chapters and confirms the fundamental requirements of the new balancing methodology, i.e. that shaft balance is improved by increasing the level of encastre simulation.

# Chapter 2

## 2.1 Causes of Residual Imbalance

Residual imbalance and the centrifugal forces emanating from it during rotation occurs when the centroid of mass of an elemental section of a shaft is offset from its axis of rotation. This can occur in a variety of ways, as given below, but it should be noted that it can never be completely eliminated.

a) Geometric profile errors resulting from imperfect machining. These are affected by the manufacturing capability to meet the primary machinery tolerances of roundness, straightness, concentricity, squareness etc. which can produce oval or bent shafts, or hollow shafts with uneven wall thickness.

b) Material faults, such as non-homogeneous material, with density variations or inclusions. Also, uneven heat treatment can cause bending of shafts under differing environmental loading conditions.

c) Interface joint errors are known to be a frequent cause of eccentric operation or “shafts not running true”. These can result from machining errors, as above, but also from movement under load with temperature changes, i.e. spigot and clamping faces, sliding or rocking on high spots. Also, it is known for spigot clearances to be opened up by centrifugal forces, thus enabling radial movement to occur. Another, frequent problem seen with joints is a result of dirt entrapment, preventing proper seating of mating faces.

d) Gearing problems are often the cause of inconsistent movement of shaft centres, with load variation or due to machining errors. For example, many shafts are centralised by forces acting at the point of contact of one or more meshing gears, which in turn is a function of factors such as: transmitted torque, lateral loading and mating friction.

e) Surface damage can cause displacement of mass, improper seating of joints or, in exceptional cases, bending of shafts.

The effects of these issues can be minimised by good design and manufacturing control so that residual imbalance is kept to a minimum. Nevertheless, perfect balance is never possible and for high-speed shafts, component and assembly balance procedures are always necessary.

Trim balance corrections are normally made to high-speed shafts in two stages. First, on low speed balance machines where mass is usually removed by localised grinding of the outer diameter of a number of balancing bands - specifically incorporated at intermediate positions along the shaft length. Secondly, during site commissioning, operating at high speed, using feedback from the bearing sensors to determine the angular position and magnitude of added masses, which are usually mounted into pre-machined, trim balancing tapped holes, at flange interfaces. In both cases the effect is equivalent to moving the local centroid of mass to produce a reduced component of eccentricity.

## 2.2 Trim Balancing Errors and Principle of Improvement

The effectiveness of current methods of trim balancing, with regard to flexible shafts, is considered as follows. Figure 2.1 shows a typical, schematic section of a plain flexible shaft, with two elemental sections, one containing a portion of shaft residual eccentricity, $e$, and the other containing a portion of shaft balancing eccentricity $e_b$, produced by the addition of a trim balance mass, affixed to its outer diameter, (not shown). For balancing purposes $e_b$ is 180º out of phase with $e$.

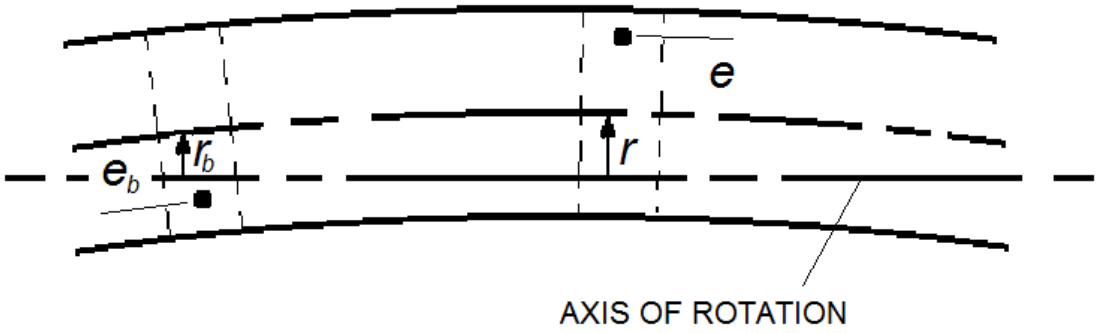


**Figure 2.1**, Section of a plain flexible shaft

Considering the centrifugal forces, (*CF*), acting on both sections of mass, $\delta M$, where $\omega$ is the angular velocity and $r$ is the local shaft deflection.

The shaft imbalance force is : $CF_{shaft} = \delta M.\omega^2.(r+e)$

and the balance correcting force is: $CF_{bal} = \delta M.\omega^2.(r_b - e_b)$.

As illustrated in Fig. 2.1, it is apparent from the flexing of the shaft that *e* is greater than $e_b$ and as a consequence the shaft is underbalanced. The bracketed terms represent the radius of the imbalance centroids, being positive for the shaft and negative for the portion of balance correction, due to its position being 180º out of phase. Hence, at higher rotational speeds the shaft deflection increases, causing the trim balance term to reduce, and the shaft imbalance term to increase.

It can therefore be seen that while trim balance corrections made on the shaft itself, (by adding or removing mass), would be satisfactory for rigid shafts, or those where the shaft deflection is very small, they are less effective for shafts with a high degree of flexibility. Hence, it can be seen that flexing of the shaft is detrimental to the efficiency of the trim balance mechanism, so in this respect, siting the trim balance on the shaft at a point

of minimum shaft deflection would be beneficial. However, even when positioned at the shaft ends, it is far from ideal and it is worth considering other mechanisms of providing trim balance correction.

Chapter 1, section 1.3, described how one possible mechanism that could cause imbalance vector change would be implemented when the rotating shaft or component has in-built compliance, thereby leading to amplification of its imbalance forces as speed increases. If this occurs adjacent to a neighbouring residual imbalance, that doesn't have this amplification feature, then by addition of the two vectors the resultant imbalance reaction imposed on the bearings can suffer from very large angular changes, sometimes approaching 180°. The cause of this can be very counter-intuitive and lead to misinterpretation, such as the operating speed having passed through a drive train critical, since it is commonly known that under such circumstances the response vector lags the excitation vector by 90° and that damping forces within the bearings continue to produce vector rotation up to 180° as the speed extends well beyond the critical. This in turn can lead to very costly and time consuming investigations, since in the Oil and Gas market for instance, API design rules demand very large lateral critical speed margins specifically to obviate this condition.

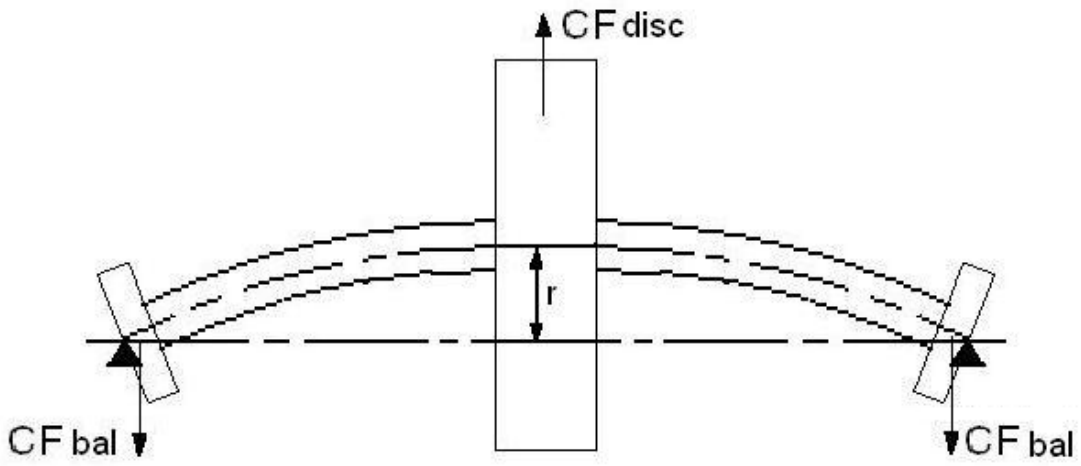


**Figure 2.2**, Large disc on a flexible shaft

However, if imbalance amplification is the cause of the problem, then a possible solution lies in an improved method of trim balance.

To show the impact of shaft flexibility, Figure 2.2 shows a heavy disc, mounted centrally on a light, flexible shaft, with mounting flanges positioned at the shaft ends, which are used for trim balancing. It is assumed that the support bearings, not shown, have very high radial stiffness, but have very low angular stiffness, such that the shaft can be deemed to be simply supported. This arrangement is commonly used for analytical purposes and is known as a Jeffcott rotor. It is chosen here as it simplifies the mathematics, but still demonstrates a typical drive train problem of obtaining a suitable balance at both low and high speed. At low speed the shaft is essentially straight and imbalance, i.e. centrifugal force, *CF*, acting on the disc as a result of its eccentricity, $e_{disc}$, is corrected by adding balance weights at the balance flanges, 180° out of phase, thereby creating eccentricity at the flanges, $e_{bal}$, so that the vector sum of the *CF* at the 2 flanges is equal and opposite to the *CF* at the disc. Hence, the net reaction load transferred to the bearings is nominally zero.

Hence for balance: $2.CF_{bal} = CF_{disc}$ (2.1)

giving, for low speed: $2.M_{bal}.\omega^2.e_{bal} = M_{disc}.\omega^2.e_{disc}$ (2.2)

and $e_{bal} = \frac{M_{disc}}{2.M_{bal}}.e_{disc}$ (2.3)

where $M_{disc}$ = Mass of Disc and $M_{bal}$ = Mass of Balance Flange

However, at higher speed the *CF* acting on the disc increases due to speed, thereby creating some bending of the shaft, which adds to the disc eccentricity to further increase disc *CF*, giving:

$$CF_{disc} = M_{disc}.\omega^2.(e_{disc} + r)$$

At the balancing flanges there is negligible shaft deflection so that the only increase in flange *CF* is due to the speed increase. Therefore, the balance criteria given in (2.1) is no longer met and a balancing error occurs that is proportional to the disc deflection, *r*,

i.e. the shaft imbalance force, applied to the bearings, = $M_{disc}.\omega^2.r$ .

Consequently it is not possible to fully balance the shaft for operation at both low and high speed. The normal solution is to minimise the disc eccentricity by making balance corrections at the disc, thereby minimising the shaft deflection, *r,* but in many drive shafts of more uniform cross section, as in coupling shafts, for instance, this is not always practical and the result is generally a balancing compromise over the operating speed range.

To correct the balancing error, it is required that the trim balance weights should also have a system of compliance to replicate the *CF* amplification seen by the disc.

It is noted that this is a very simplified analysis based the balancing criteria of minimising the reaction loading applied to the bearings, resulting from the source of the balancing problem given in chapter 1, section 1.3. But, in other instances, particularly for bladed shaft applications, the balancing objective can be to reduce shaft deflection/ blade tip clearance, thereby reducing component wear and improving overall running efficiency.

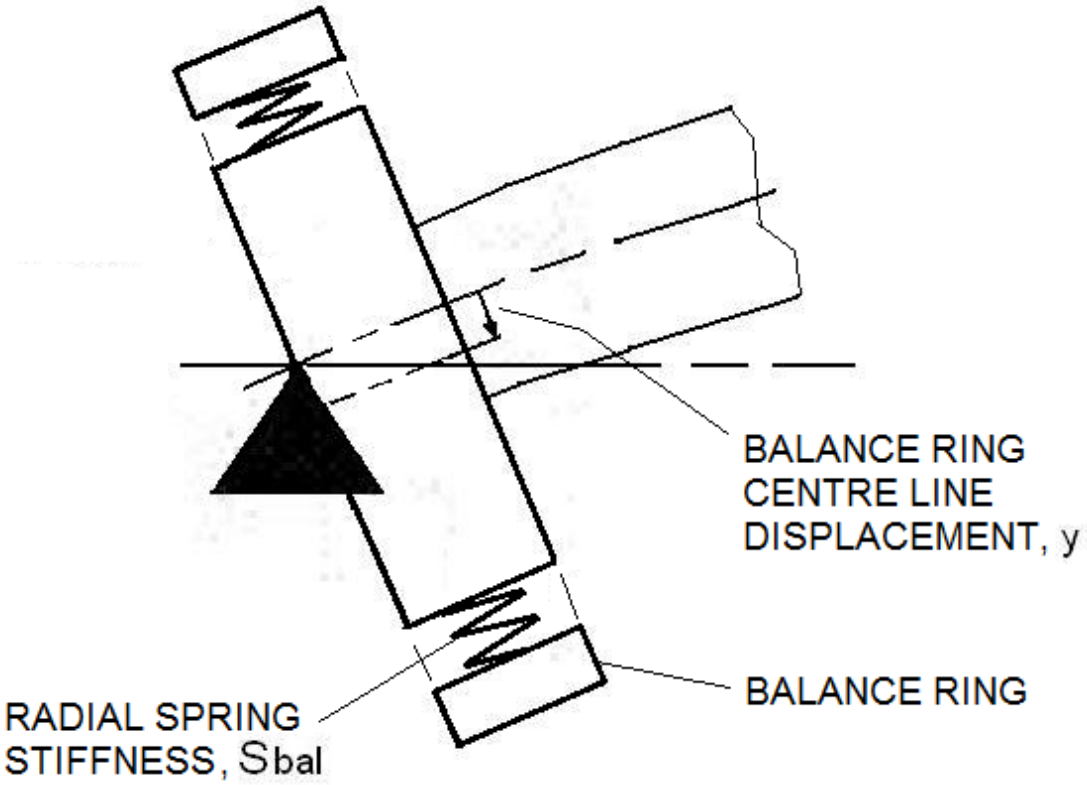


**Figure 2.3**, Mounting flange with in-built compliance

A simple schematic model of such a system is shown in Figure 2.3, where a balance ring is flexibly attached to the shaft, allowing radial movement only, by either a compliant collar or a number of radial springs. The *CF* imposed on the balance ring at higher speeds is then resisted by the net spring compression force and results in a radial deflection, *y*. Then to maintain balance, from (2.1), it is required that:

$$2.M_{bal}.\omega^2.(e_{bal}+y) = M_{disc}.\omega^2.(e_{disc}+r)$$

and subtracting (2.2) gives: $2.M_{bal}.y = M_{disc}.r$ (2.4)

Since no damping exists in this model, the individual *CF's* can be equated directly to their stiffness forces, giving:

$CF_{bal} = S_{bal}.y$ and $CF_{disc} = S_{shaft}.r$

and substituting in (2.1) gives: $2.S_{bal}.y = S_{shaft}.r$

Substituting for $r$ in (2.4) then gives: $$S_{bal} = S_{shaft}.\frac{M_{bal}}{M_{disc}} \qquad (2.5)$$

As a practicality check: $$\omega^2_{bal\_crit} = \frac{S_{bal}}{M_{bal}} = \frac{S_{shaft}}{M_{disc}} = \omega^2_{shaft\_crit}$$

where: $\omega_{bal\_crit}$ = critical speed of the balance ring, rad/sec

and $\omega_{shaft\_crit}$ = critical speed of the shaft, rad/sec.

Therefore, this very simplified model identifies that by using normal trim balancing methods, a condition of balance cannot be readily maintained across a wide operating speed range. But it also suggests a potential balancing principle, i.e. that by giving the trim balance weights a degree of compliance an improved shaft balance can be obtained, over a given speed range, even for a realistic drive train with multiple eccentricities and section geometry.

It is notable from the above analysis that $S_{bal}$ is a constant of practical magnitude since its critical speed is not less than that of the shaft, and should therefore allow safe operation of this mechanism, without introducing lower order critical speeds.

This principle of adding trim balance compliance can clearly be accomplished by a number of different detail designs, but one method of providing a spring system, with low hysteresis that maintains the good design practices required for high speed shafting, i.e. of low half weight,

rugged construction, with concentric, tight fitting joints, thereby preventing additional balancing problems, can be achieved by the proposed balance sleeve design, as shown schematically, in Figure 2.4.

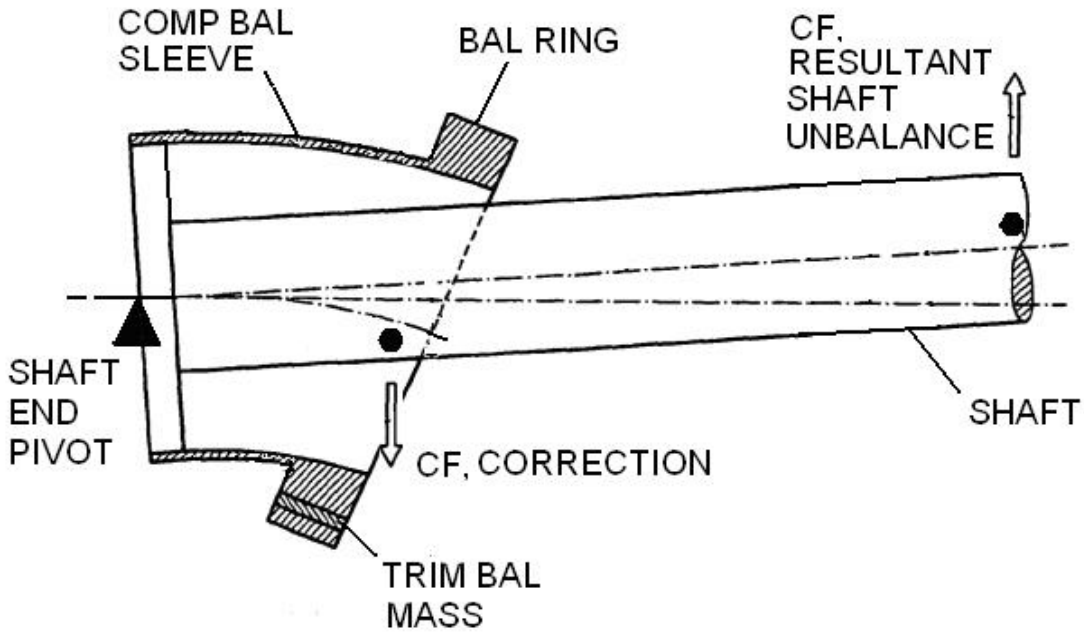


**Figure 2.4,** Schematic of a Compensated Balancing Sleeve

Here, a light weight, compensated balancing sleeve is firmly attached at one end of the shaft end mounting flange, with a relatively heavy balancing ring integrally formed by machining or forging etc., at its free end. The sleeve therefore acts as a cantilever when subjected to dynamic forces that are predominantly concentrated on the greater mass of the balancing ring. The attachment of a trim balance mass, 180° out of phase with the shaft eccentricity, into one of a series of circumferential holes, machined in the balance ring, as shown, then produces a correcting centrifugal force, upon shaft rotation, which acts to bend the sleeve in the opposite direction to the bending of the shaft. Hence, the centrifugal force developed by the trim mass is amplified by the bending of the sleeve.

This design not only produces a more efficient correcting trim balance force, but it also imparts a correcting moment to the shaft with a tendency to reduce its bending. This is shown to be very significant when analysed theoretically.

## 2.3 Theoretical Analysis of Balance Sleeve Compensation

An analytical/numerical method initially considers a simply supported, long, plain shaft, of circular cross section - thereby making gyroscopic moments negligible - operating under steady state, rotating conditions, such that both radial and angular accelerations and associated forces/ moments are zero. This assumption is made to provide a first-order simplification and is widely considered applicable [59] to long, thin shafts, with low slenderness ratios, typically < 0.12 (as employed in the site equivalent models given later). Shaft deflections due to shear effects are regarded as being “second degree” in magnitude, and are not considered here. In addition, this preliminary study is limited to a shaft having uniform eccentricity along its length.

Figure 2.5 shows a plain rotating shaft, simply supported at both ends with total mass, *Ms*, overall length, $\ell$, uniform eccentricity, *e* and deflection, *r* at length, *x*. Integrally attached to each end is a compensating balancing sleeve comprising a flexible arm with negligible mass, length, *L*, spring stiffness, *K* and deflection, *Y*, together with an equivalent lumped trim balancing mass, *m*, positioned with eccentricity, *c*, at its extreme end. The eccentricity of the lumped mass is positioned to be 180° out of phase with the shaft eccentricity such that rotation of the shaft produces centrifugal forces to act on masses $M_s$ and *m*, thereby causing corresponding deflections *r* and *Y*, in opposing directions.

*Considering forces on the compensating balance sleeve*

$$KY = m\omega^2 y \tag{2.6}$$

And from inspection of Figure 2.2, for small angles of slope:

$$y = Y + c - L(\frac{dr}{dx})_{x=0} \tag{2.7}$$

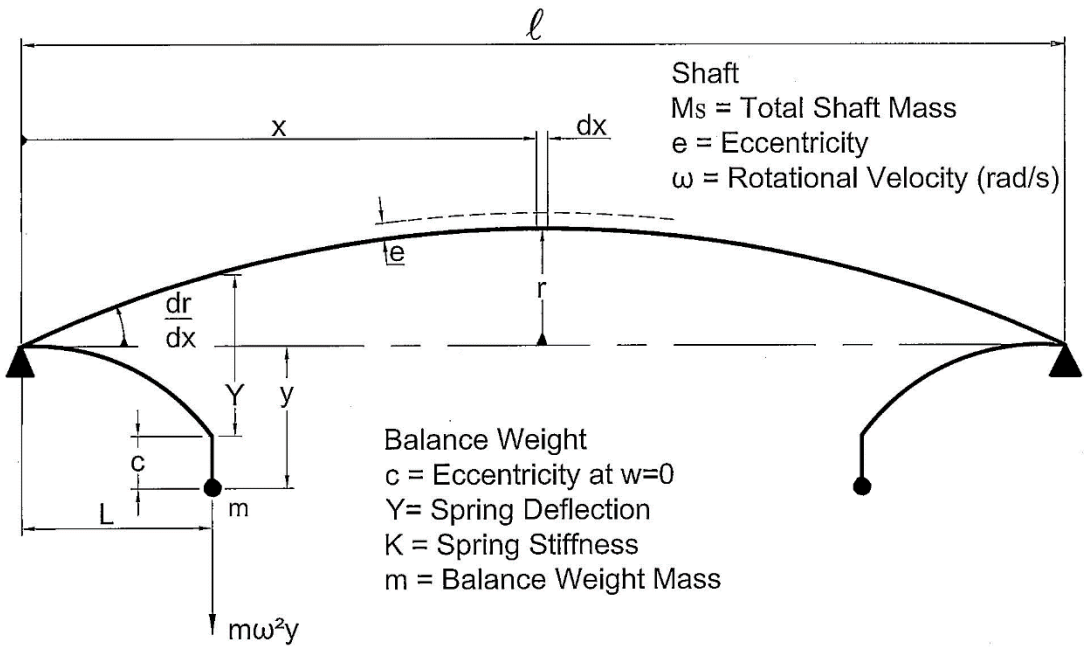


**Figure 2.5** Schematic of simply supported rotating shaft with uniform eccentricity.

giving,

$$Y = \frac{-m\omega^2\left(L(\frac{dr}{dx})_{x=0} - c\right)}{K - m\omega^2} \tag{2.8}$$

The moment imposed on shaft is: $M_0 = A\left(\frac{dr}{dx}\right)_{x=0} + B$ (2.9)

where, $A = \frac{-m\omega^2 L^2 K}{K - m\omega^2}$ (2.10), $B = \frac{m\omega^2 cLK}{K - m\omega^2}$ (2.11)

From 'Bending of Beams' theory, the dynamic loading imposed on the shaft is found from (2.9), (noting that $A(\frac{dr}{dx})_{x=0}$ is constant with respect to *x*), giving:

Dynamic Loading = $\frac{d^2M_0}{dx^2} = 0$

*Considering forces on the shaft.*

The CF acting on an elemental section $\delta x$ is: $CF = \frac{M_s}{\ell}\delta x\omega^2(r+e)$

Hence, dynamic loading, at length *x* is: $\frac{CF}{\delta x} = \frac{M_s}{\ell}\omega^2(r+e)$

*Considering the Combined Assembly*

Total Dynamic Loading = $\frac{M_s}{\ell}\omega^2(r+e)+0$

However, from beam theory, the dynamic loading = $EI\frac{d^4r}{dx^4}$,

therefore: $EI\frac{d^4r}{dx^4} = \frac{M_s}{\ell}\omega^2(r+e)+0$ (2.12)

This can be solved by use of Laplace Transforms, where $\bar{r}$ = Laplace of *r*, and *s* is the Laplace Operator:

$r_o = (r)_{x=0}$ (2.13), $r_1 = \left(\frac{dr}{dx}\right)_{x=0}$ (2.14)

$r_2 = \left(\frac{d^2r}{dx^2}\right)_{x=0}$ (2.15), $r_3 = \left(\frac{d^3r}{dx^3}\right)_{x=0}$ (2.16)

Hence from (2.12):

$$EI(s^4\bar{r} - s^3r_0 - s^2r_1 - sr_2 - r_3) = \frac{M_s}{\ell}\omega^2\bar{r} + \frac{M_s}{\ell s}\omega^2 e$$

At *x* = 0: $r_0$ = 0

and putting: $$b^4 = \frac{M_s \omega^2}{\ell EI} \qquad (2.17)$$

then: $$\bar{r}(s^4 - b^4) = \frac{b^4 e}{s} + sr_2 + s^2 r_1 + r_3 \qquad (2.18)$$

BM at $x = 0$: $$M_0 = EI\left(\frac{d^2 r}{dx^2}\right)_{x=0} = EIr_2$$

Therefore from (2.9) and (2.15): $$r_2 = \frac{Ar_1 + B}{EI} \qquad (2.19)$$

Substituting in (2.18) gives: $$\bar{r}(s^4 - b^4) = \frac{b^4 e}{s} + s\left(\frac{Ar_1}{EI} + \frac{B}{EI}\right) + s^2 r_1 + r_3$$

letting: $$A_1 = \frac{Ar_1 + B}{EI} \qquad (2.20), \qquad A_2 = r_3 \qquad (2.21)$$

gives: $$\bar{r} = \frac{b^4 e}{s.(s^4 - b^4)} + \frac{A_1 s}{s^4 - b^4} + \frac{r_1 s^2}{s^4 - b^4} + \frac{A_2}{s^4 - b^4} \qquad (2.21a)$$

Each term can be expanded, as given in Appendix A, using Partial Fractions to give:

$$\bar{r} = \frac{-e}{s} + \frac{sP}{s^2 + b^2} + \frac{Q}{s^2 + b^2} + \frac{M}{s + b} + \frac{N}{s - b}$$

where:

$$P = e/2 - A_1/2b^2 \qquad (2.22), \qquad Q = 1/2\, r_1 - A_2/2b^2 \qquad (2.23)$$

$$M = e/4 + A_1/4b^2 - r_1/4b - A_2/4b^3 \qquad (2.24)$$

$$N = e/4 + A_1/4b^2 + r_1/4b + A_2/4b^3 \qquad (2.25)$$

These terms are now in Standard Laplace form that can be inversed to give:

$$r = -e + P\cos bx + \frac{Q}{b}\sin bx + M\hat{e}^{-bx} + N\hat{e}^{bx} \qquad (2.26)$$

where $\hat{e}$ = Euler's No.

Applying the following End Conditions:

at $x = \ell$: $r = 0$ and BM = $M_0$ and noting, $\frac{d^2r}{dx^2} = \frac{BM}{EI}$ gives:

$$0 = -e + P\cos b\ell + \frac{Q}{b}\sin b\ell + M\hat{e}^{-b\ell} + N\hat{e}^{b\ell} \qquad (2.26a)$$

$$\frac{Mo}{b^2EI} = -P\cos b\ell - \frac{Q}{b}\sin b\ell + M\hat{e}^{-b\ell} + N\hat{e}^{b\ell} \qquad (2.26b)$$

(2.26a) – (2.26b) gives: $\frac{Q}{b}\sin b\ell = \frac{e}{2} - \frac{Mo}{2b^2EI} - P\cos b\ell$ (2.27)

Adding the above: $\frac{e}{2} + \frac{M_0}{2b^2EI} = M\hat{e}^{-b\ell} + N\hat{e}^{b\ell}$ (2.28)

The exponential terms can be expressed as hyperbolic functions such that:

$$M\hat{e}^{-b\ell} + N\hat{e}^{b\ell} = G\cosh b\ell + H\sinh b\ell \qquad (2.29)$$

where: $G = M + N$ (2.30) and $H = M - N$ (2.31)

Substituting in Equation (2.28) gives:

$$\frac{e}{2} + \frac{M_0}{2b^2EI} = G\cosh b\ell + H\sinh b\ell \qquad (2.32)$$

and putting (2.27) & (2.29) into (2.26) gives:

$$r = -e + P\cos bx + \frac{\frac{e}{2} - \frac{M_0}{2b^2EI} - P\cos b\ell}{\sin b\ell}\sin bx$$

$$+ G\cosh bx + H\sinh bx \qquad (2.33)$$

This equation is solvable except for $r_1$, which a constituent part of the other unknown parameters; and gives the shaft displacement for given values of shaft eccentricity, speed and Balancing Sleeve properties, etc.

It is notable that when $M_0 = 0$ the equation reduces to a classical form for the deflection of a plain rotating shaft with uniform eccentricity [62].

$r_1$ is determined by differentiating (2.33) and putting, *x = 0* , to give:

$$\frac{dr}{dx} = r_1 = b\left(\frac{\frac{e}{2} - \frac{M_0}{2b^2 EI} - P\cos b\ell}{\sin b\ell}\right) + bH \qquad (2.34)$$

Substituting (2.24) and (2.25) in (2.30) and (2.31) gives:

$$G = e/2 + A_1/2b^2 \qquad (2.35) \qquad \text{and} \qquad H = r_1/2b + A_2/2b^3 \qquad (2.36)$$

Now, substituting for *G* in (2.32):

$$H = \frac{\frac{e}{2} + \frac{M_0}{2b^2 EI} - \left(e/2 + A_1/2b^2\right)\cosh b\ell}{\sinh b\ell} \qquad (2.37)$$

and substituting (2.37) in (2.34), gives:

$$r_1 = b\left(\frac{\frac{e}{2} - \frac{M_0}{2b^2 EI} - P\cos b\ell}{\sin b\ell}\right) + b\left(\frac{\frac{e}{2} + \frac{M_0}{2b^2 EI} - (e/2 + A_1/2b^2)\cosh b\ell}{\sinh b\ell}\right)$$

Using *P* from (2.22) and $A_1$ from (2.20) gives:

$$r_1 = b\frac{\frac{e}{2} - \frac{M_0}{2b^2EI} - \left(e/2 - \frac{Ar_1 + B}{EI}/2b^2\right)\cos b\ell}{\sin b\ell}$$

$$+ b\frac{\frac{e}{2} + \frac{M_0}{2b^2EI} - \left(e/2 + \frac{Ar_1 + B}{EI}/2b^2\right)\cosh b\ell}{\sinh b\ell}$$

Let: $$A_3 = \frac{1}{2bEI} \qquad (2.38)$$

Substituting for $M_o$ from (2.9) gives:

$$r_1 = \frac{\frac{eb}{2} - A_3(Ar_1 + B) - \left(eb/2 - A_3(Ar_1 + B)\right)\cos b\ell}{\sin b\ell}$$

$$+ \frac{\frac{eb}{2} + A_3(Ar_1 + B) - \left(eb/2 + A_3(r_1 + B)\right)\cosh b\ell}{\sinh b\ell}$$

Collating $r_1$ terms and simplifying gives:

$$r_1 = \frac{\frac{eb}{2} - A_3B - \left(eb/2 - A_3B\right)\cos b\ell}{A_4 \sin b\ell} \quad + \frac{\frac{eb}{2} + A_3B - \left(eb/2 + A_3B\right)\cosh b\ell}{A_4 \sinh b\ell} \qquad (2.39)$$

Where: $$A_4 = 1 + \frac{A_3A - A_3A\cos b\ell}{\sin b\ell} - \frac{A_3A - A_3A\cosh b\ell}{\sinh b\ell} \qquad (2.40)$$

From beam theory, the vertical shear force within the beam caused by bending is given by:

$$SFv = EI\frac{d^3r}{dx^3}$$

Finally, the total reaction force applied to the supports equals internal shear force + external spring force applied by the Compensating Balance Sleeve, giving:

$$\mathrm{Re} = EIr_3 + KY \tag{2.41}$$

and from (2.36) and (2.21): $r_3 = (H - {}^{r_1}\!/_{2b})2b^3$ (2.42)

Equations (2.33) and (2.41) summarise the key expressions for comparing performance of a traditionally balanced shaft to that of one which is under some degree of balance sleeve compensation. The system is now fully determined and numerical analysis is possible.

## 2.4 Critical Speed Elimination

From (2.33), it is evident that the shaft displacement, *r*, becomes infinite when $\sin b\ell = 0$, i.e. when $b\ell = \pi$, $2\pi$, $3\pi$ etc. and it is this condition that determines the "Classical" critical speeds of the shaft without any Balance Sleeve Compensation.

From (2.17), the 1st Critical Speed: $\omega_{crit} = (\frac{\pi}{\ell})^2 \sqrt{\frac{\ell.EI}{M_s}}$ (2.43)

The only way to avoid this theoretical 'infinity' is to make the numerator of the 3rd term also equal to zero, at $b\ell = \pi$, such that by subst. (2.22), (2.20) and (2.9) into the numerator and equating to zero, gives:

$$\frac{e}{2} - \frac{Mo}{2.b^2.E.I} + \frac{e}{2} - \frac{Mo}{2.b^2.E.I} = 0$$

and $$Mo = b^2.EI.e \tag{2.44}$$

Therefore, by adjusting the Balancing Sleeve parameters so that the Balancing Moment, $Mo = b^2.EI.e$ at the speed equivalent to, $b\ell = \pi$, makes the 3rd term an indeterminate, $\frac{0}{0}$ and hence the effect of the 1st critical speed is eliminated.

## 2.5 Analytical Results

The theory described above identifies and solves all the mathematical 'unknowns' such that further investigation into balancing compensation can be carried out by numerical calculations. To this end, a Mathcad program has been compiled to analyse a simply supported, equivalent model, of the main drive coupling shaft, used on a sub-15MW, Siemens Gas Turbine, Compressor Set, using site equivalent parameter values, given in Table 2.1, below.

| Equivalent Site Parameter Values | |
|---|---|
| $M_s$ = 38.312 kg | $\ell$ = 1.707 m |
| $m$ = 0.899 kg | *E* = 207.1x10^9 N/m^2 |
| *e* = 0.00017 m | *I* = 1.468x10^-5 m^4 |
| *c* = 0.003624 m | *K* = 3.4x10^6 N/m * |

* unless otherwise stated

**Table 2.1.** Parameter Values used in Numerical Example

Figures 2.6-2.9 graphically show results from the numerical calculations derived from equations giving reaction load, (2.41), and midpoint deflection,

(2.33), (with $x = \frac{\ell}{2}$), for a range of balance compensation conditions. In all cases the trim balance weights are set to give low speed balance.

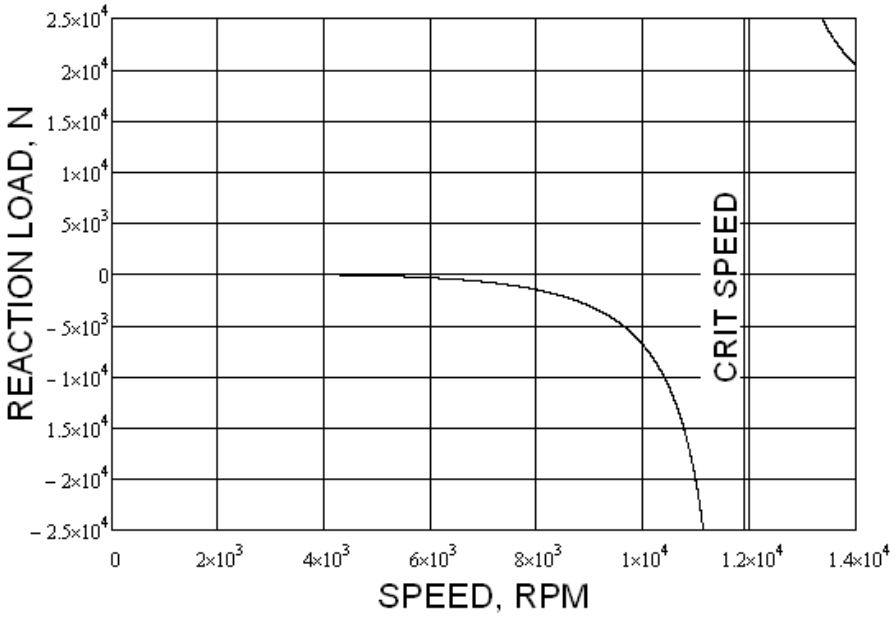


**Figure 2.6(a).** Reaction Load vs. Speed without Balance Sleeve Compensation

Specifically, Figures 2.6(a) and 2.6(b) show shaft end reaction load and midpoint deflection, plotted against speed, for normal balance conditions, i.e. without any balance sleeve compensation, modelled as zero sleeve length and extremely high stiffness. Sleeve length, $L$ = 0 and sleeve stiffness, $K = 3.4\times10^{16}$ N/m.

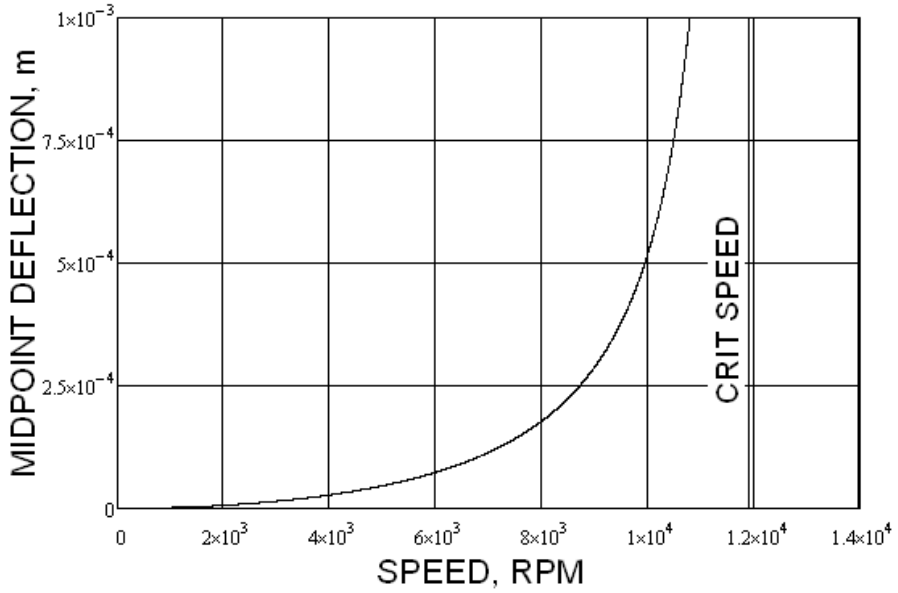


**Figure 2.6(b).** Mid point Deflection vs. Speed without Balance Sleeve Compensation

Figures 2.7(a) and 2.7(b) show reaction load and midpoint deflection, for very good lateral compensation, providing amplified trim balance correction of the reaction load only. The midpoint deflection is unaffected since the sleeve length is still zero – as per the schematic shown in Figure 2.3. Sleeve length, $L$ = 0 and sleeve stiffness, $K$ = 1.47×10$^6$ N/m.

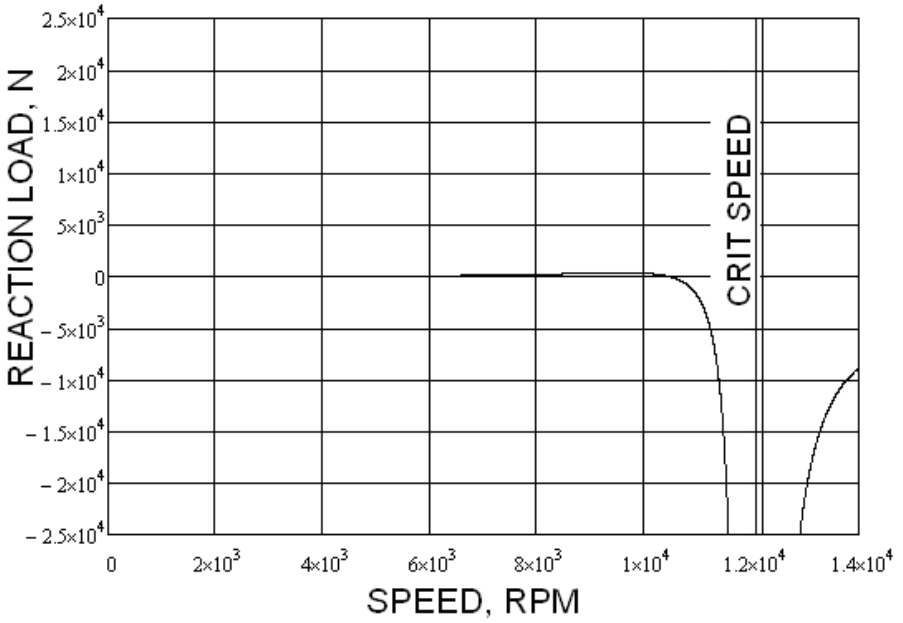


**Figure 2.7(a).** Reaction Load vs. Speed with Lateral Compensation only

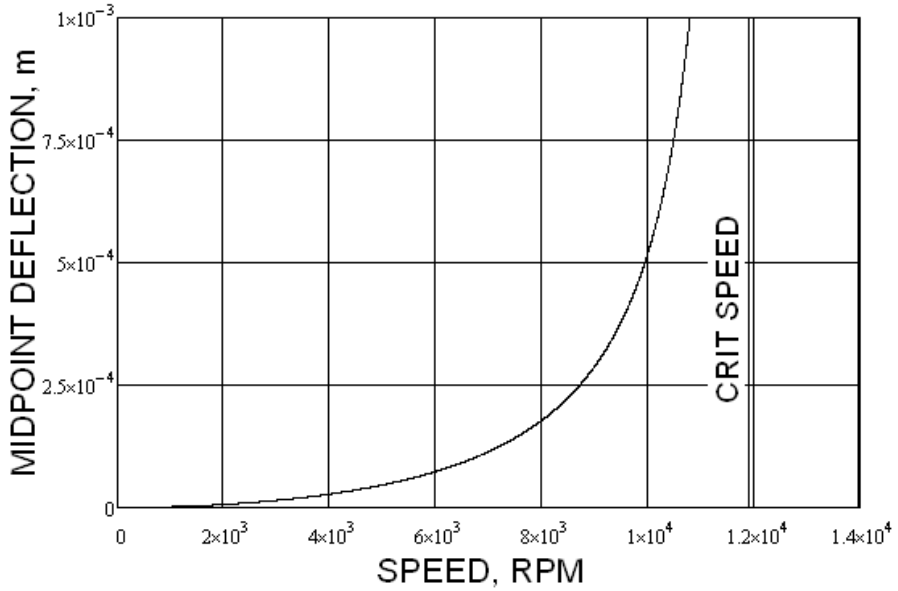


**Figure 2.7(b).** Mid point Deflection vs. Speed with Lateral Compensation only

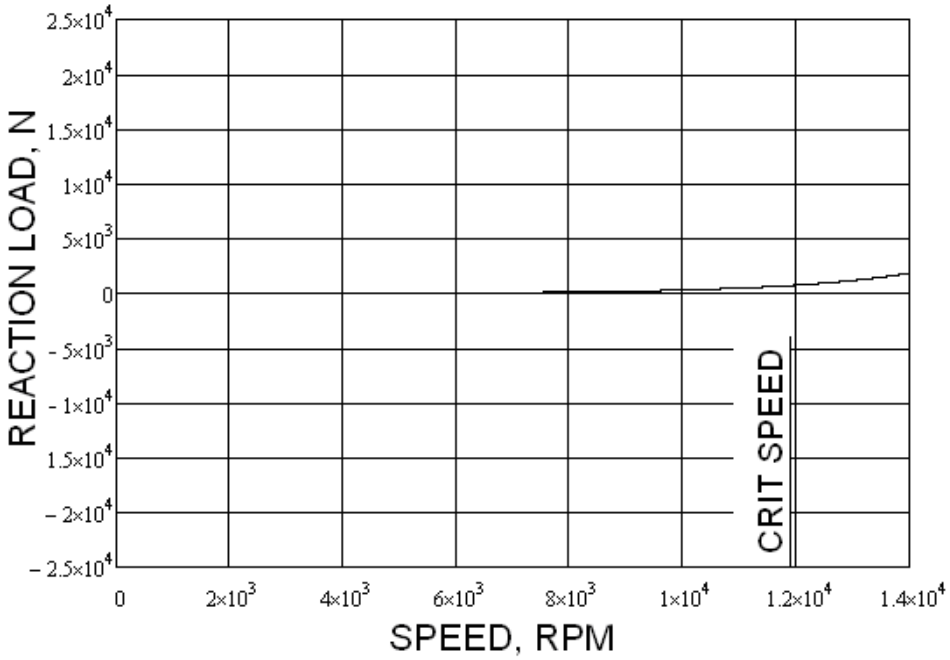


**Figure 2.8(a).** Reaction Load vs. Speed with Maximum Balance Sleeve Compensation

Figures 2.8(a) and 2.8(b) show reaction load and midpoint deflection, for maximum obtainable balance compensation, where the sleeve length is set

with extreme precision in order to investigate critical speed elimination. Sleeve length, $L$ = 0.20604728m and sleeve stiffness, $K = 3.4\times10^6$ N/m.

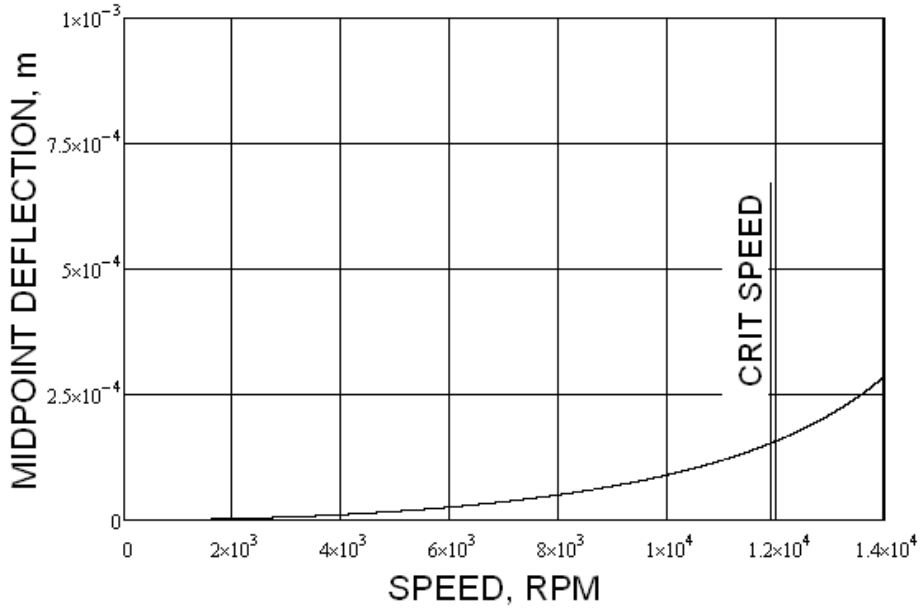


**Figure 2.8(b).** Mid Point Deflection vs. Speed with Maximum Balance Sleeve Compensation

Figures 2.9(a) and 2.9(b) show reaction load and midpoint deflection for a suggested practical level of balance compensation, providing significant reduction in Reaction Load, to exceed operational needs, without exceeding ½ mass requirements of the mating drive shaft. Note: in this instance the trim does not over correct the imbalance and risk the possibility of "flip over" of the shaft, such that its imbalance could switch to an in-phase condition with the trim balance weights. Sleeve length, $L$ = 0.13m and sleeve stiffness, $K = 3.4\times10^6$ N/m.

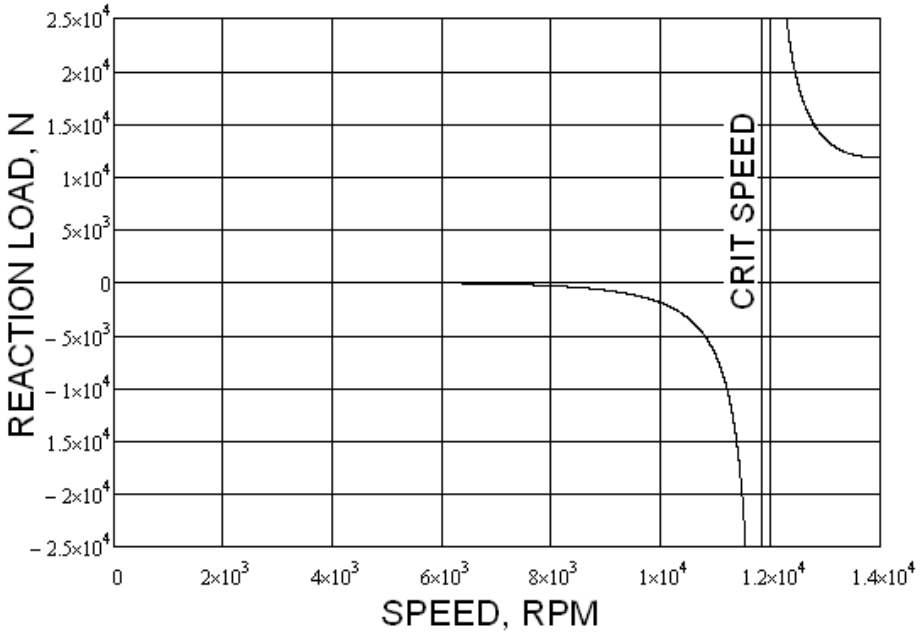


**Figure 2.9(a).** Reaction Load vs. Speed with Practical Balance Sleeve Compensation

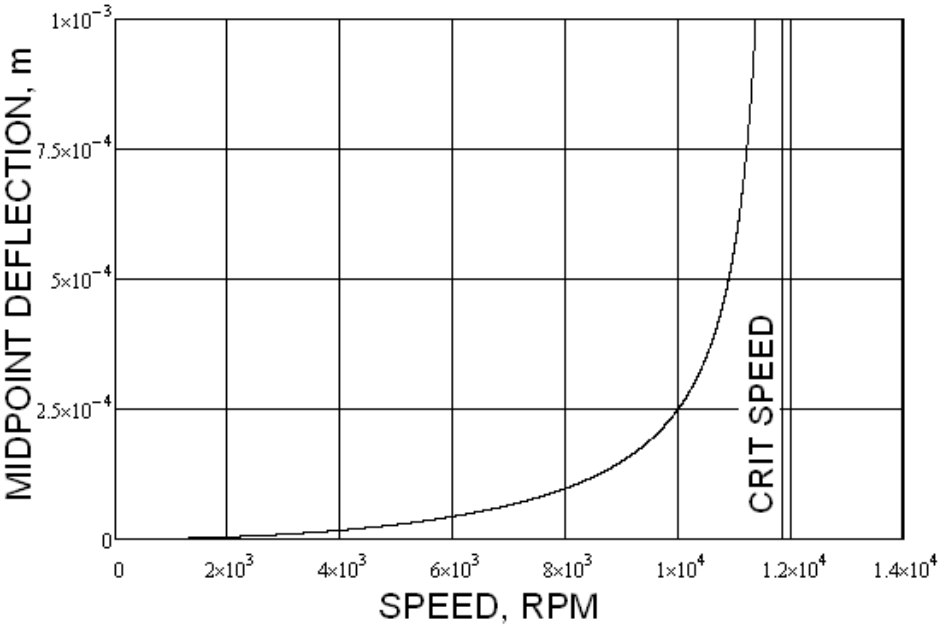


**Figure 2.9(b).** Mid Point Deflection vs. Speed with Practical Balance Sleeve Compensation

Table 2.2, provides a summary of this range of compensation effects, showing how Reaction Load and Shaft Deflection can be vastly reduced by a system of Balance Compensation without increasing the amount of trim balance.

| Figure | Configuration | Comment | Sleeve: Length,(m) Stiffness, (N/m) | Speed (rpm) | Reaction Load, (N) | Max Shaft Deflection (mm) |
|---|---|---|---|---|---|---|
| **2.6** | Without Balance Sleeve Compensation | trim balance weights set to give low speed balance | $L = 0$ $K = 3.4\times10^{16}$ | 10,500 | 11,200 | 0.75 |
| **2.7** | Reaction Load Compensation Only | trim balance weights set to give low speed balance | $L = 0$ $K = 1.47\times10^{6}$ | 10,500 | 50 | 0.75 |
| **2.8** | Max obtainable Balance Sleeve Compensation | very precise level of compensation to completely nullify the critical speed | $L = 0.20604728$ $K = 3.4\times10^{6}$ | 10,500 | 370 | 0.1 |
| **2.9** | Practical Balance Sleeve Compensation | conservative design of balance sleeve producing satisfactory reaction load reduction | $L = 0.13$ $K = 3.4\times10^{6}$ | 10,500 | 3400 | 0.35 |

**Table 2.2.** Summary of Balance Compensation Effects

## 2.6 Site Problem Simulation

Chapter 1, Section 1.3, described a typical balancing problem that is observed at some Siemens GT sites employing very flexible coupling shafts. An example characteristic is shown in Figure 1.5 - polar plot of bearing displacement versus angular displacement, produced a phase angle change of 85º between operating speeds of 7200 rpm and 8900 rpm. This means that it is possible to apply a trim balance weight at any particular angular position, but this only corrects the shaft imbalance at one corresponding speed; all other speeds remaining unbalanced to a greater or lesser degree depending on their angular offset from this one speed. It is therefore extremely difficult to achieve acceptable levels of bearing displacement, of say less than 60 microns (under normal running conditions) over the full operating speed range of the turbine.

An alternative theory (to a normal case of operating very close to a critical speed) for the cause of the vector change is illustrated in Chapter 1, Figure 1.6, suggesting that the root cause of the problem may be due to a very large increase in the imbalance centrifugal force apportioned to the coupling shaft deflection.

To corroborate this a theoretical example now assumes that a laterally very stiff, neighbouring power turbine (PT) shaft, with a residual unbalance vector of 2000 g.mm, (mass times eccentricity), acted at 150º in opposition to a coupling shaft, as analysed previously in section 2.5, and detailed in Table 2.1. The equivalent coupling shaft residual unbalance and its trim balance correction, at shaft ends, are both set to 3257 g.mm, thereby creating perfect balance at low speed, as shown in Figure 2.10.

Since the PT shaft is very stiff, the bearing reaction load generated by its imbalance increases with squared speed (unbalance $\times$ $\omega^2$) and is not subject to the magnification seen by the coupling shaft, due to its flexibility.

Hence, at 9500 rpm, the reaction loads are 2000 N, from the PT shaft and 4588 N, from the coupling shaft, as shown in the polar plot of Figure 2.11, which corresponds to the net reaction load, (coupling uniform eccentricity and shaft end trim balance), calculated without balance sleeve compensation, as in the previous example, and shown graphically in Figure 2.6(a). Therefore, whilst the coupling shaft residual unbalance is only 63% higher than that of the PT shaft, at 9500 rpm, this corresponds to a reaction load that is 230% higher, solely due to the greater flexibility of the coupling.

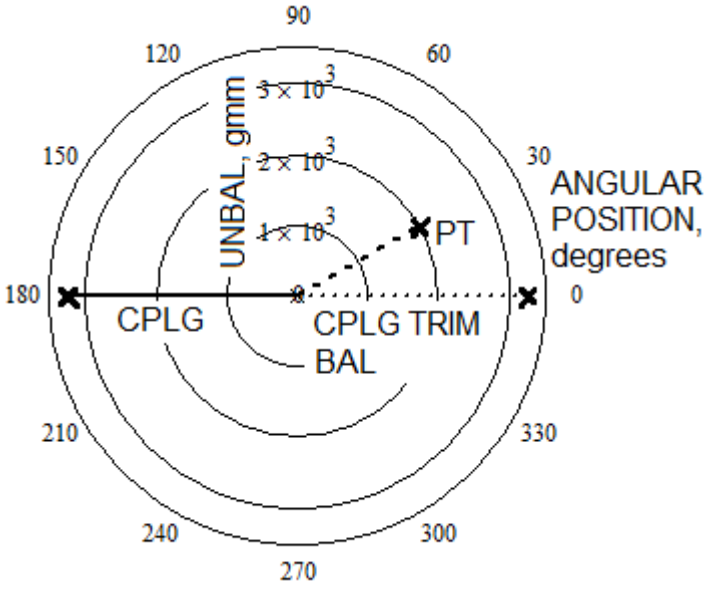


**Figure 2.10,** Polar Plot of Unbalances at Low Speed

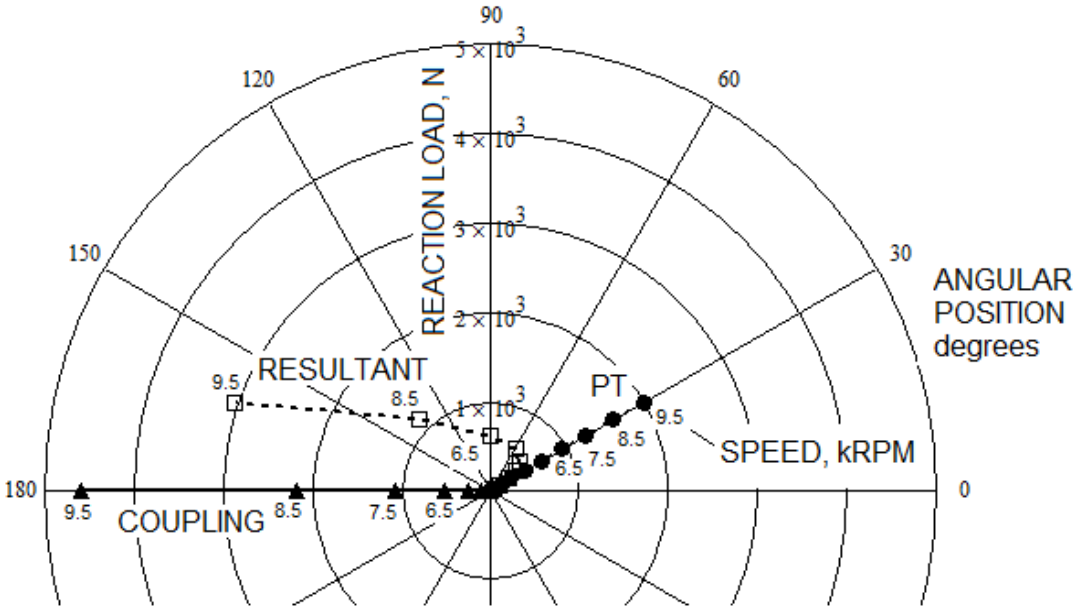


**Figure 2.11,** Polar Plot of Reaction Loads versus Speed

The resultant of the two reaction loads, applied to the bearing can be seen to rotate from 30º to approximately 160º for speeds increasing from 1500 rpm to 9500 rpm, (shown incrementally in 1000 rpm steps), reaching a maximum load of 3039 N.

For a typical bearing stiffness of $26.8 \times 10^6$ N/m, the resultant reaction load corresponds to the bearing displacements shown in Figure 2.12, with the same vector rotation. It can be seen that the shape and magnitude of this polar plot closely resembles the equivalent site example, given in Chapter 1, Figure 1.5, thereby providing corroboration with the proposed theory.

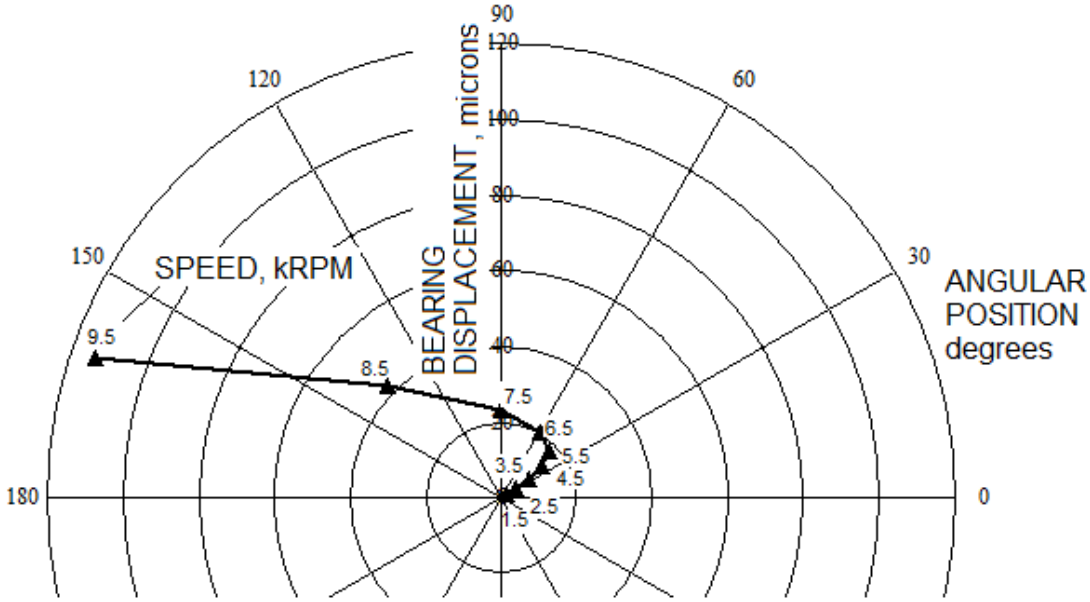


**Figure 2.12,** Polar Plot of Bearing Displacement versus Speed, without Balance Sleeve Compensation

When compensation is applied to the coupling shaft, as depicted in Figure 2.9(a), the resulting bearing displacement is reduced, both in magnitude and angular variation, as shown in Figure 2.13. This reduction is well below the prescribed 60 microns running limit which would normally initiate a “bearing close running” warning. It is therefore considered to be very acceptable and this exercise clearly demonstrates the potential of this balancing methodology to solve such vibration problems.

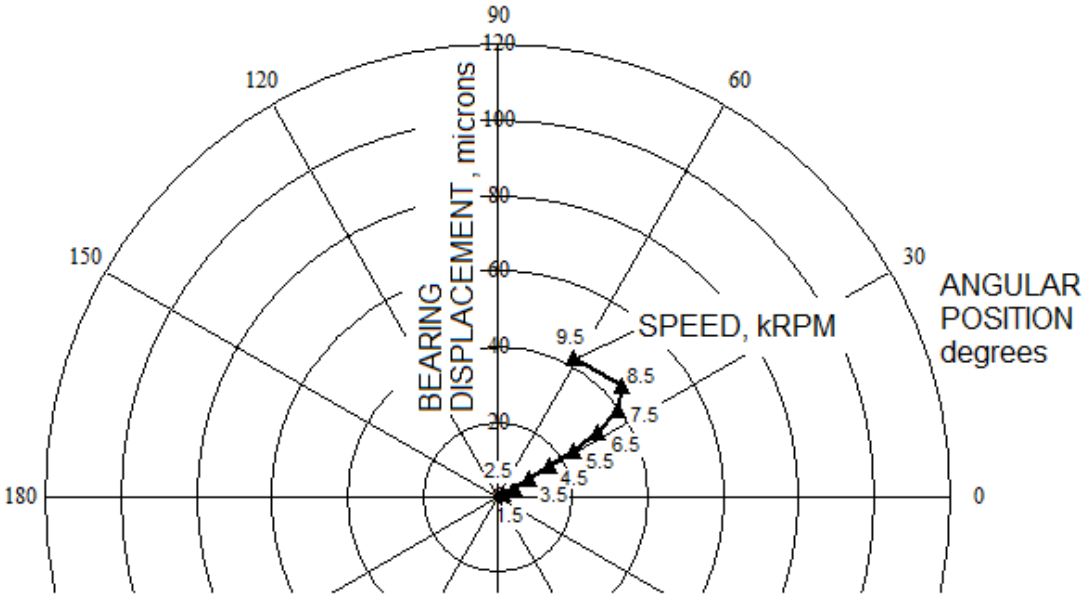


**Figure 2.13,** Polar Plot of Bearing Displacement versus Speed, with Practical Balance Sleeve Compensation

## 2.7 Estimating Equivalent Shaft Eccentricity

For initial design feasibility studies of actual site balancing problems, it is useful to model the problem shaft as an equivalent shaft with uniform eccentricity in order to apply the balancing sleeve compensation theory previously established in section 2.3. Then, from knowledge of the shaft end reaction loads (usually accurately estimated from bearing measurements, such as proximity sensors or similar devices) an equivalent level of uniform eccentricity can be obtained.

For this purpose the equations given in section 2.3 can be applied by setting the impact of the compensating sleeve parameters to zero, since the measured reaction loads are obtained from the problem shaft without any compensation. Then, by putting $A$ = 0, equation (2.40) reduces to give: $A_4 = 1$ and substituting in equation (2.39), with $B$ = 0, gives the shaft end slope as:

$$r_1 = \frac{\frac{eb}{2}.(1-\cos b\ell)}{\sin b\ell} + \frac{\frac{eb}{2}.(1-\cosh b\ell)}{\sinh b\ell} \qquad (2.45)$$

Also, from (2.9) and (2.20): $M_0$ and $A_1$ both equal zero, therefore by substitution in (2.37):

$$H = \frac{\frac{e}{2}.(1-\cosh b\ell)}{\sinh b\ell} \qquad (2.46)$$

However, from (2.42), $r_3 = (H - {}^{r_1}\!/_{2b})2b^3$ therefore substituting (2.46) and (2.45), gives:

$$r_3 = \left( \frac{\frac{e}{2}.(1-\cosh b\ell)}{\sinh b\ell} - \frac{1}{2b}.\left( \frac{\frac{eb}{2}.(1-\cos b\ell)}{\sin b\ell} + \frac{\frac{eb}{2}.(1-\cosh b\ell)}{\sinh b\ell} \right) \right) 2b^3$$

which reduces to:

$$r_3 = \frac{eb^3}{2}.\left( \frac{(1-\cosh b\ell)}{\sinh b\ell} - \frac{(1-\cos b\ell)}{\sin b\ell} \right) \qquad (2.47)$$

Therefore, the reaction load from (2.41), with both *K* and *Y* equated to zero, becomes:

$$\mathrm{Re} = \frac{eb^3}{2}.\left( \frac{(1-\cosh b\ell)}{\sinh b\ell} - \frac{(1-\cos b\ell)}{\sin b\ell} \right).EI \qquad (2.48)$$

The equivalent shaft eccentricity is therefore seen to be directly proportional to the shaft end reaction load and is readily calculated from site measurements and knowledge of the critical speed – needed to determine parameter *b*.

It is fully expected that by simple modelling of the shaft as having uniform eccentricity, as illustrated in section 2.6, reasonably accurate conservative estimates can be made of its eccentricity with sufficient accuracy for feasibility and initial development design and test purposes, in the knowledge that, if required, a more detailed finite element analysis (FEA) could be carried out if necessary.

## 2.8 Preliminary Conclusions

Consideration of current methods of applying trim balance correction to rotating shafts show that their effectiveness reduces with increased shaft flexibility. A new method of adding compliance to the mechanism has been reported that not only amplifies the magnitude of the balance correcting forces, but also applies a deflection reducing moment to the shaft. This method of balance sleeve compensation is shown to have the potential to vastly reduce the reaction loads applied to the driver and driven unit bearings. This can be seen from the results summary, Table 2.2, where the reaction load under normal low speed balance has been reduced from 11,200 N, Figure 2.6(a), to near zero, Figure 2.7(a), at 10,500 rpm. This latter condition represents lateral balance compensation only in accordance with the schematic shown in Figure 2.3, where the trim balance centrifugal force has been amplified, but only acts upon the mounting flange without applying a correcting moment to the shaft. Hence, the shaft deflection has not been reduced.

A much improved method of providing trim balance compliance is shown in Figure 2.4, with the added benefit of applying the balancing moment, $M_0$, which also reduces the shaft deflection as shown in Table 2.2, Figures 2.8(b) and 2.9(b), giving mid-point shaft deflection reduction from 0.75 mm to 0.1 mm and 0.35 mm, respectively, at 10,500 rpm.

The case shown in Figure 2.8, attempts to maximise the balance compensation and also investigate possible critical speed elimination, as mathematically shown section 2.4 (hence the 8 digit sleeve length, *L*). The results are therefore very positive with vast reductions in both reaction load and mid-point deflection being evident. Nevertheless, it is notable that this is only a theoretical possibility and a more practical condition is shown in Figure 2.9. This latter condition is considered good design compromise, as it still provides significant reduction in reaction load, to exceed operational needs, without excessive balancing sleeve length and/ or deflection.

This is also confirmed by the treatment in section 2.6, of the typical balancing problems observed at some problematic GT sites employing relatively flexible couplings, and highlighted in chapter 1. An alternative proposal for the vibration source, that the angular change of the bearing imbalance vector was a result of the coupling unbalance being amplified by its deflection, has also been corroborated. Further, the example has shown that application of balancing sleeve compensation can reduce the bearing deflection to acceptable limits, by reducing the coupling reaction load and also, as a consequence, reduce the angular change of the imbalance vector.

Section 2.7 showed that the uniform eccentricity of an equivalent shaft, is directly proportional to shaft end reaction load and therefore readily estimated, hence this analytical model can usefully be employed in design and feasibility investigations.

Further investigation of critical speed and the reduction of its impact using an analysis of Balance Sleeve Compensation, is now given in chapter 3.

# Chapter 3

## 3.1 Encastre Simulation

The effect which a compensating balance sleeve has on a simply supported shaft can be compared with the mechanics of an encastre shaft, or one angularly fixed by long bearings. An encastre shaft constrains the whirling motion of a shaft by the application of a fixing moment, $M_f$, imparted from the bearing casing to the shaft ends, of sufficient magnitude to maintain the shaft end slopes equal to zero at all operating speeds. A schematic of such an arrangement is presented in Figure 3.1.

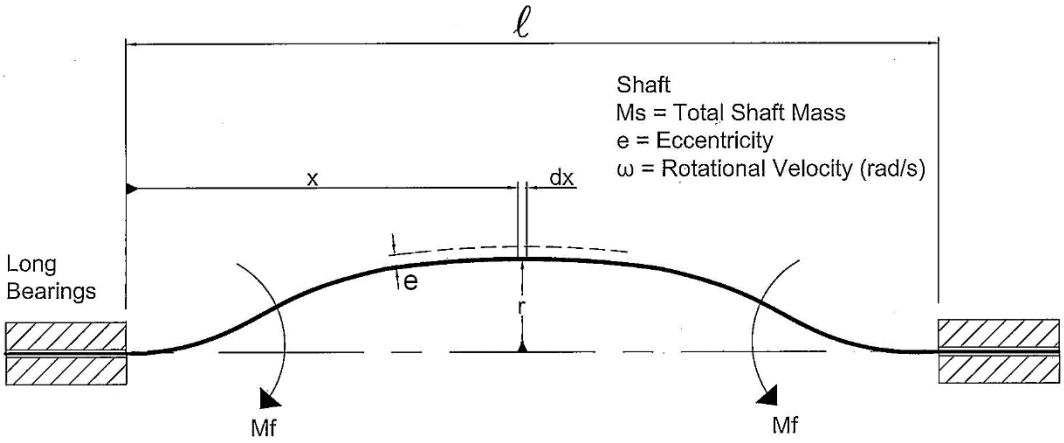


**Figure 3.1.** Schematic of encastre rotating shaft with uniform eccentricity

It is well known that the natural frequency for an encastre system is approximately 2¼ times that of the equivalent simply supported case [60]. It is therefore, reasonable to investigate the possibility of matching the balancing moment, $M_o$, created by the balance sleeve, to the fixing moment, $M_f$ , in order to simulate an encastre system.

By applying a similar analytical procedure, as per the simply supported case given in chapter 2, to the same shaft configuration, but with encastre ends, the following equations are developed:

Centrifugal Force, CF, acting on elemental section δx,

$$CF = \frac{M_s}{\ell}.\delta x.\omega^2.(r+e)$$

Dynamic Loading on the shaft = $\frac{CF}{\delta x} = \frac{M_s}{\ell}.\omega^2.(r+e)$

and, Dynamic Loading = $EI.\frac{d^4r}{dx^4}$,

giving, $EI.\frac{d^4r}{dx^4} = \frac{M_s}{\ell}.\omega^2.(r+e)$, equation (2.12), from chapter 2.

Repeating the Laplace Transformation as shown in chapter 2:

$r_o = (r)_{x=0}$ (2.13), $r_1 = \left(\frac{dr}{dx}\right)_{x=0}$ (2.14)

$r_2 = \left(\frac{d^2r}{dx^2}\right)_{x=0}$ (2.15), $r_3 = \left(\frac{d^3r}{dx^3}\right)_{x=0}$ (2.16)

Substituting in (2.12):

$$EI(s^4\bar{r} - s^3r_0 - s^2r_1 - sr_2 - r_3) = \frac{M_s}{\ell}\omega^2\bar{r} + \frac{M_s}{\ell s}\omega^2 e$$

At $x = 0$: $r_0 = 0$, and $r_1 = 0$:

$$\therefore \bar{r}(s^4 - \frac{M_s.\omega^2}{\ell EI}) = \frac{M_s.\omega^2 e}{s\ell EI} + sr_2 + r_3 \qquad (3.1)$$

From chapter 2: $b^4 = \frac{M_s\omega^2}{\ell EI}$ (2.17)

then, $\bar{r}(s^4 - b^4) = \frac{b^4 e}{s} + sr_2 + r_3$

and $\bar{r} = \frac{b^4 e}{s(s^4 - b^4)} + \frac{sr_2}{s^4 - b^4} + \frac{r_3}{s^4 - b^4}$ (3.2)

Each term can be expanded using Partial Fractions, see Appendix B, to give:

$$\bar{r} = \frac{-e}{s} + \frac{s.P_e}{s^2 + b^2} + \frac{Q_e}{s^2 + b^2} + \frac{M_e}{s+b} + \frac{N_e}{s-b} \qquad (3.3)$$

where:

$$P_e = e/2 - r_2/2b^2 \quad , \qquad Q_e = -r_3/2b^2 \, , \qquad M_e = e/4 + r_2/4b^2 - r_3/4b^3$$

$$N_e = e/4 + r_2/4b^2 + r_3/4b^3 \qquad (3.3a)$$

These terms are now in Standard Laplace forms which can be inverted to give:

$$r = -e + P_e \cos bx + \frac{Q_e}{b} \sin bx + M_e.\hat{e}^{-bx} + N_e.\hat{e}^{bx} \quad ,$$

where $\hat{e}$ = exponential value, e.

However, the exponential terms can be expressed as Hyperbolic Functions, as given Appendix C, where x represents any angle, i.e. in this case, x = $bx$ to give:

$$r = -e + P_e \cos bx + J \sin bx + G_e \cosh bx + H_e \sinh bx \qquad (3.4)$$

where $J = \frac{Q_e}{b}$, $G_e = M_e + N_e$, $H_e = N_e - M_e$ (3.4a)

but r = 0 at x = 0, $\therefore 0 = -e + P_e + G_e$ and $G_e = e - P_e$ (3.5)

Differentiating (3.4), $\frac{dr}{dx} = -bP_e \sin bx + bJ.\cos bx + bG_e \sinh x + bH_e \cosh x$

And $\frac{dr}{dx} = 0$ at x = 0, $\therefore 0 = bJ + bH_e$ and $H_e = -J$ (3.6)

Substituting (3.5) & (3.6) in (3.4) gives:

$$r = -e + P_e(\cos bx - \cosh bx) + e\cosh bx + J(\sin bx - \sinh bx) \qquad (3.7)$$

and $\dfrac{dr}{dx} = b(-P_e(\sin bx + \sinh bx) + e\sinh bx + J(\cos bx - \cosh bx))$

but at $x = \ell$, $\dfrac{dr}{dx} = 0 = b(-P_e(\sin b\ell + \sinh b\ell) + e\sinh b\ell + J(\cos b\ell - \cosh b\ell))$

$$\therefore J = \frac{P_e(\sin b\ell + \sinh b\ell) - e\sinh b\ell}{\cos b\ell - \cosh b\ell} \qquad (3.8)$$

also r = 0 at $x = \ell$ and substituting (3.8) in (3.7) gives:

$$0 = -e + P_e(\cos b\ell - \cosh b\ell) + e\cosh b\ell + \frac{P_e(\sin b\ell + \sinh b\ell) - e\sinh b\ell}{\cos b\ell - \cosh b\ell}.(\sin b\ell - \sinh b\ell)$$

$$\therefore P_e(\cos b\ell - \cosh b\ell + \frac{\sin^2 b\ell - \sinh^2 b\ell}{\cos b\ell - \cosh b\ell}) = e - e\cosh b\ell + \frac{e\sinh b\ell.(\sin b\ell - \sinh b\ell)}{\cos b\ell - \cosh b\ell}$$

$$P_e((\cos b\ell - \cosh b\ell)^2 + \sin^2 b\ell - \sinh^2 b\ell) = (\cos b\ell - \cosh b\ell).(e - e\cosh b\ell)$$

$$+ e\sinh b\ell.(\sin b\ell - \sinh b\ell)$$

$$P_e = \frac{(\cos b\ell - \cosh b\ell).(e - e\cosh b\ell) + e\sinh b\ell.(\sin b\ell - \sinh b\ell)}{(\cos b\ell - \cosh b\ell)^2 + \sin^2 b\ell - \sinh^2 b\ell}$$

$$P_e = e.\frac{\cos b\ell - \cos b\ell.\cosh b\ell - \cosh b\ell + \cosh^2 b\ell + \sin b\ell.\sinh b\ell - \sinh^2 b\ell}{\cos^2 b\ell - 2.\cos b\ell.\cosh b\ell + \cosh^2 b\ell + \sin^2 b\ell - \sinh^2 b\ell}$$

but $\sin^2 + \cos^2 = 1$ and $\cosh^2 - \sinh^2 = 1$

$$\therefore P_e = e.\frac{1 + \cos b\ell - \cos b\ell.\cosh b\ell - \cosh b\ell + \sin b\ell.\sinh b\ell}{2 - 2.\cos b\ell.\cosh b\ell}$$

and $$P_e = \frac{e}{2}.\frac{1+\cos b\ell - \cos b\ell.\cosh b\ell - \cosh b\ell + \sin b\ell.\sinh b\ell}{1-\cos b\ell.\cosh b\ell} \quad (3.9)$$

Therefore, for any given values of *b*, $\ell$ and *e*, the following parameters and shaft deflection can be determined:

$P_e$ from (3.9), *J* from (3.8) and *r* from (3.7).

Also, from beam theory, the fixing or constraining moment is given by:

$$Mf = EI.(\frac{d^2r}{dx^2})_{x=0} = EI.r_2$$

But, (3.3a) $P_e = e/2 - r_2/2b^2$, giving: $$Mf = 2b^2.EI.(\frac{e}{2} - P_e) \quad (3.10)$$

Moreover, the shaft end reaction load equals the internal shear force:

$\mathrm{Re} = E.I.r_3$ (3.10a), where, from (3.3a) and (3.4a):

$r_3 = -2.b^3.J$ (3.10b)

At *bl* = 4.73 radians, the denominator of $P_e$ equals zero, and therefore this condition represents the 1st critical speed of the system as $r = \infty$. Comparing this result with the analysis in chapter 2, the critical speed for the encastre shaft is 2.27 times greater than that of the simply supported case, which agrees with standard theory [60].

Comparison of the balancing and fixing moments can now be made, using the same site equivalent parameter values given in Table 2.1, from the simply supported case analysed in chapter 2. The results are shown graphically in Figure 3.2, where the Balancing Sleeve Length, *L* = 0.20603 m, has been optimised to give near elimination of the critical speed. It can be seen that the two moments are very close, at all speeds up to the first critical, in this case 11,900 rpm, showing the ability of the Balance Compensation method to provide very close simulation of an encastre mounted shaft.

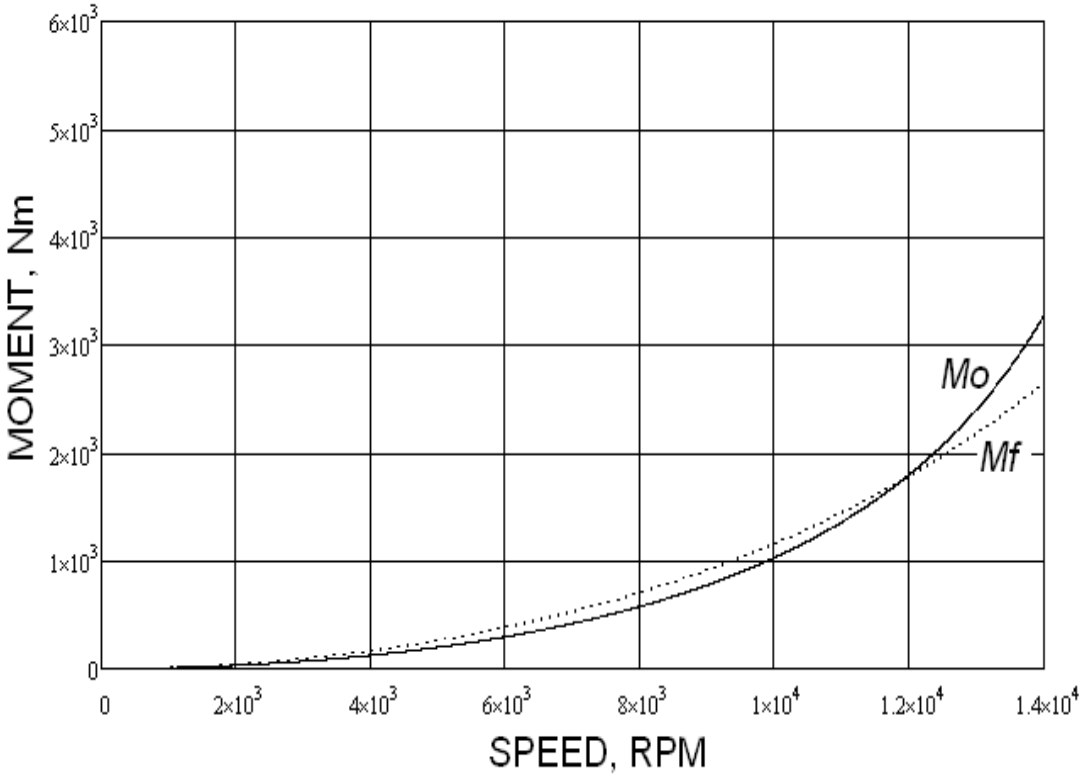


**Figure 3.2.** Fixing and balancing moment vs speed, with maximum compensation

It is also interesting to note that at $b\ell = \pi$, i.e. the Classical Critical Speed of the simply supported system, $P_e$ = 0 and the encastre fixing moment becomes,

$$Mf = b^2.EI.e \tag{3.11}$$

which is identical to equation (2.44), chapter 2, the balancing moment required for elimination of the simply supported, 1st critical speed; therefore, at this speed, $Mo = Mf$, and complete encastre simulation occurs at the intersection point between the two curves shown in Figure 3.2.

## 3.2 Compensated Critical Speeds

To further investigate encastre simulation and the resulting elimination of the simply supported critical speed, it is necessary to extend the analysis given in chapter 2.

For a Simply Supported Shaft System with Balancing Sleeve Compensation, equation (2.40) states:

$$A_4 = 1 + \frac{A_3 A - A_3 A \cos b\ell}{\sin b\ell} - \frac{A_3 A - A_3 A \cosh b\ell}{\sinh b\ell}$$

and at the Classical Critical speed, equivalent to, $b\ell = \pi$, this becomes:

$$A_4 = 1 + \frac{A_3.A + A_3.A}{0} - \frac{A_3.A - A_3.A.\cosh \pi}{\sinh \pi}$$

The 1st and 3rd terms can be ignored as negligible compared to 2nd term:

$$\therefore A_4 = \frac{2.A_3.A}{0} = \infty$$

Also from (2.39), the slope of the shaft at *x=0,* is given by

$$r_1 = \frac{\frac{eb}{2} - A_3 B - \left(eb/2 - A_3 B\right)\cos b\ell}{A_4 \sin b\ell} + \frac{\frac{eb}{2} + A_3 B - \left(eb/2 + A_3 B\right)\cosh b\ell}{A_4 \sinh b\ell}$$

which reduces to, $r_1 = \dfrac{\frac{e.b}{2} - A_3.B - (e.b/2 - A_3.B).(-1)}{\frac{2.A_3.A}{0}.0} + 0$ and:

$$r_1 = \frac{e.b - 2.A_3.B}{2.A_3.A} = \frac{\frac{e.b}{2.A_3} - B}{A}$$

Hence: $A.r_1 + B = \frac{e.b}{2.A_3} = Mo$

Making substitutions $A_3 = \frac{1}{2bEI}$ , (2.38) and $b^4 = \frac{M_s \omega^2}{\ell EI}$ (2.17)

gives $Mo = b^2.EI.e$ and $Mo = \left(\frac{\pi}{\ell}\right)^2.EI.e$ (3.12)

This has far reaching implications since it shows that *Mo* is independent of the Balance Sleeve parameters: mass, eccentricity, length and stiffness and gives a constant value for a given shaft when running at its standard, classical critical speed.

Also, since this equation is identical to (2.44), for $b\ell = \pi$, it means that the classical critical is always eliminated, regardless of the characteristics of *Mo*.

This is best illustrated graphically, using the parameter values given in Table 2.1, which shows that ALL levels of positive Balancing Sleeve Moment, *Mo*, plus the Fixing Moment, *Mf*, coincide at a point of convergence, given by equation (3.12), at the speed defined by equation (2.43). See Figure 3.3, below – where 3 characteristics of *Mo* were plotted, using 3 different Compensating Sleeve Lengths, *L*.

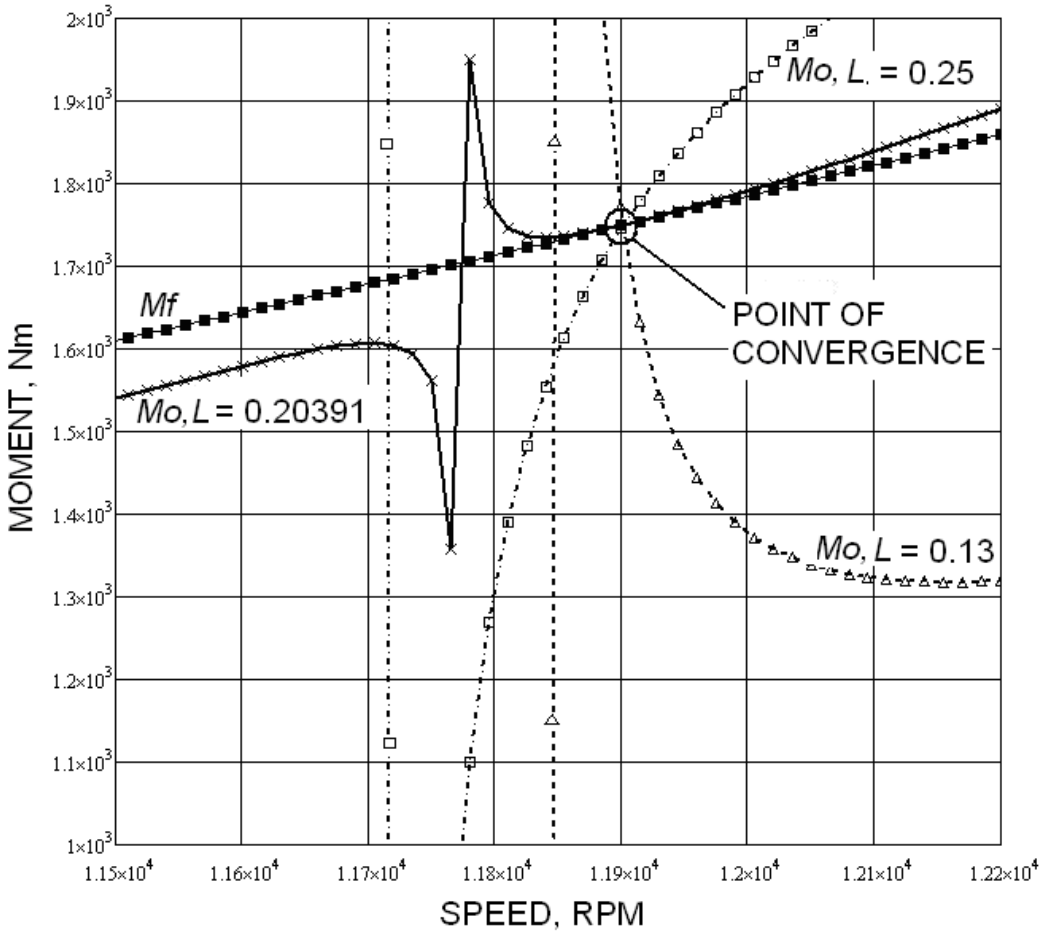


**Figure 3.3.** Close-up of point of convergence.

It is noted that the only time the Point of Convergence is avoided is when *Mo* = 0 and then the critical speed reverts to its Classical value.

From the above it is apparent that $b\ell = \pi$, $2\pi$, $3\pi$ only defines the critical speeds for simply supported shafts without any externally applied moments, i.e. when *Mo* equals zero. But, for all other arrangements the 1st critical speed can be seen to have moved away from the standard theoretical speed by a few hundred rpm. This is evident from Figure 3.3, which shows *Mo* tending to infinity, at speeds away from the Point of Convergence, and this is as a consequence of the slope $r_1$ becoming infinite.

Therefore, this condition can be used to determine the new Compensated Critical Speed**.**

Considering $r_1$, (2.39), it should be noted that it resulted from (2.7), which assumed that $r_1$ was very small, which is evidently not the case when approaching a critical speed. From Figure 3.4 below, it can be seen that in determining equation (2.7) for larger angles,

$y = Y + c - L.r_1$ should be $y = Y + c - L.\tan(r_1)$

i.e. $r_1$ should be replaced by $\tan(r_1)$.

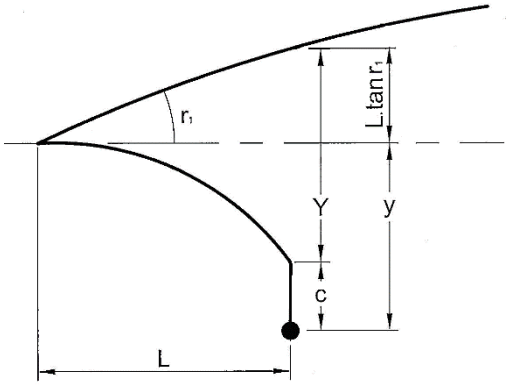


**Figure 3.4.** Close-up of shaft end.

However, for angles less than 0.035 rads, (2.0 deg.), the error produced in (2.39) from the assumption that $\tan(r_1) = r_1$ , is less than 0.03% and for all practical engineering cases, where the stresses and strains are usually kept within the elastic limit of the material, this assumption is generally valid. It is also valid for the theory regarding the elimination of the “Classical” critical speed and the Point of Convergence, of the Balancing Sleeve and Fixing Moments, since the large whirl deflections associated with the critical speed no longer exist, and hence, the slope $r_1$ is kept small.

At operating speeds close to a critical speed, (2.39), should be:

$$\tan(r_1) = \frac{\frac{eb}{2} - A_3B - \left(eb/2 - A_3B\right)\cos b\ell}{A_4 \sin b\ell} + \frac{\frac{eb}{2} + A_3B - \left(eb/2 + A_3B\right)\cosh b\ell}{A_4 \sinh b\ell} \qquad (3.13)$$

such that at a critical speed the slope becomes vertical and $\tan(r_1)$ equals infinity and it can be seen that this will occur when $A_4 = 0$.

From chapter 2:

$$A_4 = 1 + \frac{A_3A - A_3A\cos b\ell}{\sin b\ell} - \frac{A_3A - A_3A\cosh b\ell}{\sinh b\ell} \quad , \quad (2.40)$$

and by substituting the following trigonometric relationships:

$$\tan\frac{x}{2} = \frac{1-\cos x}{\sin x} \quad , \qquad \cosh x = \cosh^2\frac{x}{2} + \sinh^2\frac{x}{2} \quad ,$$

$$\sinh x = 2.\sinh\frac{x}{2}.\cosh\frac{x}{2}, \quad 1-\cosh^2 x = -\sinh^2 x,$$

gives: $$A_4 = 1 + A_3.A.\left(\tan\frac{b\ell}{2} - \frac{(1-\cosh^2\frac{b\ell}{2} - \sinh^2\frac{b\ell}{2})}{2.\sinh\frac{b\ell}{2}.\cosh\frac{b\ell}{2}}\right)$$

$$A_4 = 1 + A_3.A.\left(\tan\frac{b\ell}{2} - \frac{-2.\sinh^2\frac{b\ell}{2}}{2.\sinh\frac{b\ell}{2}.\cosh\frac{b\ell}{2}}\right) \quad . \text{ Substituting } \quad A_3 = \frac{1}{2bEI}, \quad (2.38)$$

gives: $$A_4 = 1 + \frac{A}{2.b.E.I}.(\tan\frac{b\ell}{2} + \tanh\frac{b\ell}{2}) \qquad (3.14)$$

Since at the critical speed $A_4 = 0$ and it is known that this occurs at a speed close to the equivalent of $b\ell = \pi$, whereby the tanh term tends to 1, the compensated critical speed can be defined by the condition where:

$$0 = 1 + \frac{A}{2.b.E.I}.\left(\tan\frac{b\ell}{2} + 1\right) \qquad (3.15)$$

$$\therefore \tan\frac{b\ell}{2} = -\frac{2.b.E.I}{A} - 1$$

Then by trigonometry:

$$\cot\frac{b\ell}{2} = \frac{1}{\tan\frac{b\ell}{2}} = -\frac{A}{2.b.E.I + A} = \tan(\frac{\pi}{2} - \frac{b\ell}{2})$$

Moreover since $b\ell \cong \pi$, the angle $\frac{\pi}{2} - \frac{b\ell}{2}$ must be very small such that

$$\tan(\frac{\pi}{2} - \frac{b\ell}{2}) \cong \frac{\pi}{2} - \frac{b\ell}{2} = -\frac{A}{2.b.E.I + A}$$

and $b^2.(\ell.E.I) + b.(\frac{\ell.A}{2} - \pi.E.I) - A - \frac{\pi.A}{2} = 0$

This quadratic can be solved numerically by first evaluating the classical critical speed, $\omega_{crit} = (\frac{\pi}{\ell})^2\sqrt{\frac{\ell.EI}{M}}$ from (2.43), and then $A = \frac{-m\omega^2 L^2 K}{K - m\omega^2}$ from (2.10), to determine the following parameters:

$E1 = \ell.E.I$ (3.16), $E2 = \frac{\ell.A}{2} - \pi.E.I$ (3.17), $E3 = -A - \frac{\pi.A}{2}$ (3.18)

providing a very good approximation for the compensated critical speed as:

$$b\_cc = \frac{-E2 + \sqrt{E2^2 - 4.E1.E3}}{2.E1} \qquad (3.19)$$

thence: $$\omega\_cc = (b\_cc)^2.\sqrt{\frac{\ell.EI}{M}} \qquad (3.20)$$

## 3.3 Elimination/ Nullification of Compensated Critical Speeds

Considering, (3.13):

$$\tan(r_1) = \frac{\frac{eb}{2} - A_3B - \left(eb/2 - A_3B\right)\cos b\ell}{A_4 \sin b\ell} + \frac{\frac{eb}{2} + A_3B - \left(eb/2 + A_3B\right)\cosh b\ell}{A_4 \sinh b\ell}$$

and applying the same ½ angle substitutions as to obtain (3.14), gives:

$$\tan(r_1) = \frac{(e.b/2 - A_3.B).\tan\frac{b\ell}{2} - (e.b/2 + A_3.B).\tanh\frac{b\ell}{2}}{A_4} \qquad (3.21)$$

Therefore, the compensated critical speed will be eliminated if the numerator can be made to equal zero at this speed, so that:

$$(e.b/2 - A_3.B).\tan\frac{b\ell}{2} - (e.b/2 + A_3.B).\tanh\frac{b\ell}{2} = 0.$$

And applying the same conditions and assumptions as per (3.14), then the tanh term tends to 1, and:

$$\tan\frac{b\ell}{2} = -\frac{2.b.E.I}{A} - 1, \quad \text{so that:}$$

$$-\frac{e.b^2.E.I}{A} + \frac{2.b.E.I.A_3.B}{A} - \frac{e.b}{2} + A_3.B - \frac{e.b}{2} - A_3.B = 0$$

and: $\frac{.e.b^2.E.I}{A} + e.b = \frac{B}{A} = \frac{c}{L}$, (from $A$ and $B$, see below) (3.21a)

Defining: $$D = e.b^2.E.I \qquad (3.22)$$

and substituting from chapter 2,

$$A = \frac{-m\omega^2 L^2 K}{K - m\omega^2} \qquad (2.10), \qquad B = \frac{m\omega^2 cLK}{K - m\omega^2} \qquad (2.11)$$

gives $$K = \frac{-D.m.\omega^2}{m.\omega^2.(e.b.L^2 + c.L) - D} \qquad (3.23)$$

x

This relationship (plotted in Figure 3.5), for the typical parameter values given in Table 2.1, and with regard to the assumptions used in deriving the theory, gives a good approximation for the compensating sleeve design requirements to give complete, theoretical, elimination of the compensated critical speed. Point 1, represents the *L* and *K* values used in the optimised compensation case, illustrated in Figure 3.2; and point 2, is a suggested minimum sleeve length to prevent possible instability between the sleeve critical speed equal to 13,300 rpm at this reduced stiffness, and the shaft critical speed of 11,900 rpm. Point 3 represents a mechanism having radial stiffness, but no length, as per Figure 2.3, chapter 2, which would allow compensation of the reaction load only, since the balancing moment Mo would be zero and the shaft deflection would be unaffected.

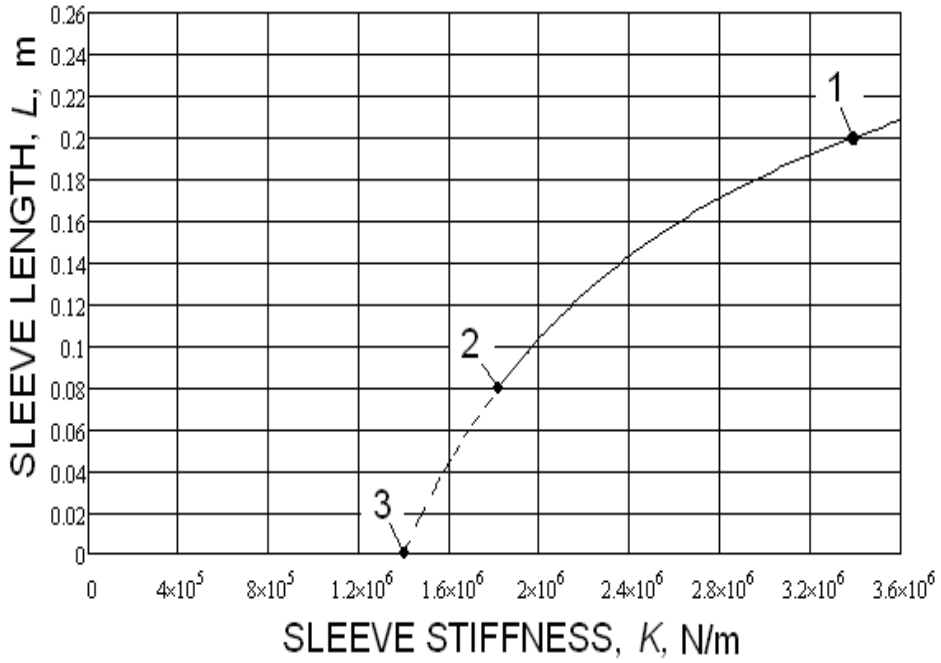


**Figure 3.5.** Sleeve Length vs Stiffness for elimination of Compensated Critical Speed

## 3.4 Encastre Points of Conversion

For beams or shafts with loading conditions that produce only small deflections, such that the material is operating within the linear elastic portion its stress/ strain curve, as is normal engineering practice for ferrous alloys, the shaft deflections and slope will be linearly proportional to the applied loads and the Theory of Superposition applies. Hence, the individual deflections produced by individual loads and moments can be summed to give the combined response of all the applied loads and moments [58].

Therefore, it is apparent that an encastre shaft is analytically the same as a simply supported shaft with the addition of end fixing moments and since it is physically possible mount any shaft in long bearings as opposed to short bearings or having a flexible element interface, then it is equally possible to

convert any shaft, of any geometric or loading variation, to an encastre form, by equating the balancing moment, *Mo,* to the fixing moment, *Mf*.

This then is the rational objective of critical speed elimination, i.e. to adjust the Balancing Sleeve Moment, *Mo*, so that it equals the encastre Fixing Moment, *Mf*. Unfortunately, it is not possible to maintain this condition throughout the whole of the operating speed range, but it is advantageous if it occurs at a speed as close as possible to the Compensated Critical Speed, so that near elimination results.

This adjustment process is illustrated in Figure 3.6 and 3.7 below.

Figure 3.6, shows a close up example of the both moments near the critical speeds, and it can be seen that there are 3 points of intersection, where *Mo* = *Mf*, and conversion occurs.

Point 1 occurs at the Compensated Critical Speed, where *Mo* instantaneously passes from minus infinity to plus infinity. This is only a theoretical possibility and consequently it is not a practical point of conversion. Note, this speed varies only slightly with Compensating Sleeve Length, *L.*

Point 2 occurs at the Classical Critical Speed, which, as defined earlier, is fixed speed and doesn't vary with length *L*.

Point 3 is the natural intersection of the 2 curves that would occur without the interruption of the critical speed points and is highly dependent on the magnitude of *L*. Hence, it is more adjustable and *L* can be used as a design variable – note, it moves to a lower speed with increasing length, *L* and vice versa.

Figure 3.7, shows how easily point 3 can be adjusted and the effect of a small increase in length *L*, from 0.20m to 0.20603m, where it can be seen

that point 3 is now very close to the Compensated Critical Speed, intersection point 1 and hence the compensation is very close to the optimal maximum level to give complete elimination.

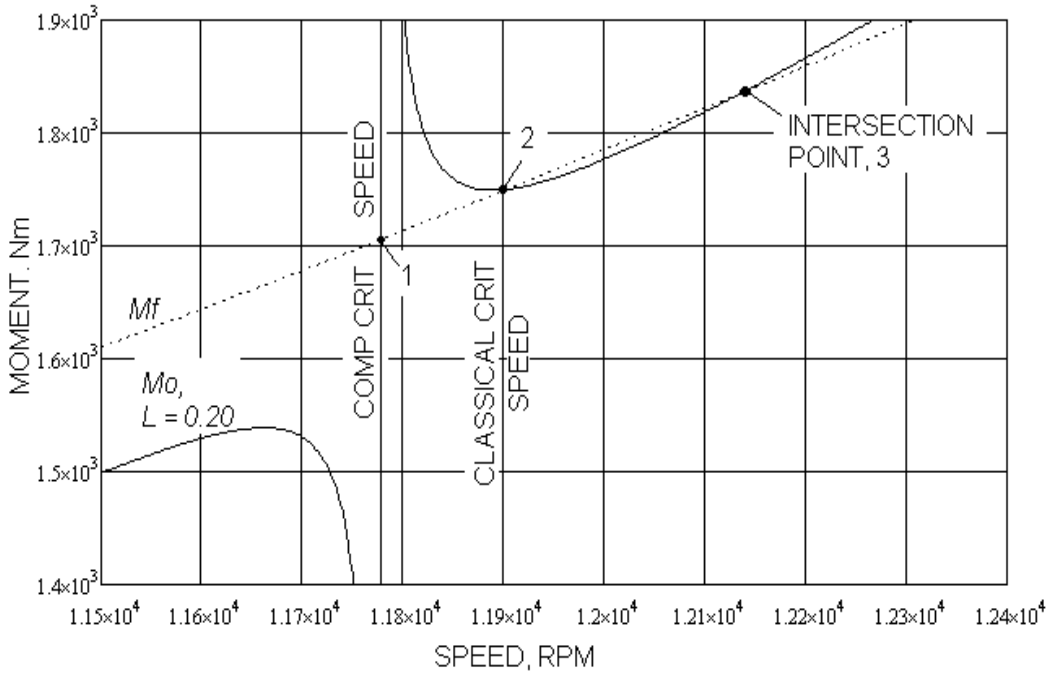


**Figure 3.6.** Close-up comparison of *Mf* & *Mo* for *L* = 0.20 m

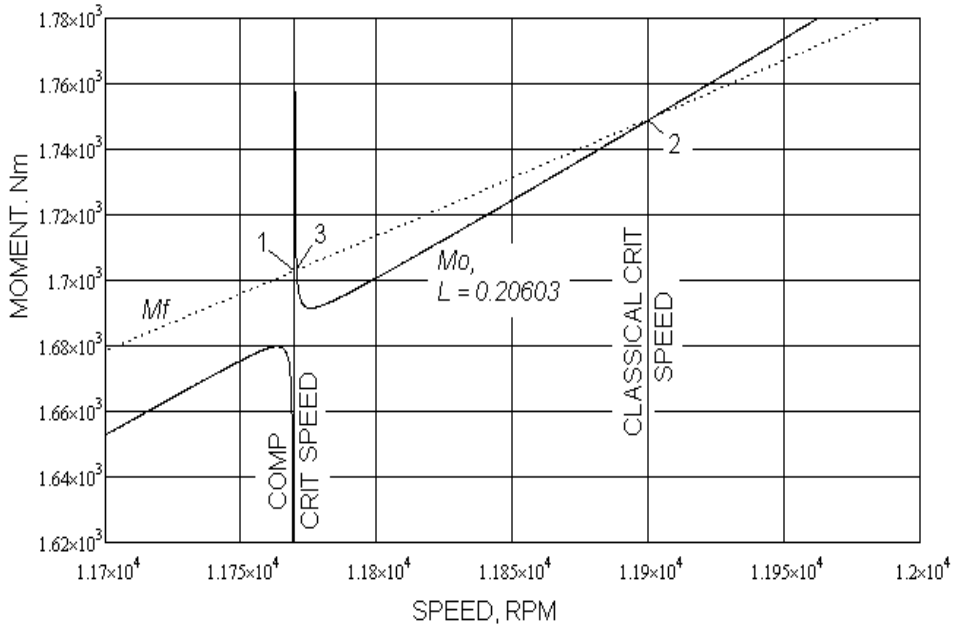


**Figure 3.7.** Close-up comparison of *Mf* & *Mo* for *L* = 0.20603 m

Exact coincidence would result in complete elimination, which although theoretically possible, is not practical due to the infinite sensitivity of the transient. It can also be noted, that the closer points 1 and 3 become, then the sharper the critical speed spike becomes, thereby minimizing the magnifying effect of the critical speed and allowing safe operation much closer to its critical speed than would otherwise be possible.

At the practical points of intersection, 2 and 3, where *Mo* = *Mf*, numerical analysis can be used to show that the shaft deflections and internal shear reaction forces are identical, thereby confirming that the points of intersection are indeed Points of Conversion where the simply supported shaft fully replicates the encastre system, albeit only for the speeds where the intersection occurs.

## 3.5 Practical Possibility of Critical Speed Elimination

Furthering the analytical investigation carried out in chapter 2, with the site equivalent parameter values, given in Table 2.1, the maximum obtainable balance compensation condition, Figure 2.6, chapter 2, is investigated.

Figure 3.8, below shows a close up of this condition, in which the reaction load has been calculated and plotted against rotational speed in very fine steps of only 0.1 rpm. However, it can be seen that the critical speed has still not been completely eliminated as a spike still occurs between 11,769.3 rpm and 11,769.5 rpm, which would go to infinity if the calculated speed could be made exactly equal to the compensated critical speed. Nevertheless, it can be seen that the act of balance sleeve compensation makes the critical speed spike much sharper until at full compensation it would be possible to theoretically operate to within 1 rpm of the actual critical speed, i.e. it is reasonable to conclude that the critical speed has been completely NULLIFIED. Note, actual elimination of the critical speed would be practically impossible since the parameter values etc. undoubtedly contain irrational numbers such as $\pi$. However, while such proximity would

not be advocated, it is clearly illustrated that the 50% API recommended lateral critical speed margin [15] could be vastly reduced, say to 5 or 10% thereby easing one of the many design constraints that apply to the shafts of high speed drive trains.

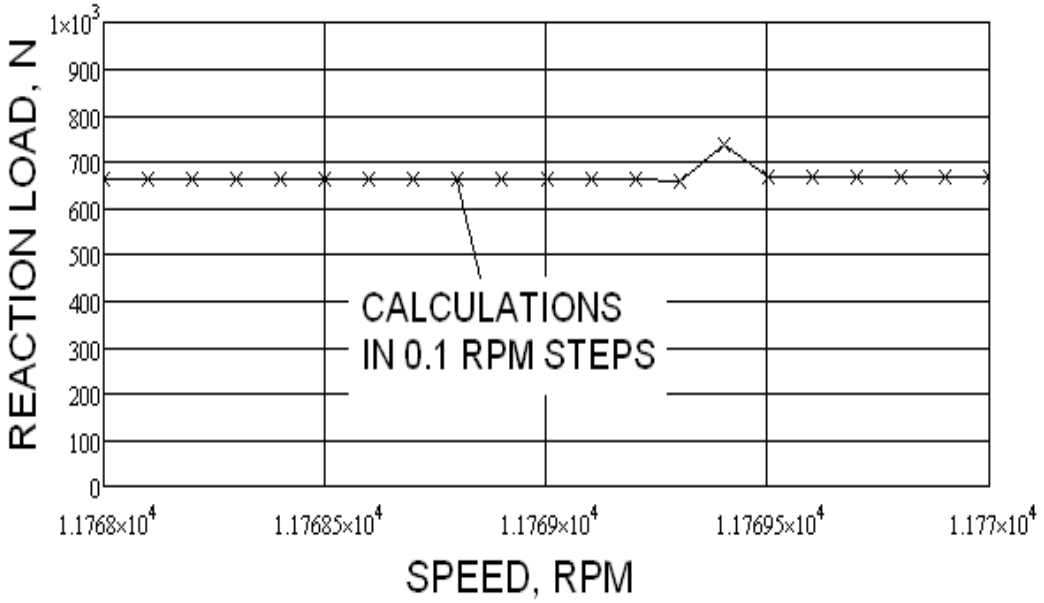


**Figure 3.8.** Close-up of Fully Compensated Critical Speed

## 3.6 Sensitivity Study

Table 2.2, chapter 2, provides an indication of the sensitivity of balance compensation with respect to sleeve length, where the sleeve stiffness is held constant, as required say, during a design exercise. Figures 2.6 and 2.7 show that the reaction load increases from 370 N, to 3,400 N, for length reduction from, $L$ = 0.206 m, to $L$ = 0.130 m, with a constant stiffness, $K$ = 3.4 x $10^6$ N/m. This compares with an uncompensated reaction load of 11,200 N.

However, for site balancing purposes, it is envisaged that the sleeve would be designed to allow length adjustments to occur in situ, hence the sleeve cross section would remain unchanged and the sleeve stiffness would be

inversely proportional to the length cubed [58]. Therefore, it is the sensitivity under this condition, that would be more useful to a commissioning engineer and this arrangement is shown in Figure 3.9, where, $\overline{R}_e$, is the non-dimensional reaction load, and $\overline{L}$, is the non-dimensional sleeve length, at 10,500 rpm:

$$\overline{R}_e = \frac{actual\_reaction\_load}{Uncomp\_reaction\_load} \qquad \overline{L} = \frac{actual\_length}{design\_length}$$

It is noted that the sensitivity figures are well within the practical limits required for design purposes, such that a 5% length change would give a very substantial 15 – 20% change in reaction load. Therefore, useful compensation should be achievable, without the risk of over-sensitivity, causing instability.

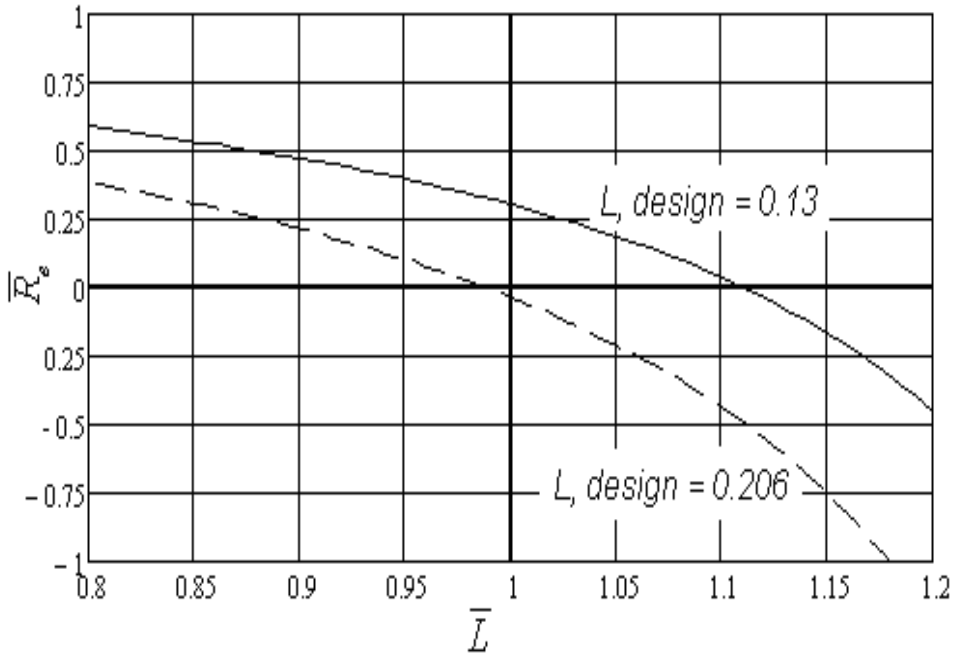


**Figure 3.9.** Balance Sleeve Sensitivity

## 3.7 Preliminary Conclusions

This chapter confirms the ability to theoretically transform a simply supported shaft to an encastre mounted equivalent and thereby facilitate the creation of a new balancing methodology for high-speed, flexible shafts. It describes the elimination of the classical critical speed and the consequential production of a new compensated critical speed, of a slightly lower level. Alternatively, it can be regarded simply that balance sleeve compensation causes a reduction in critical speed. However, the analysis further determines the operating conditions necessary to cause its elimination, or since this is only theoretically possible, it's practical nullification. Hence the potential of this system to reduce bearing reaction loads and to vastly reduce existing lateral critical speed margins has been demonstrated.

# Chapter 4

## 4.1 Generalised Analysis of Concentrated Imbalances

The analysis of balance sleeve compensation outlined in Chapters 2 and 3 provided theoretical proof of concept and illustrated the potential benefits to be gained from a proposed new methodology of balancing high-speed flexible shafts. However, the analysis was based, for simplicity, on a specialised case of shafts with uniform eccentricity. This work is now extended to cover the more generalised case of shafts with concentrated imbalance.

## 4.2 Theoretical Analysis

As in the analysis of chapters 2 and 3, this investigation considers a simply supported, long, plain shaft, of circular cross section - thereby making gyroscopic moments negligible - operating under steady state, rotating conditions, such that both radial and angular accelerations and associated forces/ moments are zero. This assumption is made to provide a first-order simplification and is widely considered applicable [59] to long, thin shafts, with low slenderness ratios, typically < 0.12 (as employed in the site equivalent models given later). Shaft deflections due to shear effects, are regarded as being “second degree” in magnitude, and are not considered here. In addition, the preliminary study is limited to single concentrated imbalance as it is shown that more complex distributions can be regarded as the summation of any number of individual imbalances, provided that the shaft deflections remain small and the material is operating within the linear portion of its stress/ strain curve (the principle of superposition is then applicable). This also allows algebraic solutions to be obtained from the equations of motion, negating the requirement for time-consuming numeric solutions from Finite Element Analysis (FEA) to be necessary during early design stages. Further, it is claimed that a greater degree of clarity and understanding can be gained from such solutions and it is shown that they

reveal new insights into the balancing mechanism that would not be apparent otherwise.

Figure 1 shows a plain rotating shaft of total mass, $M_s$, and overall length, $\ell$, simply supported at both ends, with deflection, *r*, at length, *x,* and concentrated eccentricity, *e*, between dimensions *a* and *f.* Integrally attached to each end is a Compensating Balance Sleeve, comprising a flexible arm with negligible mass, of lengths, $L_1$ and $L_2$, spring stiffness's, $K_1$ and $K_2$ and deflections, $Y_1$ and $Y_2$, together with equivalent lumped, trim balancing masses, $m_1$ and $m_2$, positioned with eccentricities, $c_1$ and $c_2$, at their extreme ends. The eccentricity of the lumped masses are positioned 180º out of phase with the shaft eccentricity such that rotation of the shaft produces CFs to act on masses $M_s$, $m_1$ and $m_2$, thereby imparting corresponding deflections *r,* $Y_1$ and $Y_2$, in opposing directions.

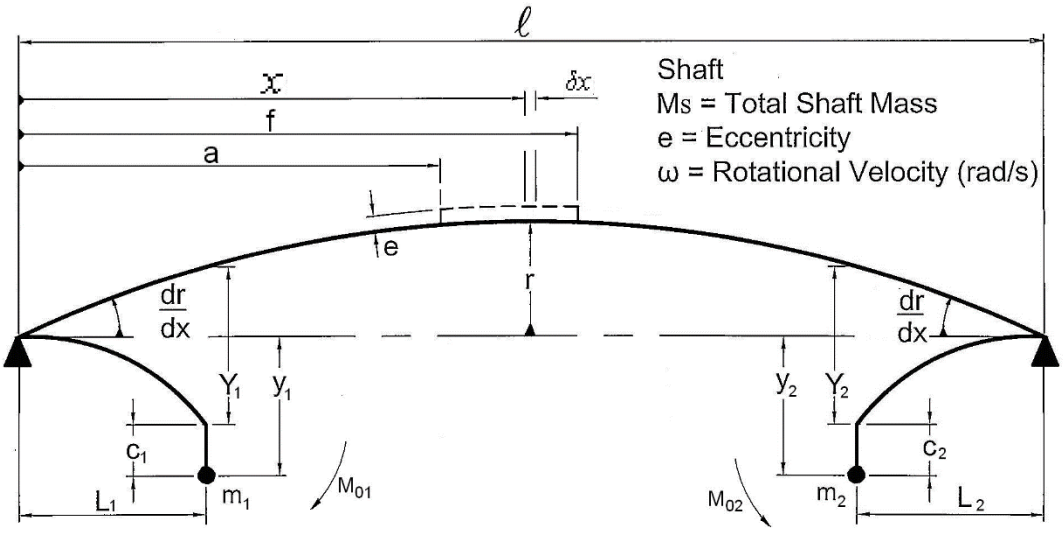


**Figure 4.1,** Schematic of simply supported, rotating shaft with concentrated eccentricity

Concentrated imbalance caused by localised manufacturing or material defect, or possibly a point of external damage, can be considered as an

equivalent additional mass, $M_u$, acting at radius, $R$. This can be likened to a trim balance mass, $M_u$, typically fastened to the outer diameter of the shaft, and for the purpose of analysis, is represented by a short zone of length, ($f$ – $a$), with uniform eccentricity, $e$, and a zone mass, $M_p$, as shown in Figure 4.2.

Taking mass moments about the axis of rotation and assuming $M_u$ and $r$ are much less than $M_p$ and $R$, the zone eccentricity approximates to [6]:

$$e @ \frac{M_u}{M_p}.R \tag{4.1}$$

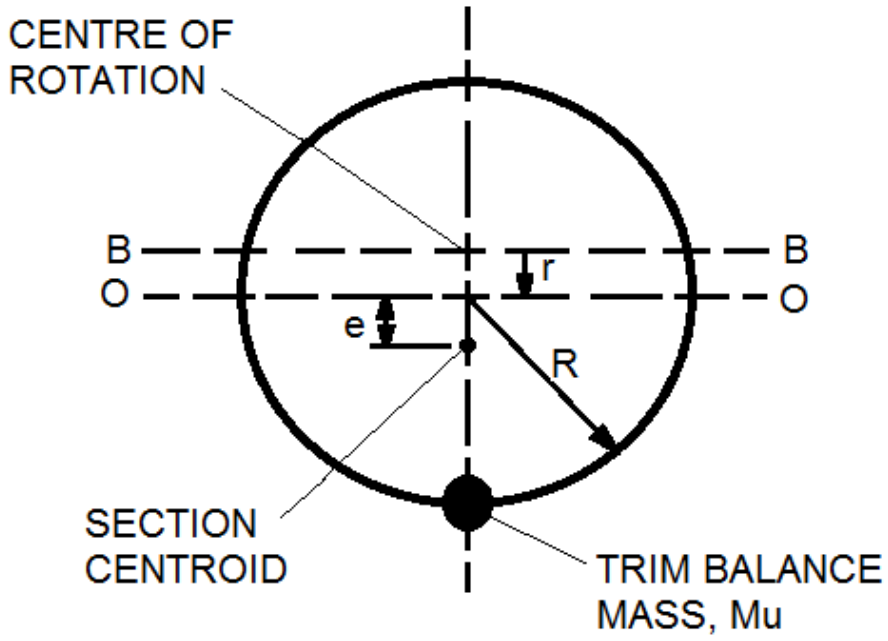


**Figure 4.2,** Schematic of concentrated imbalance zone eccentricity

*Considering forces on the Compensating Balance Sleeves:*

Centrifugal Force, at LHS, $CF_1 = m_1.\omega^2.y_1$ (4.2)

From inspection of Figure 1, for small angles of slope:

$$y_1 = Y_1 + c_1 - L_1(\frac{dr}{dx})_{x=0} \tag{4.3}$$

$$Y_1 = \frac{-m_1\omega^2\left(L_1(\frac{dr}{dx})_{x=0} - c_1\right)}{K_1 - m_1\omega^2} \qquad (4.4)$$

The moment imposed on shaft is:

$$M_{01} = A_{01}\left(\frac{dr}{dx}\right)_{x=0} + B_{01} \qquad (4.5)$$

where $A_{01} = \frac{-m_1\omega^2 L_1{}^2 K_1}{K_1 - m_1\omega^2}$ (4.6) $B_{01} = \frac{m_1\omega^2 c_1 L_1 K_1}{K_1 - m_1\omega^2}$ (4.7)

Similarly for Compensating Balance Sleeve 2, noting that the slope, $(\frac{dr}{dx})_{x=l}$ is –ve, gives:

$$Y_2 = \frac{m_2\omega^2\left(L_2(\frac{dr}{dx})_{x=l} + c_2\right)}{K_2 - m_2\omega^2} \qquad (4.8)$$

The moment imposed on shaft is: $M_{02} = A_{02}\left(\frac{dr}{dx}\right)_{x=l} + B_{02}$ (4.9)

where $A_{02} = \frac{m_2\omega^2 L_2{}^2 K_2}{K_2 - m_2\omega^2}$ (4.10) $B_{02} = \frac{m_1\omega^2 c_2 L_2 K_2}{K_2 - m_2\omega^2}$ (4.11)

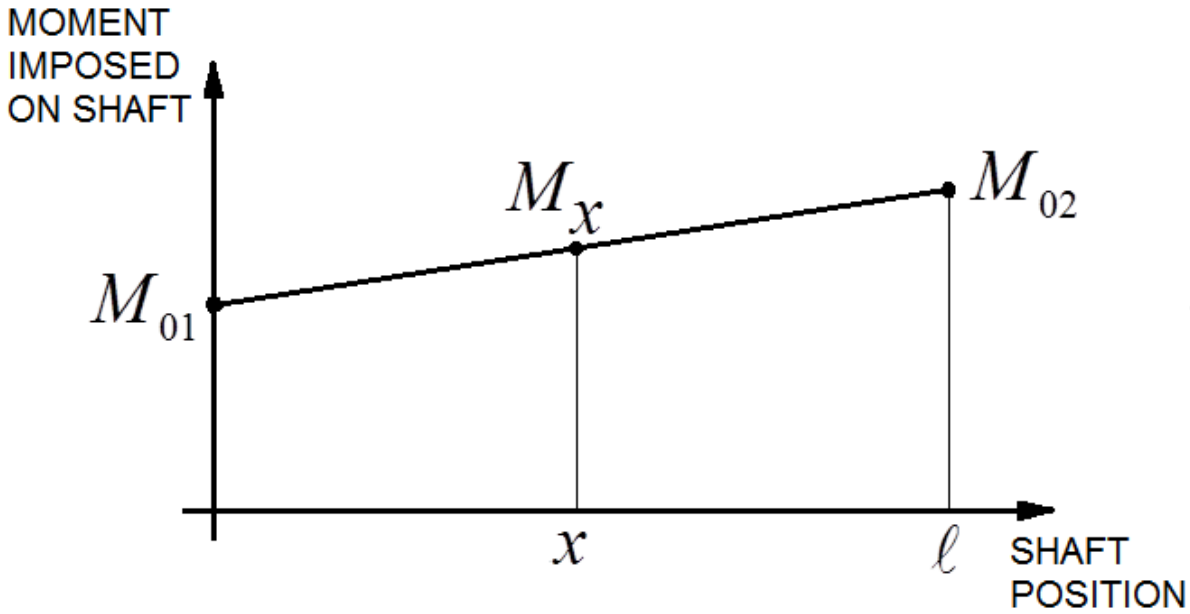


**Figure 4.3,** Balancing Sleeve Moments imposed on the shaft

The external moment, *Mx*, imposed on the shaft, at any position *x,* by the balance sleeves, will be a straight line between the end moments[60], $M_{01}$ and $M_{02}$, as shown in Figure 4.3, such that:

$$Mx = M_{01} + \frac{M_{02} - M_{01}}{\ell}.x \qquad (4.12)$$

From 'Bending of Beams' theory, the dynamic loading imposed on the shaft is found from differentiating *Mx*, (but noting that $(\frac{dr}{dx})_{x=0}$ and $(\frac{dr}{dx})_{x=l}$ are constant with respect to x), so that:

Dynamic Loading = $\frac{d^2Mx}{dx^2} = 0$

*Considering Forces on the shaft:*

At any point, *x,* along the shaft, the eccentricity can be expressed as, $e_x$, where, *H*, denotes the Heaviside Function.

$$e_x = e.[H(x-a) - H(x-f)]$$

Then the CF acting on any elemental section $\delta x$ is:

$$CF = \frac{M_s}{\ell}\delta x\omega^2(r + e_x)$$

Hence, dynamic loading, at length *x* is:

$$\frac{CF}{\delta x} = \frac{M_s}{\ell}\omega^2(r + e_x)$$

*Considering the Combined Assembly*:

Total Dynamic Loading = $\frac{M_s}{\ell}\omega^2(r + e_x) + 0$

$$= \frac{M_s}{\ell}\omega^2 r + \frac{M_s}{\ell}\omega^2 e.[H(x-a) - H(x-f)]$$

(4.13)

However, from beam theory, the dynamic loading = $EI\frac{d^4r}{dx^4}$,

therefore: $EI\frac{d^4r}{dx^4} = \frac{M_s}{\ell}\omega^2 r + \frac{M_s}{\ell}\omega^2 e.[H(x-a) - H(x-f)]$

Applying Laplace Transforms, (where $\hat{e}$ = exponential value, e), gives:

$$EI(s^4\bar{r} - s^3r_0 - s^2r_1 - sr_2 - r_3) = \frac{M_s}{\ell}\omega^2\bar{r} + \frac{M_s}{\ell}\omega^2 e.(\frac{\hat{e}^{-as}}{s} - \frac{\hat{e}^{-fs}}{s})$$

At *x* = 0: $r_0$ = 0, and using: $b^4 = \frac{M_s\omega^2}{\ell EI}$ (2.17) from chapter 2,

gives: $\bar{r}.(s^4 - b^4) = b^4 e.(\frac{\hat{e}^{-as}}{s} - \frac{\hat{e}^{-fs}}{s}) + s^2.r_1 + s.r_2 + r_3$

At $x$ = 0, Bending Moment =

$$M_{01} = A_{01}\left(\frac{dr}{dx}\right)_{x=0} + B_{01} = E.I.(\frac{d^2 r}{dx^2})_{x=0} = E.I.r_2$$

$$\therefore r_2 = \frac{A_{01}.r_1 + B_{01}}{E.I}$$

and by substitution

$$\bar{r}.(s^4 - b^4) = b^4 e.(\frac{\hat{e}^{-as}}{s} - \frac{\hat{e}^{-fs}}{s}) + s^2.r_1 + s.(\frac{A_{01}.r_1 + B_{01}}{E.I}) + r_3$$

Let $A_1 = \frac{A_{01}.r_1 + B_{01}}{E.I}$ , (4.14) and $A_2 = r_3$ , (4.15)

Then $\bar{r} = \frac{b^4 e}{s.(s^4 - b^4)}.(\hat{e}^{-as} - \hat{e}^{-fs}) + \frac{A_1 s}{s^4 - b^4} + \frac{r_1 s^2}{s^4 - b^4} + \frac{A_2}{s^4 - b^4}$

Expanding using Partial Fractions, as per Uniform Eccentricity Theory gives:

$$\bar{r} = \left[\frac{-e}{s} + \frac{e/2.s}{s^2 + b^2} + \frac{e/4}{s+b} + \frac{e/4}{s-b}\right].\hat{e}^{-as} - \left[\frac{-e}{s} + \frac{e/2.s}{s^2 + b^2} + \frac{e/4}{s+b} + \frac{e/4}{s-b}\right].\hat{e}^{-fs}$$

$$- \frac{A_1/2b^2.s}{s^2 + b^2} + \frac{A_1/4b^2}{s+b} + \frac{A_1/4b^2}{s-b} + \frac{1/2.r_1}{s^2 + b^2} - \frac{1/4b.r_1}{s+b} + \frac{1/4b.r_1}{s-b} - \frac{1/2b^2.A_2}{s^2 + b^2} - \frac{1/4b^3.A_2}{s+b} + \frac{1/4b^3.A_2}{s-b}$$

Collating denominator similar terms, and putting:

$P = -A_1/2b^2$ , (4.16) $Q = 1/2.r_1 - A_2/2b^2$ , (4.17)

$M = A_1/4b^2 - r_1/4b - A_2/4b^3$ , (4.18) $N = A_1/4b^2 + r_1/4b + A_2/4b^3$ (4.19)

Gives:

$$\bar{r} = \left[\frac{-e}{s} + \frac{e/2.s}{s^2 + b^2} + \frac{e/4}{s+b} + \frac{e/4}{s-b}\right].\hat{e}^{-as} - \left[\frac{-e}{s} + \frac{e/2.s}{s^2 + b^2} + \frac{e/4}{s+b} + \frac{e/4}{s-b}\right].\hat{e}^{-fs}$$

$$+\frac{s.P}{s^2+b^2}+\frac{Q}{s^2+b^2}+\frac{M}{s+b}+\frac{N}{s-b}$$

It is convenient to split this equation into terms with and without Heaviside functions such that:

$$\bar{r}=\overline{R}_1+\overline{R}_2 \tag{4.20}$$

where

$$\overline{R}_1=\left[\frac{-e}{s}+\frac{e/2.s}{s^2+b^2}+\frac{e/4}{s+b}+\frac{e/4}{s-b}\right].\hat{e}^{-as}-\left[\frac{-e}{s}+\frac{e/2.s}{s^2+b^2}+\frac{e/4}{s+b}+\frac{e/4}{s-b}\right].\hat{e}^{-fs}$$

and $$\overline{R}_2=+\frac{s.P}{s^2+b^2}+\frac{Q}{s^2+b^2}+\frac{M}{s+b}+\frac{N}{s-b}$$

Considering $\overline{R}_1$ and performing a reverse Laplace Operation gives:

$$R_1=\left[-e+\frac{e}{2}.\cos b(x-a)+\frac{e}{4}.\hat{e}^{-b(x-a)}+\frac{e}{4}.\hat{e}^{b(x-a)}\right].H(x-a)$$
$$-\left[-e+\frac{e}{2}.\cos b(x-f)+\frac{e}{4}.\hat{e}^{-b(x-f)}+\frac{e}{4}.\hat{e}^{b(x-f)}\right].H(x-f)$$

And since generally, $\overline{M}\hat{e}^{-z}+\overline{N}\hat{e}^{z}=\overline{G}\cosh z+\overline{H}\sinh z$ , for any value of *z*, where:

$\overline{G}=\overline{M}+\overline{N}=\frac{e}{2}$ and $\overline{H}=\overline{N}-\overline{M}=0$ substituting in $R_1$ gives:

$$R_1=\left[-e+\frac{e}{2}.\cos b(x-a)+\frac{e}{2}.\cosh b(x-a)\right].H(x-a)$$
$$-\left[-e+\frac{e}{2}.\cos b(x-f)+\frac{e}{2}.\cosh b(x-f)\right].H(x-f) \tag{4.21}$$

In order to determine the end conditions at *x* = $\ell$, let $R_1$ and its corresponding differentials be:

$$R_{1l}=\left[-e+\frac{e}{2}.\cos b(\ell-a)+\frac{e}{2}.\cosh b(\ell-a)\right].H(\ell-a)$$
$$-\left[-e+\frac{e}{2}.\cos b(\ell-f)+\frac{e}{2}.\cosh b(\ell-f)\right].H(\ell-f) \tag{4.22}$$

$$\dot{R}_{1l}=\left[-\frac{eb}{2}.\sin b(\ell-a)+\frac{eb}{2}.\sinh b(\ell-a)\right].H(\ell-a)$$
$$+\left[\frac{eb}{2}.\sin b(\ell-f)-\frac{eb}{2}.\sinh b(\ell-f)\right].H(\ell-f) \tag{4.23}$$

$$\ddot{R}_{1l} = \left[ -\frac{eb^2}{2}.\cos b(\ell - a) + \frac{eb^2}{2}.\cosh b(\ell - a) \right].H(\ell - a)$$
$$+ \left[ \frac{eb^2}{2}.\cos b(\ell - f) - \frac{eb^2}{2}.\cosh b(\ell - f) \right].H(\ell - f) \qquad (4.24)$$

$$\dddot{R}_{1l} = \left[ \frac{eb^3}{2}.\sin b(\ell - a) + \frac{eb^3}{2}.\sinh b(\ell - a) \right].H(\ell - a)$$
$$- \left[ \frac{eb^3}{2}.\sin b(\ell - f) + \frac{eb^3}{2}.\sinh b(\ell - f) \right].H(\ell - f) \qquad (4.25)$$

NOTE, the 1st part of (4.20), together with its end conditions at $x = \ell$, has now been determined.

Now, considering $\overline{R}_2$ and performing a reverse Laplace Operation gives:

$$R_2 = P.\cos bx + \frac{Q}{b}.\sin bx + M.\hat{e}^{-bx} + N.\hat{e}^{bx} \qquad (4.26)$$

But, $r = R_1 + R_2 = 0$, at x = $\ell$, therefore:

$$0 = R_{1l} + P.\cos b\ell + \frac{Q}{b}.\sin b\ell + M.\hat{e}^{-b\ell} + N.\hat{e}^{b\ell} \qquad (4.27)$$

Also, at $x = \ell$,

$$\frac{d^2r}{dx^2} = \frac{M_{02}}{E.I} = \ddot{R}_{1l} - b^2 P.\cos b\ell - b^2 \frac{Q}{b}.\sin b\ell + b^2 M.\hat{e}^{-b\ell} + b^2 N.\hat{e}^{b\ell}$$

$$\therefore \frac{M_{02}}{b^2 E.I} = \frac{\ddot{R}_{1l}}{b^2} - P.\cos b\ell - \frac{Q}{b}.\sin b\ell + M.\hat{e}^{-b\ell} + N.\hat{e}^{b\ell} \qquad (4.28)$$

Adding and Subtracting (4.27) and (4.28) gives:

$$\frac{M_{02}}{b^2.E.I} = R_{1l} + \frac{\ddot{R}_{1l}}{b^2} + 2.(M.\hat{e}^{-b\ell} + N.\hat{e}^{b\ell}) \qquad (4.29)$$

$$-\frac{M_{02}}{b^2.E.I} = R_{1l} - \frac{\ddot{R}_{1l}}{b^2} + 2.P.\cos b\ell + \frac{2.Q}{b}.\sin b\ell$$

giving $$\frac{Q}{b}.\sin b\ell = -\frac{M_{02}}{2b^2.E.I} - \frac{R_{1l}}{2} + \frac{\ddot{R}_{1l}}{2b^2} - P.\cos b\ell \qquad (4.30)$$

Substituting (4.30) in (4.26) gives:

$$r = R_1 + R_2 = R_1 + P.\cos bx - \frac{\frac{M_{02}}{2b^2.E.I} + \frac{R_{1l}}{2} - \frac{\ddot{R}_{1l}}{2b^2} + P.\cos b\ell}{\sin b\ell}.\sin bx + M.\hat{e}^{-bx} + N.\hat{e}^{bx}$$

As previously shown in chapter 2, (2.30) and (2.31), converting into hyperbolic functions gives:

$$r = R_1 + P.\cos bx - \frac{\frac{M_{02}}{2b^2.E.I} + P.\cos b\ell + \frac{R_{1l}}{2} - \frac{\ddot{R}_{1l}}{2b^2}}{\sin b\ell}.\sin bx + G\cosh bx + H\sinh bx \tag{4.31}$$

NOTE: This is the general equation for the shaft deflection, at any position *x* and the unknown parameters will be determined as follows.

From (4.18), (4.19) and (4.16): $G = M + N = \frac{A_1}{2b^2} = -P$ (4.32)

and $H = N - M = {}^{r_1}\!/_{2b} + {}^{A_2}\!/_{2b^3}$ (4.33)

By re-arranging (4.29) and using the above hyperbolic conversion:

$$M.\hat{e}^{-b\ell} + N.\hat{e}^{b\ell} = \frac{M_{02}}{2.b^2.E.I} - \frac{R_{1l}}{2} - \frac{\ddot{R}_{1l}}{2.b^2} = G\cosh b\ell + H\sinh b\ell$$

Substituting for *G* from (30) and solving for *H* gives:

$$H = \frac{\frac{M_{02}}{2.b^2.E.I} - \frac{R_{1l}}{2} - \frac{\ddot{R}_{1l}}{2.b^2} - \frac{A_1}{2b^2}.\cosh b\ell}{\sinh b\ell} \tag{4.34}$$

From (9) and by differentiating (4.31) at x = $\ell$:

$$\left(\frac{dr}{dx}\right)_{x=l} = \frac{M_{02} - B_{02}}{A_{02}}$$

$$= \dot{R}_{1\ell} - Pb.\sin b\ell - b\left[\frac{\frac{M_{02}}{2b^2.E.I} + P.\cos b\ell + \frac{R_{1l}}{2} - \frac{\ddot{R}_{1l}}{2b^2}}{\sin b\ell}\right].\cos b\ell$$

$$+ bG\sinh b\ell + bH\cosh b\ell$$

Substituting: $\cos^2 z = 1 - \sin^2 z$ and substituting *G* and H from (4.32) and (4.34) gives:

$$\frac{M_{02} - B_{02}}{A_{02}} = \dot{R}_{1\ell} - \frac{M_{02}}{2b.E.I}\frac{\cos b\ell}{\sin b\ell} - \frac{2Pb + bR_{1\ell}.\cos b\ell - \frac{\ddot{R}_{1l}}{b}\cos b\ell}{2.\sin b\ell}.- bP\sinh b\ell$$

$$+ b\left[\frac{\frac{M_{02}}{2.b^2.E.I} - \frac{R_{1l}}{2} - \frac{\ddot{R}_{1l}}{2.b^2} + P.\cosh b\ell}{\sinh b\ell}\right].\cosh b\ell$$

Substituting: $\cosh^2 z = 1 + \sinh^2 z$ and grouping $M_{02}$ terms gives:

$$\frac{M_{02} - B_{02}}{A_{02}} + \frac{M_{02}}{2b.E.I}\frac{\cos b\ell}{\sin b\ell} - \frac{M_{02}}{2b.E.I}\frac{\cosh b\ell}{\sinh b\ell} = \dot{R}_{1\ell} - \frac{2Pb + b.\left(R_{1\ell}.- \frac{\ddot{R}_{1l}}{b^2}\right).\cos b\ell}{2.\sin b\ell}$$

$$- b.\left(R_{1l} + \frac{\ddot{R}_{1l}}{b^2}\right).\frac{\cosh b\ell}{2.\sinh b\ell} + \frac{Pb}{\sinh b\ell}$$

$$\therefore M_{02}\left(\frac{1}{A_{02}} + \frac{1}{2b.E.I}.\frac{\cos b\ell}{\sin b\ell} - \frac{1}{2b.E.I}.\frac{\cosh b\ell}{\sinh b\ell}\right) =$$

$$\frac{B_{02}}{A_{02}} + \dot{R}_{1\ell} - \frac{2Pb + b.\left(R_{1\ell}.- \frac{\ddot{R}_{1l}}{b^2}\right).\cos b\ell}{2.\sin b\ell} + \frac{2Pb - b.\left(R_{1l} + \frac{\ddot{R}_{1l}}{b^2}\right).\cosh b\ell}{2.\sinh b\ell}$$

Simplifying by letting: $A_3 = C_1 + C_2.P + C_3 + C_4.P + C_5$

where: $C_1 = \frac{B_{02}}{A_{02}} + \dot{R}_{1\ell}$ (4.35), $C_2 = -\frac{b}{\sin b\ell}$ (4.36),

$$C_3 = -b.\frac{\left(R_{1\ell}. - \frac{\ddot{R}_{1l}}{b^2}\right).\cos b\ell}{2.\sin b\ell} \quad (4.37)$$

$$C_4 = \frac{b}{\sinh b\ell} \quad (4.38), \qquad C_5 = -b.\frac{\left(R_{1\ell}. + \frac{\ddot{R}_{1l}}{b^2}\right).\cosh b\ell}{2.\sinh b\ell} \quad (4.39)$$

$$C_6 = C_2 + C_4 \quad (4.40), \qquad C_7 = C_1 + C_3 + C_5 \quad (4.41)$$

Let: $$A_4 = \frac{1}{A_{02}} + \frac{1}{2b.E.I}.\frac{\cos b\ell}{\sin b\ell} - \frac{1}{2b.E.I}.\frac{\cosh b\ell}{\sinh b\ell} \quad (4.42)$$

$$\therefore M_{02} = \frac{A_3}{A_4} = \frac{P.C_6 + C_7}{A_4} \quad (4.43)$$

By differentiating (4.31) and noting that $R_1 = 0$ at *x = 0*

$$\left(\frac{dr}{dx}\right)_{x=0} = r_1 = -b.\left(\frac{\frac{M_{02}}{2b^2.E.I} + P.\cos b\ell + \frac{R_{1l}}{2} - \frac{\ddot{R}_{1l}}{2b^2}}{\sin b\ell}\right) + b.H \quad (4.44)$$

Combining (4.14) and (4.16) and re-arranging gives:

$r_1 = -\frac{2b^2 EIP + B_{01}}{A_{01}}$ and substituting in (4.44) together with *H* from (4.34) gives:

$$-\frac{2b^2.E.I.P + B_{01}}{A_{01}} = -b.\left(\frac{\frac{M_{02}}{2b^2.E.I} + P.\cos b\ell + \frac{R_{1l}}{2} - \frac{\ddot{R}_{1l}}{2b^2}}{\sin b\ell}\right) + b.\left(\frac{\frac{M_{02}}{2.b^2.E.I} - \frac{R_{1l}}{2} - \frac{\ddot{R}_{1l}}{2.b^2} + P.\cosh b\ell}{\sinh b\ell}\right)$$

$$-\frac{2b^2.E.I.P+B_{01}}{A_{01}}=M_{02}.\left(\frac{1}{2b.E.I.\sinh b\ell}-\frac{1}{2b.E.I.\sin b\ell}\right)-b.\left(\frac{P.\cos b\ell+\frac{R_{1l}}{2}-\frac{\ddot{R}_{1l}}{2.b^2}}{\sin b\ell}\right)$$

$$+b.\left(\frac{P.\cosh b\ell-\frac{R_{1l}}{2}-\frac{\ddot{R}_{1l}}{2.b^2}}{\sinh b\ell}\right)$$

Simplifying by letting: $D_1.P+D_2=D_3.M_{02}+D_4.P+D_5+D_6.P+D_7$ (4.45)

where: $D_1=-\frac{2b^2.E.I.P}{A_{01}}$ (4.46), $D_2=-\frac{B_{01}}{A_{01}}$ (4.47)

$D_3=\frac{1}{2b.E.I.\sinh b\ell}-\frac{1}{2b.E.I.\sin b\ell}$ (4.48), $D_4=-\frac{b.\cos b\ell}{\sin b\ell}$ (4.49)

$D_5=-b.\frac{\frac{R_{1l}}{2}-\frac{\ddot{R}_{1l}}{2.b^2}}{\sin b\ell}$ (4.50), $D_6=\frac{b.\cosh b\ell}{\sinh b\ell}$ (4.51)

$D_7=-b.\frac{\frac{R_{1l}}{2}+\frac{\ddot{R}_{1l}}{2.b^2}}{\sinh b\ell}$ (4.52)

$D_8=\frac{D_1-D_4-D_6}{D_3}$ (4.53), $D_9=\frac{D_2-D_5-D_7}{D_3}$ (4.54)

$$\therefore M_{02}=P.\left(\frac{D_1-D_4-D_6}{D_3}\right)+\left(\frac{D_2-D_5-D_7}{D_3}\right)=P.D_8+D_9 \quad (4.55)$$

Equating (4.43) and (4.55) gives: $\frac{P.C_6+C_7}{A_4}=P.D_8+D_9$

and hence: $P=\frac{A_4.D_9-C_7}{C_6-A_4.D_8}$ (4.56)

Therefore, all the unknown parameters *P, $M_{02}$, G* and *H,* required to calculate the shaft deflection, for any position *x,* from equation (4.31), can now be determined from (4.56), (4.55), (4.32) and (4.34).

To determine the Reaction Loads, from beam theory, the vertical shear force within the beam caused by bending is given by: $SFv = EI\,\frac{d^3 r}{dx^3}$

At $x = 0$, from (4.33) and (4.15), $r_3 = (H - {}^{r_1}\!/_{2b})2b^3$ (4.57)

and at $x = \ell$, by differentiating (4.31)

$$\dddot{r}_\ell = \dddot{R}_{1\ell} + Pb^3.\sin b\ell + b^3.\left[\frac{\frac{M_{02}}{2b^2.E.I} + P.\cos b\ell + \frac{R_{1l}}{2} - \frac{\ddot{R}_{1l}}{2b^2}}{\sin b\ell}\right].\cos b\ell$$

$$+ b^3 G\sinh b\ell + b^3 H\cosh b\ell \qquad (4.58)$$

which is solvable knowing $\dddot{R}_{1\ell}$ from (4.25).

Finally, the total reaction force applied to the supports equals internal shear force + external spring force applied by the Compensating Balance Sleeve.

At $x = 0$: $\mathrm{Re}_1 = E.I.r_3 + K_1.Y_1$ (4.59)

and at $x = \ell$, $\mathrm{Re}_2 = -E.I.\dddot{r}_\ell + K_2.Y_2$ (4.60)

(note: shear force is –ve at RHS).

The system is now fully determined and numerical analysis is possible by inserting the above equations into a suitable analytical computer programme.

## 4.3 Eliminating/ Nullifying the Impact of the 1st Critical Speed

From (4.31):

$$r = R_1 + P.\cos bx - \frac{\frac{M_{02}}{2b^2.E.I} + P.\cos b\ell + \frac{R_{1l}}{2} - \frac{\ddot{R}_{1l}}{2b^2}}{\sin b\ell}.\sin bx + G\cosh bx + H\sinh bx$$

it can be seen that shaft displacement, *r*, becomes infinite, thereby identifying the critical speeds, when $\sin b\ell = 0$, i.e. when $b\ell = \pi$, $2\pi$, $3\pi$ etc., thereby defining the first critical frequency as $\omega_{crit} = (\frac{\pi}{\ell})^2 \sqrt{\frac{\ell.EI}{M}}$.

To avoid the singularity, the 3rd term numerator can also be made equal to zero, at $b\ell = \pi$, by substitution of *P,* (4.16), $A_{1,}$ (4.14) and $M_{01}$, (4.5) to give:

$$-\left(\frac{M_{02}}{2b^2.E.I} + \frac{M_{01}}{2b^2.E.I} + \frac{R_{1l}}{2} - \frac{\ddot{R}_{1l}}{2b^2}\right) = 0 \qquad (4.61)$$

But, from (4.22) and (4.24) and for both $(\ell - a)$ and $(\ell - f)$ >0:

$$\frac{R_{1l}}{2} - \frac{\ddot{R}_{1l}}{2b^2} = \frac{1}{2}.\left[-e + \frac{e}{2}.\cos b(\ell - a) + \frac{e}{2}.\cos b(\ell - a) + \frac{e}{2}.\cosh b(\ell - a) - \frac{e}{2}.\cosh b(\ell - a)\right].$$

$$+\frac{1}{2}.\left[+e - \frac{e}{2}.\cos b(\ell - f) - \frac{e}{2}.\cos b(\ell - f) - \frac{e}{2}.\cosh b(\ell - f) + \frac{e}{2}.\cosh b(\ell - f)\right]$$

Hence, $$\frac{R_{1l}}{2} - \frac{\ddot{R}_{1l}}{2b^2} = \frac{e}{2}.\cos b(\ell - a) - \frac{e}{2}.\cos b(\ell - f) \qquad (4.61a)$$

and, through the application of trigonometric substitution:

$$\frac{R_{1l}}{2} - \frac{\ddot{R}_{1l}}{2b^2} = \frac{e}{2}.\left[\cos b\ell.\cos ba + \sin b\ell.\sin ba - \left(\cos b\ell.\cos bf + \sin b\ell.\sin bf\right)\right]$$

.

At, $b\ell = \pi$, $$\frac{R_{1l}}{2} - \frac{\ddot{R}_{1l}}{2b^2} = \frac{e}{2}.\left[-\cos ba + \cos bf\right] = e.k \qquad (4.62)$$

By defining a Concentrated Imbalance Coefficient as:

$$k = \frac{\left[-\cos ba + \cos bf\right]}{2} \qquad (4.63)$$

and substituting into (4.61) gives: $$-\left(\frac{M_{02}}{2b^2.E.I} + \frac{M_{01}}{2b^2.E.I} + e.k\right) = 0$$

therefore $$M_{01} + M_{02} = -e.k.2b^2.E.I = -2.k.\left(b^2.E.I.e\right) \qquad (4.64)$$

This equation provides the requirements for balance sleeve compensation to enable elimination, (more exactly, move to a higher speed), of the 1st critical frequency of a simply supported shaft with concentrated imbalance.

In the case of uniform eccentricity, chapter 2, the requirement for "classical" critical speed elimination, (corresponding to $b\ell = \pi$), determined that both balancing sleeve moments are $M_o = b^2.EI.e$. Comparing with the case for concentrated imbalance, the requirement is seen to be a fixed portion of the same equation since the Concentrated Imbalance Coefficient, *k* will be a constant for given values of *a* and *f*, as also shown graphically in Figure 4.4.

It is also seen that *k* is an absolute maximum when $a = 0$ and $f = \ell$, giving $k = -1$, i.e. the condition of uniform eccentricity. Under such conditions, from (4.64):

$M_{01} + M_{02} = 2.b^2.EI.e = 2.Mo$, thereby providing a direct correlation between the analysis for concentrated imbalance and that for uniform eccentricity.

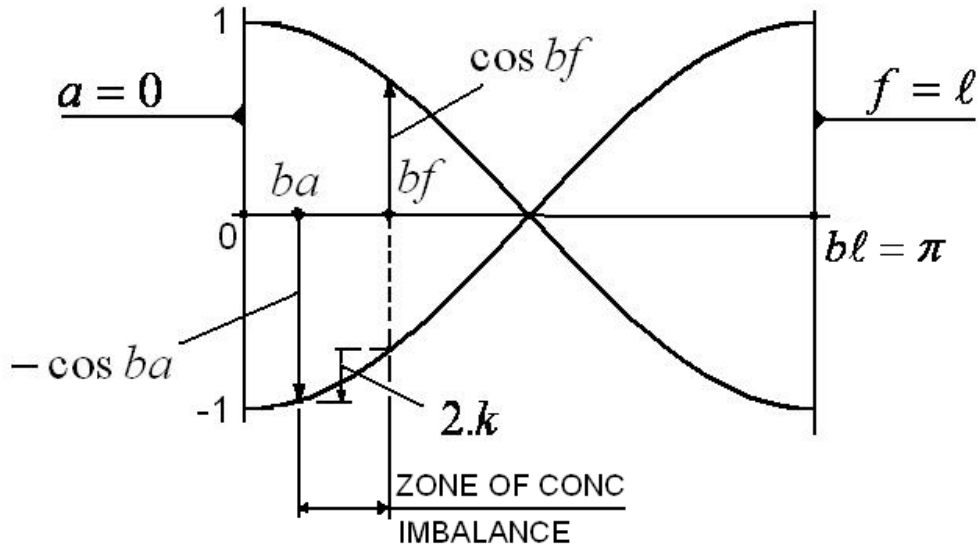


**Figure 4.4,** Zone of concentrated imbalance

It is notable from (4.64), that for balancing operations, it is only necessary to estimate the product of the equivalent eccentricity, *e,* and the concentrated imbalance coefficient, *k*, (other parameters being known from detail design). This can be regarded simply as an equivalent level of uniform eccentricity and is therefore linearly proportional to the shaft end reaction loads at any given speed. Hence, it is readily determined from either low speed balancing data or site vibration information, and detailed knowledge of individual magnitudes or axial positions of imbalances is not needed.

## 4.4 Encastre Simulation

Double encastre mounting, i.e. fixed at both shaft ends, constrains whirling motion of the shaft via the application of fixing moments, $M_{f1}$ and $M_{f2}$ imparted from bearing casings to the ends of the shaft, of sufficient magnitude to maintain shaft-end slopes equal to zero at all operating speeds. The natural frequency then increases by a factor of ~2¼ times that of the equivalent simply supported case [60]. Similarly, single encastre mounting only fixes one end of the shaft with the other remaining simply supported, but in this case the natural frequency is increased by a factor of ~1½.

The chapter 3 study of a balance sleeve using uniform eccentricity showed that a very good state of balance can be achieved by making the balance sleeve moments as close as possible to the fixing moments, for all operating speeds, but particularly those close to the critical speed. Points of encastre conversion are then produced where exact ‘moment equalisation’ occurs. It is concluded in that the process of critical speed elimination of a simply supported shaft constitutes a conversion process at this speed, to an encastre shaft, with a much higher natural frequency. Although this is only theoretically possible due to the critical frequency being irrational, it is apparent that the closer the replication of the balancing moments are to the fixing moments (the more accurate the encastre approximation), the better the resulting state of balance.

To confirm that these conditions also apply to the more generalised case of a single concentrated imbalance, equivalent double and single encastre shafts have been analysed. By applying a similar analytical methodology to that used in chapter 3, but with boundary conditions set such that the shaft end slope or bending moment is zero, for appropriate encastre or simply supported ends, the equation for shaft deflection becomes:

$$r_e = R_1 + P_e.(\cos bx - \cosh bx) + \frac{Q_e}{b}.(\sin bx - \sinh bx) \qquad (4.65)$$

for both double and single encastre cases, where the suffix *e* denotes the encastre condition,

$$P_e = -\frac{R_{1l}.(\cos b\ell - \cosh b\ell) - \frac{\dot{R}_{1l}}{b}.(\sin b\ell - \sinh b\ell)}{2 - 2.\cos b\ell.\cosh b\ell} \text{ , double encastre} \qquad (4.66)$$

$$P_e = \frac{R_{1l}.(\sin b\ell + \sinh b\ell) + \frac{\ddot{R}_{1l}}{b^2}.(\sin b\ell - \sinh b\ell)}{2.\sin b\ell.\cosh b\ell - 2.\cos b\ell.\sinh b\ell} \text{ , single encastre}$$

$$Q_e = -\frac{b.R_{1l}.(\sin b\ell + \sinh b\ell) + \dot{R}_{1l}.(\cos b\ell - \cosh b\ell)}{2 - 2.\cos b\ell.\cosh b\ell} \text{ , double encastre} \qquad (4.67)$$

$$Q_e = \frac{b.R_{1l}.(\cos b\ell + \cosh b\ell) + \frac{\ddot{R}_{1l}}{b}.(\cos b\ell - \cosh b\ell)}{2.\cos b\ell.\sinh b\ell - 2.\sin b\ell.\cosh b\ell} \text{ , single encastre}$$

The double- and single-encastre denominators of $P_e$ and $Q_e$, become zero and represent the 1st critical speed of the system as $r \to \infty$, when $b\ell = 4.73$ radians and $b\ell = 3.93$ radians, respectively. Comparing these results with the simply supported case, the critical speeds are correspondingly 2.27 and 1.56 times greater.

Further analysis gives the corresponding fixing moments as:

$M_{f1} = -2b^2.P_e.E.I$ , $M_{f2} = E.I.(\ddot{R}_{1l} - b^2.R_{1l} - 2b^2.P_e.\cos b\ell - 2.b.Q_e.\sin b\ell)$,

for double encastre, and

$M_{f1} = -2b^2.P_e.E.I$ , $M_{f2} = 0$, for single encastre mounting (4.68)

Notably, for a speed corresponding to $b\ell = \pi$, the sum of the fixing moment reduces to:

$M_{f1} + M_{f2} = -e.k.2b^2.E.I$ , for both cases (4.69)

which is identical to the moment requirement for elimination of the simply supported system, given by (4.64). Hence, moment equalisation occurs producing encastre conversion and the critical speed is theoretically eliminated. This is illustrated graphically in Figure 4.5 through use of a case study of both sets of moments, (set close to optimum balance compensation), using the site equivalent parameter values, shown in Table 4.1, for a Siemens sub-15MW gas turbine compressor. Note, for comparison purposes, these are slightly modified versions of the parameters given in Table 2.1, chapter 2, to take account of the change from uniform eccentricity to a single concentrated eccentric zone. It can be seen that the characteristic curves intersect at the classical critical speed, (11,902 rpm, given by $b\ell = \pi$) and that only a small moment spike is evident in the vicinity.

From beam theory, the encastre shaft end reaction loads are given by:

$\mathrm{Re}_{e1} = E.I.r_{e3}$ where $r_{e3} = -2.Q_e.b^2$

and $\mathrm{Re}_{e2} = -E.I.\dddot{r}_{e\ell}$ , (shear force –ve at RHS)

where $\dddot{r}_{e\ell} = \dddot{R}_{1l} + b^3.P_e.[.\sin b\ell - \cosh b\ell] + b^2.Q_e.[-\cos b\ell - \sinh b\ell]$

| Site Equivalent Model Parameter Values | |
|---|---|
| $M_s$ = 38.312 kg | $\ell$ = 1.707 m |
| $m_1$ = 0. 9 kg | $m_2$ = 0. 9 kg |
| *e* = 0.005804 m | *I* = 1.468x10^-5 m^4 |
| $c_1$ = 0.005656 m | $c_2$ = 0.001592 m |
| $K_{1,2}$ = 3.4x10^6 N/m * | *E* = 207 x 10^9 N/m^2 |
| $L_{1,2}$ = 0.130 m * | *a = 0.350* m * |
| *f = 0.400* m * | |

* Unless otherwise stated

**Table 4.1.** Parameter values used for numerical studies

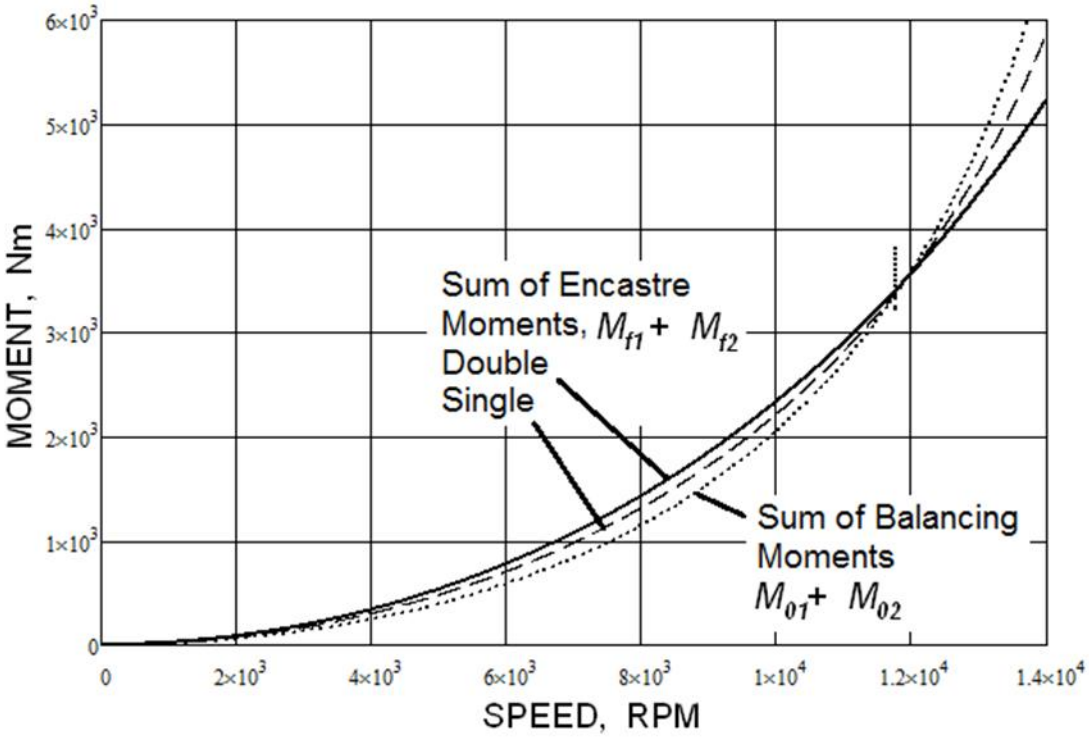


**Figure 4.5.** Fixing and balancing moments vs speed, with maximum compensation.

## 4.5 Compensated critical speed nullification

Considering the case of uniform eccentricity analysed in chapter 2, the critical frequency is always eliminated by any balancing moment and is replaced by a compensated critical frequency. This is also the case for concentrated imbalance loading considered here. By way of example, consider the close up of a number of different balancing moments versus speed, shown in Figure 4.6, using parameters given in Table 4.1, whereby:

a) Series 1 shows $M_{01}+M_{02}$ vs. speed, generated using equal sleeve lengths and stiffness', $L$ = 0.130 m and stiffness', $K$ = 3.4×10$^6$ N/m.

b) Series 2 shows $M_{01}+M_{02}$ vs. speed, generated using equal sleeve lengths and stiffness', $L$ = 0.206 m and stiffness', $K$ = 3.4×10$^6$ N/m.

c) Series 3 shows the moment required for elimination given by (4.64), i.e. $2.k.b^2.EI.e$ vs. speed.

d) Series 4 shows the equivalent double encastre moments, $M_{f1}+M_{f2}$ vs. speed. (note: for clarity, the single encastre case, $M_{f1}+M_{f2}$ vs. speed is not included, but actually passes between series' 2 and 4).

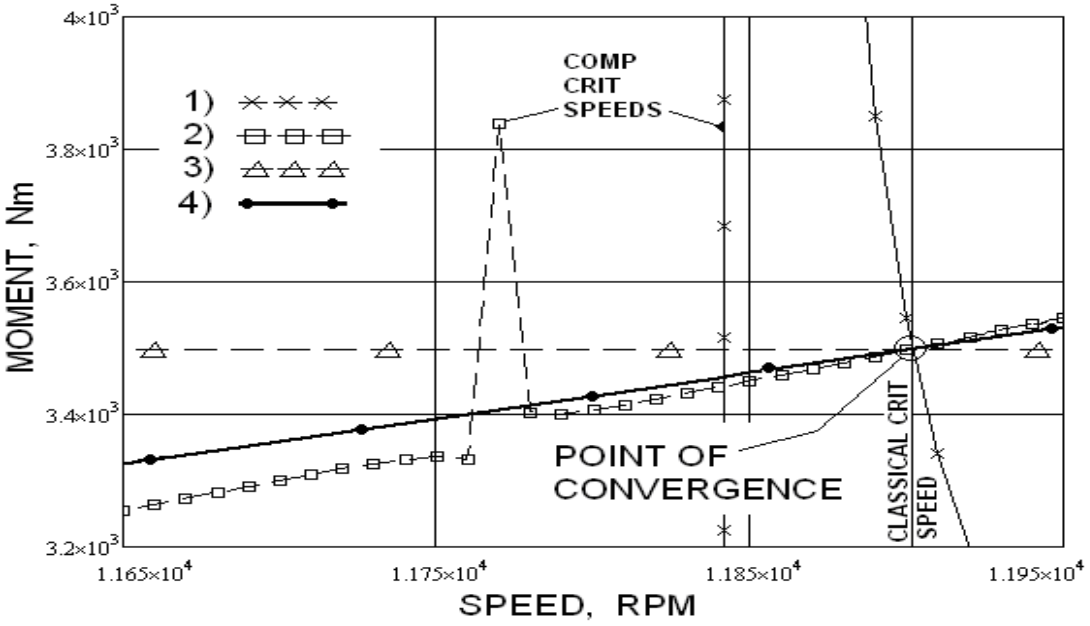


**Figure 4.6,** Close-up of a number of balancing moments vs. speed

Notably, the point of convergence coincides with the classical critical frequency, hence inducing elimination. However, as evident from the peaks of series 1 and 2, a compensated critical frequency is produced that is always very close to the classical critical frequency and therefore, as in the case of uniform eccentricity, the magnitude of the elimination moment, defined in equation (4.64), is very close to the value required for complete elimination. Hence, from a practical perspective this value can be used for design purposes, with small trim adjustments being made at site during commissioning, if required. It is also noted that complete critical speed elimination, or transfer to a higher level, is only possible in theory, due to the practically un-achievable requirement for exactly satisfying (4.64). In practice therefore, the critical speed will only be nullified.

## 4.6 Practical implications

From (4.64), it is the sum of the two balancing moments $M_{01}$ and $M_{02}$ that determine the condition for critical speed elimination, and the position/length of the concentrated imbalance zone only affects the magnitude of this sum, by varying the Concentrated Imbalance Coefficient, *k*, (4.63). This can be seen by considering two extreme conditions:

i) using the same parameters as in the previous example, but with sleeve compensation at the LHS set to give near elimination of the critical speed, and with sleeve compensation at the RHS set to zero, such that:

$M_{01} = -2.k.\left(b^2.E.I.e\right)$ and $M_{02} = 0$, i.e. replicating LHS, single encastre shaft. The reaction loads and compensating moments versus speed, are shown in Figure 4.7.

ii) Similarly, but with compensation reversed to give:

$M_{01} = 0$ and $M_{02} = -2.k.\left(b^2.E.I.e\right)$, the reaction loads and compensating moments are shown in Figure 4.8, replicating a RHS, single encastre shaft.

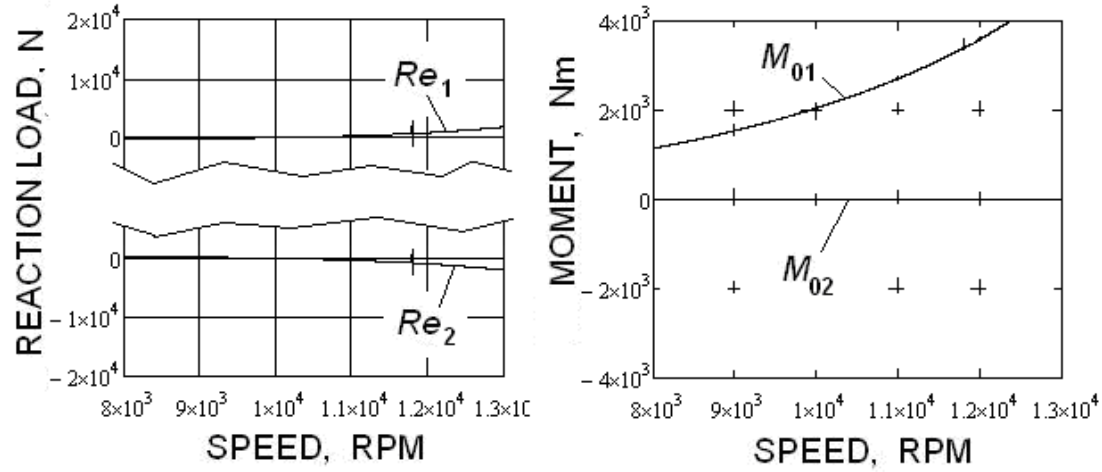


**Figure 4.7,** Reaction loads and moments with compensation at LHS only

Hence, near elimination of the critical speed can be achieved using a single compensating balance sleeve fitted at either end. This provides important insight into the characteristics imparted by the compensating sleeve—it facilitates increased design flexibility and enables a reduction in the size and cost of components.

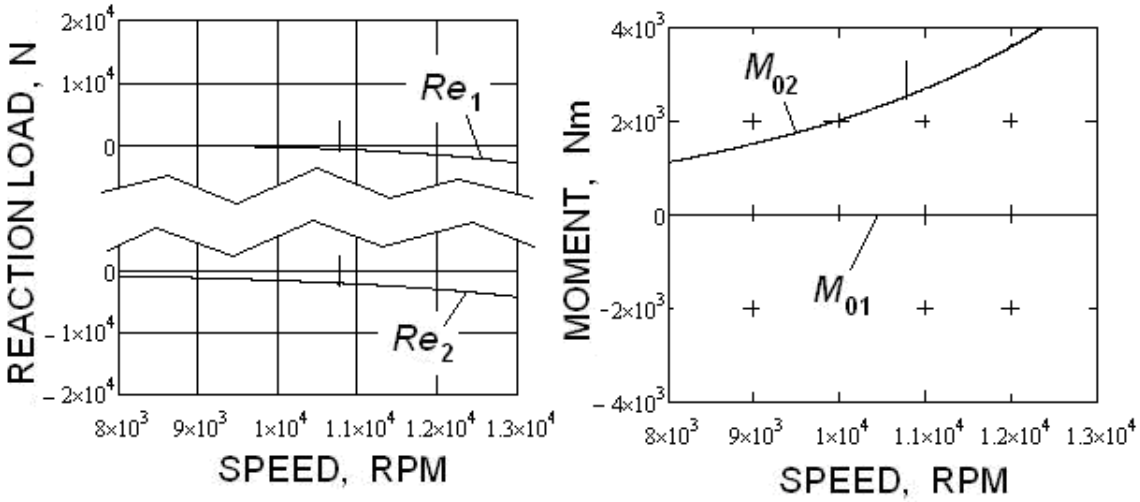


**Figure 4.8,** Reaction loads and moments with compensation at RHS only

From a practical perspective, it may still be beneficial to incorporate two balancing sleeves in some instances in order to maintain sensible size and masses, but there remain advantages to be gained from requiring only fine adjustments to be made at one end, of say, a coupling shaft. This benefits commissioning as access and adjustment time is reduced, especially where

applications require a firewall between the prime mover and driven units with separate coupling guard assemblies on either side (which would normally require removal and subsequent re-assembly).

## 4.7 Additional Elimination/ Nullification of the 2nd Critical Speed

It is well known that a uniform shaft operating near its 2nd critical speed can be analysed simply as two half-length shafts, connected in series, and operating independently at their 1st critical speeds [62]. Due to symmetry, this is readily confirmed from the earlier assertions that shaft deflection becomes (theoretically) infinite when $b\ell = \pi$, $2\pi$, $3\pi$ etc. thereby defining the critical speeds. Since the 1st critical speed of the half shaft is defined by the condition $b\ell_1 = \pi$, and the 2nd of the full shaft by: $b\ell_2 = 2\pi$, then $\ell_2 = 2.\ell_1$, i.e. the node point is positioned in the middle of the shaft. However, since it has been shown that the 1st critical speed of the half shaft can be theoretically eliminated by a single compensating sleeve then it similarly follows that the full shaft 2nd critical speed can be eliminated by applying this condition to both half shafts, as shown in Figure 4.9.

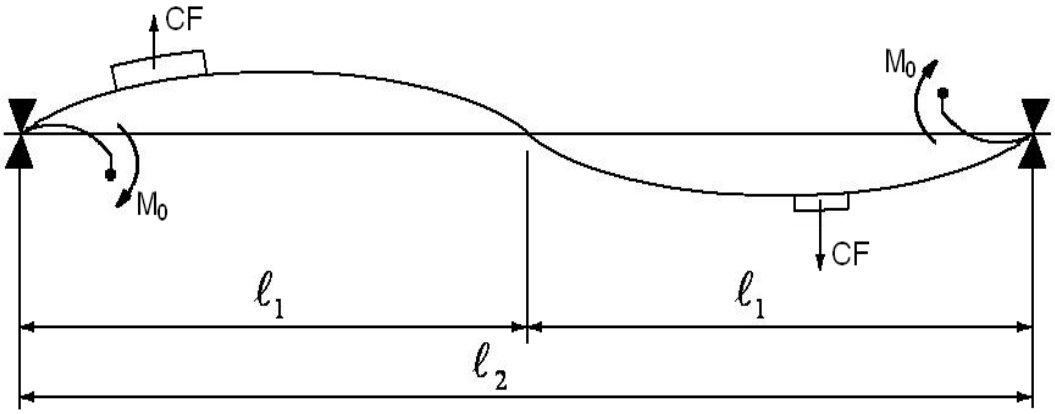


**Figure 4.9,** Diagrammatic representation of 2nd critical speed balancing

Clearly, each half shaft could be balanced using two compensating sleeves, if preferred, thereby requiring a 3rd and 4th balancing sleeve either side of the full-shaft node point, at the expense of a small increase in the mass at this point. These could be readily trim-balanced since the shaft deflection at

this point is zero. Therefore, theoretical elimination, i.e. practical nullification of the 2nd critical speed, is evidently possible.

For uniform shafts, the analysis can be applied to higher critical speeds due to the symmetry of each section of shaft between the nodes. In most practical circumstances, however, shafts that are not uniform require more complex analysis that is better performed numerically (by FEA for instance). Nevertheless, this simple representation highlights the potential of the proposed system to improve balance for higher order critical speeds.

## 4.8 General Imbalance Distribution

The system has been fully analysed for the case of a single concentrated imbalance and by the theory of superposition, the generalised case of any imbalance distribution, consisting of a number of concentrated imbalances of varying magnitude, position and angular placement along the shaft, is possible. This can be achieved by simple vector summation of the individual forces and deflections, in the vertical and horizontal planes (under the proviso that the shaft deflections remain small and the material is operating within the linear portion of its stress/ strain curve). For example, total reaction loads for a sum of, *N,* imbalances, in any given plane, is given by:

$$\mathrm{Re}_{(1,2),total} = \sum_{n=1}^{N} \mathrm{Re}_{(1,2),n} \tag{4.70}$$

where *n* is the imbalance index number.

The same summation can be applied to determine any of the other system variables: radial deflection, balance sleeve moment, etc. In addition, individual conditions determined for elimination of critical speeds can also be summed to give the overall condition for elimination of the total imbalance distribution.

## 4.9 Analytical Results: site equivalent model with a single offset imbalance

For comparison with chapters 2 and 3, (specific case studies into shafts with uniform eccentricity), similar numerical examples of concentrated imbalance loading are now presented, compiled using similar parameter values, as per Table 4.1. The concentrated zone of imbalance is arbitrarily chosen to provide offset loading by making, $a$ = 0.350 m and $f$ = 0.400 m.

Figures 4.10 and 4.11 graphically show comparative results from the numerical calculations, for reaction loads and shaft mid-point deflection. In both cases the trim balance masses are set to give low speed balance, resulting in differing trim balance eccentricities, $c_1$ and $c_2$, due to the offset nature of shaft imbalance. Figures 4.10, (a) and (b) show shaft end reaction loads, $\mathrm{Re}_1$ and $\mathrm{Re}_2$, versus speed, for three conditions of balance: firstly, without any balance sleeve compensation, i.e. both sleeves modelled as zero length and with extremely high stiffness', $K = 3.4\times10^{16}$ N/m. Then, for two compensated cases with sleeves stiffness', $K = 3.4\times10^{6}$ N/m, and a), equal length sleeves, $L$ = 0.130 m and b), equal length sleeves, $L$ = 0.206 m, to give near maximum compensation with double encastre replication.

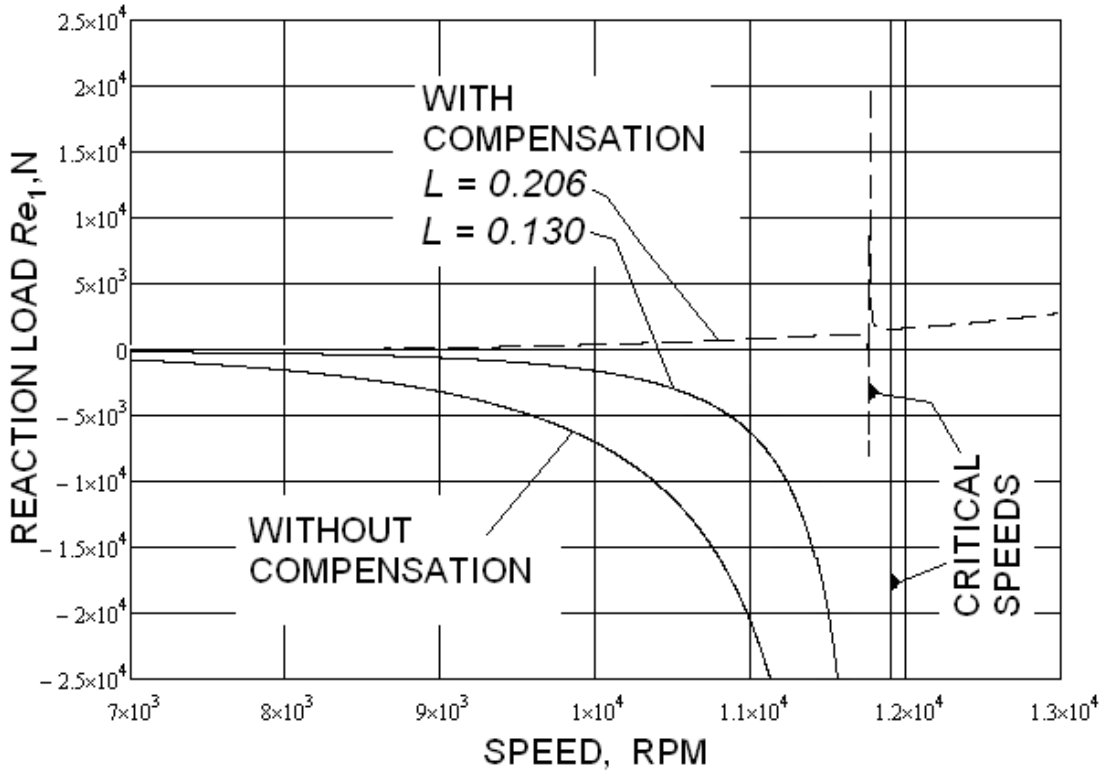


**Figure 4.10(a),** Reaction load, $Re_1$ vs. speed with & without balance sleeve compensation

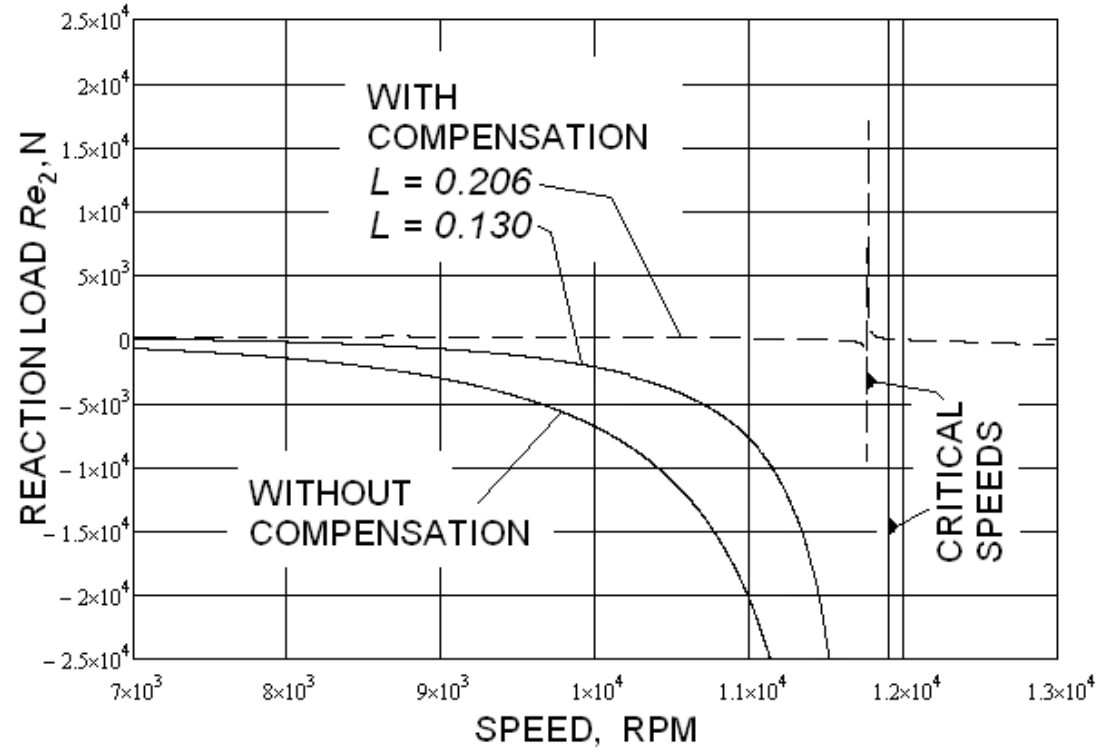


**Figure 4.10(b),** Reaction load, $Re_2$ vs. speed with & without balance sleeve compensation

Similarly, for the same conditions, Figure 4.11 shows the shaft mid-point deflection versus speed. It can be seen from the results that the system of balancing sleeve compensation is as equally effective for shafts with concentrated imbalance, as per the previous uniform eccentricity cases shown in chapter 2. $\mathrm{Re}_1$ and $\mathrm{Re}_2$ reaction loads are shown to have been reduced from an un-compensated, 11,130 N and 11,110 N to maximum compensated, 570 N and 140 N, respectively and the shaft mid-point deflection has been similarly reduced from 0.75 mm to 0.1 mm, at 10,500 rpm. The evident non-symmetry is a consequence of the offset imbalance loading applied to the shaft.

It is notable that the critical speed has reduced slightly as the compensation is applied. This is in line with the previous chapter 2 and 3 analysis of uniform eccentricity which shows that the classical critical speed is always eliminated, but is replaced by a compensated critical speed.

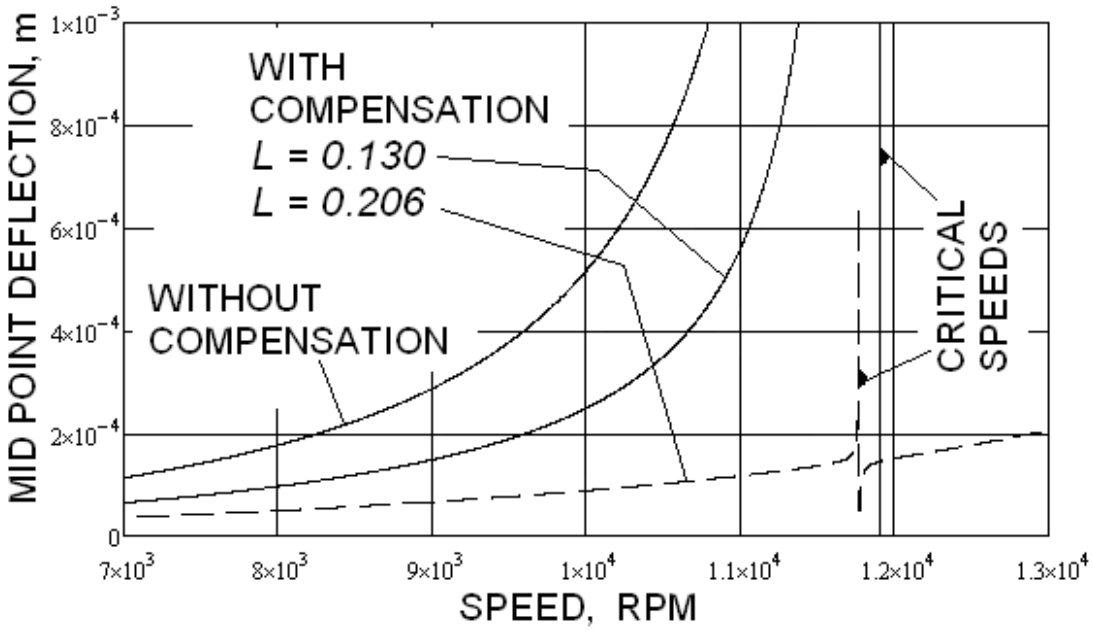


**Figure 4.11,** Mid-point deflection vs. speed with & without balance sleeve compensation

## 4.10 Preliminary Conclusions

Chapter 4 extends the special case study – analysis of uniform eccentricity given in chapters 2 and 3, - to demonstrate the suitability of the new methodology for the generalised condition of shaft loading with a single concentrated imbalance. By extension, it is shown that the principle of superposition allows for more practical imbalance distributions to be analysed by the process of vector addition of any number of individual concentrated imbalances, of various magnitude/ position. Further, the analysis reveals that a series of concentrated imbalances can be regarded simply as an equivalent level of uniform eccentricity, hence the previous conclusions developed in chapters 2 and 3 apply equally to this generalised case of imbalance loading.

The study shows that the nullification of critical speeds is dependent not on individual discrete values of the balancing moments applied by the balancing sleeves, but on the sum of those moments; the position or size of the imbalance only determining the required magnitude of the sum. Hence, nullification can be achieved by the use of a single compensating balance sleeve fitted at either end of the shaft, thereby replicating a single encastre shaft. Alternatively, it is only necessary to make balance corrections at one end, thereby reducing commissioning and site maintenance times.

It is also illustrated that by extending this concept to counter the mode shape of the 2nd critical speed, that nullification of this, and to a lesser extent higher orders, is possible.

In addition, the system also enables balance corrections to be made at more accessible positions, closer to the shaft ends, as opposed to the usual inboard positions where higher masses are located; thereby making it useful to those industries where maintenance is difficult or even dangerous, as in some nuclear installations. This will be further enhanced if, as envisaged, future designs will allow for remote adjustment of the balancing moment.

# Chapter 5

This chapter introduces a Shear Force Reaction ratio which determines the effective reduction in the equivalent level of residual eccentricity in a shaft when subjected to maximum balance sleeve compensation. It also investigates the possible benefits of applying compensation to higher order critical speeds by the definition/ determination of a Simulation Ratio.

## 5.1 Shaft end Reaction Loads

Previous analysis presented in chapters 2 and 3, of plain, simply supported and encastre mounted shafts with uniform eccentricity, derived the following equations for shaft end reaction loads.

### 5.1.1 *Simply Supported Shafts*

In the case of simply supported shafts, with balance sleeve compensation, from chapter 2, equation (2.41), the shaft end reaction force was shown to be the sum of internal shear force and the external spring force applied by the compensating balance sleeve, giving:

$\mathrm{Re}\_ss = EIr_3 + KY$, where shaft derivatives at $x = 0$ were defined by $r_1 = \left(\frac{dr}{dx}\right)_{x=0}$, $r_2 = \left(\frac{d^2r}{dx^2}\right)_{x=0}$ and $r_3 = \left(\frac{d^3r}{dx^3}\right)_{x=0}$ from (2.14), (2.15) and (2.16).

Further it was determined from (2.42) that: $r_3 = (H - {r_1}/{2b})2b^3$,

$$H = \frac{\frac{e}{2} + \frac{Mo}{2.b^2.E.I} - ({e}/{2} + {A_1}/{2.b^2}).\cosh b\ell}{\sinh b\ell} \quad (2.37)$$ and

$$r_1 = \frac{\frac{eb}{2} - A_3B - \left({eb}/{2} - A_3B\right)\cos b\ell}{A_4 \sin b\ell} + \frac{\frac{eb}{2} + A_3B - \left({eb}/{2} + A_3B\right)\cosh b\ell}{A_4 \sinh b\ell} \quad (2.39)$$

where the following parameters are defined as:

$A = \frac{-m\omega^2L^2K}{K - m\omega^2}$ (2.10), $A_1 = \frac{Ar_1 + B}{EI}$ (2.20), $A_3 = \frac{1}{2bEI}$ (2.38)

$B = \frac{m\omega^2cLK}{K - m\omega^2}$ (2.11), $A_4 = 1 + \frac{A_3A - A_3A\cos b\ell}{\sin b\ell} - \frac{A_3A - A_3A\cosh b\ell}{\sinh b\ell}$ (2.40)

Also, the balancing sleeve moment was defined by: $M_0 = A.\left(\frac{dr}{dx}\right)_{x=0} + B$ (2.9).

However, for a shaft with zero balance correction, i.e. just a plain shaft with uniform eccentricity but without balance sleeves, then *A,* $A_1$, *B, K, Y* and $M_0$ are all zero, so that:

$A_4 = 1$ and $H = \frac{\frac{e}{2}(1-\cosh b\ell)}{\sinh b\ell}$. Also $r_1 = \frac{eb}{2}.\left[\frac{1-\cos b\ell}{\sin b\ell} + \frac{1-\cosh b\ell}{\sinh b\ell}\right]$

giving: $r_3 = \frac{eb^3}{2}.\left(-\frac{1-\cos b\ell}{\sin b\ell} + \frac{1-\cosh b\ell}{\sinh b\ell}\right)$ (5.1)

hence the shaft end reaction load consists of internal shear only:

$$\text{Re}\_ss = \frac{eb^3 EI}{2}.\left(-\frac{1-\cos b\ell}{\sin b\ell} + \frac{1-\cosh b\ell}{\sinh b\ell}\right) \quad (5.2)$$

### 5.1.2 *Encastre Mounted Shafts*

Similarly for the case of encastre mounted shafts the dynamic analysis provided in chapter 3 produced the following parameter equations (3.9) and (3.8):

$$P_e = \frac{e}{2}.\frac{1+\cos b\ell - \cos b\ell.\cosh b\ell - \cosh b\ell + \sin b\ell.\sinh b\ell}{1-\cos b\ell.\cosh b\ell}$$

$$J = \frac{P_e(\sin b\ell + \sinh b\ell) - e\sinh b\ell}{\cos b\ell - \cosh b\ell}$$

and from (3.10b), shaft end reaction load, $\text{Re}\_en = EIr_3$ (3.10a),

where, $r_3 = -2.b^3 J$

Note, in this case the reaction load consists solely of the shaft's internal shear force.

By defining $T = 1-\cos b\ell.\cosh b\ell$ and $S = \cos b\ell - \cosh b\ell$

and making $P_e$ and $J$ substitutions, gives:

$$r_3 = -eb^3.\left[\frac{\frac{T+S+\sin b\ell.\sinh b\ell}{T}.(\sin b\ell+\sinh b\ell)-2.\sinh b\ell}{S}\right] \quad \text{and}$$

$$\text{Re\_}en = -eb^3 EI.\left[\frac{\frac{T+S+\sin b\ell.\sinh b\ell}{T}.(\sin b\ell+\sinh b\ell)-2.\sinh b\ell}{S}\right].$$

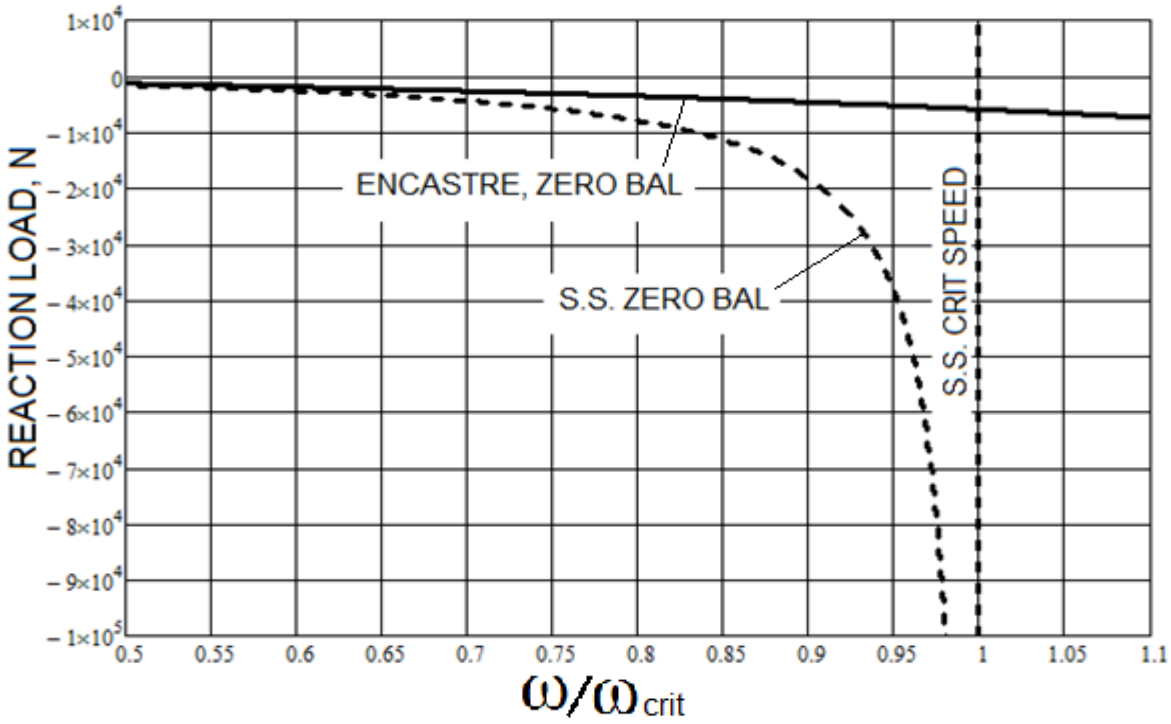


**Figure 5.1,** Reaction Load, (shear Force only), versus non-dimensional speed

The encastre and simply supported reaction loads, (shear force only since there is zero balance correction), versus non-dimensional speeds are shown in Figure 5.1, using the same parameter values given in chapter 2, Table 2.1. It can be seen, that for the encastre shaft, the reaction load is considerably reduced, especially close to the critical speed.

## 5.2 Shear Force Reaction Ratio

It is apparent that a good indication of the possible benefits of encastre simulation can be obtained by considering the ratio of the two reaction loads for both mounting conditions; hence, by defining:

Shear Force Reaction Ratio, $RR = \frac{S.S.Reaction\ Force}{Encastre\ Reaction\ Force}$

gives,

$$RR = \frac{\mathrm{Re}\_ss}{\mathrm{Re}\_en} = \frac{\left(\frac{1-\cosh b\ell}{\sinh b\ell} - \frac{1-\cos b\ell}{\sin b\ell}\right)}{2.\left[2.\sinh b\ell - \frac{T+S+\sin b\ell.\sinh b\ell}{T}.(\sin b\ell + \sinh b\ell)\right]} \quad (5.3)$$

A graphical representation of (5.3) is given in Figure 5.2, which shows the reaction ratio, *RR,* versus non-dimensional speed, $\omega/\omega_{crit}$ between 0.5 and 1.0. Notably the ratio increases as the non-dimensional speed approaches unity, indicating the positive benefit of shaft balancing by encastre simulation, since the methodology of balance sleeve compensation becomes more effective at the operating regions where the intensity of shaft imbalance is normally most severe.

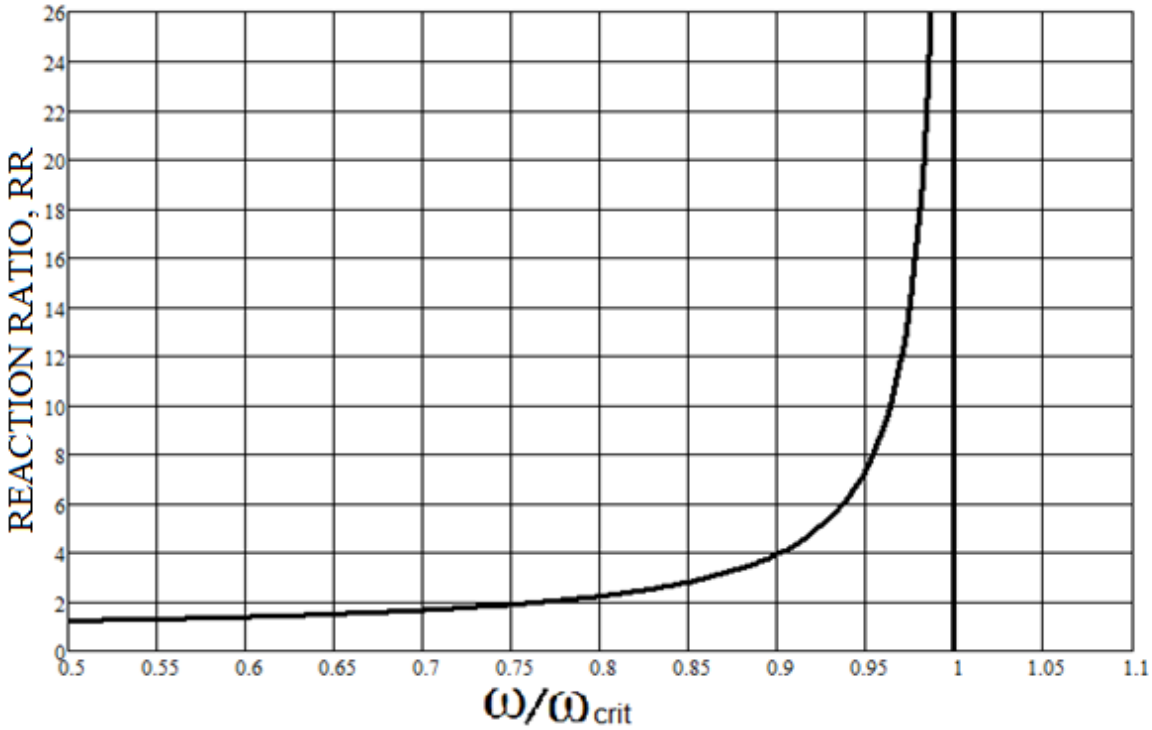


**Figure 5.2,** Reaction Ratio, *RR*, versus non-dimensional speed

It is also notable that eccentricity terms cancel so that the Reaction Ratio is independent of the level of residual eccentricity present in the shaft. Since *RR* is inversely proportional to reaction load reduction, and also noting that reaction load is directly proportional to eccentricity, then it follows that this ratio is an indication of the effective, or equivalent level of reduction in shaft eccentricity possible under conditions of encastre simulation/maximum compensation.

## 5.3 Applicability of the Shear Force Reaction Ratio

### 5.3.1 *Plain Shafts with Concentrated Imbalances*

The reaction ratio, *RR*, although resulting from the analysis of shafts with uniform eccentricity, is also typical of shafts with any number of concentrated imbalances, as it was shown in Chapter 3 that such cases can

be regarded as an equivalent level of the uniform eccentricity. The following section now provides further evidence to support this conclusion.

Re-arranging the previous simply supported equation, (5.1), for the differential term, $r_3$, for uniform eccentricity, gives:

$$r_3\_un = -eb^3.\left(\frac{1-\cos b\ell}{2.\sin b\ell} - \frac{1-\cosh b\ell}{2.\sinh b\ell}\right) \tag{5.4}$$

Similarly, for a single concentrated shaft imbalance, the previous analysis of chapter 4, produced equation (4.57), which is written as:

$$r_3\_con = (H - {}^{r_1}\!/_{2b})2b^3 \tag{5.5}$$

Also from chapter 4, (4.34), with zero balance correction making $M_{01}$, $M_{02}$, $A_1$, and $P$, all equal to zero, gives:

$$H = \frac{0 - \frac{R_{1l}}{2} - \frac{\ddot{R}_{1l}}{2.b^2} - 0}{\sinh b\ell} = \frac{-\frac{R_{1l}}{2} - \frac{\ddot{R}_{1l}}{2.b^2}}{\sinh b\ell}$$

However, from chapter 4, (4.62), at, $b\ell = \pi$, $\quad \frac{R_{1l}}{2} - \frac{\ddot{R}_{1l}}{2b^2} = e.k$

where $\quad k = \frac{\left[-\cos ba + \cos bf\right]}{2}$, Concentrated Imbalance Coefficient

Hence, $\quad -\frac{R_{1l}}{2} - \frac{\ddot{R}_{1l}}{2.b^2} = e.k - R_{1l}$ and $\quad H = \frac{e.k - R_{1l}}{\sinh b\ell}$ (5.6)

From chapter 4, (4.22), for positive $(\ell - a)$ and $(\ell - f)$:

$$R_{1l} = \frac{e}{2}.\left[\cos b(\ell - a) - \cos b(\ell - f) + \cosh b(\ell - a) - \cosh b(\ell - f)\right] \tag{5.7}$$

Considering the hyperbolic terms only and applying trigonometric substitution:

$$\begin{aligned}\cosh b(\ell - a) - \cosh b(\ell - f) &= \cosh b\ell.\cosh(-ab) + \sinh b\ell.\sinh(-ab) \\ &\quad - \left[\cosh b\ell.\cosh(-fb) + \sinh b\ell.\sinh(-fb)\right] \\ &= \cosh b\ell.\left[\cosh(-ab) - \cosh(-fb)\right] \\ &\quad + \sinh b\ell.\left[\sinh(-ab) - \sinh(-fb)\right]\end{aligned}$$

For operating speeds approaching critical, i.e. $b\ell > 2$, $\cosh b\ell \cong \sinh b\ell$, and making further trigonometric substitution gives:

$$= \cosh b\ell.[\cosh(ab) - \cosh(fb) - \sinh(ab) + \sinh(fb)] \quad (5.8)$$

Substituting $fb = ab + \Delta$ and expanding gives:

$$\cosh(fb) = \cosh ab.\cosh\Delta + \sinh ab.\sinh\Delta$$

and $$\sinh(fb) = \sinh ab.\cosh\Delta + \sinh\Delta.\cosh ab$$

For a concentrated imbalance where $(a-b)$ is relatively small, $\Delta \cong 0$, hence, these terms can be reduced to:

$\cosh(fb) = \cosh ab$ and $\sinh(fb) = \sinh ab$

Substituting in (5.8) then gives:

$$\cosh b(\ell - a) - \cosh b(\ell - f) = \cosh b\ell.[\cosh ab - \cosh ab - \sinh ab + \sinh ab]$$

Hence, $\cosh b(\ell - a) - \cosh b(\ell - f) = 0$

and substituting for the hyperbolic terms in (5.7) gives:

$$R_{1l} = \frac{e}{2}.[\cos b(\ell - a) - \cos b(\ell - f)] = e.k$$

since from chapter 4, (4.61a), for $b\ell = \pi$,

$$[\cos b(\ell - a) - \cos b(\ell - f)] = e.k$$

Substituting in (5.6) then gives: $$H = \frac{e.k - e.k}{\sinh b\ell} = 0$$

Therefore, from chapter 4, (4.44), $$r_1 = -b.\left(\frac{0 + 0 + e.k}{\sin b\ell}\right) + 0$$

and by substitution in (5.5):

$$r_3\_con = eb^3.k.\left(\frac{1}{\sin b\ell}\right) \quad (5.9)$$

In order to compare the two differential terms, $r_3$, for the cases of uniform eccentricity and concentrated imbalance, Figure 5.3 shows a plot of the bracket terms of equations (5.4) and (5.9) and it can be seen that they are approximately equal for non-dimensional operating speeds between 0.5

and 1.0, (based on chapter 2, Table 2 parameters, with *a* = 0.35 and *b* = 0.40 m, but note, this equality is independent of shaft imbalance terms, *a, b* and eccentricity.

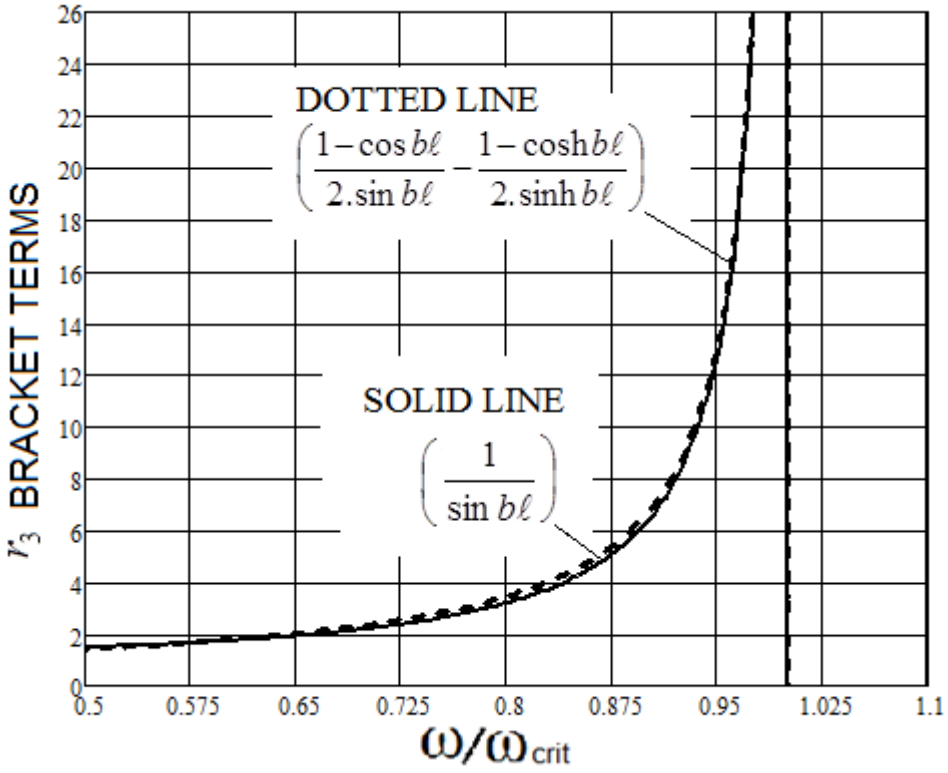


**Figure 5.3,** $r_3$ Bracket Terms versus non-dimensional speed

Therefore, the bracketed term of (5.9) can be replaced by the bracketed term of (5.4), giving:

$$r_3\_con = eb^3.k.\left(\frac{1-\cos b\ell}{2.\sin b\ell}-\frac{1-\cosh b\ell}{2.\sinh b\ell}\right),$$

and further from (5.4): $$r_3\_con = eb^3.k.\frac{r_3\_un}{eb^3} = k.r_3\_un \qquad (5.10)$$

Hence, it is apparent that the case of concentrated imbalance loading can be regarded simply as a reduced case of uniform eccentricity. Although only providing a first degree of approximation, its value is supported by comparing the reaction force of the case with concentrated imbalance

against a case of uniform eccentricity with a constant reduction, *k*, (near elimination), as shown in Figure 5.4. Hence, the conclusions and indicative value of the reaction ratio, *RR,* shown in Figure 5.2, obtained from the simplified analysis, are also valuable for the more generalised case of any number of concentrated shaft imbalances.

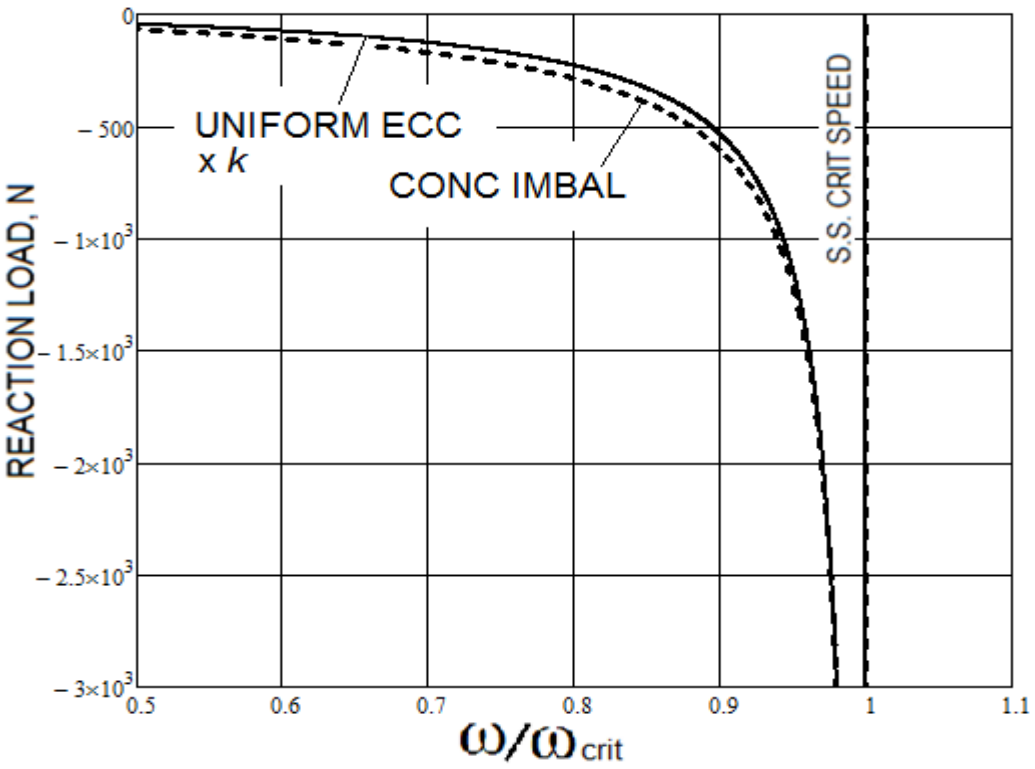


**Figure 5.4,** Comparison of concentrated imbalance and *k* times reduction in uniform eccentricity

### 5.3.2 *Shaft Mounted Discs*

To assess the effectiveness of the reaction ratio, *RR*, as an indicator of the benefits to be gained from encastre simulation, for shaft mounted discs, it is necessary to investigate the variation in shaft bending stiffness between shafts that have either encastre or simply supported, end mountings.

Applying standard bending theory of beams to the shaft schematics shown in Figure 5.5, the equations for the deflection of a beam under a load, *W,* are as follows.

For simply supported mounting,

$E.I.y\_ss = R_1.\frac{a^3}{6} + A.a$ , where $R_1 = \frac{W.b}{\ell}$

and $$A = -\frac{W.b}{6.\ell}.\left(\ell^2 - b^2\right), \qquad (5.11)$$

*y_ss* is the beam deflection under the load *W*, and the beam length is $\ell = a + b$.

Similarly for encastre mounting,

$E.I.y\_en = -M_1.\frac{a^2}{2} + R_1.\frac{a^3}{6}$, where $R_1 = \frac{W.b^2}{\ell^3}.(3.\ell - 2.b)$ and

$$M_1 = \frac{W.b^2}{\ell}.\left(1 - \frac{b}{\ell}\right), \qquad (5.12)$$

*y_en* is the beam deflection under the load *W.*

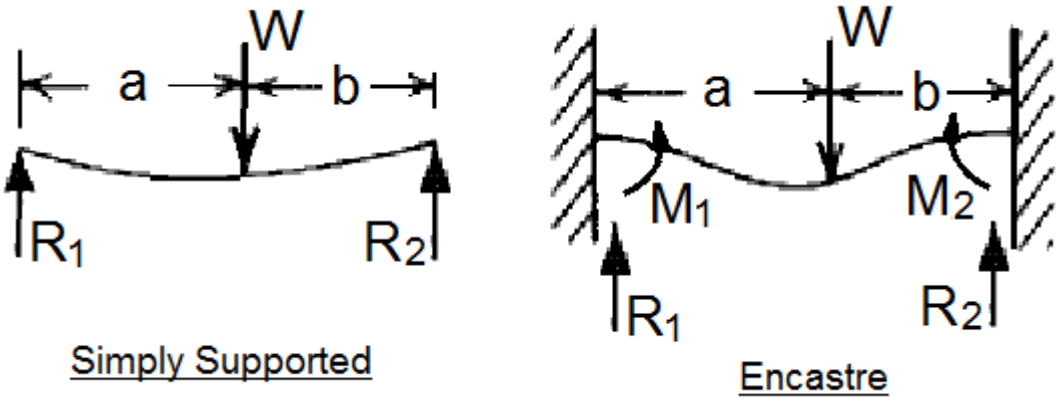


**Figure 5.5,** Shaft mounting schematics

In each of the cases the shaft stiffness, *K,* at load position, *a,* is given,

by $K = \frac{W}{y}$, (5.13)

and the Ratio of Shaft Stiffness, encastre to simply supported,

$R\_stiff = \frac{K\_en}{K\_ss}$ becomes: $R\_stiff = \frac{y\_ss}{y\_en}$ (5.14)

as shown plotted against the non-dimensional disc position, $a/\ell$, in Figure 5.6. It can be seen that the stiffness ratio varies between a minimum of 4.0 and 11.11 over the central 80% of the shaft length, i.e. between 10% and

90% of its length and notably this is the portion of the shaft where the majority of discs are mounted, since bearings, seals and hubs etc. are usually positioned at the shaft ends.

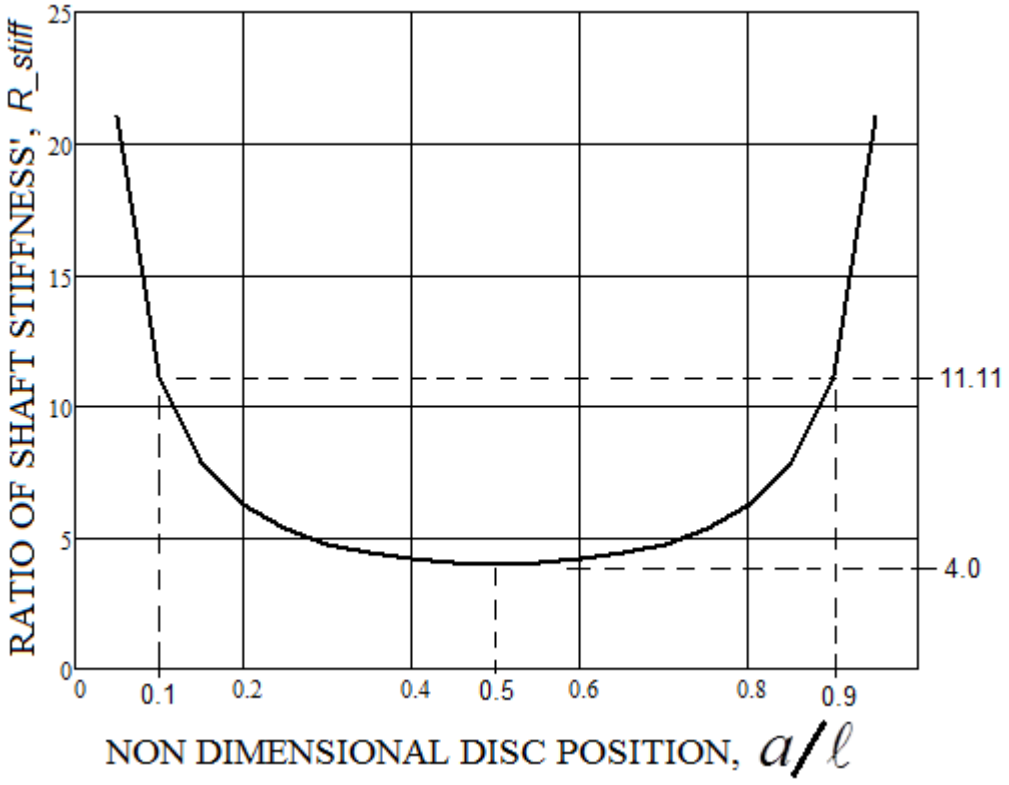


**Figure 5.6,** Shaft stiffness ratio versus non-dimensional disc position

For a single disc mounted on a plain, massless shaft, as in the Jeffcott rotor illustration shown in Figure 5.7, the following general equations for centrifugal force, *CF,* and disc displacement, *r,* are applicable.

Generally, $CF = K.r = M.\omega^2.(r+e)$, giving: $r = \dfrac{e.M.\omega^2}{K - M.\omega^2}$

$$CF\_ss = \left( \frac{e.M.\omega^2}{K\_ss - M.\omega^2} \right).K\_ss \tag{5.15}$$

and $$CF\_en = \left( \frac{e.M.\omega^2}{K\_en - M.\omega^2} \right).K\_en \tag{5.16}$$

Since the disc mass and its eccentricity are common to both mounting arrangements for this comparison, the ratio of centrifugal forces becomes:

$$\frac{CF\_ss}{CF\_en} = \frac{K\_en - M.\omega^2}{K\_ss - M.\omega^2} \cdot \frac{K\_ss}{K\_en}.$$

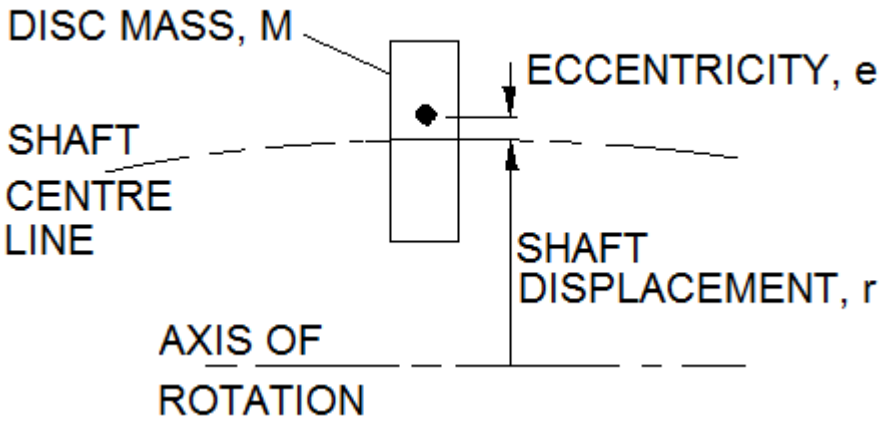


**Figure 5.7**, Jeffcott Rotor - Disc mounted shaft

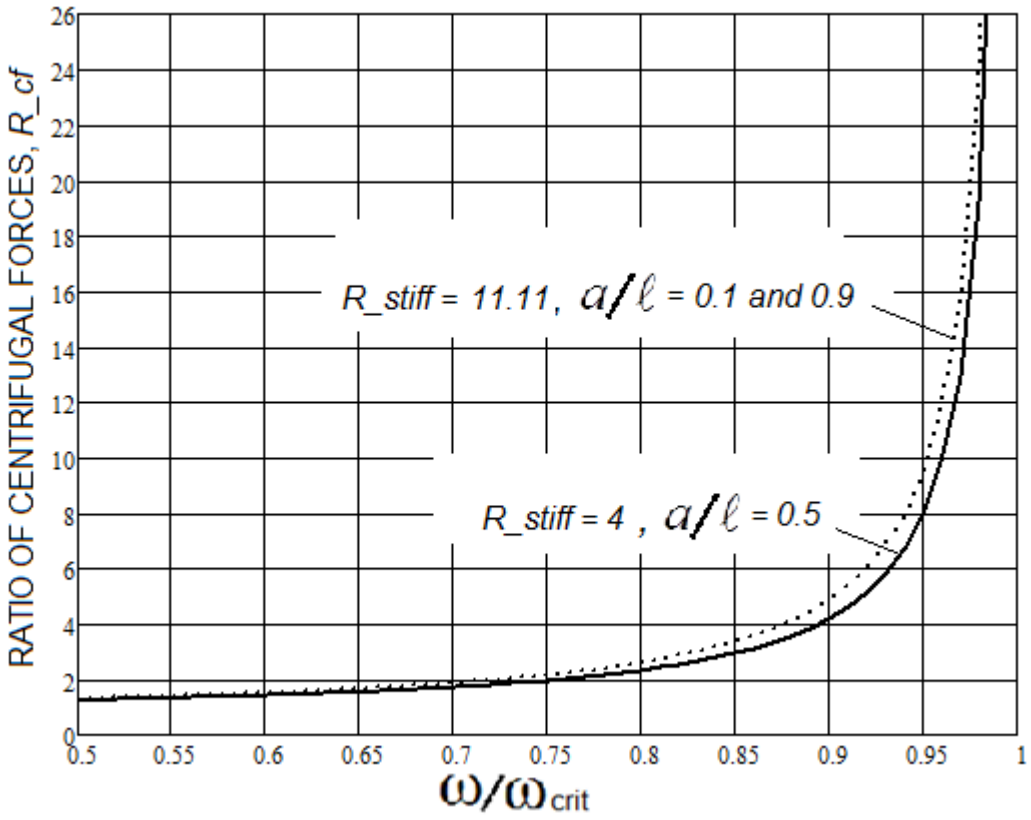


**Figure 5.8**, Ratio of centrifugal forces versus non-dimensional speed

However, $R\_stiff = \frac{K\_en}{K\_ss}$ and for a Jeffcott rotor: $\omega^2_{crit\_ss} = \frac{K\_ss}{M}$

By substitution: $$\frac{CF\_ss}{CF\_en} = \frac{1 - M.\omega^2 / R\_stiff.K\_ss}{1 - \omega^2 / \omega^2_{crit\_ss}}$$

Then, defining the speed ratio as: $\lambda = \frac{\omega}{\omega_{crit\_ss}}$,

gives the CF ratio, $$R\_cf = \frac{CF\_ss}{CF\_en} = \frac{1 - \lambda^2 / R\_stiff}{1 - \lambda^2} \qquad (5.17)$$

and this is shown plotted against non-dimensional speed in Figure 5.8 for the two extreme stiffness ratios of 4.0 and 11.11.

Since the CF's are proportional to their respective shaft end reaction loads, the ratio of CF's is equivalent to, and by comparison with Figure 5.2 approximately equal to, the shear force reaction ratio, *RR.* Using superposition, the *RR* is also applicable to any number of discs mounted on a shaft. Hence, for practical purposes, all multi-disc shafts – where the discs are mounted within the central 80% of shaft length, the conclusions and indicative value of the reaction ratio, *RR,* obtained from the simplified uniform eccentricity analysis to derive Figure 5.2, are also applicable to many systems that have shaft mounted discs.

## 5.4 Balancing Sleeve design

To provide a good encastre simulation and reduction in reaction loads, the compensating balancing sleeves must be designed appropriately for the elimination/ nullification of the compensated critical speed, as given in Chapter 3, which produced the following parametric equations:

$$\frac{e.b^2.E.I}{A} + e.b = \frac{B}{A} = -\frac{c}{L} \qquad (3.21a)$$

$$K = \frac{-D.m.\omega^2}{m.\omega^2.(e.b.L^2 + c.L) - D} \quad (3.23), \quad \text{where} \quad D = e.b^2.E.I \quad (3.22).$$

Equation (3.21a) determines that the sleeve eccentricity, *c,* must be proportional to the shaft eccentricity, *e.* Therefore, by studying equation (3.23) for sleeve stiffness, *K,* it is apparent that since each term is proportional to the shaft eccentricity, *e,* hence, it follows that *K* is independent of *e.* This means that the sleeve design can be carried out without any prior knowledge of the residual imbalance of the shaft, (magnitude of eccentricity or position), based solely on the shaft's physical parameters and its critical speed. The designer is then free to decide on the required sleeve parameters, limited only by a pre-decided maximum shaft eccentricity limit, in order to evaluate the maximum sleeve displacement and associated bending stress.

To obtain encastre simulation it is necessary to achieve near moment equalisation between the balancing moments and the encastre fixing moments. This requires a means of obtaining fine adjustment of the balancing sleeve moment which can be readily achieved by either varying the magnitude of its balancing mass or its positional length or a combination. It is therefore possible to envisage many different detail designs to satisfy a specific requirement.

For illustration purposes, the required sleeve length versus stiffness resulting from the above equations is shown graphically in Figure 5.9, based on Chapter 3 parameter values for uniform eccentricity—Notably 1) represents the length and stiffness values used to obtain maximum compensation, 2) provides a suggested minimum sleeve length to prevent possible interaction between the sleeve and shaft critical speeds, and 3) represents a mechanism having radial stiffness but no length, allowing sole compensation of the reaction since the balancing moment would be zero and the shaft deflection would not be reduced.

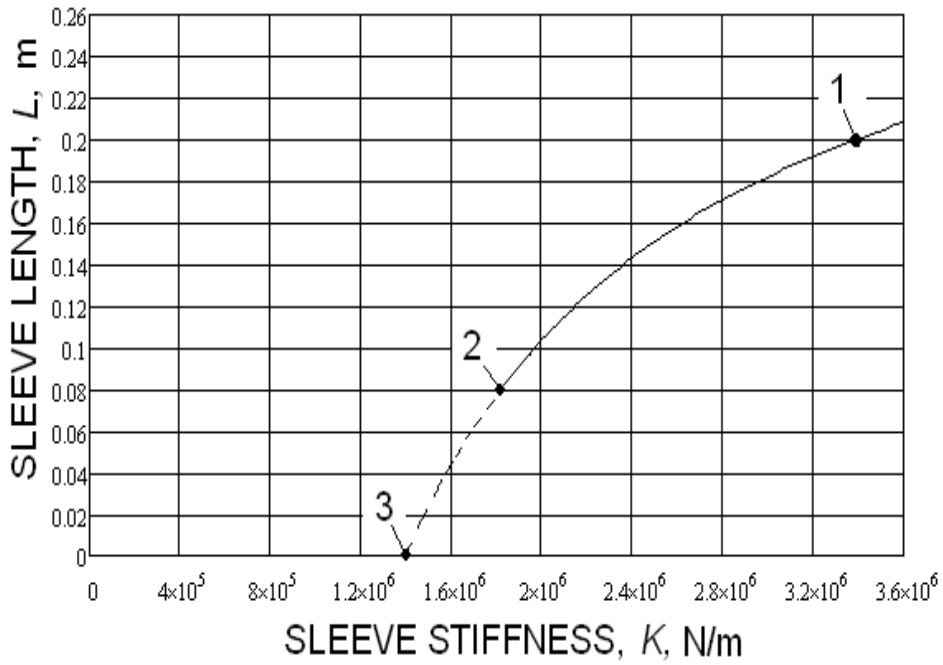


**Figure 5.9,** Sleeve Length versus Sleeve Stiffness

## 5.5 Effect of Double Encastre Mounting on Higher Order Critical Speeds

The previous account given in Chapter 4 of plain, simply supported and encastre mounted shafts loaded with a single concentrated imbalance, showed that it is the sum of the balancing moments that determined the point of conversion from simply supported shaft to encastre mounted replication. Hence, it follows that single ended, encastre replication can be achieved by employing only one balancing sleeve, and further, the 2nd mode of excitation can be compensated using two end-mounted balancing sleeves. It is therefore plausible that an extension of such arrangements can have a beneficial impact on higher critical speeds.

The analysis determined that for double encastre mounted shafts the deflection was given by:

$$r = R_1 + P_e.(\cos bx - \cosh bx) + \frac{Q_e}{b}.(\sin bx - \sinh bx) \qquad (4.65)$$

where $$P_e = -\frac{R_{1l}.(\cos b\ell - \cosh b\ell) - \frac{\dot{R}_{1l}}{b}.(\sin b\ell - \sinh b\ell)}{2 - 2.\cos b\ell.\cosh b\ell} \qquad (4.66)$$

and $$Q_e = -\frac{b.R_{1l}.(\sin b\ell + \sinh b\ell) + \dot{R}_{1l}.(\cos b\ell - \cosh b\ell)}{2 - 2.\cos b\ell.\cosh b\ell}$$

Also, the parameters, $P_e$ and $Q_e$ produce infinite shaft deflections when their denominator equates to zero, hence critical speeds are determined when: $1 - \cos b\ell.\cosh b\ell = 0$.

To investigate the impact on higher order critical speeds, a graphical solution to the aforementioned equation is given in Figure 5.10, using parameter values given in Table 2.1.

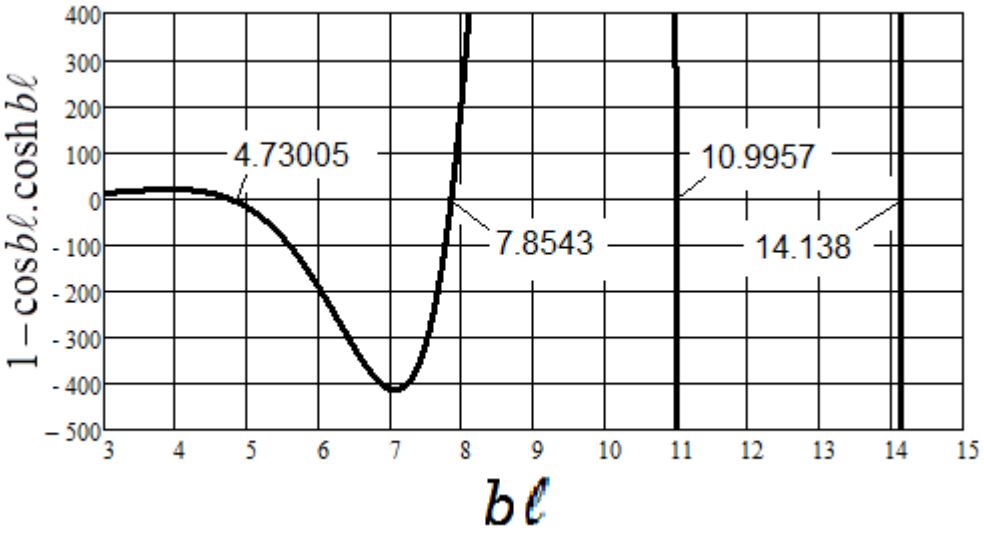


**Figure 5.10,** Graphical determination of Critical Values of *bl*.

Critical values of *bl* are identified at the zero intercepts and the corresponding encastre critical speeds are shown below (Table 5.1).

Empirical examples of the mode shapes for the first four critical speeds are shown in Figure 5.11 and it is noted that the zero slope at both ends of the

shaft, resulting from encastre mounting, is clearly visible, (note: these are based on examples of offset concentrated shaft imbalance analysed previously in Chapter 4, without trim balance correction, for speeds close to the corresponding critical).

| Order | *bl* | Critical Speed rpm |
|---|---|---|
| 1st | 4.7005 | 26,980 |
| 2nd | 7.8543 | 74,390 |
| 3rd | 10.9957 | 145,800 |
| 4th | 14.138 | 241,000 |

**Table 5.1,** Encastre Critical Speeds

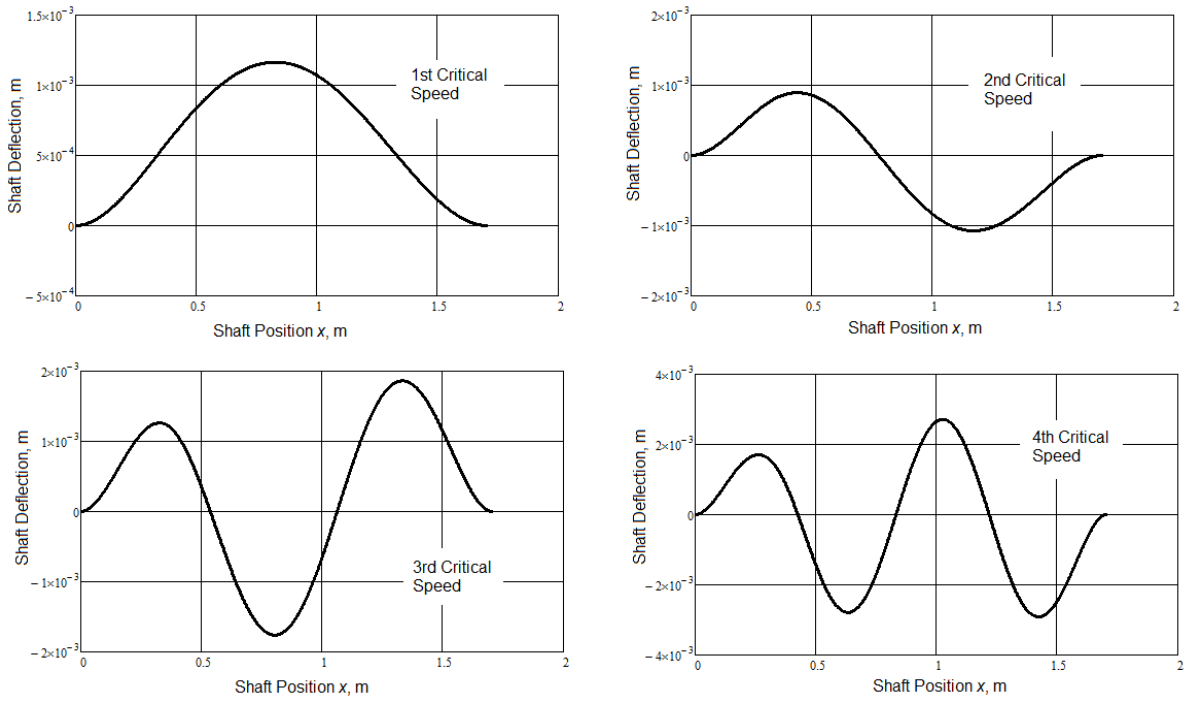


**Figure 5.11,** Examples of Encastre Empirical Mode Shapes

This is as a result of the fixing moments, reacting against the bearing casings onto the rotating shaft, and it is these fixing moments, replicated by the balancing moments during compensation, that raises the bending

stiffness of the shaft and thereby increases its critical speeds, above those of an equivalent, simply supported shaft.

## 5.6 Simulation Ratio

For comparison purposes, previous analysis of equivalent simply supported shafts, chapter 2, section 2.4, based on Table 2.1 parameter values, produced the following critical speeds, shown in Table 5.2.

Noting that for a simple spring-mass system, stiffness is proportional to natural frequency squared, then by defining:

Simulation Ratio, $SR = \left(\frac{Encastre\ Crit\ Speed}{S.S.Crit\ Speed}\right)^2$.

It can be seen that this ratio, as shown in Table 5.3, reduces as the critical speed increases, since each additional undulation of the mode shape reduces the influence of the fixing moments, i.e. it is only the end undulations that are effectively single encastre mounted, whereas the remaining undulations are simply supported, since they are not restrained by fixing moments.

| Order | *bl* | Critical Speed rpm |
|---|---|---|
| 1st | π | 11,900 |
| 2nd | 2π | 47,610 |
| 3rd | 3π | 107,100 |
| 4th | 4π | 190,400 |

**Table 5.2,** Simply Supported Critical Speeds

Therefore, the *SR* ratio gives an indication of the overall stiffening effect of the fixing moments on a full shaft assembly and by analogy the possible benefits to be gained by encastre simulation, provided the balancing sleeve

moments are optimised to give near elimination of the simply supported critical speed.

It is notable that the benefit of encastre simulation also depends on the zone of the required operating speed, since to gain maximum effect, the zone needs to be close to a simply supported critical speed, but sufficiently away from an encastre critical speed. Further, since the simulation ratio is an indication of the increased stiffness of an encastre shaft over a simply supported shaft, it is noted that there remain potential benefits to be gained from similar shafting fitted with discs, as employed in gas turbine and compressor units for instance, as opposed to the plain coupling shafts used in this analysis, since the added masses would lower the critical speeds in both cases without greatly affecting the ratio. This is confirmed by the analysis given in section 5.3.2.

Confirmation that the *SR* ratio represents increased stiffening of an encastre shaft is shown in Figures 5.12 and 5.13, where, by multiplying the simply supported shaft stiffness by the value of *SR,* corresponding to the critical speed under consideration, the reaction load (only 1$^{st}$ end shown) closely approximates that of the equivalent encastre shaft. This correlation is illustrated for operating speeds adjacent to the 1$^{st}$ and 3$^{rd}$ critical speeds, respectively, based on examples of concentrated shaft imbalance analysed previously in Chapter 4, but without any trim balance correction. For comparison purposes, Figures 5.12 and 5.13 also include the simply supported characteristic of a standard stiffness shaft for the same zero balance correction.

| Order | Critical Speed Ratio | Simulation Ratio, SR |
|---|---|---|
| 1st | 2.267 | 5.139 |
| 2nd | 1.563 | 2.443 |
| 3rd | 1.361 | 1.852 |
| 4th | 1.266 | 1.603 |

**Table 5.3,** Simulation Ratio, *SR*

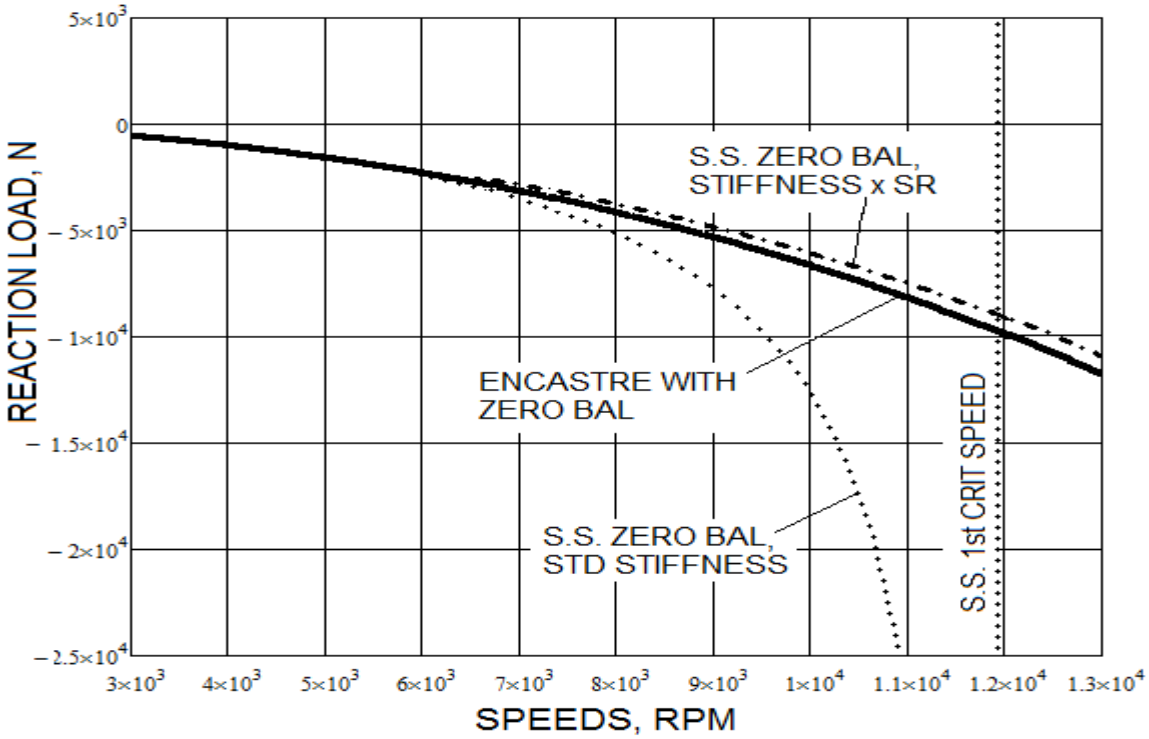


**Figure 5.12,** Increasing simply supported shaft stiffness adjacent to the 1st critical speed

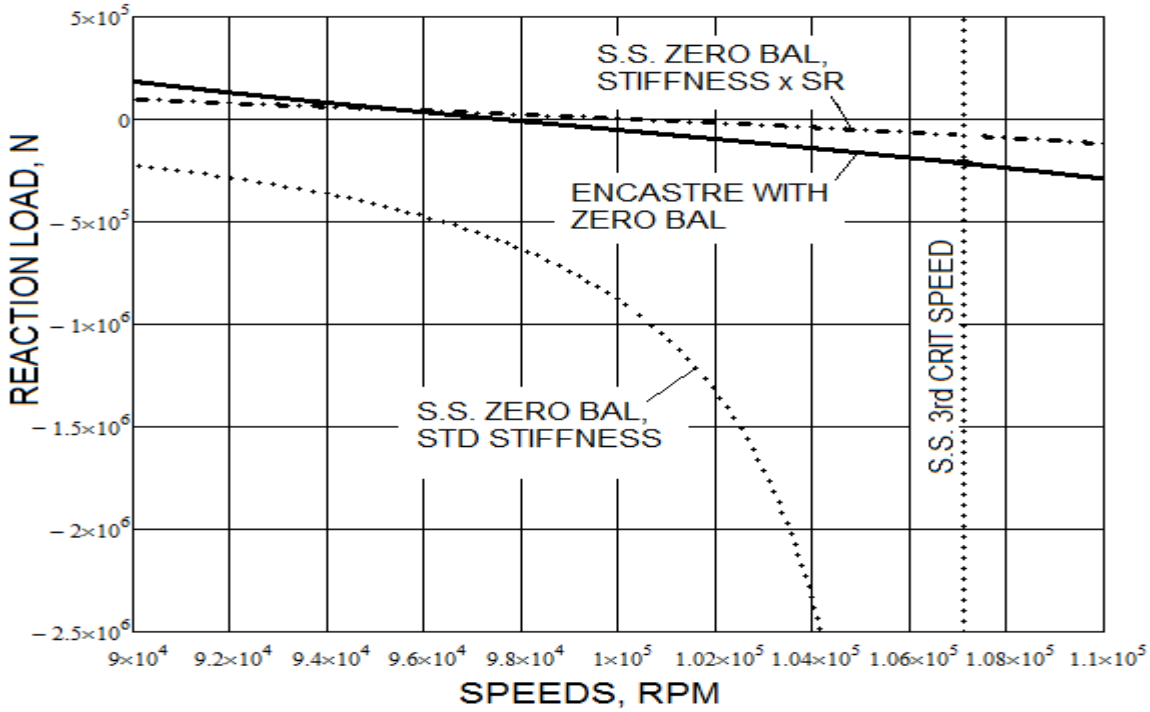


**Figure 5.13,** Increasing simply supported shaft stiffness adjacent to the 3rd critical speed

Study of the simply supported equations, chapter 4, section 4.3, determined that the requirements for elimination of the 1st classical critical speed and by substitution of the values of *bl* corresponding to the higher order critical speeds, ($b\ell = 2\pi$, $3\pi$, $4\pi$ etc.), that the same controlling condition applies for these critical speeds, i.e.

$M_{01} + M_{02} = -e.k.2b^2.E.I$ , equation (4.64).

Also, when the same values of *bl* are applied to the sum of the encastre fixing moments to represent encastre operation at simply supported critical speeds, the requirement is also unchanged, i.e. $M_{f1} + M_{f2} = -e.k.2b^2.E.I$ , equation (4.69).

This identity is the same as that derived for the 1st classical critical speed in Chapter 3, and the resulting equalisation of the balancing and fixing moments shows that encastre conversion is also present at these higher

critical speeds. Therefore, they are always eliminated, but are replaced by a compensated critical frequency situated nearby.

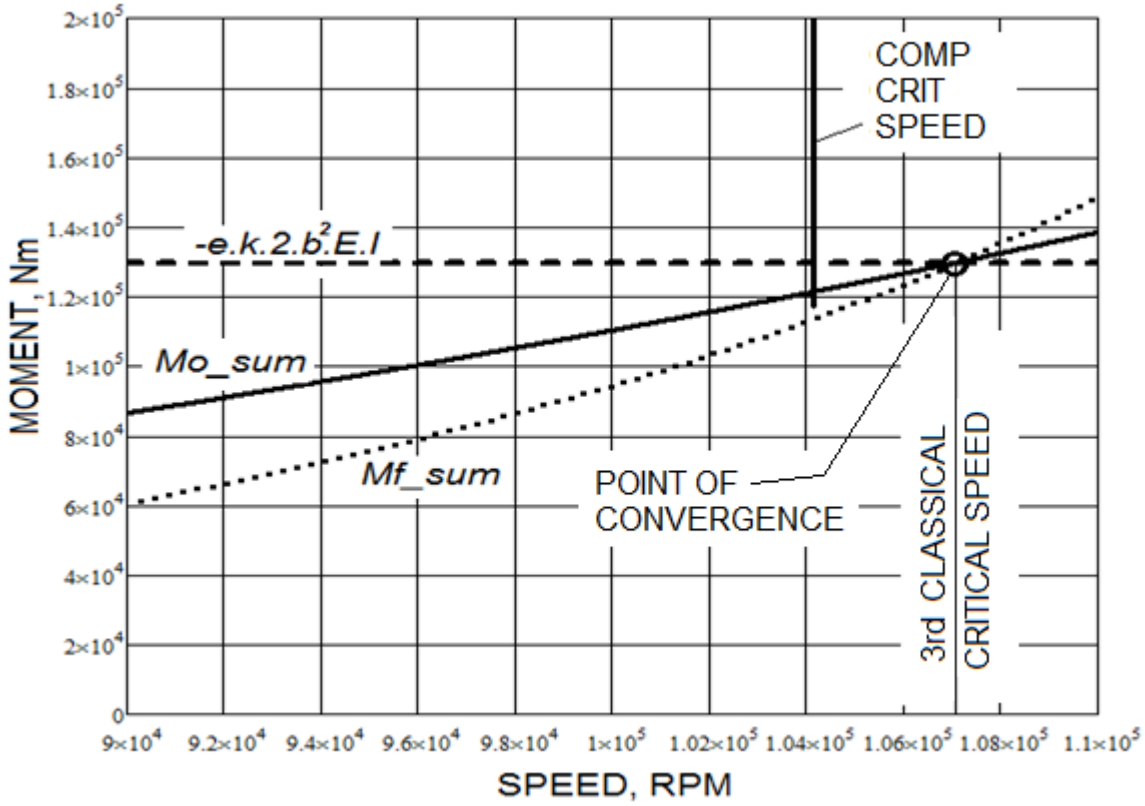


**Figure 5.14,** Elimination of the 3rd Classical Critical Speed

Figure 5.14 provides an example of this, showing the point of convergence of the sum of the encastre fixing moments and the sum of the simply supported balancing sleeve moments, together with the algebraic magnitude of these moments at equalisation. The concentrated imbalance loading and shaft parameter values are the same as those used in Chapter 3, but the operating speed range has been extended to cover the 3rd critical speed, (107,118 rpm), corresponding to $b\ell = 3\pi$ .

The benefits of encastre simulation at this higher critical speed can be clearly seen in Figure 5.15, which shows the reduction of the 1st end reaction load with maximum balancing sleeve compensation, compared to that without any compensation, but with low speed balance correction at shaft ends only.

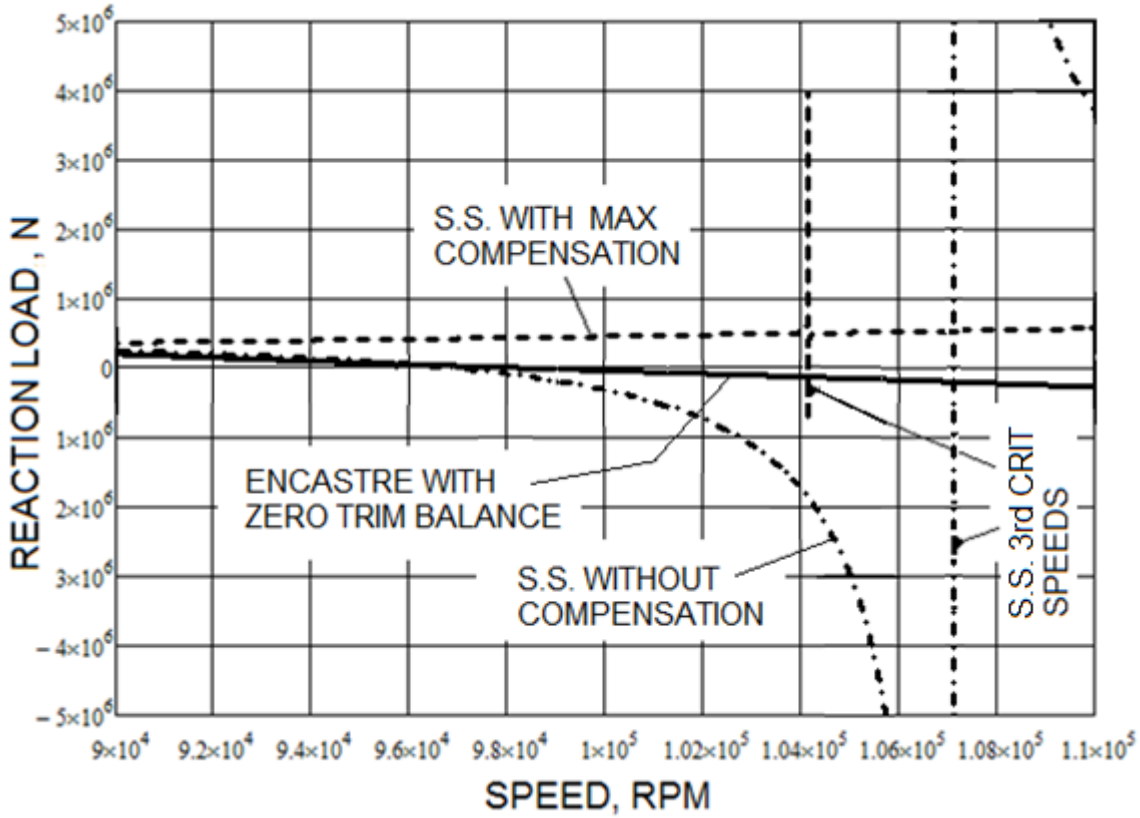


**Figure 5.15,** Reaction Loads vs. Speed adjacent to the 3rd critical speed

Further, to show the possible advantages of an actual encastre shaft - i.e. one mounted in long, or multiple, very tight clearance bearings so as to maintain zero shaft slopes at the ends, Figure 5.15 also shows the reaction load for this case i.e. for the same concentrated shaft imbalance condition but without any trim balance correction. It is seen that this arrangement could be very advantageous in terms of reaction load reduction, but is often compromised by shaft alignment problems and will incur higher costs due to increased lengths and complexity of the overall drive train.

It is the lack of trim balance loading that causes a further reduction in reaction load compared with that of the maximum compensated case, as in Figure 5.15. The compensating balancing sleeves not only replicate the encastre fixing moments, but also impart a lateral load on the ends of the shaft, equal to the centrifugal forces acting on the eccentric masses at the free ends of the sleeves. In the encastre case, the bearing reaction loads

that counter-balance their fixing moments are much smaller due to the much greater length of the moment arm, i.e. the full length of the shaft compared with the much shorter length of the balancing sleeves.

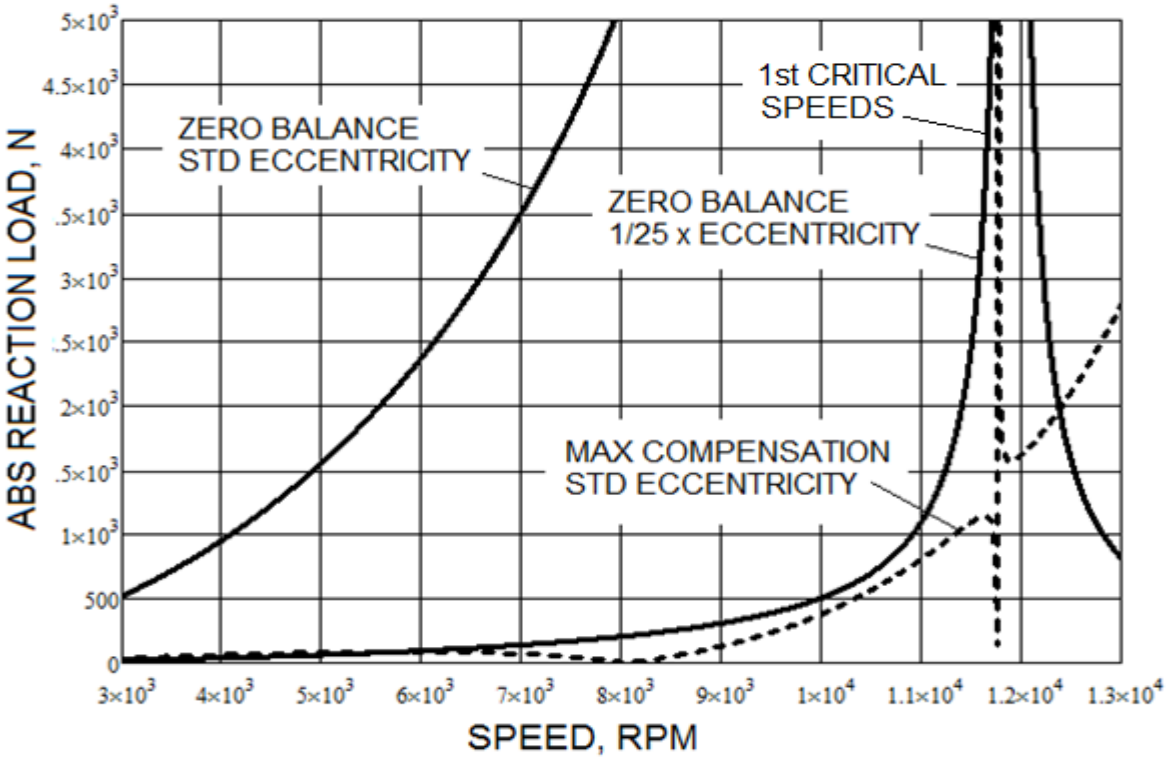


**Figure 5.16,** Equivalent Shaft Eccentricity for operation adjacent to the 1st critical speed

The reduction in the *SR* ratio and its indication of the possible effectiveness of encastre simulation at higher critical speeds is shown in Figures 5.16 and 5.17. Using equivalent shaft eccentricity as a measure of balancing sleeve efficiency, Figure 5.16 plots the absolute reaction loads versus operating speeds, adjacent to the 1st critical speed, for simply supported cases: first, of zero balance correction and second, with maximum compensation, both with standard eccentricity, and a third case, of zero balance, but with a much reduced eccentricity. This latter case shows that maximum compensation is approximately equivalent to reducing standard shaft eccentricity by a 1/25th.

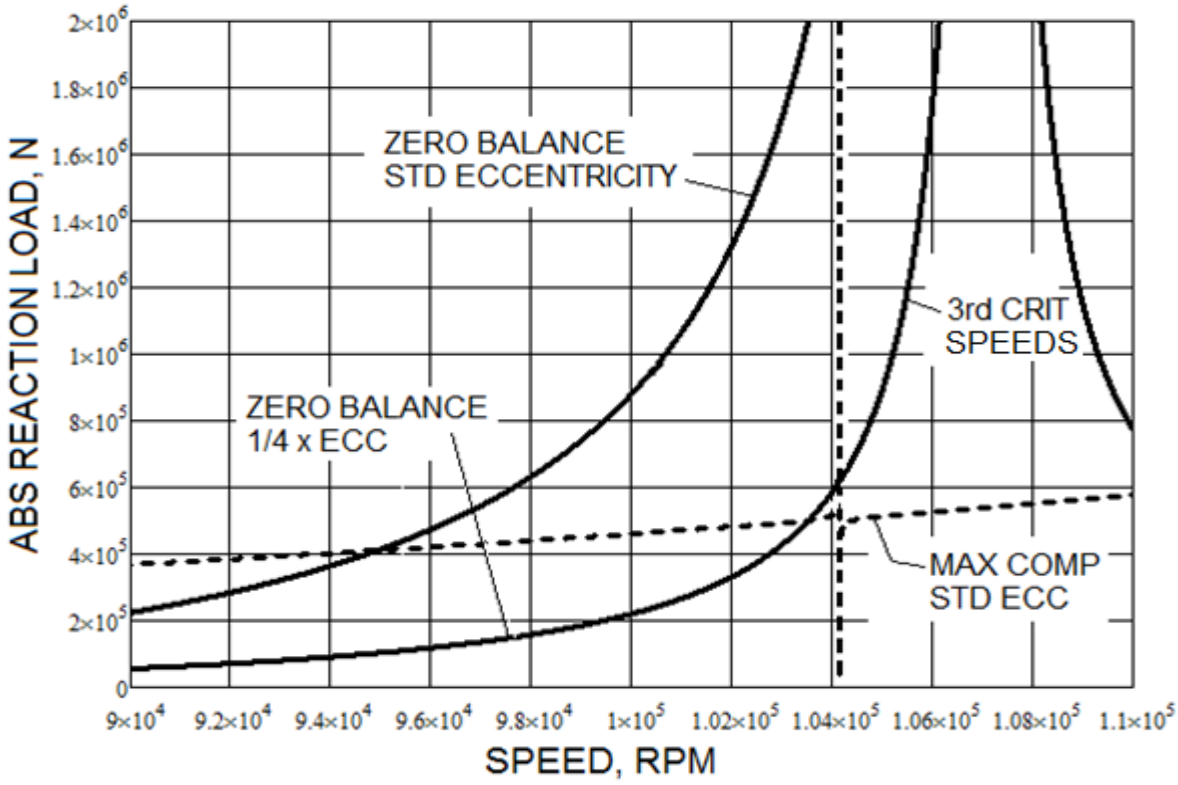


**Figure 5.17,** Equivalent Shaft Eccentricity for operation adjacent to the 3rd critical speed

A similar account is shown in Figure 5.17 for operating speeds adjacent to the 3rd critical speed. However, in this case the maximum compensation can be emulated by reducing the equivalent shaft eccentricity by only a 1/4$^{th}$ of the standard. This shows that for the 3$^{rd}$ critical speed the equivalent reduction in shaft eccentricity is very much lower than for the 1$^{st}$ critical speed and confirms that balancing efficiency is reduced at the higher critical speeds when employing only double encastre simulation. This could be improved by applying balancing sleeve compensation at the node positions of some, or all, of the individual shaft undulations.

## 5.7 Preliminary Conclusions

The analysis of balancing sleeve compensation of the higher critical speeds confirms that the magnitude of the Simulation Ratio, *SR,* provides a good indication of the shaft stiffening effect and the reaction load reduction benefits to be gained from applying compensation at shaft ends only. As

expected, this ratio and its associated benefits are reduced as the order of the critical speed increases since it is only the end undulations that are subjected to single encastre simulation, and remaining undulations act as if simply supported. However, notably, the analysis also confirms that encastre simulation is still possible at higher critical speeds providing the same mathematical requirements, (as for the 1st critical speed) are met, i.e. the sum of the balancing moments equals the sum of the encastre fixing moments, $M_{01} + M_{02} = M_{f1} + M_{f2} = -e.k.2b^2.E.I$ .

It is also noted that due to the very high rotational speeds, even with maximum balance sleeve compensation, the reaction loads are an order of magnitude higher than when operating near the 1st critical speed. Hence the importance of achieving the lowest possible degree of residual imbalance for high speed machinery remains paramount. However, design of very high speed machinery remains a compromise between cost and layout possibilities, for example: 1) by minimising eccentricity, through maintaining material stability by close control of density, grain structure and internal properties such as creep and hysteresis; together with ultra-high precision machining of multi component assemblies or alternatively, by production of one piece rotors, 2) by maintaining large, lateral critical speed, LCS, margins, i.e. ensuring that the critical speed is well away from the running speed; this is usually a conflicting requirement needing rotating components to be of both of high lateral stiffness and of low mass. Alternately, LCS margins may be increased by the use of additional bearings, at shaft ends and/ or mid span, as per actual encastre mounting. However, all these possibilities invariably add to the overall complexity of the design layout with associated issues. Hence, achieving and maintaining (often during very arduous operating conditions) a very low degree of residual unbalance is not easy, and consequently installations often suffer from severe vibration problems at particular speeds and/ or loading conditions.

Therefore, even at the higher critical speeds, with its reduced benefits, the possibility of near elimination/ nullification of an adjacent critical speed as offered by shaft-end balance compensation, still has the potential to help reduce shaft vibrations. And, it is noted that overall shaft balance could be improved even further, if required, by applying balancing sleeve compensation at node positions along the shaft so as to replicate encastre mounting of some, or all, of the intermediate shaft undulations.

The analysis of the shear force reaction ratio, *RR,* has showed that it can be considered independent of the shaft eccentricity, and provides an indication of the possible benefits to be gained by encastre simulation for any given level of shaft eccentricity. This means that even if a shaft has been previously balanced by a maximum practical amount, for example on a high speed balancing machine, then this methodology has the effect of further reducing the eccentricity by *RR* (noting that the internal shear reaction force is directly proportional to shaft eccentricity), even allowing for the fact that the exact value of the ratio applies only at the speed at which encastre conversion occurs, i.e. when the balancing sleeve moments equate to the encastre fixing moments. Moreover, since the ratio greatly increases the closer the operating speed is to the critical speed, then it follows that the balancing improvements also increase to counter the usual increase in rotor vibration that occurs at these higher speeds – an ideal situation.

The example case of maximum compensation of the 1$^{st}$ critical speed, shown in Figure 5.16, produced an equivalent reduction in shaft eccentricity that was greater than 25x. If utilised it would be extremely advantageous to many industrial machines, by imparting improved system performance, if allowed to operate with reduced lateral critical speed margins.

The analysis implies that this is also feasible for most designs of high-speed flexible shafts. Although the analysis is based on a simple plain shaft with

uniform eccentricity, it is shown that the benefits also apply to shafts with concentrated imbalances and/or multiple discs that are mounted within the central 80% of the shaft length, i.e. most practical shafting. Also, it is shown that the characteristic design of the balancing sleeves to achieve maximum balance compensation is independent of shaft eccentricity. Therefore, prior knowledge of the residual imbalance of the shaft (magnitude of eccentricity or position) is not needed and fine adjustment of the balancing sleeve moment to give encastre simulation should be possible by a variety of detailed designs, capable of achieving near micrometer accuracy, in response to feedback data from the bearing sensors (a pre-requisite in most large industrial high-speed drive trains).

The significant potential of this novel balancing methodology to provide improvements in the balancing of high-speed, flexible shafts, has therefore been shown.

# Chapter 6

## 6.1 Test Rig Design

The production of a full size test shaft that replicates the drive couplings employed by Siemens sub 15MW turbine packages is prohibitively expensive, both in terms of capital and commission costs, and infrastructure. However, validation of balance sleeve compensation theory and its practical potential can be met using a scaled test rig facility designed to have full speed capability. The speed matching maintains parity between site and test critical speeds, and is sized to accommodate a reduced scaled model example of a turbine coupling shaft. The test facility is described below.

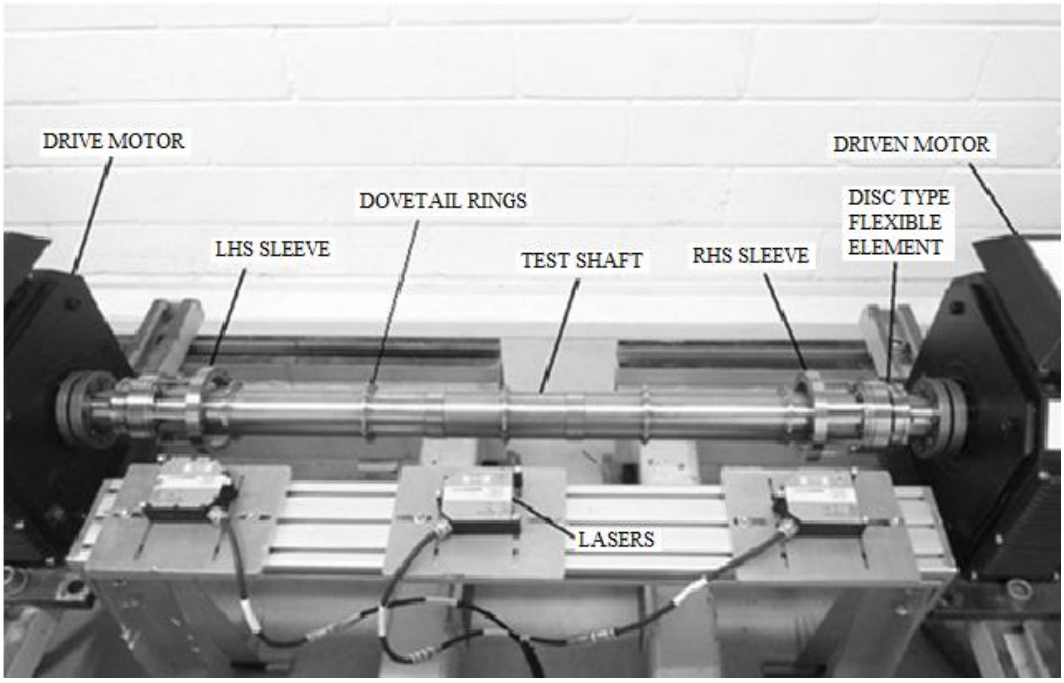


**Figure 6.1,** Test Rig

The drive system is comprised of two Oswald, Type QDi13 2 2, variable speed, 0 – 20,000 rpm, 49 kW, electric motors, LHS driving, RHS acting as a feedback generator, so that only the accelerating torque and drive train losses needed to be powered electrically by the mains supply. The motors and its control package is designed and supplied by Control Techniques Ltd., as specified in Appendix D1.

The motors are mounted on individual bed plates, via a pair of slide rails, to allow lengthwise adjustment of a test shaft, which is centrally mounted between the shaft ends, as shown in Figure 6.1.

## 6.2 Instrumentation

Instrumentation is used to measure the balance condition of the test shaft under a known level of shaft imbalance at a variety of steady state speeds—initially without any trim balance correction and then with a series of balancing sleeve compensations. A non-contacting system of measurement is used so as to avoid affecting the vibration measurements—laser based systems are capable of measuring deflection of high speed rotating elements and therefore adequately meet this requirement. Optical triangulation is used to determine deflection.

Instrumentation consists of 3x Micro-Epsilon, free standing lasers systems (optoNCDT, type ILD 2300-20), as specified in Appendix D2, positioned to separately enable deflection measurements of the LHS sleeve, the shaft mid-point and the RHS sleeve, as a result of their respective unbalance during shaft rotation.

Markers are bonded at the top dead centre (TDC) position on the outside diameter of each laser location to provide a consistent key phaser/trigger point during each rotation of the shaft. This allowed vector formulation of peak—to–peak, deflections and angular offsets between the local heavy

spot of section unbalance and the shaft TDC position. Hence, at each test speed it is possible to translate local deflections onto the plane of unbalance produced by a known level of added shaft unbalance, thereby allowing a direct comparisons to be made with theoretical results, for validation purposes.

## 6.3 Test Coupling Shaft

With reference to balancing problems seen by some Siemens sub 15MW turbine applications and the site equivalent analytical models developed in Chapters 2 and 3, the application of Buckingham's Pi theorem, of non-dimensional analysis, determined that a suitably scaled test shaft could be produced provided parity was maintained between the two critical speeds.

Whilst complying with this requirement, a test shaft was designed in conjunction with Bibby Turboflex Transmissions Ltd., details of which are given in Table 6.1. A laminated, disc type, flexible element assembly pack, from their standard Torsiflex range of couplings is used. This is a 6 bolt design of similar construction to couplings typically used for mechanical drive contracts and their minimum size, code number TF27, is found to be an appropriate match with the size requirements of the spacer tube, as specified in Appendix D3. The spacer tube is a plain tubular component fitted between the flexible element assembly packs.

For validation purposes it is necessary to apply imbalance masses to the spacer tube to replicate a point of concentrated unbalance, as in the analysis given in Chapter 4. It is also recognised that any method of imbalance attachment must have a minimum effect on the tube's bending stiffness and mass so as to avoid changes to its critical speed. This is achieved by the addition of 5 narrow, low profile, dovetail rings, positioned at the mid point of 5 zones, of approximately equal length, set out axially

along of the spacer tube, together with 2 small balance clamps per ring. These are attached to individual dovetails as shown in Figure 6.2, and their angular position set to provide a combined resultant concentrated unbalance of known magnitude at each zone position, as detailed in Appendix D3.

| | TUBE LENGTH, mm | TUBE O/D, mm | TUBE I/D, mm | TUBE MASS, Kg | CPLG ½ MASS, Kg | CRITICAL SPEED, RPM |
|---|---|---|---|---|---|---|
| SITE EQUIV. MODEL | 1707 | 207 | 201 | 38.3 | 48 | 11,900 |
| SCALED TEST MODEL | 922 | 62 | 56 | 4.0 | 3.6 | 11,900 |

**Table 6.1,** Site Equivalent and Scaled Test Shaft details

Figure 6.3a shows a schematic of the test coupling, with pairs of plain bore hubs, element packs and compensating balance sleeves, separated by a plain spacer tube, with the dovetail rings and balance clamps as described above. In detail the assembly is comprised of a tubular spacer, (62 mm o/d x 56 mm i/d x 864 mm long), laminated disc type, flexible elements, (920 mm between element centres), coupling shaft, (950 mm, Distance Between Shaft Ends – DBSE), as per Bibby Drawing Number 10625 sht 1, with balance sleeves, as per Bibby Drawing Number 10625-5, mounted at each end. Appendix D3 provides further details.

For design purposes the assembly is analysed using the fundamental equations determined in chapter 2, (2.43), critical speed and chapter 4, (4.31), (4.59) and (4.60), shaft deflections and reaction loads, as a plain tube, of the same cross section as the spacer tube and simply supported at the ends with a nominal length corresponding to the element pack, centre to centre distance. The length is then further modified to provide the same critical speed as the test coupling assembly, determined by the manufacturer using FEA analysis. The minor length variation is assumed to

be due to the physical differences between the test coupling assembly and the plain tubular model, i.e. interface joints, fastener masses etc. The mathematical model is shown in Figure 6.3b, together with the 5-off concentrated loading positions.

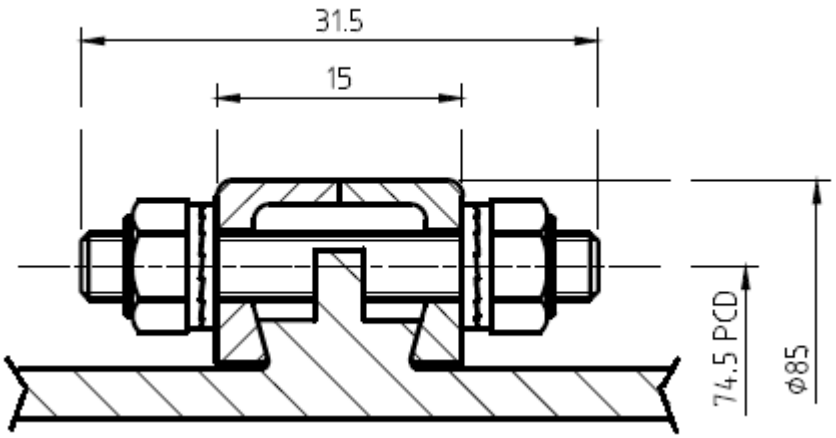


**Figure 6.2,** Detail of Balance Clamp/ Test Weight, attachment to a Dovetail Ring

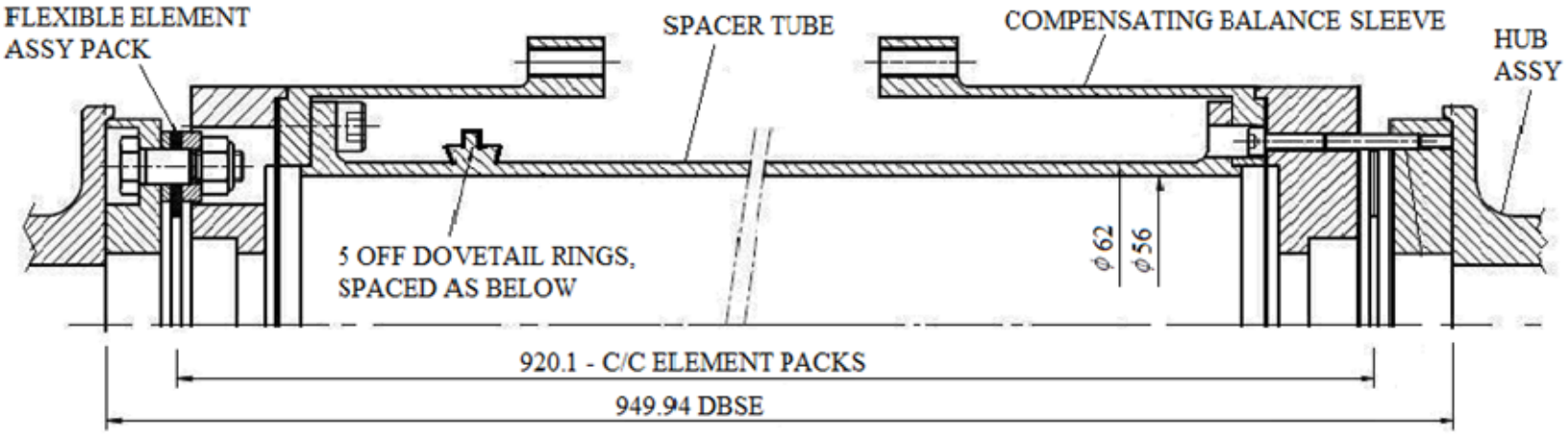


**Figure 6.3a,** Test Coupling Assembly

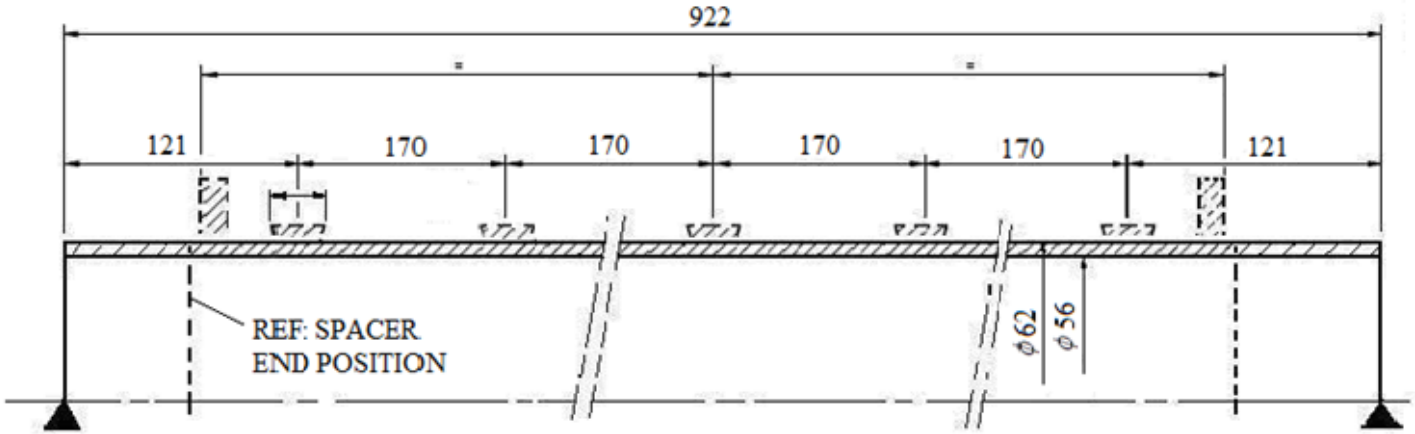


**Figure 6.3b,** Plain Tube, mathematical model showing concentrated load positions

# Chapter 7

This chapter determines the detail design requirements of a compensating balancing sleeve to be used in conjunction with the test coupling shaft of the previous chapter, for experimental development and validation testing.

## 7.1 Compensating Balancing Sleeve Design

Chapter 2 determined the benefit of adding compliance to a trim balance mass and that this could be achieved, very effectively, by a simple cantilever construction, as shown in Figure 2.4. This gives the appearance that the moment arm was constructed with a full 360 tubular cross section, which need not necessarily be the case, but initial sizing calculations quickly showed that such a design would have a lateral bending stiffness that was far greater than required for the test coupling shaft, as detailed in chapter 6. However, it also became evident that a lower stiffness could be achieved by machining slots in the tube, so as to produce a number of equally spaced, longitudinal spars, between the fixed mounting flange and the compliant balancing ring, as shown in Figure 7.1.

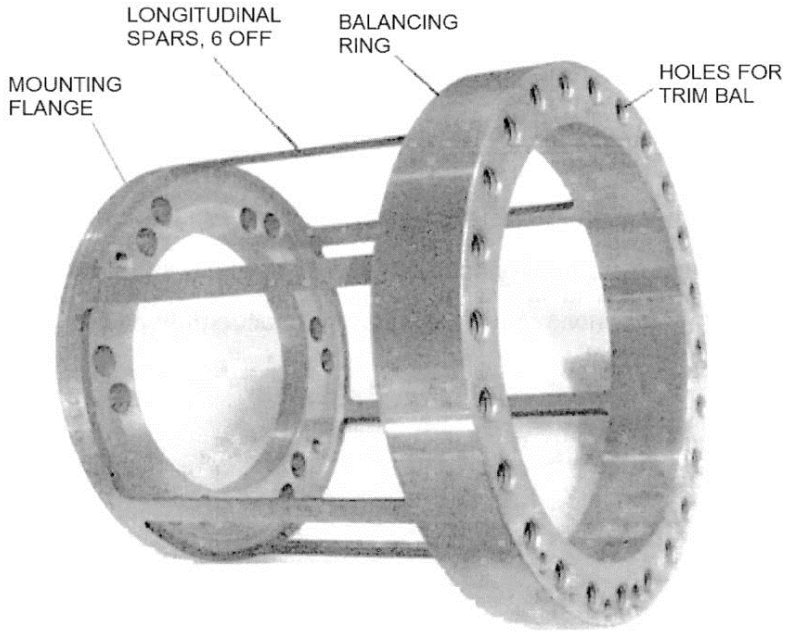


**Figure 7.1,** Compensating Balance Sleeve – Multiple Spar Design.

With this arrangement the centrifugal force acting on a trim balance mass during rotation would produce lateral bending of the spars and cause the balancing ring to be displaced vertically downwards, as shown in Figure 7.2. Each spar then will bend individually, as per a double encastre beam, since its stiffness is relatively small compared with that of the two end plates, and unlike in a tube construction there is no shear connection to link the spars together, hence the mechanism is similar to that of a 4-bar chain producing parallel motion between the balancing ring and the mounting flange.

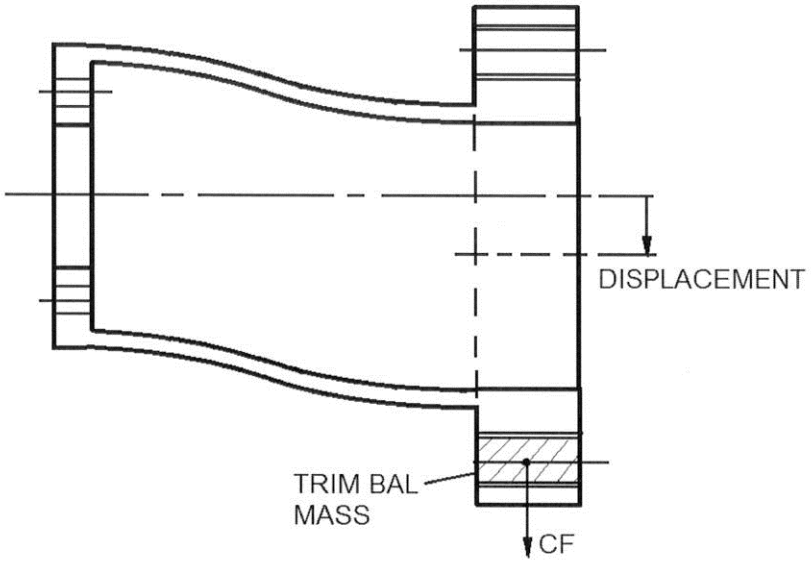


**Figure 7.2,** Balancing Sleeve Spars – double encastre bending mode

Analysis of the bending stiffness of the sleeve assembly therefore first requires calculation of the 2nd moment of area, (moment of inertia $I_{cc}$) of each spar angular cross section, about a horizontal axis through its own centroid. This can be accomplished by angular integration, with reference to Figure 7.3.

Elemental area $\delta A$ is given by: $$\delta A = R.\delta\theta.\delta R \qquad (7.1)$$

Hence, elemental sector area: $$A' = \delta\theta.\int_{R_1}^{R_2} R.\delta R = \left[\frac{R_2^{\,2} - R_1^{\,2}}{2}\right].\delta\theta$$

Spar cross sectional area: $A = \int_{\theta_1}^{\theta_2} A'.\delta\theta = \left[\frac{R_2{}^2 - R_1{}^2}{2}\right].(\theta_2 - \theta_1)$ (7.2)

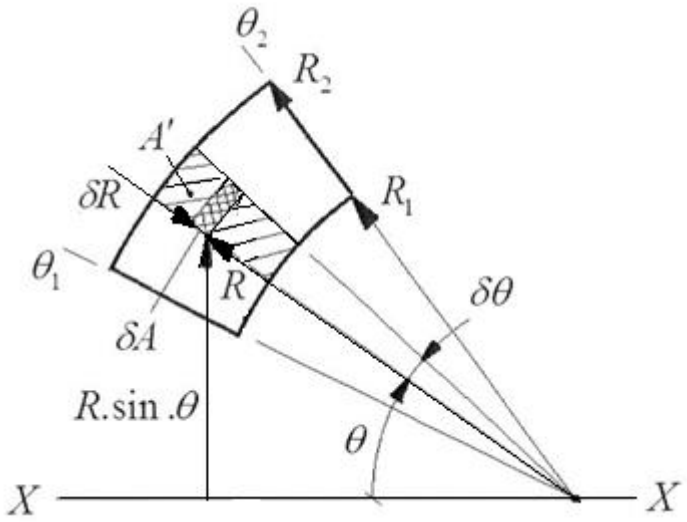


**Figure 7.3,** Single Spar Cross Sectional Analysis.

The 1st moment of area about axis X – X, of the spar cross section, *A,* is given by:

$M_1 = \int_{\theta_1}^{\theta_2}\int_{R_1}^{R_2} R.\sin\theta.\delta A$, and substituting from (7.1) gives:

$M_1 = \int_{\theta_1}^{\theta_2}\left(\int_{R_1}^{R_2} R^2.\delta R\right).\sin\theta.\delta\theta$, and integrating wrt *R* gives:

$M_1 = \left[\frac{R_2{}^3 - R_1{}^3}{3}\right].\int_{\theta_1}^{\theta_2}\sin\theta.\delta\theta$, and integrating wrt *θ* gives:

$$M_1 = \left[\frac{R_2{}^3 - R_1{}^3}{3}\right].\left(\cos\theta_1 - \cos\theta_2\right), \qquad (7.3)$$

Therefore, the centroid height of the spar cross section, above axis X – X, is given by:

$$h = \frac{M_1}{A}, \tag{7.4}$$

and is readily obtainable from (7.3) and (7.2).

Similarly, the 2nd moment of area about axis X – X, (moment of inertia, $I_{xx}$) of the spar cross section, *A,* is given by:

$M_2 = \int_{\theta_1}^{\theta_2} \int_{R_1}^{R_2} \left(R.\sin\theta\right)^2 .\delta A$, and substituting from (7.1) gives:

$$M_2 = \int_{\theta_1}^{\theta_2} \int_{R_1}^{R_2} \left(R.\sin\theta\right)^2 .R.\delta\theta.\delta R = \int_{\theta_1}^{\theta_2} \left( \int_{R_1}^{R_2} R^3 .\delta R \right).\sin^2\theta.\delta\theta$$

$$M_2 = \left[ \frac{{R_2}^4 - {R_1}^4}{4} \right].\int_{\theta_1}^{\theta_2} \sin^2\theta.\delta\theta$$

Substituting, $\sin^2\theta = \frac{1-\cos 2\theta}{2}$, and integrating gives:

$$M_2 = \left[ \frac{{R_2}^4 - {R_1}^4}{4} \right].\left( \frac{\theta_2}{2} - \frac{\sin 2\theta_2}{4} - \frac{\theta_1}{2} + \frac{\sin 2\theta_1}{4} \right), \tag{7.5}$$

The 2nd moment of area, or moment of inertia, through the centroid can now be determined from the parallel axis theorem:

$$I_{xx} = I_{cc} + A.h^2$$

Hence, the moment of inertia for an individual spar is given by:

$$I_{cc} = M_2 - A.h^2 \tag{7.6}$$

Since each spar will experience the same deflection, the individual bending stiffness' are deemed to act in parallel and the overall stiffness, of the complete assembly, will be the summation of all the individual stiffness'. Also, beam theory states that for elastic deflection, the stiffness of a beam is directly proportional to its moment of inertia, so it follows that the sleeve

assembly can be treated as a single beam with unitary bending properties, where:

$$I_{sleeve} = \sum_{i-1}^{n} I_{cc\_i} \ , \qquad \text{where } n = \text{total number of spars} \qquad (7.7)$$

It is notable that since $I_{sleeve}$ is a constant, for a given sleeve design, then its lateral stiffness will be a constant for all angular positions of trim balance correction applied to the sleeve.

## 7.2 Double Encastre Beam

From section 7.1, it is possible to represent the complete sleeve assembly schematically as a single beam, with double encastre end restraints, as shown in Figure 7.4, where *u* represents the sleeve deflection, when subjected to a lateral load, *R,* representative of the centrifugal force, *CF,* and *M* is the internal fixing moment between the mounting flange and the spar, at the LHS and similarly between the balancing ring and the spar, at the RHS.

The characteristic equations for a double encastre beam can be determined by double integration of the bending moment equation.

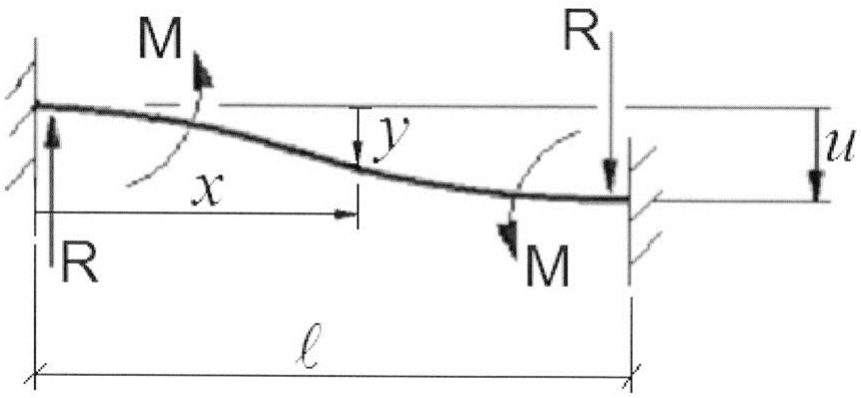


**Figure 7.4,** Schematic of a Double Encastre Beam

From beam theory, the bending moment, *BM,* is equal to:

$$BM = E.I.\frac{d^2y}{dx^2} = -M + R.x\,, \tag{7.8}$$

By integration, $$E.I.\frac{dy}{dx} = -M.x + \frac{R.x^2}{2} + A$$

$$E.I.y = -\frac{M.x^2}{2} + \frac{R.x^3}{6} + A.x + B$$

where A and B are constants of integration and both are equal to zero, since at $x = 0$, $y = 0$ and $\frac{dy}{dx} = 0$, therefore:

$$E.I.y = -\frac{M.x^2}{2} + \frac{R.x^3}{6}\,, \tag{7.9}$$

The LHS of (7.8) and (7.9) equal *M* and -*EI.u*, respectively for $x = \ell$ giving:

$$M = \frac{R.\ell}{2}\,, \tag{7.10}$$

and by substitution $$-E.I.u = -\frac{R.\ell^3}{12}\,, \tag{7.11}$$

Combining (7.10) and (7.11) gives $$M = \frac{6.u.EI}{\ell^2}\,, \tag{7.12}$$

The beam/ sleeve stiffness is then given by $$K = \frac{R}{u} = \frac{12.EI}{\ell^3}\,, \tag{7.13}$$

The maximum bending stress in any given spar appears at shaft ends resulting from the imposed fixing moments, and is given by:

$$f\_\max = \frac{M}{I}.y_{fibre}\,,$$

where $y_{fibre}$ is the extreme fibre, seen during bending, i.e. the vertical height of the outmost point on the spar cross section above the centroid position.

Substituting (7.12) gives $$f\_\max = \frac{6.u.E}{\ell^2}.y_{fibre}, \qquad (7.14)$$

which is independent of the moment inertia, *I*. Therefore, the highest value of $f\_\max$ will occur in the spar in which $y_{fibre}$ is the greatest, i.e. the 4 spars nearest to the horizontal axis, as shown in Figure 7.5.

In addition to the vertical bending moments, *BM_defl,* imposed on the spars due to rotation of the trim balance mass, there will also be independent bending moments, *BM_bow,* imposed in a radial direction, resulting from the centrifugal forces acting on the mass of the spars, thereby giving them a tendency to bow outwards.

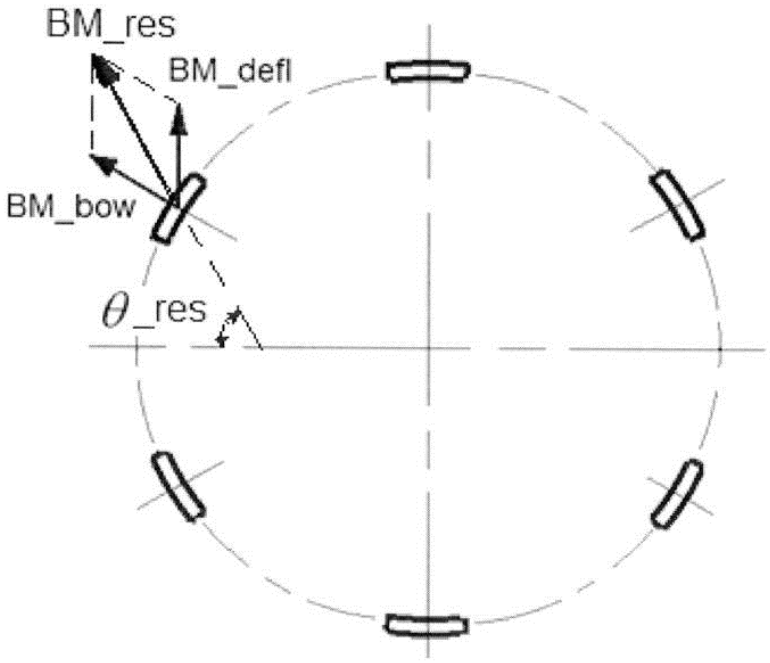


**Figure 7.5,** Bending Moments imposed on Spars during rotation

This mode of bending can be represented by a plain shaft with uniform eccentricity which is subjected to centrifugal forces during rotation. As such, is identical to the double encastre shaft analysed in chapter 3, so that the maximum bending moments and resulting stresses can be determined from

the equations, (3.9) and (3.10), given in chapter 3, by setting the shaft diameter to give the same 2nd moment of area as the top most spar, Figure 7.5, and it's eccentricity equal to the mean radius of the spars in their unloaded condition.

Each spar will then be subjected to both vertical and radial bending moments, as shown in Figure 7.5, and the maximum imposed bending stress will result from the resultant bending moment, *BM_res*, of the two vectors, *BM_defl* and *BM_bow*, applied at the corresponding cross section moments of inertia, acting at the resultant angle,

Hence, an optimize detail design of the balancing sleeves is now possible to obtain the required sleeve stiffness together with practical machining dimensions and suitable operating stresses etc., by simply inserting the above equations into a suitable analytical computer program.

As a final check, it is noted that the introduction of balancing sleeves adds 2 extra vibration modes, i.e. Degrees of Freedom, DOF, to the shaft assembly and hence possible sources of instability. In order to ensure that they are not excited by imbalance it is prudent to design their sleeve critical speeds to be well above that of the shaft and this is illustrated by the Campbell, Figure 7.6, for the complete test shaft assembly.

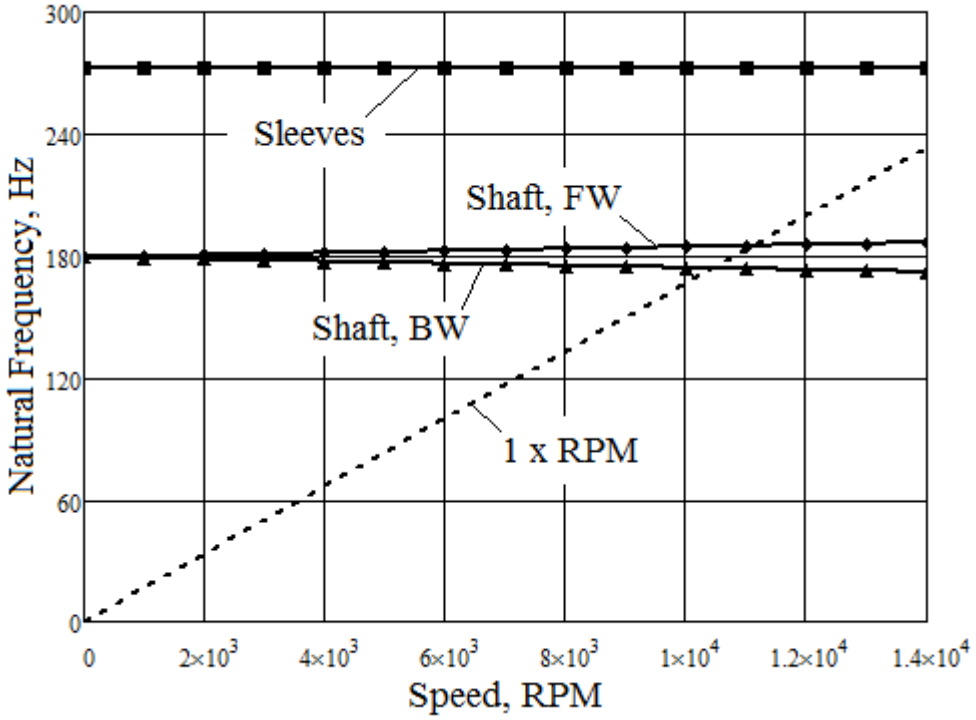


**Figure 7.6,** Campbell Diagram of Test Shaft

# Chapter 8

## 8.1 Test Requirements

Following the establishment of balance sleeve compensation and its associated encastre simulation theory, Chapters 2, 3 and 4, the results require practical validation. An instrumented test rig and scaled coupling test shaft has therefore been designed and commissioned, as described in Chapter 6.

Experimental trials are conducted in accordance with the following procedures.

## 8.2 Test Procedure

### SAFETY PRECAUTIONS APPLICABLE TO ALL TESTS

To prevent failure of the coupling shaft assembly, operation close to the critical speed is limited by laser monitoring and manual shutdown if safe shaft and sleeve deflections are reached/exceeded.

Safe Limits are set at shaft mid-point and sleeve balance ring deflections of 6.0 mm and 0.35 mm, respectively, (corresponding stresses; 65% and 70% of yield).

Measurements to be taken at steady state operating speeds with step changes gradually reduced as deflection readings increase, to maintain shaft and sleeve deflections below stated safe limits. Chart 1 is to be used as a guide to likely increases in shaft dynamic magnification of deflections in the zero balance correction condition, with shaft critical speed proximity.

Note, the sleeve critical speed is much higher than that of the shaft, therefore its contribution to dynamic magnification during these tests is low.

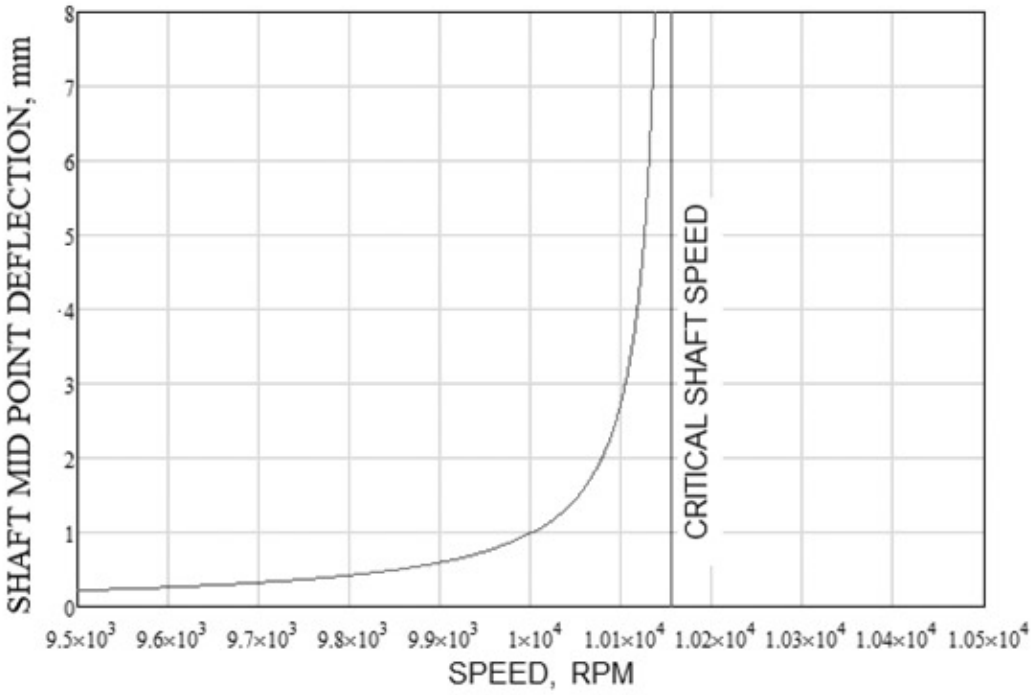


**Chart 1,** Typical Change in Shaft Deflection vs. Critical Speed Proximity

**TP.1**, Test Setup: with the coupling hubs mounted onto the motor shaft ends and fastened by tightening Tollok Locking Couplings, assemble the Test Coupling between the hubs, Figures 8.1 and 8.2. Align the two motor shafts using Rotalign Laser Alignment Equipment to obtain the following offset settings, at LHS and RHS hubs, 1 and 2: $X_1$ , $Y_1$ and $X_2$ , $Y_2$ = 0.0 +/- 0.2 mm.

Axially align 3 off marker strips, (Triggers), to the shaft's Top Dead Centre position, (TDC), Figure 8.3, and bond on the outer diameter of the LHS and RHS Sleeve Balancing Rings, and to the coupling shaft mid-point, adjacent the 3rd dovetail ring.

With reference to Figures 8.1 and 8.2, mount 3 off, laser measuring heads on their free standing slideway and align to allow deflection measurements at the shaft mid-point and LHS + RHS sleeve balance ring positions, as per the manufacturer, Micro-Epsilon's, Instruction Manual – ref. Chapter 6, Appendix D2.

**TP.2**, Residual Unbalance Test: without any imbalance or correction masses fitted to the test shaft or balance sleeves; start rig and incrementally increase speed from 0 to 8,500 rpm. Fast data collection to be used to obtain key phaser position of maximum deflections at various speeds. Plot shaft deflection vs. speed.

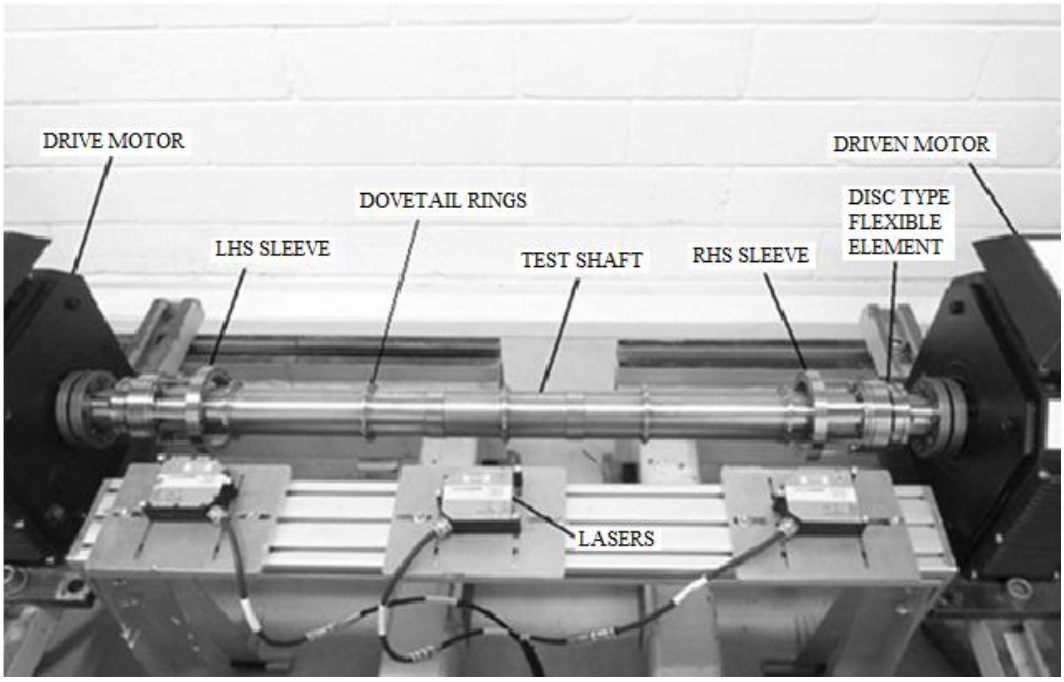


**Figure 8.1,** Test Rig

**TP.3**, Residual Balance Correction: Calculate the positions and sizes of shaft residual unbalance and incrementally make corrections, as necessary,

by adding or removing metal from the sleeves and the two central balancing rings on the shaft, and re-check test TP.2.

Repeat as necessary to achieve repeatable low levels of shaft deflections, (less than 0.5 mm), at speeds up to 10,200 rpm. Plot ‘Residual’ shaft deflection vs speed.

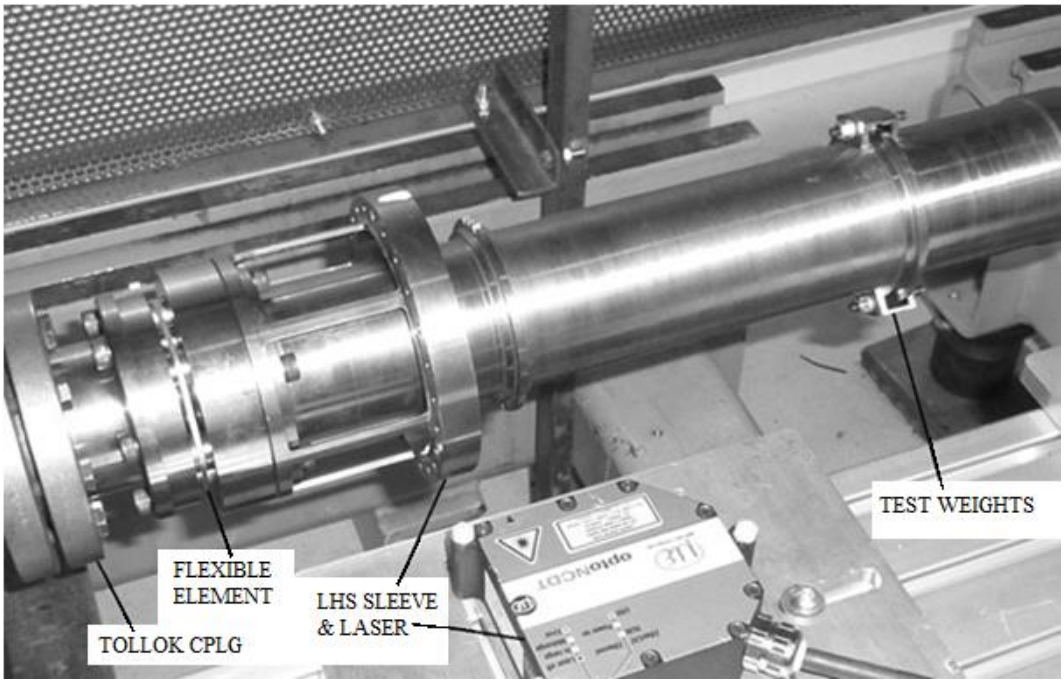


**Figure 8.2,** Close-Up of Test Weights & LHS Laser Configuration

**TP.4**, Shaft Test Weight Unbalance with Zero Correction - without Compensation: affix balance clamps to give 67.5 g.mm of imbalance, (2 clamps fitted to 2nd dovetail ring, 9º from diametric opposite position, arranged as per Figure 8.3). Start rig and incrementally increase speed from 0 to 8,500 rpm. Fast data collection to be used to obtain key phaser position of maximum deflection at various speeds. Plot ‘Measured’ shaft and sleeve deflection vs. speed.

Check results and if deflections are well within stated limits, repeat test at up to 10,000 rpm.

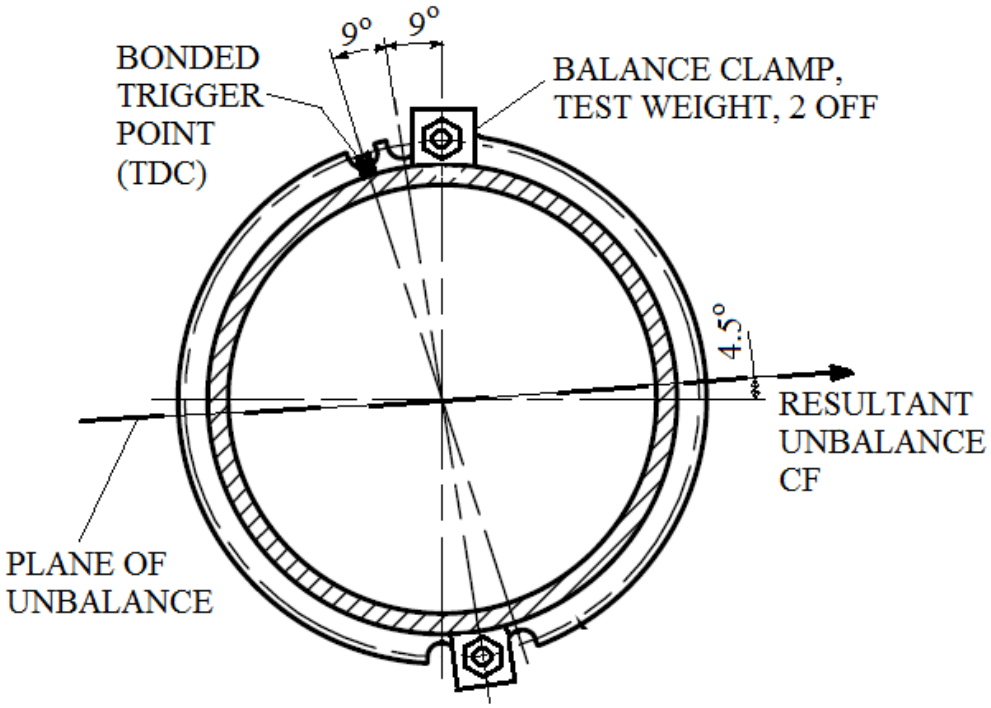


**Figure 8.3,** Angular relationship of Test Weights and Trigger (TDC) position

**TP.5**, Double Sleeve Compensation Test: repeat step TP.4, with 68 gmm, (1.3 gram at 51 mm radius) of balance sleeve compensation, 180 degrees out of phase with shaft imbalance centrifugal force, CF, Figure 8.3, at both balance sleeves. Plot 'Measured' shaft and sleeve deflection vs. speed.

**TP.6**, Analyse results and incrementally make further balance adjustments/ re-tests as appropriate to achieve maximum obtainable balance compensation.

**TP.7** Single Sleeve Compensation Test, LHS: repeat steps TP.5 and TP.6, with 136 gmm, (2.6 gram at 51 mm radius), of balance sleeve compensation, 180 degrees out of phase with shaft imbalance, at LHS balance sleeve only – zero compensation at RHS sleeve. Plot 'Measured' shaft and sleeve deflection vs. speed.

**TP.8**, Analyse results and incrementally make further balance adjustments/ re-tests as appropriate to achieve maximum obtainable balance compensation.

**TP.9** Single Sleeve Compensation Test, RHS: repeat steps TP.5 and TP.6, with 136 gmm, (2.6 gram at 51 mm radius) of balance sleeve compensation, 180 degrees out of phase with shaft imbalance, at RHS balance sleeve only – zero compensation at LHS sleeve. Plot 'Measured' shaft and sleeve deflection vs. speed.

**TP.10**, Analyse results and incrementally make further balance adjustments/ re-tests as appropriate to achieve maximum obtainable balance compensation.

**TP.11** Critical Speed Determination Test: repeat Residual Unbalance Test TP.2 with a rapid speed transit of the critical speed to 12000 rpm to establish the critical speed of the unbalanced shaft.

## 8.3 Test Results

### 8.3.1 General Measurement Orientation

As described in Section 1.2.6, for sub-critical rotation of a long, thin, plain shaft, mounted on symmetrical supports, as per the test shaft arrangement the residual unbalance only acts on the Forward Whirl dynamic mode and produces a circular orbit. Moreover, due to low system damping (confirmed

by later results) there is very little phase rotation of the heavy spot until shaft speeds are very close to the critical speed. Hence, the location of the heavy spot is always at the furthest position from the axis of rotation, as shown diagrammatically in Figure 8.4.

It can be seen that the laser beam acts horizontally to monitor the nearest position of the shaft along this axis such that due to its circular motion, the measured output is sinusoidal and the bonded marker/ trigger, as drawn, lags the heavy spot by $\theta^{o}$.

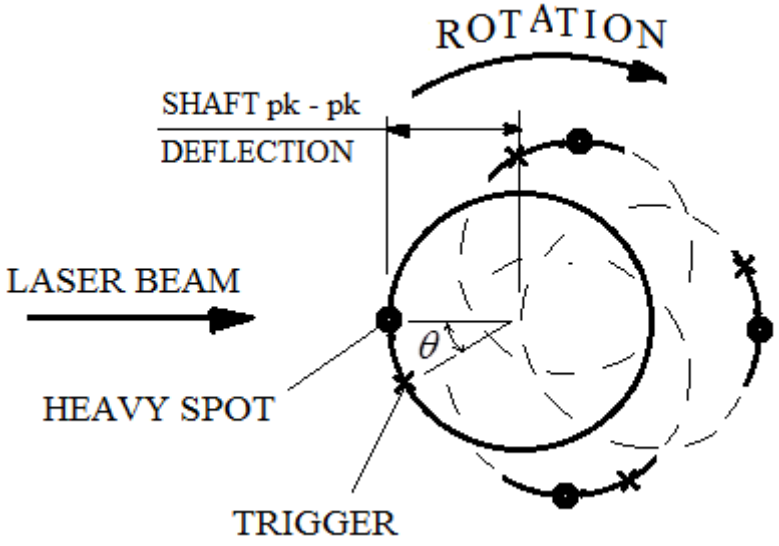


**Figure 8.4,** Heavy Spot orbit and Trigger position

Figure 8.5 shows an example laser plot, obtained during testing of cyclic deflection vs. time; each reading, or dot, representing an instantaneous position of the shaft, with the vertically aligned dots being produced by the protrusion of the bonded marker/ trigger. These plots allowed vector formulation of the maximum measured pk – pk, deflections and the angular offset, $\theta^{o}$, between its position and the laser trigger point/ TDC.

Figure 8.6 shows the relative angular positions of the heavy spot/ maximum deflection to the plane of unbalance, defined by the resultant angle of the two CFs produced by the test weights.

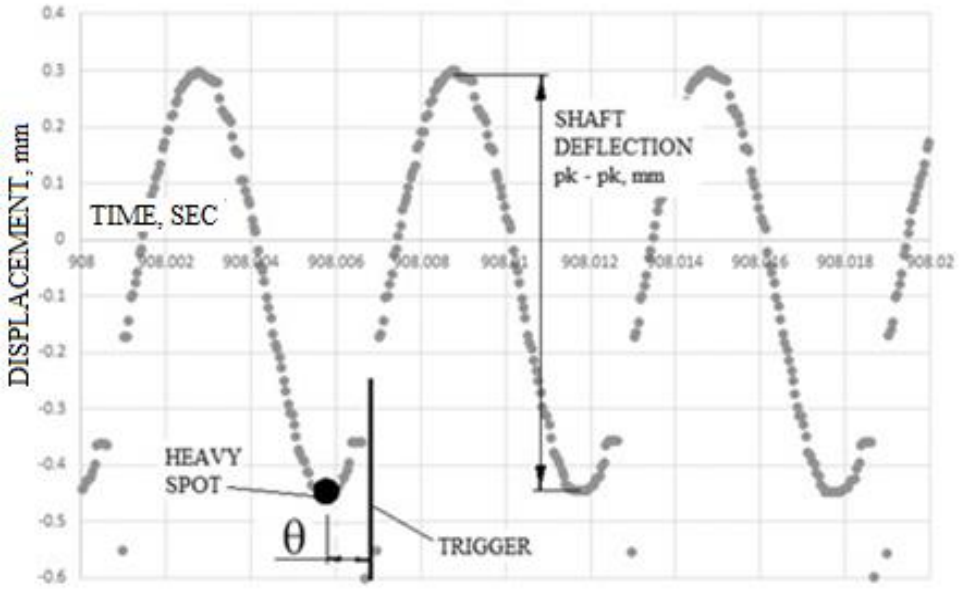


**Figure 8.5,** Typical Laser Plot

Hence, for each test speed it is possible to transcribe the local deflections onto the plane of unbalance to determine the corresponding amplitude component, 0 – pk, which can be attributed to unbalance present in this plane. Note, this is the resultant of the two test weight imbalances plus the component of any remaining residual unbalance.

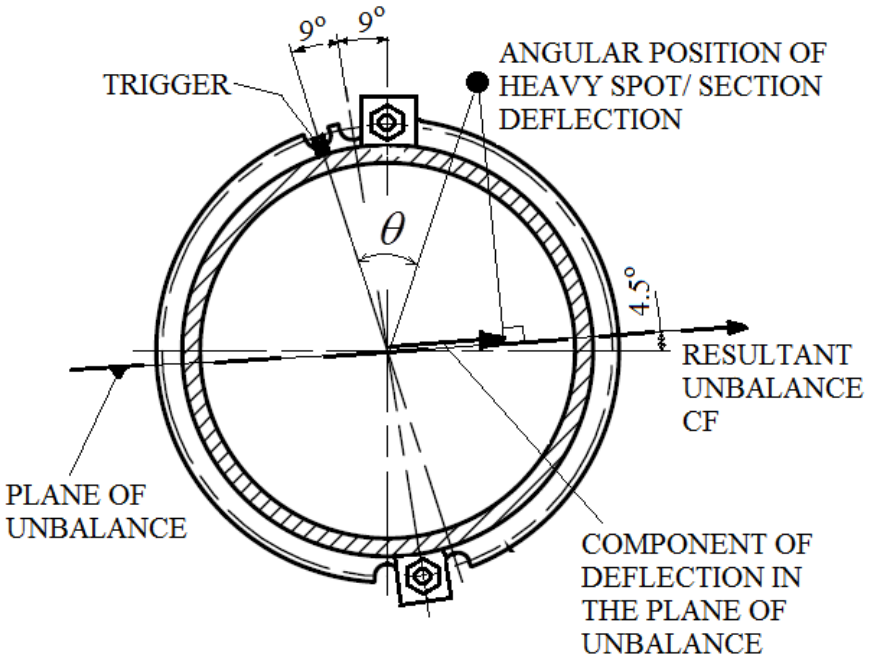


**Figure 8.6,** Component of Deflection in the Plain of Unbalance

### 8.3.2 Test Data from Residual and Test Weight Unbalance, Tests TP.2 - TP.10

For the purpose of theory validation and assessment of the level of compensation obtained during test, sleeve deflections at the maximum test speed of 10,000 rpm are used to determine the actual balancing sleeve moments applied during the compensation tests. Sleeve deflections at lower speeds and for other tests are not used, hence, it is only these readings that have been recorded in the following tables.

8.3.2.1, Shaft Residual Unbalance and its Theoretical Equivalence

The levels of shaft mid-point deflections resulting from residual unbalance determined by Tests TP.2 and TP.3, and its referred components in the Plane of Unbalance are given in Table 8.1.

| Speed, kRPM | 7.0 | 7.5 | 8.0 | 8.5 | 9.0 | 9.2 | 9.4 |
|---|---|---|---|---|---|---|---|
| Meas'd Defl'n, pk-pk, mm | 0.12 | 0.12 | 0.14 | 0.15 | 0.16 | 0.17 | 0.22 |
| Ang Offset, θ deg | 22 | 22 | 26 | 26 | 26 | 27 | 25 |
| Defl'n in Unbal Plane, 0-pk, mm | 0.009 | 0.009 | 0.015 | 0.016 | 0.017 | 0.020 | 0.022 |

| Speed, kRPM | 9.6 | 9.8 | 9.9 | 10.0 | 10.10 | 10.20 |
|---|---|---|---|---|---|---|
| Meas'd Defl'n, pk-pk, mm | 0.20 | 0.26 | 0.31 | 0.38 | 0.52 | 0.76 |
| Ang Offset, θ deg | 32 | 39 | 40 | 46 | 43 | 39 |
| Defl'n in Unbal Plane, 0-pk, mm | 0.032 | 0.056 | 0.069 | 0.102 | 0.128 | 0.165 |

**Table 8.1,** Residual Unbalance Shaft Deflections for steady state speeds

To determine a theoretical representation of the referred component of residual unbalance, a Mathcad numerical program of a compensated shaft with a single concentrated imbalance is compiled to calculate expected balance characteristics from the analytical equations developed in Chapter 4 and using parameter values given in Table 8.2. These complied with the mathematical model of the test shaft given in Chapter 6, but with the shaft length increased to $\ell$ = 970 mm to give a critical speed of 10,750 rpm in order to align it with the measured mean value of the two critical speeds obtained from Test TP.11, (Forward and Backward Gyroscopic Critical Speeds), as shown in Figure 8.12.

Through an iterative process, comparing theoretical and measured shaft deflections in the plane of unbalance, a first order approximation of a theoretical level of equivalent residual unbalance is assessed to be 50% of the test weight unbalance, equal to 33.75 g.mm. Figure 8.7 shows this provides a good relative comparison and is therefore subsequently added to the test weight unbalance, thereby setting the theoretical level of concentrated unbalance to 101.25 g.mm for the theory evaluation tests TP.4 to TP.10, and the results subsequently shown in Figures 8.9, 8.10 and 8.11.

| Test Shaft Parameters | |
|---|---|
| $M_s$ = 4.2287 kg | $\ell$ = 0.970 m |
| $m_1$ = 0. 3864 kg | $m_2$ = 0. 3864 kg |
| *e* = 7.744 x 10^-4 m, Fig 8.7<br>*e* = 2.323 x 10^-3 m, Fig 8.8, 8.9, 8.10 | *I* = 2.426 x 10^-7 m^4 |
| $c_1$ = 0, Fig 8.7<br>$c_1$ = 0.0001119 m, Fig 8.8<br>$c_1$ = 0.0004441 m, Fig 8.9<br>$c_1$ = 0, Fig 8.10 | $c_2$ = 0, Fig 8.7<br>$c_2$ = 0.0003526 m, Fig 8.8<br>$c_2$ = 0.0002357 m, Fig 8.9<br>$c_2$ = 0.0004774 m, Fig 8.10 |
| $K_{1,2}$ = 1.136 x 10^6 N/m | *E* = 207 x 10^9 N/m^2 |
| $L_{1,2}$ = 0.06148 m | *a* = 0.318 m |
| f = 0.328 m | |

**Table 8.2,** Parameter values used for numerical studies

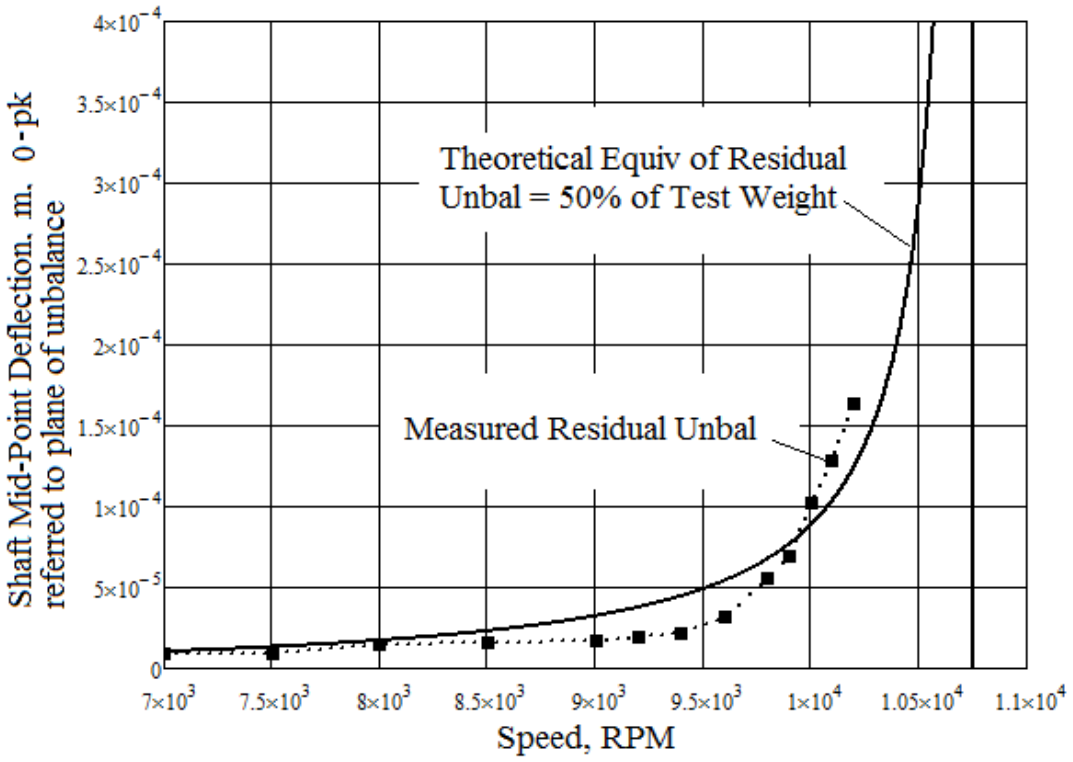


**Figure 8.7,** Estimation of Equivalent Theoretical Level of Shaft Residual Unbalance

8.3.2.2, Results from test TP.4**:** Test Weight Unbalance with Zero Correction

The levels of shaft mid-point deflections resulting from test TP.4**:** Shaft Test Weight Unbalance with Zero Correction (without balance compensation), are shown in Table 8.3.

| Speed, kRPM | 7.0 | 7.5 | 8.0 | 8.5 | 9.0 |
|---|---|---|---|---|---|
| Meas'd Defl'n, pk-pk, mm | 0.11 | 0.12 | 0.17 | 0.22 | 0.25 |
| Ang Offset, θ deg | 40 | 41 | 43 | 42 | 41 |
| Defl'n in Unbal Plane, 0-pk, mm | 0.025 | 0.028 | 0.042 | 0.052 | 0.058 |

| Speed, kRPM | 9.2 | 9.4 | 9.6 | 9.8 | 9.9 | 10.0 |
|---|---|---|---|---|---|---|
| Meas'd Defl'n, pk-pk, mm | 0.27 | 0.33 | 0.33 | 0.45 | 0.55 | 0.73 |
| Ang Offset, θ deg | 40 | 40 | 49 | 53 | 56 | 54 |
| Defl'n in Unbal Plane, 0-pk, mm | 0.06 | 0.074 | 0.096 | 0.143 | 0.186 | 0.237 |

**Table 8.3,** Test Weight Unbalance Shaft Deflections for steady state speeds

8.3.2.3, Results from test TP.5**:** Test Weight Unbalance with LHS + RHS compensation

The levels of shaft mid-point and sleeve deflections, resulting from test TP.5**:** Shaft Test Weight Unbalance with LHS + RHS Compensation, are shown in Table 8.4a and Table 8.4b, respectively.

| Speed, kRPM | 7.0 | 7.5 | 8.0 | 8.5 | 9.0 |
|---|---|---|---|---|---|
| Meas'd Defl'n, pk-pk, mm | 0.11 | 0.12 | 0.14 | 0.14 | 0.14 |
| Ang Offset, θ deg | 18 | 29 | 22 | 17 | 13 |
| Defl'n in Unbal Plane, 0-pk, mm | 0.004 | 0.016 | 0.010 | 0.004 | 0.0 |

| Speed, kRPM | 9.2 | 9.4 | 9.6 | 9.8 | 10.0 |
|---|---|---|---|---|---|
| Meas'd Defl'n, pk-pk, mm | 0.16 | 0.20 | 0.16 | 0.23 | 0.35 |
| Ang Offset, θ deg | 20 | 18 | 26 | 31 | 37 |
| Defl'n in Unbal Plane, 0-pk, mm | 0.009 | 0.007 | 0.017 | 0.035 | 0.070 |

**Table 8.4a** Test Weight Unbalance Shaft Deflections with LHS + RHS Compensation for steady state speeds

| Measurements at 10,000 RPM | | |
|---|---|---|
| | LHS Sleeve | RHS Sleeve |
| Meas'd Defl'n, pk-pk, mm | 0.24 | 0.40 |
| Ang Offset, θ deg | -13 | -75 |
| Defl'n in Unbal Plane, 0-pk, mm | 0.053 | 0.20 |
| Moment in Unbal Plane, Nm | 3.74 | 13.97 |

**Table 8.4b** Test Weight Unbalance Sleeve Deflections with LHS + RHS Compensation for steady state speeds

8.3.2.4, Results from test TP.7**:** Test Weight Unbalance with mainly LHS compensation

The levels of shaft mid-point and sleeve deflections resulting from test TP.7**:** Shaft Test Weight Unbalance with mainly LHS Compensation, are shown in Table 8.5a and Table 8.5b, respectively.

| Speed, kRPM | 7.0 | 8.0 | 8.5 | 8.8 |
|---|---|---|---|---|
| Meas'd Defl'n, pk-pk, mm | 0.10 | 0.12 | 0.12 | 0.12 |
| Ang Offset, θ deg | 17 | 12 | 8 | -5 |
| Defl'n in Unbal Plane, 0-pk, mm | 0.003 | -0.002 | -0.006 | -0.019 |

| Speed, kRPM | 9.0 | 9.4 | 9.8 | 10.0 |
|---|---|---|---|---|
| Meas'd Defl'n, pk-pk, mm | 0.10 | 0.12 | 0.19 | 0.26 |
| Ang Offset, θ deg | 16 | 15 | 21 | 17 |
| Defl'n in Unbal Plane, 0-pk, mm | 0.0022 | 0.0016 | 0.012 | 0.008 |

**Table 8.5a** Test Weight Unbalance Shaft Deflections with mainly LHS Compensation for steady state speeds

8.3.2.5, Results from test TP.9**:** Test Weight Unbalance with RHS only compensation

The levels of shaft mid-point and sleeve deflections resulting from test TP.9**:** Shaft Test Weight Unbalance with RHS Only Compensation, are shown in Table 8.6a and Table 8.6b, respectively.

| Measurements at 10,000 RPM | | |
|---|---|---|
| | LHS Sleeve | RHS Sleeve |
| Meas'd Defl'n, pk-pk, mm | 0.53 | 0.28 |
| Ang Offset, θ deg | -81 | -83 |
| Defl'n in Unbal Plane, 0-pk, mm | 0.26 | 0.14 |
| Moment in Unbal Plane, Nm | 18.4 | 9.70 |

**Table 8.5b** Test Weight Unbalance Sleeve Deflections with mainly LHS Compensation for steady state speeds

| Speed, kRPM | 7.0 | 7.5 | 8.0 | 8.5 | 9.0 |
|---|---|---|---|---|---|
| Meas'd Defl'n, pk-pk, mm | 0.11 | 0.12 | 0.15 | 0.14 | 0.11 |
| Ang Offset, θ deg | 30 | 20 | 23 | 21 | 22 |
| Defl'n in Unbal Plane, 0-pk, mm | 0.016 | 0.007 | 0.012 | 0.009 | 0.008 |

| Speed, kRPM | 9.2 | 9.4 | 9.6 | 9.8 | 10.0 |
|---|---|---|---|---|---|
| Meas'd Defl'n, pk-pk, mm | 0.13 | 0.14 | 0.10 | 0.13 | 0.20 |
| Ang Offset, θ deg | 26 | 25 | 30 | 42 | 45 |
| Defl'n in Unbal Plane, 0-pk, mm | 0.014 | 0.014 | 0.014 | 0.031 | 0.052 |

**Table 8.6a** Test Weight Unbalance Shaft Deflections with RHS Only Compensation for steady state speeds

| Measurements at 10,000 RPM | | |
|---|---|---|
| | LHS Sleeve | RHS Sleeve |
| Meas'd Defl'n, pk-pk, mm | 0.031 | 0.60 |
| Ang Offset, θ deg | 4 | -101 |
| Defl'n in Unbal Plane, 0-pk, mm | 0.0025 | 0.27 |
| Moment in Unbal Plane, Nm | 0.18 | 19.07 |

**Table 8.6b** Test Weight Unbalance Sleeve Deflections with RHS Only Compensation for steady state speeds

### 8.3.3 Bearing Reaction Loads

Although bearing reaction loads have not been directly measured during these tests, assessments of their condition can be made from the results given above. Figure 8.8 shows measurements of shaft mid-point deflections, pk – pk mm, resulting from tests TP.4 to TP.10: (Test Weight Unbalance, with and without balance compensation) in their plane of measurement without any vector angle adjustment. Hence, disregarding the external effect of the applied balancing sleeve CF on the reaction loads, these provide a good approximation of the relative magnitudes of the corresponding reaction loads that are seen by the shaft end bearings resulting from the shaft's bending/ internal shear forces.

It is also noted that these tests are conducted primarily to validate the theoretical analysis of balancing sleeve compensation determined in earlier chapters, and as a consequence the level of compensation has not been optimised to minimise the reaction loads. Nevertheless, it is evident that significant load reductions have occurred and that further reductions would be possible by increased levels of compensation.

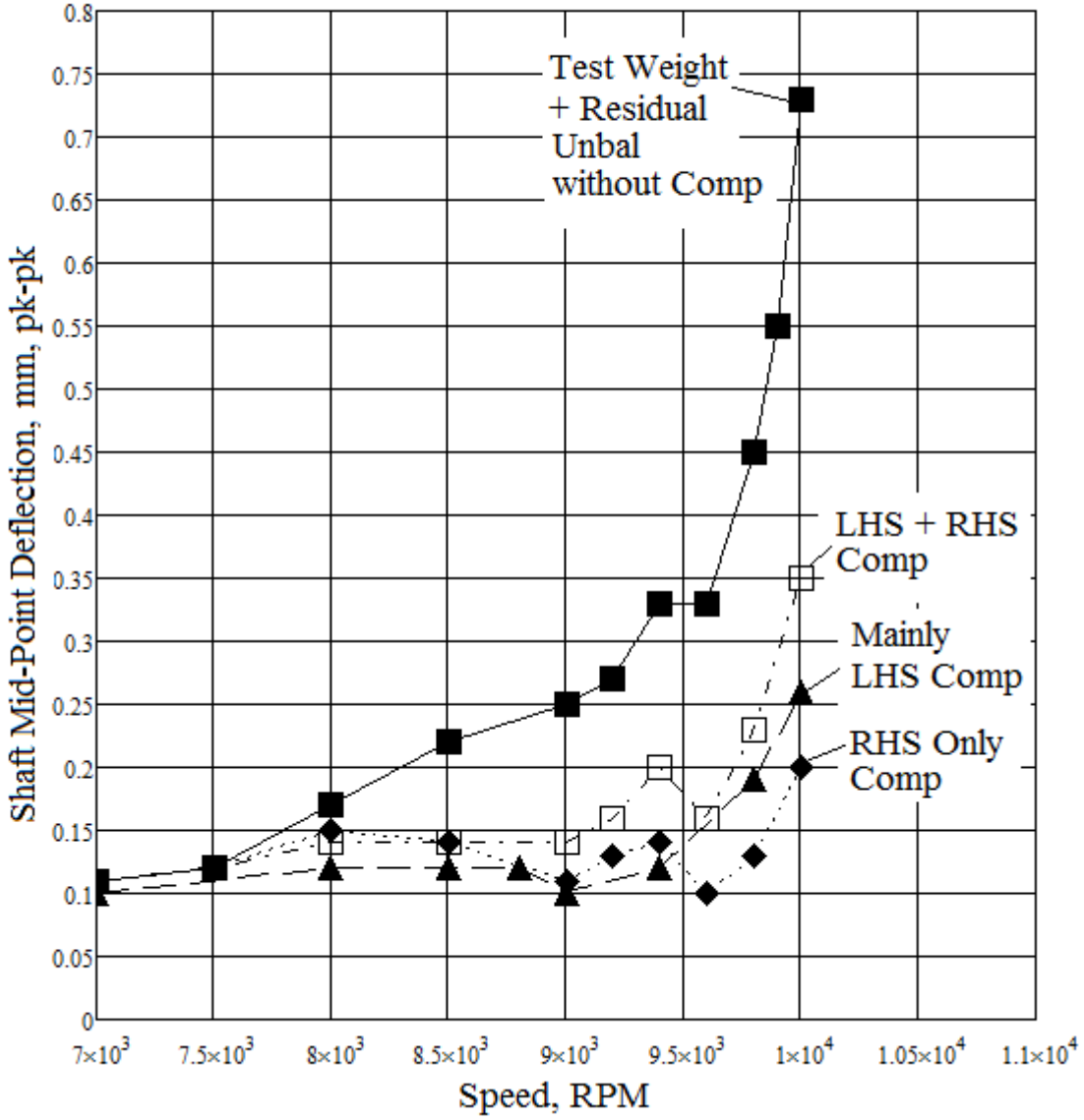


**Figure 8.8,** Comparison plots of Shaft Deflections, in their plane of measurement, with and without Balance Compensation

### 8.3.4 Test and Theoretical Comparisons

To provide a valid comparison between theoretical shaft deflections and their corresponding test results, the theoretical values of the LHS and RHS compensating moments, *Mo1* and *Mo2*, are matched to their respective test quantities. The test moments are determined from the sleeve deflections, at 10,000 rpm, (adjudged to be sufficiently close to the critical speed for comparison with the required moment for its elimination/ nullification), multiplied by the sleeve stiffness and its length.

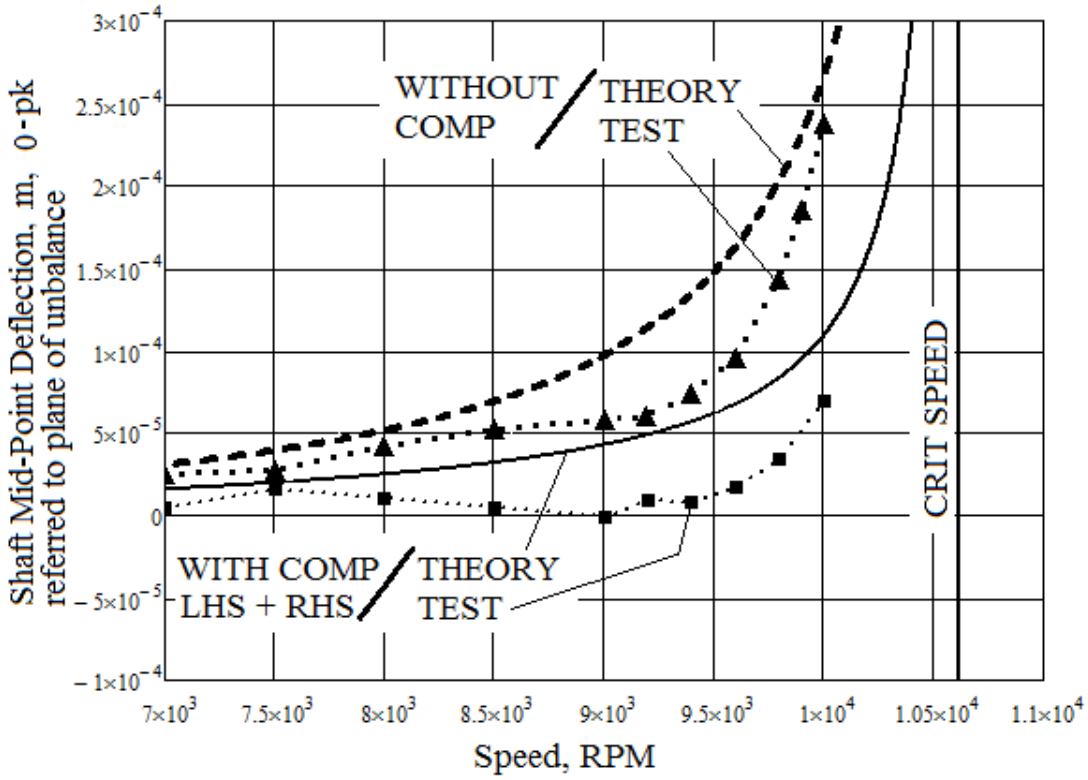


**Figure 8.9,** Comparison of Theoretical and Test levels of LHS + RHS Balance Compensation, CR = 0.654

Figure 8.9 shows the results of test TP.4, Shaft Test Weight Unbalance with Zero Correction and test TP.5 - Double Sleeve Compensation, LHS + RHS, together with their respective theoretical displacements.

The measured moments and theoretically matched values are as follows:

Test: *Mo1* = 3.74 Nm, *Mo2* = 13.97 Nm, Total = 17.71 Nm

Theory: *Mo1* = 3.72 Nm, *Mo2* = 13.88 Nm

Compensation Ratio = 0.654, see below.

To assess the level of compensation achieved during the tests, a Compensation Ratio is defined as:

Compensation Ratio, $CR = \frac{\text{test moments, } Mo1 + Mo2}{\text{max compensation moment}}$

where the maximum compensation moment (approximate moment for critical speed elimination) is the calculated sum of both moments determined by proportionally increasing the moments until near nullification is obtained, as shown in Figure 8.10, leading to:

*Mo1* = 6.37 Nm, *Mo2* = 20.73 Nm, Total = 27.1 Nm.

The total value is theoretically a constant for all the balance compensation tests, (as established in Chapter 4), and Figure 8.10 is typical of the theoretical levels of shaft deflection for all these tests if subjected to maximum compensation.

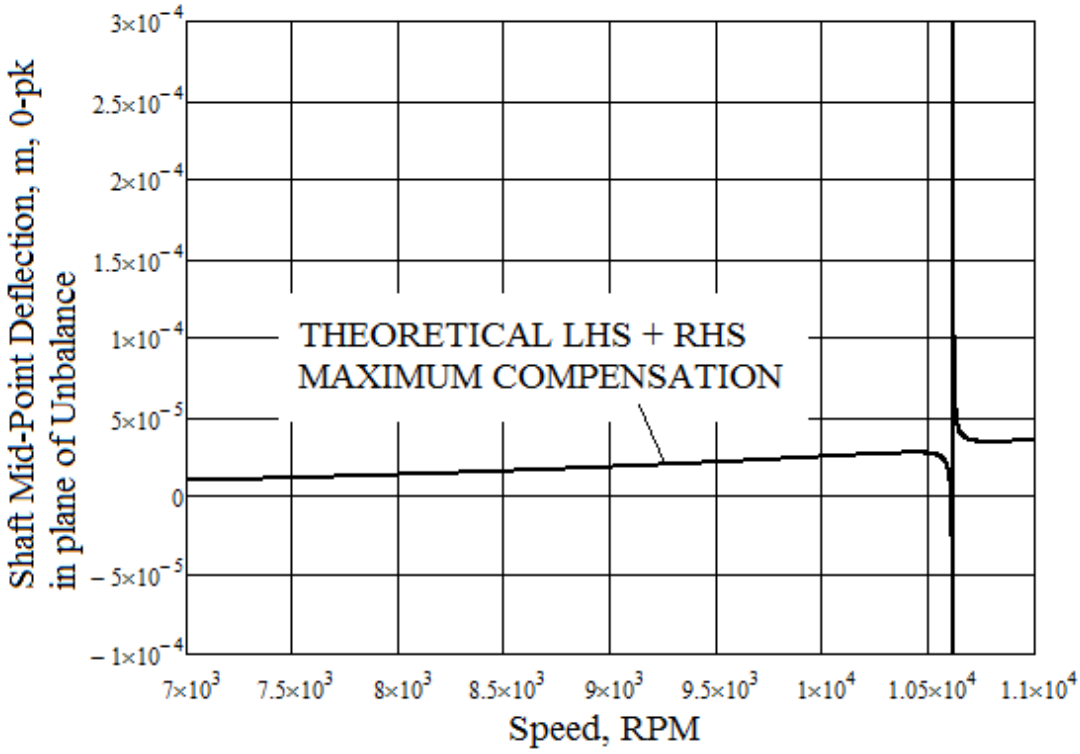


**Figure 8.10,** Theoretical LHS + RHS with maximum Balance Compensation, *CR* = 1.0

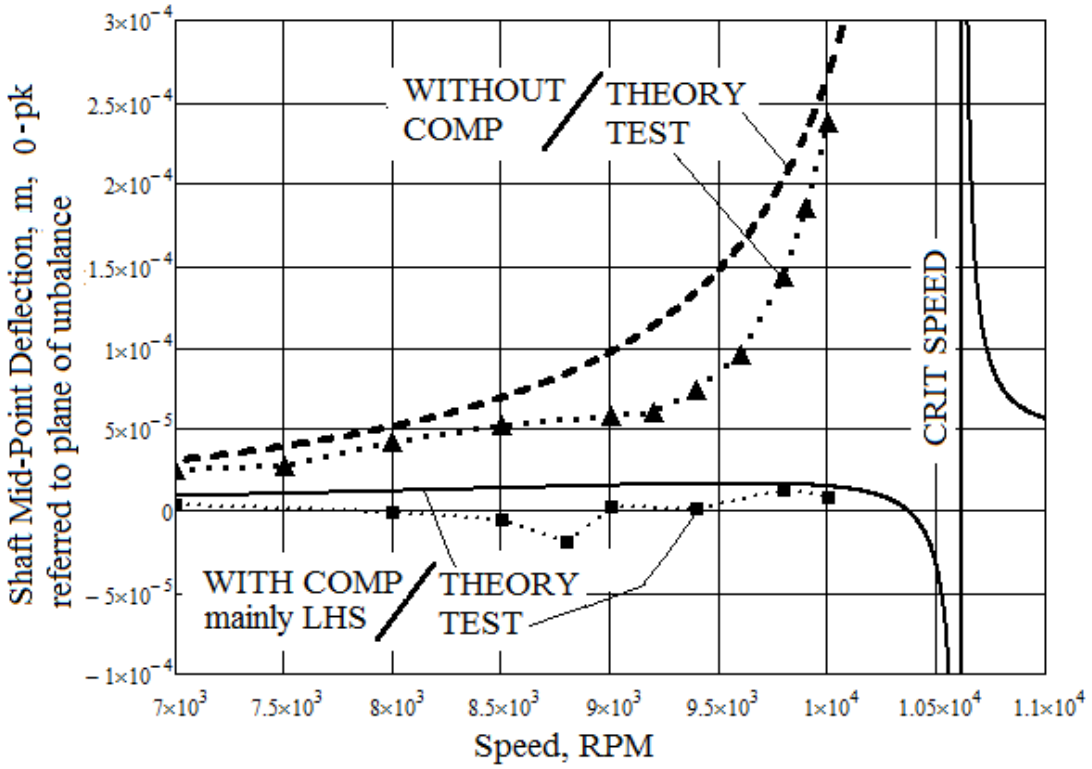


**Figure 8.11,** Comparison of Theoretical and Test levels of mainly LHS Balance Compensation, *CR* = 1.037

Figure 8.11 shows results from test TP.4, Shaft Test Weight Unbalance with Zero Correction and test TP.7 - Single Sleeve Compensation, mainly LHS, (since some residual unbalance existed in the RHS) together with their respective theoretical displacements.

The measured moments and theoretically matched values are as follows:

Test: *Mo1* = 18.4 Nm, *Mo2* = 9.7 Nm, Total = 28.1 Nm

Theory: *Mo1* = 18.41 Nm, *Mo2* = 9.74 Nm

Compensation Ratio = 1.037

Figure 8.12 compares the same test results of Figure 8.11 with their theoretical equivalents without compensation, first with standard shaft eccentricity, (concentrated unbalance = 101.25 g.mm, as per previous

calculations) and secondly with only 1/25$^{th}$ of standard eccentricity (concentrated unbalance = 4.05 g.mm).

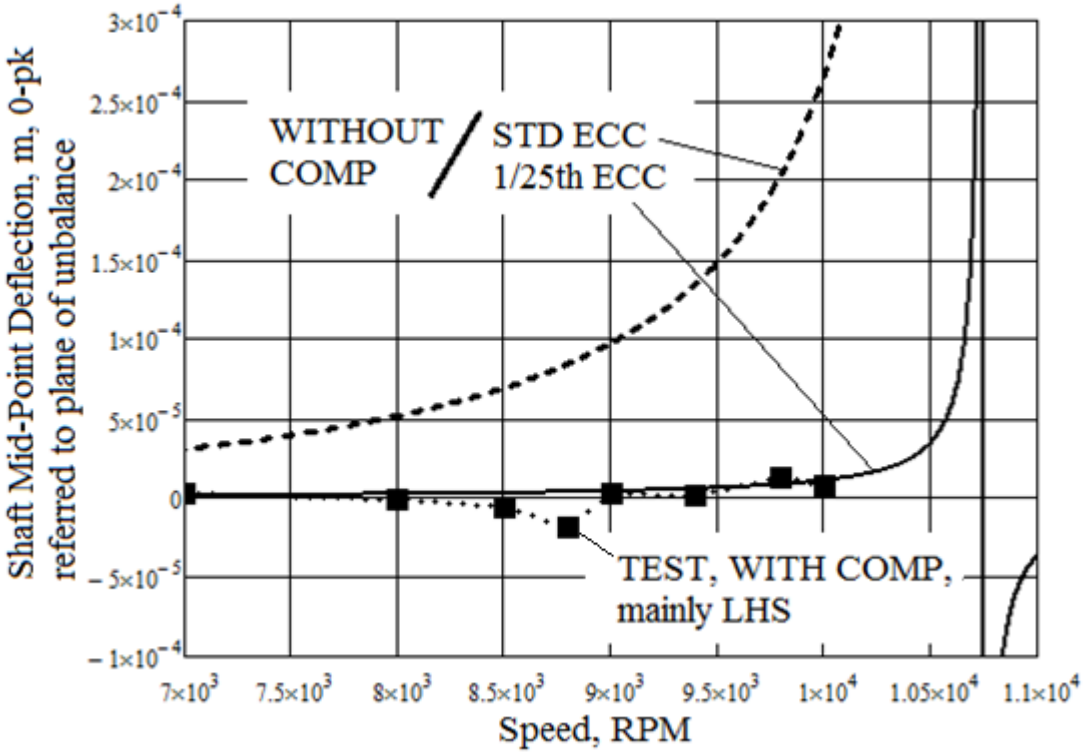


**Figure 8.12,** Comparison of Test levels of mainly LHS Balance Compensation, *CR* = 1.037, with theoretical cases of Standard Eccentricity and 1/25$^{th}$ reduced Eccentricity

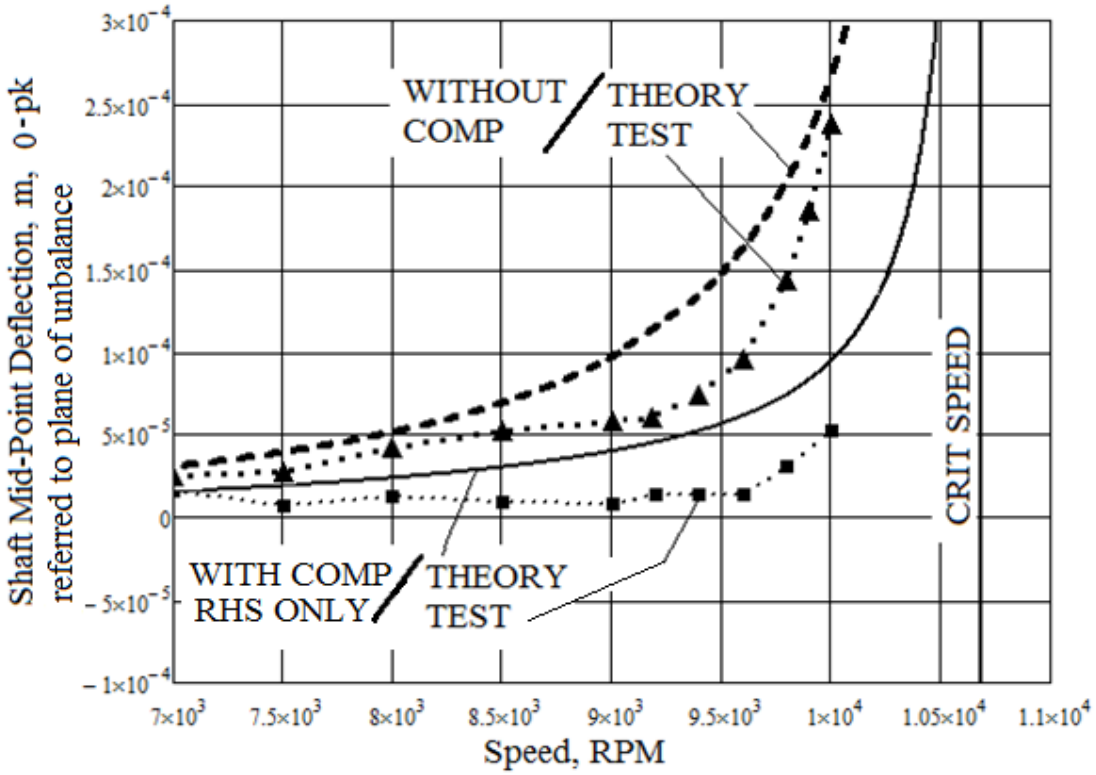


**Figure 8.13,** Comparison of Theoretical and Test levels of RHS Only Balance Compensation, *CR* = 0.710

Figure 8.13 shows the results of test TP.4, Shaft Test Weight Unbalance with Zero Correction and test TP.9 - Single Sleeve Compensation, RHS only, together with their respective theoretical displacements.

The measured moments and theoretically matched values are as follows:

Test: *Mo1* = 0.18, *Mo2* = 19.07 Nm, Total = 19.25 Nm

Theory: *Mo1* = 0, *Mo2* = 19.22 Nm

Compensation Ratio = 0.710

For clarity, Measured Moments and the Compensation Ratio for each test trial are given in Table 8.7.

| TEST | MEASURED MOMENTS At 10,000 rpm | | | COMPENSATION RATIO, *CR* |
|---|---|---|---|---|
| | *Mo1* | *Mo2* | Total | |
| TP.2, Residual unbalance only | 0 | 0 | 0 | 0 |
| TP.4 Residual + Test Weight | 0 | 0 | 0 | 0 |
| TP.5, as TP.4 with LHS + RHS Comp. | 3.74 | 13.97 | 17.71 | 0.654 |
| TP.7 as TP.4 with mainly LHS Comp. | 18.4 | 9.7 (resid-ual) | 28.1 | 1.037 |
| TP.9, as TP.4 with RHS Only Comp. | 0.18 (resid-ual) | 19.07 | 19.25 | 0.710 |
| TP.11, as TP.2, Fast Transit thro' Critical Speed | 0 | 0 | 0 | 0 |

**Table 8.7**. Test Details and Compensation Ratio

Figure 8.14 shows the results of test TP.11 – determination of the critical speed. The laser output shows shaft mid-point deflection versus time recorded during a rapid transit of the critical speed. It clearly shows two critical speeds produced by both positive and negative gyroscopic moments, resulting from disc like action of the sleeve balancing rings. These are relatively small, agreeing with the assumptions made in the theoretical analysis of Section 2.3 and is confirmed by the narrow speed band between them, ($1^{st}$ = 10,384 rpm, $2^{nd}$ = 11,093 rpm).

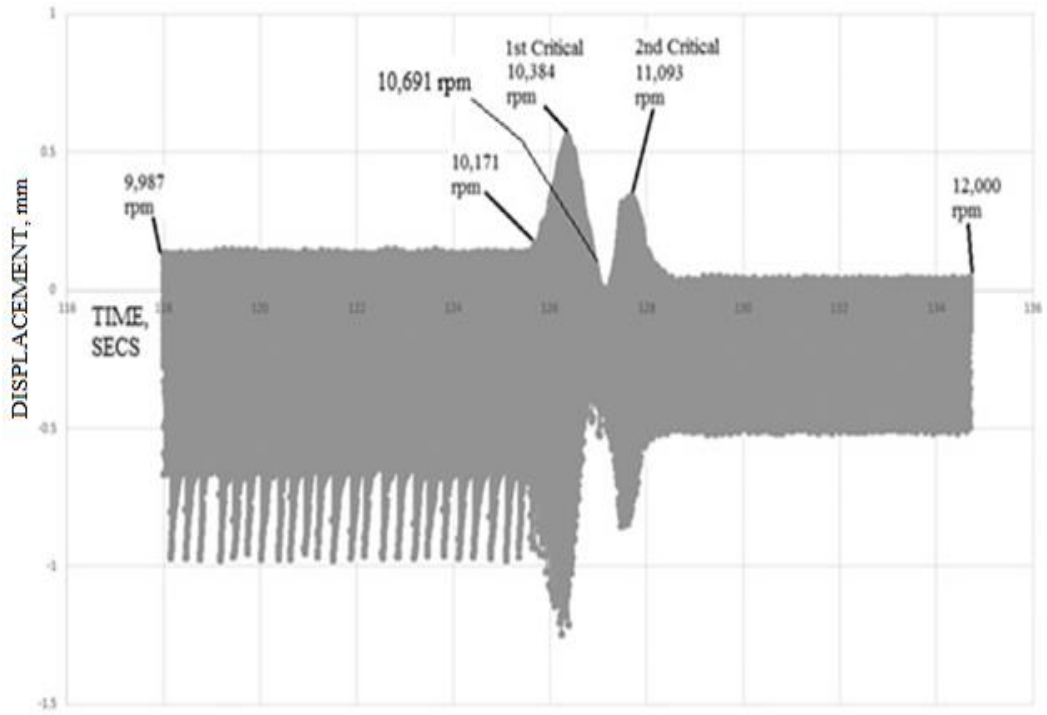


**Figure 8.14,** Rapid Transit of Critical Speeds

The approximate mean value, 10,750 rpm, is used to determine the shaft length of the mathematical model, $\ell$ = 970 mm, for the theoretical calculations, as this is the assumed critical speed with zero gyroscopic action.

Figure 8.15 is a close up of Figure 8.14, just either side of the 1st critical speed, and shows that the laser trigger point/ TDC position rotates approximately 180º through this time period as the shaft speed increases from 10,171 rpm, through the 1st critical speed, to 10,691 rpm. Standard dynamic theory of rotating shafts [62], shows that the phase angle between the unbalance excitation force and the shaft response (position of maximum deflection) is always 90º at the critical speed, but that the speed band between approximately zero and 180º phase angles varies with damping ratio; being theoretically zero for systems without damping. The narrowness of the speed band shown in Figure 8.15 therefore confirms that there is very

little damping in the test set-up, and consequently the measurement orientation shown in Figure 8.4 is fit for purpose.

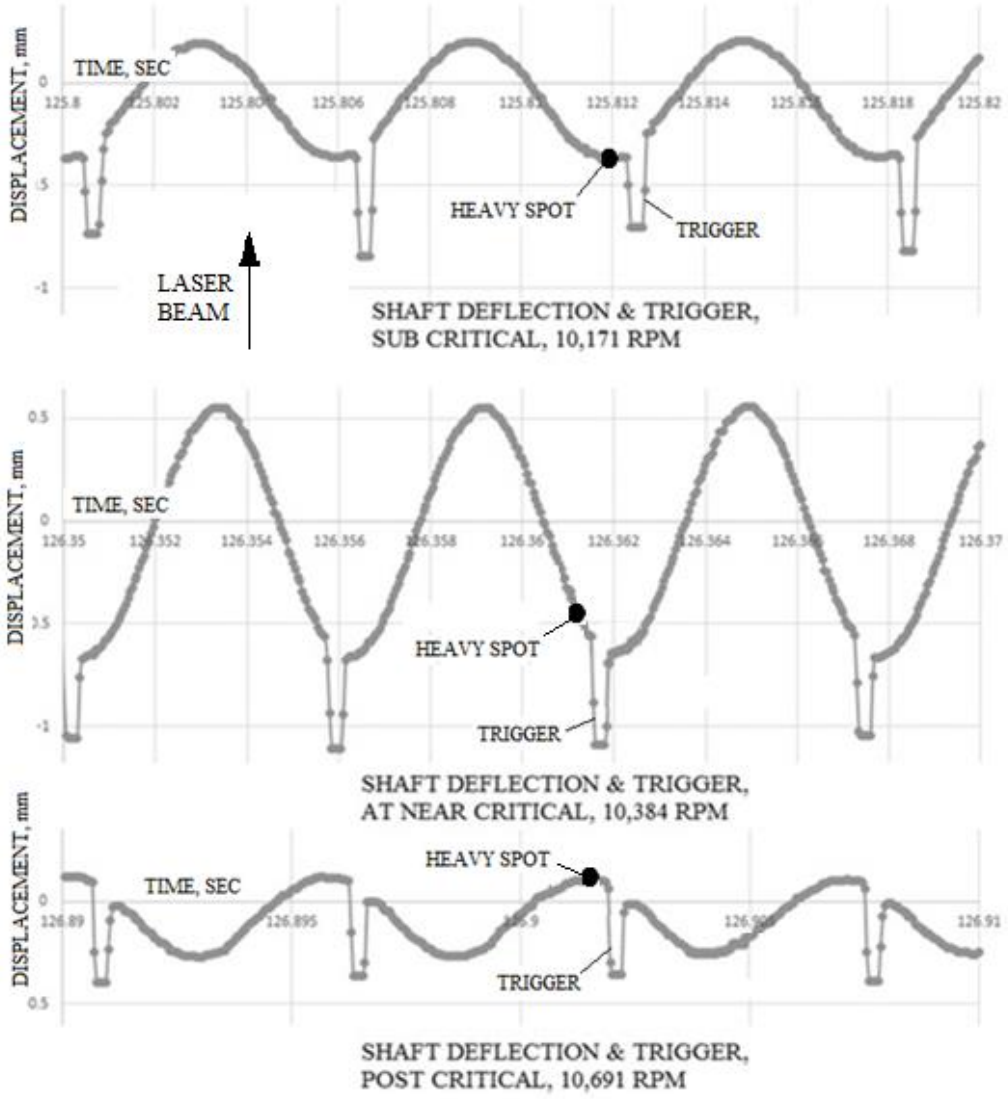


**Figure 8.15,** Trigger Rotation through the 1st Critical Speed

## 8.4 Preliminary Conclusions

Tests are conducted with the primary aim of checking the practical validity of the theory/conclusions resulting from the preceding chapters and are therefore not optimised for maximum possible balance compensation in this

instance. However, it is possible to draw very strong conclusions from the results, namely:

1. Tests including balance sleeve compensation, Figure 8.9, Figure 8.11 and Figure 8.12, show that the shaft mid-point deflections have been reduced from their zero balance condition without compensation as speed increases up to the maximum test speed of 10,000 rpm, (93% of the mean critical, 96% of the 1$^{st}$ forward mode). Consequently, it has been demonstrated that balance sleeve compensation definitely performs as expected and the condition of shaft balance is improved.

2. The preceding tests show a good correlation between reductions in shaft deflection and their corresponding Compensation Ratio, *CR*, such that the closer *CR* is to 1.0, the less bending of the shaft occurs and the better the condition of shaft balance. Figure 8.11 with *CR* = 1.037 is particularly significant, having near maximum compensation and a very close alignment with predicted theory. Hence, the tests strongly support the principle of the new balancing methodology of aligning the sum of the sleeve balancing moments to the sum of the equivalent encastre fixing moments.

3. Figure 8.13, with RHS (only) balance compensation (the small LHS compensating moment, due of residual imbalance within the balancing ring is of negligible proportions) confirms the conclusions of Chapter 4 that compensation/ balance adjustment need only be applied at one end of a shaft.

4. Figure 8.12, shows that when compensation is close to maximum, *CR* = 1.037, the balance condition is equivalent to reducing the amount of residual unbalance by 1/25$^{th}$ of its original value. This test confirms the theoretical analysis given in Chapter 5, reference: Shear

Force Reaction Ratio, *RR*, Figure 5.2 and the equivalent reduction in standard eccentricity, shown in Figure 5.16. Chapter 5 also shows that the Reaction Ratio, *RR*, is independent of shaft eccentricity such that the benefits of encastre simulation apply to any pre-determined level of residual eccentricity. It is therefore concluded that these balancing gains should be possible even on previously balanced shafts. Therefore, the potential exists to vastly reduce shaft imbalance and hence to safely operate high-speed machinery much closer to its lateral critical speed than is currently allowed.

# Chapter 9

## 9.1 Conclusions

This research resulted from industrial balancing problems encountered by certain turbine/ compressor packages, employing flexible, high-speed coupling shafts; which determined the need for an examination into currently available balancing techniques, coupled with an investigation into possible ways of reducing the consequentially high level of reaction loads imposed on shaft bearings.

The work successfully formulated the requirements of a new balancing technique with the potential to vastly reduce the reaction loads imparted on shaft end bearings, and it has also uncovered several beneficial insights into the controlling mechanism of the methodology.

Chapter 2 showed that by applying trim balance correction directly onto rotating shafts, as per existing balancing methodologies, that their effectiveness reduces with increased shaft speed/ bending deflection. This is because the rotational radius of their mass centroid, remains either constant, or possibly reduces, depending on its lengthwise position along the shaft, whereas the equivalent radius of shaft imbalance increases. Hence, a balancing error is created, as a result of the rigidity of the trim balance mass.

To counter this problem, chapter 2 further describes a new concept of adding compliance to a trim balancing mechanism such that amplification of the correcting forces occurs by the use of a pair of compensating balancing sleeves. This also has the added benefit of imparting balancing moments onto the shaft, acting to reduce its deflection. This effect is investigated by dynamic analysis of a simply supported, high-speed, plain, flexible shaft,

with uniform eccentricity, which concluded that considerable reductions in both reaction loads and shaft deflection are possible.

It is also shown that the balancing moments enable the theoretical elimination of the 1st classical, critical speed and chapter 3 shows that nullification of a neighbouring compensating critical speed is also possible by closely matching the balancing moments to the fixing moments of an equivalent encastre mounted shaft. This requirement then forms the essence of a new balancing methodology whereby reaction loads and shaft deflections are reduced by the process of encastre simulation.

Further insights are revealed by the analysis given in Chapters 4, which shows that it is the sum of the balancing moments that produce nullification and this can be achieved by the use of a single compensating balance sleeve fitted at either end of the shaft, thereby replicating a single encastre shaft.

The applicability of the new methodology to the majority of practical shafts, with any distribution of concentrated imbalances and/ or multiple discs, provided they are mounted within the central 80% of the shaft length, is demonstrated in chapter 5.

Further, analysis of the shear force reaction ratio, *RR,* showed it to be independent of the shaft eccentricity, hence the reduction in the equivalent shaft eccentricity, made possible by this methodology, is in addition to any balance reductions that may have been made prior to encastre simulation; for example by, component and/ or assembly balancing procedures. It is shown that these reductions are as high as 25x at operations close to the 1st critical speed, hence, extremely low levels of equivalent eccentricity are possible.

Chapter 5, also shows that the magnitude of a Simulation Ratio, *SR,* provides a good indication of shaft stiffening effects produced by balance sleeve compensation and hence, that double encastre simulation, could be beneficially applied to shafts operating at higher critical speeds.

The potential balancing improvements and practical insights revealed in these chapters are strongly supported by the validating test results reported in chapter 8. These confirm that:

1. shaft mid-point deflections and by association, shaft end reaction loads can be considerably reduced by applying balancing sleeve compensation,

2. the Compensation Ratio, *CR* is a good indicator of shaft balance, such that the closer *CR* is to 1.0, the less bending of the shaft occurs, confirming the requirement to closely align the sum of the sleeve balancing moments to the sum of the equivalent encastre fixing moments,

3. balance compensation/ adjustment can be successfully performed at a single shaft end,

4. with compensation close to its maximum (test value *CR* = 1.037) the balance condition is equivalent to reducing the amount of residual unbalance by 1/25$^{th}$ of its original value.

It is therefore concluded that balancing sleeve compensation has been proven to work satisfactorily under laboratory conditions, but further work would be required if commercial acceptance is to be obtained, requiring site testing of a full sized prototype.

It is realised that encastre simulation, by application of balancing sleeve moments, could be achieved by a large variety of designs and bending mechanisms. Hence, it is possible that different drive train arrangements would be better served by a particular balancing sleeve design, some examples of which are discussed below.

For external application, high bending stiffness of a large, tubular sleeve can be problematic and its reduction by machining of axial slots, to produce a number of spars, as per the test shaft, may not be the best method. As an alternative, many composite designs are possible, including materials with a lower Young's Modulus, such as plastic, titanium, aluminium etc., combined with an inbuilt, heavier material, balancing ring.

A further patented alternative [120] shown in Figure 9.1, makes use of laminated, flexible, disc elements, item (95), as commonly used in high speed drive coupling applications, (as per the test shaft). These are therefore of proven design and are commercially available in several pack sizes so that the bending stiffness could be set accordingly by varying the number of laminations. The method of element fastening is a standard feature of these types of flexible couplings to allow for angular misalignment and is therefore an ideal, low cost method of adding an angular stiffness component to the balancing sleeve (97). Hence, it is not necessary to reduce the bending stiffness of the sleeve as in previous designs for external applications.

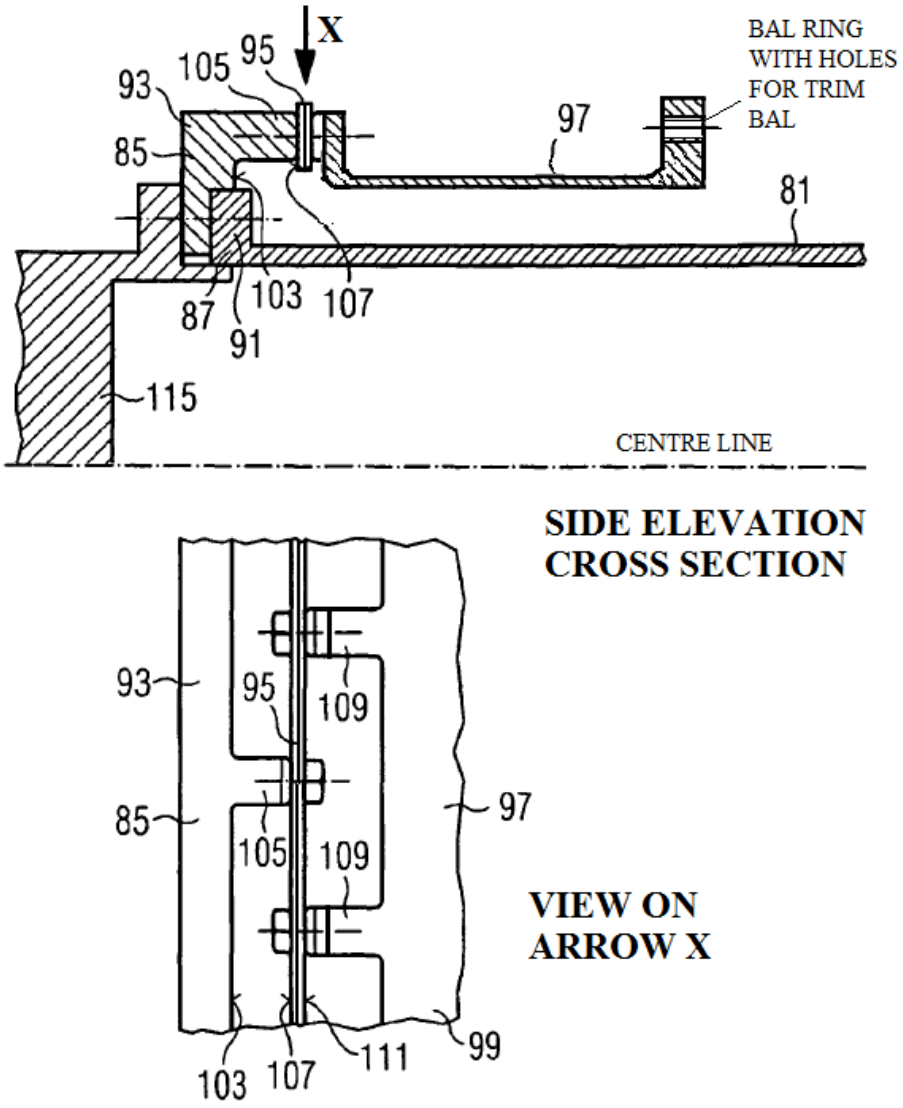


**Figure 9.1,** Alternative Balancing Sleeve Design for external application

Where space is available, designs for internal applications, preferably with external adjustment, would appear to be advantageous, offering zero additional windage (drag caused by shaft rotation) and because of the reduction in sleeve diameter, lower bending stiffness. One such patent pending design [124] is shown in Figure 9.2.

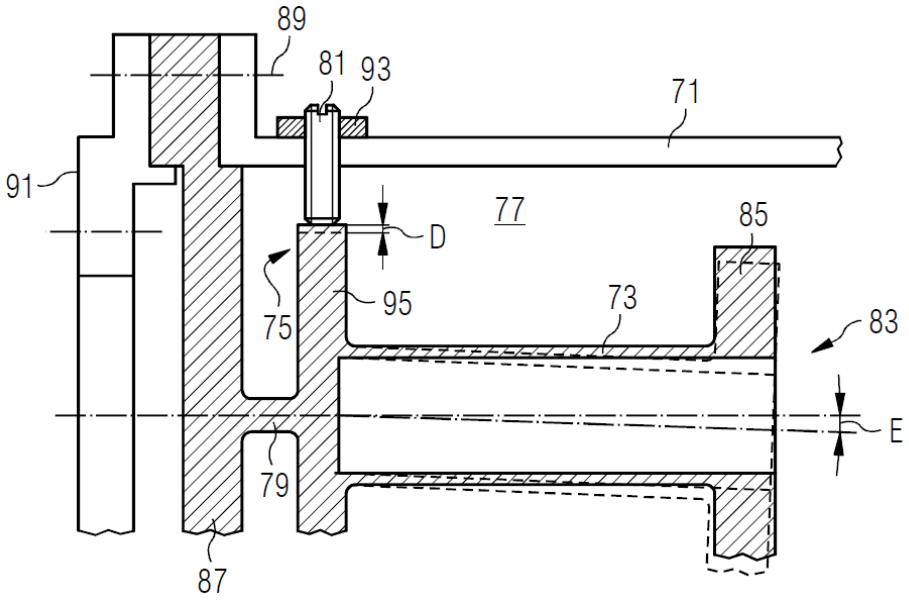


**Figure 9.2,** Alternative Balancing Sleeve Design for internal application

In this design external adjustment is achieved via 3 or 4 off screws (81) positioned equally around spacer tube (71), which are set to produce an offset, E, of the balance ring (85) by forcibly causing partial bending of the thin neck (79). The centrifugal force acting on the balance ring eccentricity, offset, E, then causes bending of the sleeve (73) as speed increases in the normal manner.

This design lends itself nicely to remote operation of low energy, permanent magnet stepper motors, as shown in Figure 9.3, and energised by a non-contacting, inductive supply (not shown). The motors simply take the place of the adjusting screws (81) in Figure 9.2 and are locked in place when de-energised by the holding torque of the permanent magnets. Since many modern drive trains are already remotely monitored for bearing vibration and balance condition, the possibility of remote balance adjustment would appear to be a very desirable addition feature and a next evolutionary step.

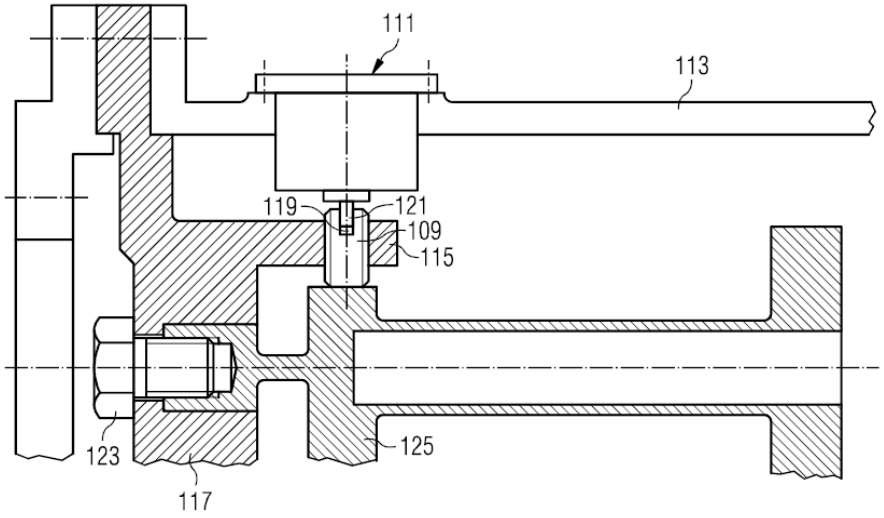


**Figure 9.3,** Remotely Operated Balancing Sleeve Design for internal application

The above Figures are regarded as possible examples for future development and are not definitive designs. Also, they are based mainly on long, flexible coupling shafts because of their association with lateral balancing problems. Therefore, it would appear to be sensible to continue the acceptance programme, initially in this direction. However, it is expected that, in time, balancing sleeve compensation will prove useful to many types of flexible shafting within any machinery that would benefit from being able to operate with reduced lateral critical speed margins and from reduced shaft bending deflection/ blade tip clearance. As such it should be possible to extend a machine's operating speed range, reduce component wear and improve overall operating efficiency. Hence, this should be applicable to a wide variety of machines in all sectors of industry and it is envisaged that future development will also be extended to any flexible, high-speed, component shafts, of such machines.

## References


[1] Dunkerley S. On the Whirling and Vibration of Shafts. Phil Trans Roy Soc , London, Series A 1894;185.

[2] Jeffcott HH. The lateral vibration of loaded shafts in the neighbourhood of a whirling speed. - The effect of want of balance. Philosophical Magazine 1919;6:37:304-314.

[2a] Cerminaro A.M. Simulation of Internal Damping in a Rotating System supported by Magnetic Bearings. MSc Thesis, Tuffs University, 1999.

[3] Rankine W. On the Centrifugal Force of Rotating Shafts. Engineer, London 1869;247:249.

[4] Prabhakar S, Sekhar A.S, Mohanty A.R. Vibration analysis of a misaligned rotor-coupling-bearing system passing through the critical speed. Proc Instn Mech Engrs Vol 215, 2001.

[5] Stodola A. Steam and gas turbines. McGraw-Hill, New York. English translation, 1927.

[6] Campbell W. The protection of steam-turbine disk wheels from axial vibration. Trans. ASME, 1924.

[7] Kimball, A. L. Vibration preventionin engineering. J. Wiley & Sons. London 1932

[8] Newkirk B.L. Shaft whipping/ rubbing/ whirling. General Electric Rev. 27,28. 1924-1926.

[9] Nelson F. Damping in structural analysis and design, impact and friction solids, structures and machines. Birkhauser In Press, 1999.

[10] Kramer E. Dynamics of rotors and foundations. Springer-Verlag Berlin Heidelberg. 1993.

[11] Dimarogonis A. D. Analytical methods in rotor dynamics. Applied science publishers, London, 1983.

[12] Ehrich F.F. Shaft whirling induced by rotor internal damping. Journal of applied mechanics. 1964.

[13] Robertson D. Hysteretic influences on whirling of rotors. Proc. Of the Inst. Of Mech. Eng. 1935.

[14] Smith D.M. The motion of a rotor carried by a flexible shaft in flexible bearings. Proc. Royal Society, London. 1933.

[15] Special Purpose Couplings for Petroleum, Chemical and Gas Industry Services. API Standard 671. 4th ed. 2007

[16] Mancuso J.R. The manufacturer's world of coupling potential unbalance. Kop-Flex Emerson Power Transmission Corp, JRM 10.PDF. 1985 circa.

[17] ISO 1940-1:2003. Balance quality requirements for rotors of constant (rigid) state.

[18] ISO 1940-2:1997. Mechanical vibration. Balance quality requirements for rigid rotors. Balance errors.

[19] Gas turbines for the petroleum, chemical and gas industry services. API 616. 4th ed. 1998.

[20] Recommended practice for packaged combustion gas turbines. API RP 11PGT:1992

[21] 100 years of balancing technology, Schenck USA, www.schenck-usa/company/information/history.php

[22] ISO 5406-1980. The mechanical balancing of flexible rotors.

[23] ISO 7919-4 2nd Edition 2009-10-01 Mechanical Vibration – Evaluation of machine vibration by measurements on rotating shafts : Part 4 Gas turbines sets with fluid-film bearings.

[24] ISO 10816-4 2nd Edition 2009-10-01 Mechanical Vibration – Evaluation of machine vibration by measurements on non-rotating shafts : Part 4 Gas turbines sets with fluid-film bearings.

[25] Bishop R. Gladwell G. The vibration and balancing of an unbalanced flexible rotor. *IMechE Part C: J Mechanical Engineering Science* 1959; 1: 66-77

[26] Bishop R. The Vibration of Rotating Shafts. *IMechE Part C: J. Mechanical Engineering Science* 1959; 1: 50-65

[27] Corcoran JP. What is Acceptable Coupling Lateral Critical Speed? *Turbomachinery International* 2003; May/ June: 18-21.

[28] Garvey SD, Friswell MI, Williams EJ, Care ID. Robust balancing for rotating machines. *IMechE Part C: J Mechanical Engineering Science* 2002; 216: 1117-1130.

[29] Gladwell G, Bishop R. The vibration of rotating shafts in flexible bearings. IMechE Part C: J Mechanical Engineering Science 1959;1:195-206.

[30] Hylton PD. Low Speed Balance for Supercritical Shafting in Gas Turbines. *Proceedings of ASME Turbo Expo 2008: Power for Land, Sea and Air*, Berlin, Germany, 9-13 June 2008; Paper Number GT2008-50077. New York: ASME.

[31] Morton PG. Modal balancing of flexible shafts without trial weights IMechE Part C:J Mechanical Engineering Science 1985;199:71-78.

[32] Parkinson AG. Balancing of rotating machinery. *IMechE Part C: J Mechanical Engineering Science* 1991; 205: 53-66.

[33] Parkinson A.G, Bishop R.E.D. Residual vibration in modal balancing. Journal Mechnical Science. 1965

[34] Yu JJ. On two plane balancing of symmetric rotors. Proceedings of ASME Turbo Expo 2012 2012

[35] Genta G. Dynamics of Rotating Systems, Springer, Mechanicak Engineering Series, 2005

[36] Sergio G. Torres Cedillo. Unbalanced identification and balancing of nonlinear rotordynamic systems. Proc of ASME Turbo Expo, GT2014-25290

[37] Genta G, Silvagni M. On centrifugal softening in finite element method rotordynamics, Journal of applied mechanics. ASME Jan 2004 Vol 81/ 011001-1

[38] Nelson F. Rotor dynamics without equations. Int journal of COMADEM, 10(3) july 2007,PP.2-10

[39] Nandi A, Neorgy S. Modelling of rotors with three-dimensional solid finite elements. Journal of strain analysis. Vol 36. No4. 2001.

[40] Black H.G. Lateral vibration of shafts having radial symmetry and appreciable gyro action. Journal of mechanical engineering science. Vol 6, 1964.

[41] Saldarriaga M. V, Steffren V, Hagopian J, mahfoud J. On the balancing of flexible rotating machines by using an inverse problem approach. Journal of vibration and control. 2010

[42] Lees A.W, Friswell M.I. The evaluation of rotor imbalance in flexibly mounted machines. Journal of sound and vibration. 1997.

[43] Xiaofeng L, Longxi Z, Zhenxia L. Balancing of rotors without trial weights based on finite element modal analysis. Journal of sound and vibration. 2012.

[44] El-Shafei A,El-Kabbany A.S, Younan A.A. Rotor balancing without trial weights. Trans ASME, July 2004.

[45] Racic Z, Hidalgo J. Practical balancing of flexible rotors for power generation. Proc ASME 2007 Int Des Eng Tech Conf. DETC2007-34333.

[46] Nicholas J.C, Gunter E.J, Allaire P.E. Effect of residual shaft bow on unbalance response and balancing of a single mass flexible rotor. Journal of engineering gas turbines power. 1976.

[47] Edwards S, Lees A.W, Friswell M.I. Fault diagnosis of rotating machinery. Shock and vibration digest. 1998.

[48] Gunter E.J, Barrett L.E, Allaire P.E. Balancing of multimass flexible rotors. Proc. 5th Turbomachinery Symposium. 1976.

[49] Sinha J.K, Friswell M.I, Lees A.W, Sinha R.K. Robust method for the rotor unbalance estimation. Proc. VECTOMAC-2, 2002.

[50] Thearle E.L. Dynamic balancing of rotating machinery in the field. Proc. ASME 1934.

[51] Zhao Q.L, Wang H.Q, Yao J.F. A novel method of dynamic balance weighting for single-disc rotor system. WSEAS trans. On systems. 2012.

[52] Kellenberger W. Should a flexible rotor be balanced in N or (N+2) planes. Journal Manuf. Sci. Eng. 1972.

[53] Hundal M.S, Harker R.J. Balancing of flexible rotors having arbitrary mass and stiffness distribution. Journal of Engineering for Industry. 1966.

[54] Zang C, Lees A.W, Friswell M.I. Multi plane balancing of a rotating shaft using a single transducer. IFToMM 6th Conference on Rotor Dynamics. 2002

[55] Goodman T.P. A least squares method for computing balance corrections. ASME Journal of Engineering for Industry. 1964

[56] Green R.B. Gyroscopic effects on the critical speeds of flexible rotors. Journal Applied Mechanics, trans. Amer. Soc. Mech. Engrs. 1948

[57] Saravanamuttoo HIH. Rogers GFC. Cohen H. Straznicky PV. *Gas Turbine Theory.* 6th ed. Harlow: Pearson Education Limited 2009

[58] Thomson WT. *Mechanical Vibrations*. 4th ed. London: Chapman & Hall 1996

[59] Friswell M, Penney J, Garvey S, Lees A. *Dynamics of rotating machines*. New York: Cambridge University Press, 2010.

[60] Rhyder GH. Strength of Materials. 3rd ed. Basingstoke: Macmillan Press. 1992.

[61] Timoshenko S, Young DH, Weaver Jr W. Vibration problems in engineering. : John Wiley and Sons, 1974

[62] Wilcox JB. *Dynamic Balancing of Rotating Machinery*. London: Pitman. 1967.

[63] De Jong F.M.Application of a heat barrier sleeve to prevent synchronous rotor instability, Proc Turbomachinery Symposium, 1998

[64] Sloetjes P.J. Vibration reduction and power generation with piezoceramic sheets mounted to a flexible shaft. Journal of Intelligent Material Systems and Structures, Vol. 19, Jan 2008

[65] Marin M.A. Rotor dynamics of overhung rotors: hysteretic dynamic behavior. Proc of ASME Turbo Expo, GT2012-68285

[66] Al-Khazali H.A, Askari M. Modal analysis design to exposure gyroscopic effect in rotating machinery using experimental and analytical/ computational techniques. Int journal Eng Science & tech, (IJEST), Vol 3, Sept 2011.

[67] Feese T.D, Grazier P.E. Balance this! Case histories from difficult to balance jobs. Proc Turbomachinery Symposium, Sept 2004.

[68] Childs D.W, Vance J.M. Annular gas seals and rotordynamics of compressors and turbines. Proc Turbomachinery Symposium, 1997.

[69] Zhang Q. Study of the stiffness loss and its affecting factors of the spline joint used in rotor systems. Proc of ASME Turbo Expo, GT2014-26876

[70] Weimeng MA. Dynamic analysis of asymmetric rotor bearing system based on three dimensional finite element method. Proc of ASME Turbo Expo, GT2014-25304

[71] Dutt J.K, Nakra B.C. Dynamics of rotor shaft system on flexible supports with gyroscopic effects. Mech Research Communications, Vol 22, 1995. Pergamon.

[72] Sinou J.J, Villa C, Thouverez F. Experimental and numerical investigations of a flexible rotor bearing supports. Int journal of rotating machines. 2005:3

[73] Werner U. Mathematical rotordynamic model regarding excitation due to elliptical shaft journals in electrical motors considering the gyroscopic effect. Applied Mathematics, 2013, 4, 57-74. Scientific Research.

[74] Greenhill L.M. Lease V.J. Additional investigations into natural frequencies and critical speeds of a rotating, flexible shaft-disk system. Proc of ASME Turbo Expo, GT2007-28065

[75] Edwards S, Lees A.W, Friswell M.I. The influence of torsion on rotor/ stator contact in rotating machinery. Journal of sound and vision. 1999

[76] Madden R.J, Sawicki J.T, Pesch A.H. Model validation for identification of damage dynamics. Proc of ASME Turbo Expo 2014, GT2014-27341

[77] Wu X, Meagher J. A two-disc extended Jeffcott rotor model distinguishing a shaft crack from other rotating asymmetries. Int journal of rotating machinery. 2008.

[78] Chattoraj C. Whirling of a rotor on isotropic shaft considering gyroscopic effects and asymmetric bearing stiffness. NaCoMM-09Paper ID: DVAMCC1.

[79] Shiau T.N. Nonlinear dynamic study on effects of rub-impact caused by oil rupture in a multi-shaft turbine with a squeeze damper. Proc of ASME Turbo Expo, GT2014-27221

[80] Zilli A. Non-linear dynamics of a simplified model of an overhung rotor subjected to intermittent annular rubs. Proc of ASME Turbo Expo, GT2014-26826.

[81] Wang C. Study of stiffness loss and the dynamic influence on rotor system of the bolted flange joint. Proc of ASME Turbo Expo, GT2014-26191

[82] Aleyaasin M, Ebrahimi M, Whalley R. Multi-mass rotating shaft analysis and identification. IMechE Part K: Proc Instn Mech Engrs Vol 213, 1999

[83] De Jong F.M, Morton P.G. The synchronous instability of a compressor rotot due to bearing journal differential heating. Trans ASME Vol 118, Oct 1996

[84] Whalley R, Ebrahimi M, Abdul-Ameer A. High-speed rotor-shaft systems and whirling identification. IMechE Part C: J. Mechanical Engineering Science 2007, Vol 221

[85] Swanson E, powell C.D, Weissman S. A practical review of rotating machinery critical speeds and modes. Sound and Vibration, May 2005.

[86] Tadeo A.T, Cavalca K.L, Brennan M.J. Dynamic characterization of a mechanical coupling for a rotating shaft. IMechE Part C: J. Mechanical Engineering Science 2010, Vol 225

[87] Varun Kumar M, Ashiwini kumar B. Model analysis of axially symmetric linear rotating structures. Int Journal of Eng & Advanced Technology, (IJEAT). Vol-2, Iss-4 April 2013.

[88] Mushi S.E, Lin Z, Allaire P.E, Evans S. Aerodynamic cross-coupling in a flexible rotor: control design and implementation. 11th Int Symposium on magnetic bearings. Aug 26-29, Nara, Japan.

[89] Adams M.L. Rotating machinery vibration from analysis to troubleshooting. New York. Marcel Dekker Inc. 2001.

[90] Rao J.S. A note on Jeffcott warped rotor. Mechanism and machine theory. Pergamon. Jan 2001.

[91] Mushi S.E, Lin Z, Allaire P.E. Design, construction and modeling of a flexible rotor active magnetic bearing test rig. Proc of ASME Turbo Expo, GT2010-23619.

[92] Samantaray A.K. Steady-state dynamics of a non-ideal rotor with internal damping and gyroscopic effects. Nonlinear Dyn (2009) 56:443-451, DOI 10.1007/s11071-008-9413-8, Sprnger.

[93] Rodrigues DJ. Champneys AR, Friswell MI, Wilson RE. Automatic balancing of a rigid rotor with misaligned shaft. *Applied Mechanics and Materials* 2006; 5-6: 231-236

[94] Jerzy T. Sawicki. Stability of cracked rotor subjected to parametric excitation. Proc of ASME Turbo Expo, GT2014-26741

[95] Horst H.G., Wolfel H.P. Active vibration control of a high speed rotor using PZT patches on the shaft surface. Journal of Intelligent Material Systems and Structures, Vol. 15, Sept 2004.

[96] Greenhill L.M, Cornejo G.A.Critical speeds resulting from unbalance excitation of backward whirl modes. Design Eng Tech Conf. Vol 3-Part B, ASME 1995.

[97] Gosiewski Z. Analysis of coupling mechanism in lateral/ torional rotor vibrations. Journal of theoretical and applied mechanics. 2008

[98] Zhou S, Shi J. Active balancing and vibration control of rotating machinery: A survey. The shock and vibration digest. Vol 33. No 4. 2001.

[99] Saldarriaga M. V, Steffren V. Balancing of flexible rotors without trial weights by using optimisation techniques. Proc of COBEM 2003

[100] Alauze C, Der Hagopian J, Gaudiller L. Active balancing of turbomachinery: application to large shaft lines. Journal of vibration and control. 2001.

[101] Ehyaei J, Moghaddam M.M. Dynamic response and stability analysis of an unbalanced flexible rotating shaft equipped with n automatic ball-balancers. Journal of sound and vibration. 2008.

[102] Rodrigues D, Champneys A, Friswell M, Wilson E. A consideration of support asymmetry in an automatic ball balancing system. ENOC 2008.

[103] Foppl. A, Das problem der Laval'schen turbinenwelle. Civil Ingenieur, 1895.

[104] Levine W. S. Control Systems fundamentals. CRC Press. 1999

[105] Nataraj C. vibration of mechanical systems. Cengage Learning. 2012.

[106] Green W.G. Theory of machines. Blackie & sons. London/ Glasgow. 1964.

[107] Muszynska A. Lateral-torsional vibrations of a rotor. BRDRC Report No. 2, 1984.

[108] Vance J. M. Rotodynamics of turbomachinery. John Wiley & Sons.1988

[109] Balachandran B, Magrab E.B. Vibrations. Cengage Learning. 2009.

[110] Broch J.T. Mechanical vibration and shock measurements. Bruel & Kjaer. 1980.

[111] McConnell K.G. Vibration testing, theory and practice. John Wiley & Sons. 1995.

[112] Langthjem M.A, Nakamura T. Dynamics of the fluid balancer: Perturbation solution of a forced Korteweg-de vries-burgers equation.

[113] Lees A.W, Sinha J.K, Friswell M.I. The identification of the unbalance of a flexible rotating machine from a single run-down. Proc of Turbo Expo, 2002, GT-2002-30420.

[114] Burrows CR. Keogh PS. Sahinkaya MN. Progress towards smart rotating machinery through the use of active bearings. *IMechE Part C: J Mechanical Engineering Science* 2009; 223: 2849-2859

[115] Yoon S.Y. Control of surge in centrifugal compressors by active magnetic bearings. Advances in industrial control, DOI 10.1007/978-1-4471-4240-9_2, Springer-Verlag London 2013

[116] Bonello P. Adaptive tuned vibration absorbers: design principles, cocepts and physical implementation. Vibration analysis and control - new trends and developments. Intech, 2011.

[117] Kirk A, Knowles G, Stewart J Bingham C. Mathematical development and modelling of a counter balance compensating sleeve for the suppression of lateral vibrations in high speed flexible couplings" *ASME Turbo Expo* San Antonio, TX, 3-7 June 2013; Paper number GT2013-95634. New York: ASME.

[118] Knowles G, Kirk A. Theoretical investigation into balancing high-speed flexible-shafts, by the use of a novel compensating balancing sleeve. *IMechE Part C: J Mechanical Engineering Science* 2013; Article No. 517376.

[119] Knowles G, Kirk A, Bingham C. Bickerton R. Generalised analysis of compensating balancing sleeves with experimental results from a scaled industrial turbine coupling shaft. IMechE Part C: Journal of Mechanical Engineering Science - submitted 2016; Knowles G, Kirk A, Bingham C, Bickerton R, - PENDING

[120] Knowles G. An apparatus comprising a shaft and a balancing sleeve. European Patent EP2226529B1. 2012.

[121] Knowles G. An apparatus comprising a shaft and a balancing sleeve. United States Patent US8556738B2. 2012.

[122] Knowles G. An apparatus comprising a shaft and balancing device. European Patent EP2568194A1. 2013.

[123] Knowles G. An apparatus comprising a shaft and a balancing device for balancing the shaft. European Patent EP2703689A1. 2014.

[124] Knowles G. An apparatus comprising a shaft and a compensator balancing sleeve for balancing the shaft. European Patent EP2806186A1. 2014.

# Appendix A

**Partial Fractions: Ref. Chapter 2, Section 2.3**

$$\bar{r} = \frac{b^4 e}{s(s^4 - b^4)} + \frac{A_1 s}{s^4 - b^4} + \frac{r_1 s^2}{s^4 - b^4} + \frac{A_2}{s^4 - b^4} \qquad (2.21a)$$

The Laplace equation for the combined assembly, (2.21a), can be expanded, by the use of Partial Fractions, so as to express each term into a standard Laplace form as follows:

For the 1st term, let:

$$\frac{b^4 e}{s(s^4 - b^4)} = \frac{b^4 e}{s(s^2 + b^2)(s + b)(s - b)} = \frac{A}{s} + \frac{Bs + C}{s^2 + b^2} + \frac{D}{s + b} + \frac{E}{s - b}$$

Then, equating numerators gives:

$$b^4 e = A(s^2 + b^2)(s + b)(s - b) + (Bs + C)s(s + b)(s - b) + Ds(s^2 + b^2)(s - b) + Es(s^2 + b^2)(s + b)$$

For s = b, $b^4 e = Eb(2b^2)(2b) = 4Eb^4 \qquad \therefore E = \frac{e}{4}$

For s = -b, $b^4 e = D(-b)(2b^2)(-2b) = 4Db^4 \quad \therefore D = \frac{e}{4}$

Equating $s^3$ terms, $0 = 0 + C - Db + Eb \qquad \therefore C = 0$

Equating $s^2$ terms, $0 = 0 - b^2 B + b^2 D + b^2 E \qquad \therefore B = \frac{e}{2}$

Equating $s^4$ terms, $0 = A + B + D + E \qquad \therefore A = -e$

Therefore, by substitution the 1st term of (Ex1) becomes:

$$\frac{b^4 e}{s(s^4 - b^4)} = \frac{-e}{s} + \frac{e/2\, s}{s^2 + b^2} + \frac{e/4}{s + b} + \frac{e/4}{s - b}$$

Similarly for 2nd term, let:

$$\frac{A_1 s}{s^4 - b^4} = \frac{A_1 s}{(s^2 + b^2)(s + b)(s - b)} = \frac{As + B}{s^2 + b^2} + \frac{C}{s + b} + \frac{D}{s - b}$$

To give:

$$A = -\frac{A_1}{2b^2}, \qquad B = 0, \qquad C = \frac{A_1}{4b^2}, \qquad D = \frac{A_1}{4b^2}$$

Therefore, by substitution the 2nd term equation becomes,

$$\frac{A_1 s}{(s^4 - b^4)} = \frac{-A_1/2b^2 . s}{s^2 + b^2} + \frac{A_1/4b^2}{s + b} + \frac{A_1/4b^2}{s - b}$$

Similarly for 3rd term, let:

$$\frac{s^2}{s^4 - b^4} = \frac{As + B}{s^2 + b^2} + \frac{C}{s + b} + \frac{D}{s - b}$$

to give: $A = 0, \quad B = \frac{1}{2}, \quad C = -\frac{1}{4b}, \quad D = \frac{1}{4b}$

and $$\frac{r_1 s^2}{s^4 - b^4} = \frac{1/2 . r_1}{s^2 + b^2} + \frac{-1/4b . r_1}{s + b} + \frac{1/4b . r_1}{s - b}$$

Similarly for 4th term, let:

$$\frac{1}{s^4 - b^4} = \frac{As + B}{s^2 + b^2} + \frac{C}{s + b} + \frac{D}{s - b}$$

to give: $A = 0, \quad B = -\frac{1}{2b^2}, \quad C = -\frac{1}{4b^3}, \quad D = \frac{1}{4b^3}$

and $$\frac{A_2}{s^4 - b^4} = \frac{-1/2b^2 . A_2}{s^2 + b^2} + \frac{-1/4b^3 . A_2}{s + b} + \frac{\frac{1}{4b^3} . A_2}{s - b}$$

By summing the 4 expanded terms and collating similar common denominators, (2.21a) is converted, as below, to standard Laplace form and suitable for inversion:

$$\bar{r} = \frac{-e}{s} + \frac{sP}{s^2 + b^2} + \frac{Q}{s^2 + b^2} + \frac{M}{s + b} + \frac{N}{s - b}$$

Where:

$$P = {}^{e}\!/_{2} - {}^{A_1}\!/_{2b^2} \qquad (2.22)$$

$$Q = {}^{1}\!/_{2}\, r_1 - {}^{A_2}\!/_{2b^2} \qquad (2.23)$$

$$M = {}^{e}\!/_{4} + {}^{A_1}\!/_{4b^2} - {}^{r_1}\!/_{4b} - {}^{A_2}\!/_{4b^3} \qquad (2.24)$$

$$N = {}^{e}\!/_{4} + {}^{A_1}\!/_{4b^2} + {}^{r_1}\!/_{4b} + {}^{A_2}\!/_{4b^3} \qquad (2.25)$$

# Appendix B

**Partial Fractions: Ref. Chapter 3, Section 2.2**

$$\bar{r} = \frac{b^4 e}{s(s^4 - b^4)} + \frac{s r_2}{s^4 - b^4} + \frac{r_3}{s^4 - b^4} \qquad (3.2)$$

Expanding equation (3.2) using Partial Fractions, as per Appendix A, to obtain standard Laplace forms, gives:

$$\frac{b^4 e}{s(s^4 - b^4)} = \frac{-e}{s} + \frac{e/2\, s}{s^2 + b^2} + \frac{e/4}{s + b} + \frac{e/4}{s - b} \qquad (B1)$$

$$\frac{s.r_2}{(s^4 - b^4)} = \frac{-r_2/2b^2 .s}{s^2 + b^2} + \frac{r_2/4b^2}{s + b} + \frac{r_2/4b^2}{s - b} \qquad (B2)$$

$$\frac{r_3}{s^4 - b^4} = \frac{-r_3/2b^2}{s^2 + b^2} + \frac{-r_3/4b^3}{s + b} + \frac{r_3/4b^3}{s - b} \qquad (B3)$$

By summing the 3 expanded terms and collating similar common denominators, (3.2) is converted, as below, to standard Laplace formation and suitable for inversion:

$$\bar{r} = \frac{-e}{s} + \frac{s.P_e}{s^2 + b^2} + \frac{Q_e}{s^2 + b^2} + \frac{M_e}{s + b} + \frac{N_e}{s - b}$$

(3.3)

Where: $P_e = e/2 - r_2/2b^2$ , $Q_e = -r_3/2b^2$ ,

$$M_e = e/4 + r_2/4b^2 - r_3/4b^3 \qquad N_e = e/4 + r_2/4b^2 + r_3/4b^3 \qquad (3.3a)$$

# Appendix C

## Hyperbolic Functions

For any angle x

Let $M\hat{e}^{-x} + N\hat{e}^{x} = G\cosh x + H\sinh x$ (C1)

But by definition: $\sinh x = \frac{\hat{e}^{x} - \hat{e}^{-x}}{2}$ giving $H\sinh x = \frac{H}{2}.\hat{e}^{x} - \frac{H}{2}.\hat{e}^{-x}$

Similarly: $\cosh x = \frac{\hat{e}^{x} + \hat{e}^{-x}}{2}$ giving $G\cosh x = \frac{G}{2}.\hat{e}^{x} + \frac{G}{2}.\hat{e}^{-x}$

Hence $G\cosh x + H\sinh x = \frac{H+G}{2}.\hat{e}^{x} + \frac{G-H}{2}.\hat{e}^{-x}$

Substitution in (C1) gives: $N = \frac{H+G}{2}$ and $M = \frac{G-H}{2}$

Hence $H = 2N - G$ and $2M = G - 2N + G$

So that $G = M + N$ and $H = N - M$ (3.4a)

# Appendix D

## D1: MOTOR/ GENERATOR DETAILS

**CONTROL TECHNIQUES**

Process Description / Control Philosophy
The Test Rig specification, in brief, comprises of a common bus system whereby only the accelerating torque
and losses need to be supplied by the mains.The motoring drive will be capable of generating the following
output shaft powers at the desired speeds, and will be capable of generating constant torque over the complete
speed range (i.e. constant torque from 0 - motor base speed).
Motoring Drive Output shaft capacity 49kW @ 7,320 RPM. ( Base Speed )
Loading Drive shaft capacity of 49kW @7,320 RPM ( Base Speed )
The control configuration will be commissioned with the Input Drive configured to mainly operate in speed
control, although the operation / functionality of the drives is easily re-configurable.
We acknowledge that the Test Rig Drive System will be controlled by the University by Lab view or similar
control.Ethernet communications has been provided to both drives for data collection , control and analysis.
We have allowed for emergency stop operation / timed safety relay and basic stop start functionality.

## Scope of Supply

## AC Drive & Control Cubicle Suite

**Item Qty Description**
**General CT Scope / Specification**
This Drive System will be fully engineered, manufactured and tested to **ISO9001:2000** (inc.BS5750 part2) at Control Techniques Telford Drive Centre, and will be supplied complete with set of CAD Schematic Diagrams, Drive and System Test Certificates and User Manuals.
The cubicle will be constructed of sheet steel to IP54/44 protection - Manufactured from floor standing type enclosures and will include a 100 or 200mm plinth as required. The layout arrangement will be designed for bottom cable entry and front access only unless specified differently on the order. - Cubicle finish painted to the standard RAL 7032 grey specification.
The cubicle suite overall dimensions will measure approximately : **2,200(H) x 800(W) x 500(D)mm.** Cubicle ventilation will be incorporated via door mounted cubicle fans and filtered louvers. Cubicle internal fluorescent lighting will be fitted complete with door activating switches. Cubicle internal equipment shrouding using clear Makralon is incorporated as standard to the high degree of IP2X British & European specifications.

**Main Incomer Section**
Main System Door Interlocking Isolator / Load Break Switch

- Mains Busbars & MCBs
- Cubicle Suite Cooling Fans & Filtered Louvers
- Main 110V AC control transformer with mcb protection
- Control Circuit Fusing
- Unidrive SP – SP4403 Motoring Drive
- Unidrive SP – SP4403 Loading Drive
- Ethernet modules ( x2 )
- SM Applications Plus Modules ( x2 )
- Main Contactor
- 24V DC Power Supply
- PSU Fusing
- Main System Preventa E-Stop fail safe module
- Auxiliary Supply MCBs / 3 Phase / 3 pole (as requisite)
- Control System Relays (4)
- Power on indicator
- Emergency Stop Function
- EMC Directives as standard
- Emergency stop rated braking resistor
- Drives Healthy
- Speed / Torque control selection

AC Drive & Control Cubicle Suite Photo ( Typical )

## Circuit Diagram

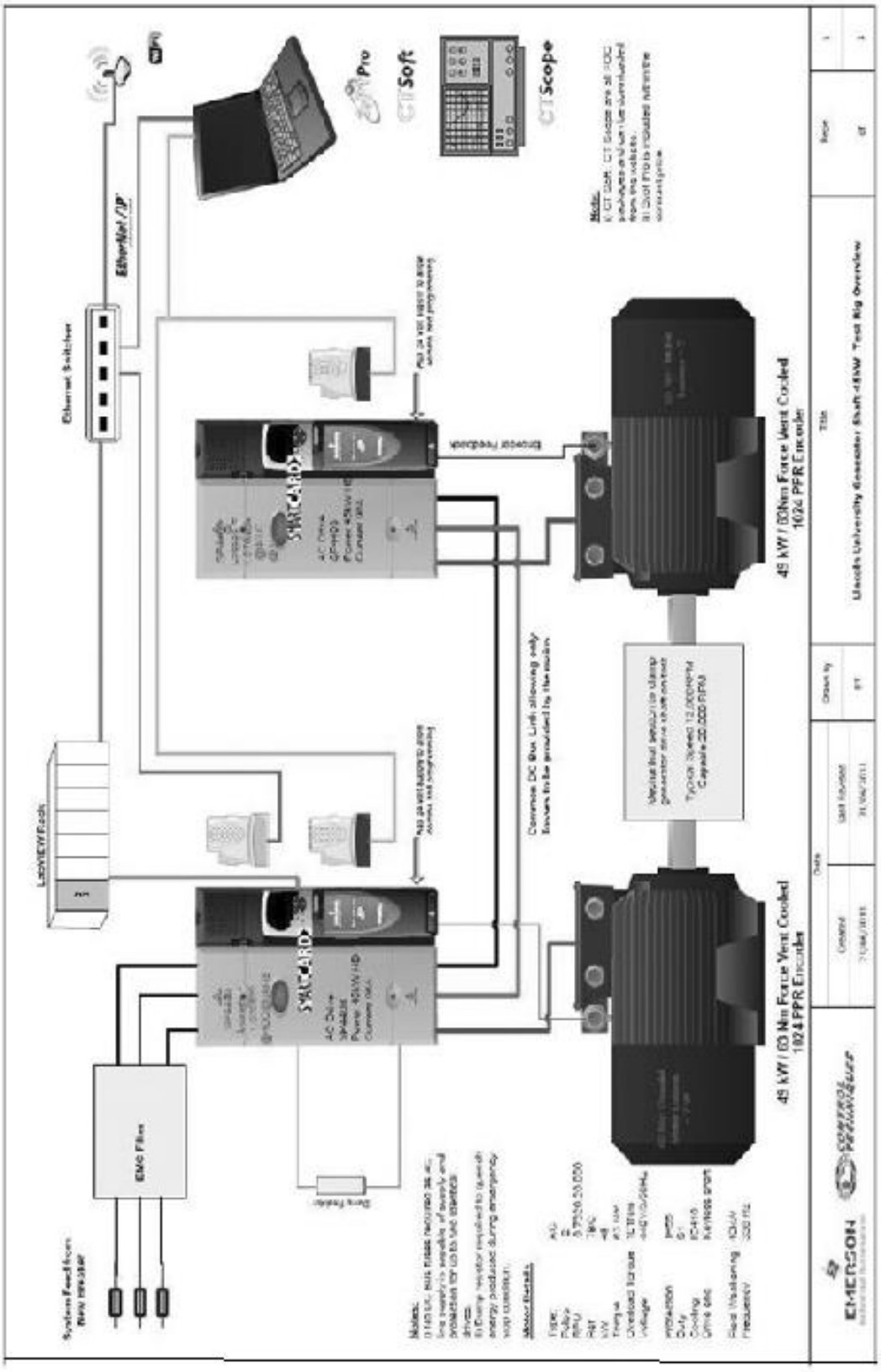

# AC Motor Details

Based on the supply of 2 off Oswald QDi13 2-2Fi
Type QDi13 2 2
Voltage 440 Volt
FLC 77A
Base Speed 7,320 RPM
Max Speed 20,000 RPM
Power 49kW
Frequency 123/326 Hz
Poles 2
IP Rating 23
Bearings Insulated
Encoder Heidenhaim 512 PPR TTL 5 V Quadrature

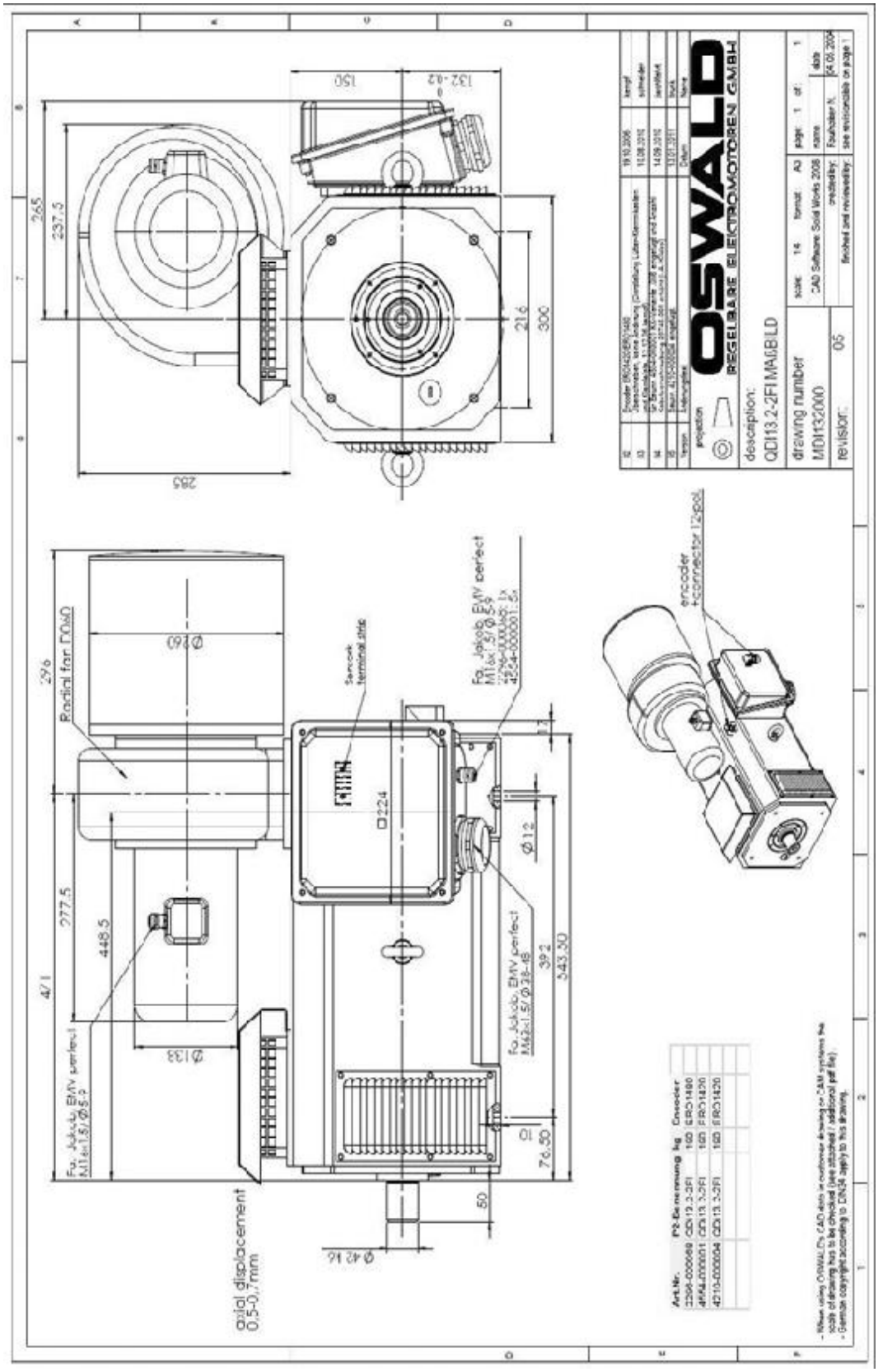
OSWALD
REGELBARE ELEKTROMOTOREN GMBH
description:
QDI13.2-2FIMAßBLD
drawing number
MDI132000
revision: 05
scale: 1:4
format: A3
page: 1 of: 1
CAD Software Solid Works 2008
name
date
checked by:
Faulhaber N.
24.05.2004
Revised and reviewed by:
see revision table on page 1
encoder
connector 12pol.
axial displacement
0,5-0,7mm
Fa. Jakob BMV serie
M16x1,5/Ø5,5
Fa. Jakob BMV serie
M16x1,5/Ø38,48
Radial fan Ø260
Ø260
Ø133
Ø224
Ø12
Ø42,16
265
237,5
285
150
132,42
21,6
300
296
471
277,5
448,5
392
343,50
76,50
50
Art.Nr.
Bezeichnung
kg
Encoder

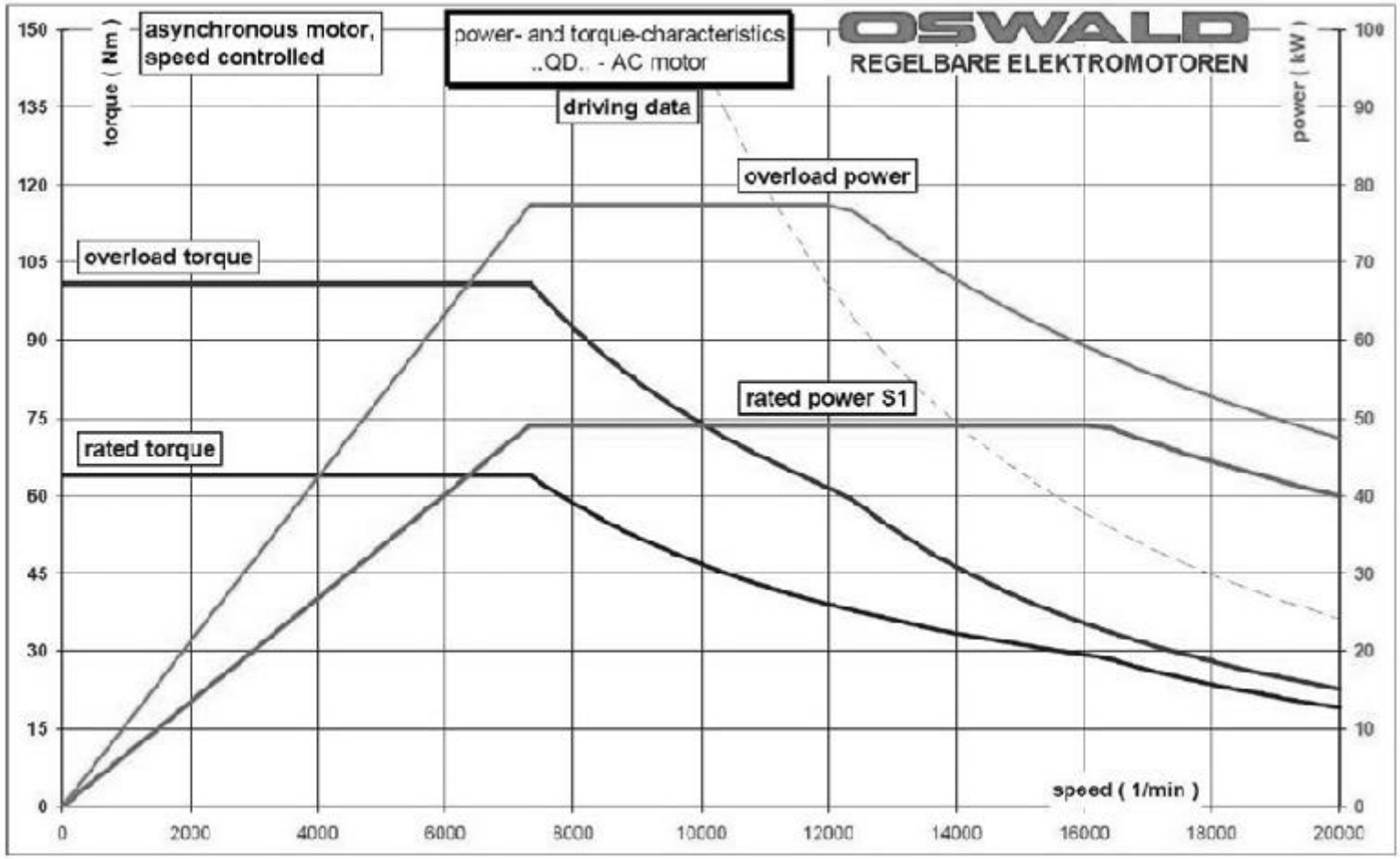
asynchronous motor,
speed controlled
power- and torque-characteristics
..QD.. - AC motor
OSWALD
REGELBARE ELEKTROMOTOREN
driving data
overload power
overload torque
rated power S1
rated torque
torque ( Nm )
power ( kW )
speed ( 1/min )
150
135
120
105
90
75
60
45
30
15
0
100
90
80
70
60
50
40
30
20
10
0
0
2000
4000
6000
8000
10000
12000
14000
16000
18000
20000

# D2: LASER MEASUREMENT DETAILS

**MICRO-EPSILON**

MICRO-EPSILON
MESSTECHNIK
GmbH & Co. KG
Königbacher Strasse 15

94496 Ortenburg / Germany

Tel. +49 (0) 8542 / 168-0
Fax +49 (0) 8542 / 168-90
e-mail info@micro-epsilon.de
www.micro-epsilon.com

MICRO-EPSILON

Certified acc. to DIN EN ISO 9001: 2008

EtherCAT® is registered trademark and patented technology, licensed by Beckhoff Automation GmbH, Germany.

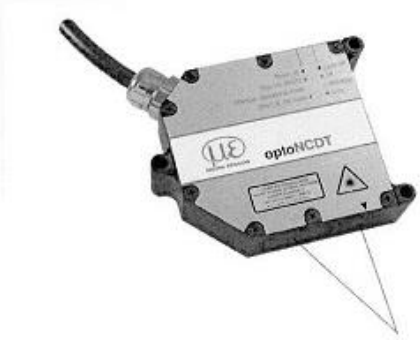


Instruction Manual
**optoNCDT 2300**

| | | | | |
|---|---|---|---|---|
| ILD 2300-2 | ILD 2300-50 | ILD2300-2LL | ILD2300-2BL | ILD 2310-10 |
| ILD 2300-5 | ILD 2300-100 | ILD2300-10LL | ILD2300-5BL | ILD 2310-20 |
| ILD 2300-10 | ILD 2300-200 | ILD2300-20LL | ILD2310-50BL | ILD 2310-50 |
| ILD 2300-20 | | ILD2300-50LL | | |
| ILD 2300-40 | | | | |

## 2. Laser Class

The optoNCDT 2300 sensors operate with a semiconductor laser with a wavelength of 670 nm (visible/red ILD 2300-x) resp. 405 nm (visible/blue ILD 2300-xBL). The sensors fall within Laser Class 2 (II). The laser is operated on a pulsed mode, the average power is ≤ 1 mW in each case, the peak power can be up to 1.2 mW. The pulse frequency depends on the adjusted measuring rate /1.5 ... 49.02 kHz). The pulse duration of the peaks is regulated depending on the measuring rate and reflectivity of the target and can be 0.5 up to 542 µs.

Comply with all regulations on lasers!

Although the laser output is low looking directly into the laser beam must be avoided. Due to the visible light beam eye protection is ensured by the natural blink reflex. The housing of the optical sensors may only be opened by the manufacturer, see Chap. 13. For repair and service purposes the sensors must always be sent to the manufacturer.

The following warning labels are attached to the cover (front and/or rear side) of the sensor housing. The laser warning labels for Germany have already been applied (see above). Those for other non German-speaking countries an IEC standard label is included in delivery and the versions applicable to the user's country must be applied before the equipment is used for the first time. Laser operation is indicated by LED, see Chap. 3.5.

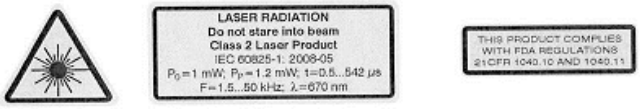


*IEC label* *Only for USA*

## 3. Functional Principle, Technical Data

### 3.1 Short Description

The optoNCDT 2300 uses the principle of optical triangulation, that is, a visible, modulated point of light is projected onto the target surface. The sensor measures distances in the diffuse arrangement, distances in the direct arrangement distances or the thickness of a transparent target.

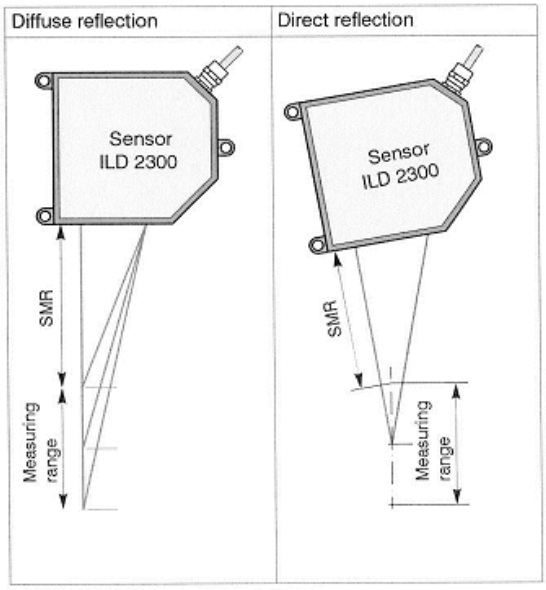


| Sensor | Distance | Thickness |
|---|---|---|
| ILD 2300-2 | • | • |
| ILD 2300-5 | • | • |
| ILD 2300-10 | • | • |
| ILD 2300-20 | • | • |
| ILD 2300-40 | • | |
| ILD 2300-50 | • | |
| ILD 2300-100 | • | |
| ILD 2300-200 | • | |
| ILD2300-2LL | • | |
| ILD2300-10LL | • | |
| ILD2300-20LL | • | |
| ILD2300-50LL | • | |
| ILD2300-2BL | • | |
| ILD2300-5BL | • | |
| ILD2310-50BL | • | |
| ILD 2310-10 | • | |
| ILD 2310-20 | • | |
| ILD 2310-50 | • | |

| Type | ILD 2300- | 2 | 5 | 10 | 20 | 30 | 40 | 50 | 100 | 200 |
|---|---|---|---|---|---|---|---|---|---|---|
| Measuring range [1] | mm | 2 / 2 (.08 / .08) | 5 / 2 (.20 / .08) | 10 / 5 (.39 / .20) | 20 / 10 (.79 / .39) | 40 / 20 (1.57 / 79) | 40 / 20 (1.57 / .79) | 50 / 25 (1.97 / .99) | 100 / 50 (3 94 / 1.97) | 200 / 100 (1.57 / 3.94) |
| Start of measuring range | mm | 24 / 24 (.94 / .94) | 24 / 24 (.94 / .94) | 30 / 35 (1.18 / 1 38) | 40 / 50 (1.57 / 1 97) | 175 / 195 (6.89 / 7.68) | 175 / 195 (6.89 / 7.68) | 45 / 70 (1.77 / 2.76) | 70 / 120 (2 76 / 4.72) | 130 / 230 (5.12 / 9.06) |
| Midrange | mm | 25 / 25 (.98 / .98) | 26.5 / 25 (1.04 / .98) | 35 / 37 5 (1.38 / 1.48) | 50 / 55 (1.97 / 2.17) | 195 / 205 (6.89 / 8.07) | 195 / 205 (6.89 / 8.07) | 70 / 82.5 (2.76 / 3.25) | 120 / 145 (4.72 / 5.71) | 230 / 280 (9.06 / 11.02) |
| End of measuring range | mm | 26 / 26 (1.02 / 1.02) | 29 / 26 (1.14 / 1.02) | 40 / 40 (1.57 / 1 57) | 60 / 60 (2.36 / 2.36) | 215 / 215 (8.46 / 8.46) | 215 / 215 (8.46 / 8.46) | 95 / 95 (3.74 / 3.74) | 170 / 170 (6 69 / 6.69) | 330 / 330 (13.0 / 13.0) |
| Linearity | µm | 0.6 | 1.5 | 2 | 4 | 12 | 12 | 10 | 30 | 60 |
| Resolution (at 20 kHz) [2] | µm | 0.03 | 0.08 | 0.15 | 0.3 | 0.6 | 0.6 | 0.8 | 1.5 | 3 |
| Measuring rate, programmable | | 49.02 / 30 / 20 / 10 / 5 / 2.5 / 1.5 kHz (49.02 kHz with reduced measuring range) | | | | | | | | |
| Light source (Laser diode) | | Wave length 670 nm, red, max. power 1 mW, laser class 2 | | | | | | | | |
| Permissible ambient light | | 10,000 lx … 40,000 lx | | | | | | | | |
| Light spot diameter (±10 %) | SMR, µm | 55 x 85 | 70 x 80 | 75 x 85 | 140 x 200 | 230 | 230 | 255 x 350 | 350 | 1300 |
| | MR, µm | 23 x 23 | 30 x 30 | 32 x 45 | 46 x 45 | 210 | 210 | 70 x 70 | 130 | 1300 |
| | EMR, µm | 35 x 85 | 70 x 80 | 110 x 160 | 140 x 200 | 230 | 230 | 255 x 350 | 350 | 1300 |
| Operating temperature | | 0 ... +50 °C (+32 °F up to +122 °F) | | | | | | | | |
| Storage temperature | | -20 ... +70 °C (-4 °F up to +158 °F) | | | | | | | | |
| Protection class | | IP 65 (with plugged connection) | | | | | | | | |
| Power supply $U_B$ | | 24 VDC (11 ... 30 V); P < 3 W | | | | | | | | |
| Measurement value output, | | RS422, Ethernet, EtherCAT (selectable) | | | | | | | | |
| Synchronization programmable | | Simultaneous or alternating | | | | | | | | |
| Sensor cable (standard) | | 0.25 m (with cable jack) | | | | | | | | |
| Electromagnetic compatibility | | EN 61326-1: 2006-10; DIN EN 55011: 2007-11 (group 1, class B); EN 61 000-6-2: 2006-03 | | | | | | | | |
| Vibration (acc. to IEC 60068-2-6) | | 2 g / 20 ... 500 Hz | | | | | | | | |
| Shock (acc. to IEC 60068-2-29) | | 15 g / 6 ms / 3 axes | | | | | | | | |
| Weight (with 25 cm cable) | | 550 g | | | | 600 g | 600 g | 550 g | | 600 g |

1) 1. value: Measuring rate of 1.5 kHz up to 30 kHz. 2. value: Measuring rate 49.02 kHz, see Page 17.

# D3: TEST COUPLING DETAILS

**BIBBY TURBOFLEX TRANSMISSIONS LTD**

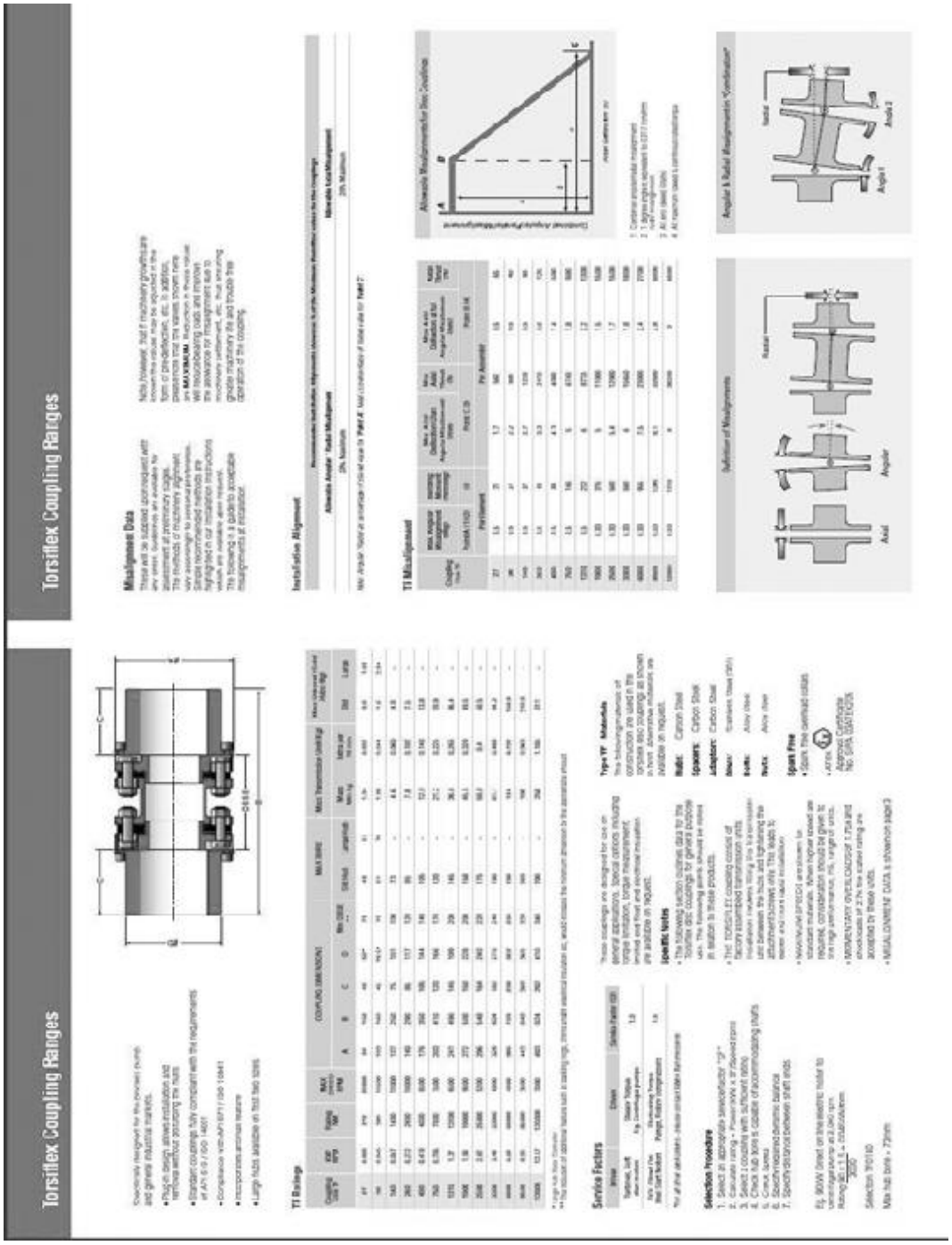

| DUTY REQUIREMENTS | | | |
|---|---|---|---|
| RATED POWER (KW) | 49 | MOMENTARY TORQUE (KNm) | - |
| RATED SPEED (RPM) | 11900 | TRIP/OVERSPEED (RPM) | - |
| RATED TORQUE (KNm) | 0.039 | TRANSIENT TORQUE (KNm) | - |
| MAX. TORQUE (KNm) | - | No. Of CYCLES | - |

| COUPLING MASS ELASTIC TOTALS | | |
|---|---|---|
| MASS (Kg) | 7.2 ⚠ | |
| INERTIA, $mr^2$ (Kg.$m^2$) | - | |
| TORSIONAL STIFFNESS MNm/rad | - | |
| (Including 1/3rd shaft penetration) | | |

| COUPLING CAPACITIES | | | |
|---|---|---|---|
| 1st LATERAL CRITICAL (RPM) | 11900 | CONTINUOUS TORQUE TkN (KNm) | 0.27 |
| | | PEAK TORQUE Tkmax (KNm) | 0.73 |
| MAX. ALLOW. SPEED (RPM) | - | No. Of CYCLES (FOR PEAK TORQUE) | - |
| | | MOMENTARY TORQUE (KNm) | 0.47 |

DRIVE END 'A'
MOTOR

DRIVEN END 'B'
refed

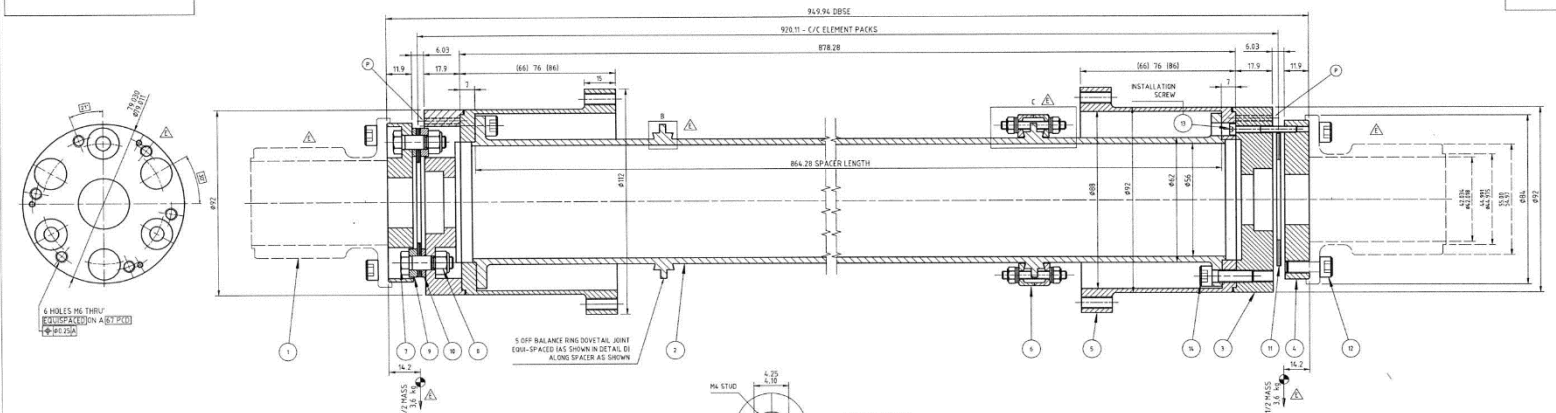


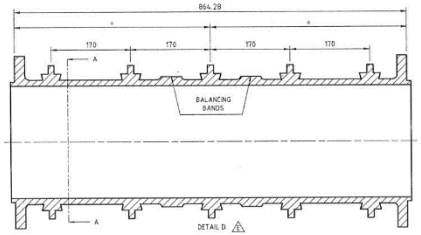


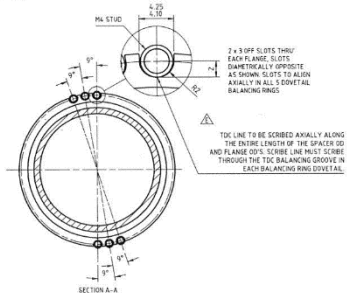


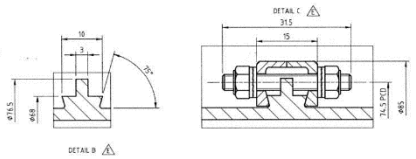





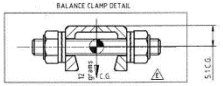


| TRIM BALANCE HOLE DETAILS | | | |
|---|---|---|---|
| QTY | SIZE | PCD | POSITION |
| 6 | M3 | 81 | P |

| Item | Description | Qty | ID Number | Material | |
|---|---|---|---|---|---|
| 14 | CAPSCREW M6 x 25 SHCS * | 12 | M625SCP | Gr 12.9 | |
| 13 | CAPSCREW M3 x 30 SHCS # × | 6 | M330SC | Gr 12.9 | |
| 12 | CAPSCREW M6 x 16 SHCS * | 12 | M616SCP | Gr 12.9 | |
| 11 | ELEMENT BLADE | 16 | D6EB | AISI.301 | |
| 10 | ELEMENT WASHER | 12 | D682EW | BS970 605M36T | |
| 9 | OVERLOAD WASHER * | 12 | D682GZOW | BSB23 | |
| 8 | LOCKNUT M6 STAYTITE * | 12 | M6SL10 | Gr 10. | |
| 7 | COUPLING BOLT * | 12 | TF0027M6CB | S.99 | |
| 6 | BALANCE CLAMP ASSEMBLY | 10 | 10625-9 | GRADE 5 TITANIUM | ⚠ |
| 5 | BALANCE SLEEVE | 6 | 10625-5 | BS970 817M40V | |
| 4 | ADAPTOR | 2 | 10625-4 | GRADE 5 TITANIUM | |
| 3 | SPACER ADAPTOR | 2 | 10625-3 | GRADE 5 TITANIUM | |
| 2 | SPACER | 1 | 10625-8 | BS970 817M40T | ⚠ |
| 1 | HUB (NOT SUPPLIED) | 0 | FREE ISSUE | BS970 817M40V | ⚠ |

KEY: # ALL REMOVABLE PARTS TO BE PAINTED YELLOW AND MUST BE REMOVED PRIOR TO OPERATION.
× PARTS TO BE BALANCE WEIGH TO WITHIN 0.1g or 0.05% OF INDIVIDUAL PART MASS WHICHEVER IS GREATER.

RECOMMENDED TIGHTENING TORQUES
(ALL BOLT VALUES ARE BASED ON USING ANTI-FRICTION BEARING GREASE i.e. BP ENERGREASE L21M OR EQUIVALENT)

| BOLT No. | NUT No. | TORQUE (Nm) | STRETCH (µm) |
|---|---|---|---|
| 12 | | 9 | |
| 14 | | 9 | |

DO NOT TAMPER WITH THE FOLLOWING FASTENERS.
THEY ARE TIGHTENED BY BIBBY TURBOFLEX AS A FACTORY ASSEMBLED JOINT

| BOLT No. | NUT No. | TORQUE (Nm) | STRETCH (µm) |
|---|---|---|---|
| 7 | 8 | 9 | 36 |

NOTES:
1) COUPLING SUPPLIED MATCH-MARKED IN ACCORDANCE WITH T.I.S. 5-248
2) COUPLING SUPPLIED ETCHED WITH SERIAL NUMBER IN ACCORDANCE WITH T.I.S. 5-250

BALANCE REQUIREMENT - API671, METHOD 3
- COMPONENT BALANCE
- ASSEMBLY BALANCE,
MAXIMUM ALLOWABLE RESIDUAL UNBALANCE:
END 'A' 7.2 gmm (WITHIN 7.2)
END 'B' 7.2 gmm (WITHIN 7.2)

COUPLING CHARACTERISTICS

ALLOWABLE MISALIGNMENTS

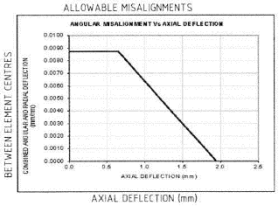


AXIAL THRUST CURVES

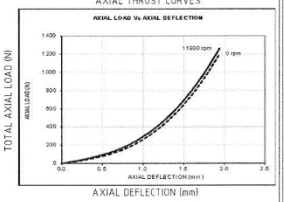


COUPLING CHARACTERISTICS PRODUCED
——— RATED DUTY SPEED
– – – 0 RPM

AXIAL NATURAL FREQUENCY API 671 4TH EDITION PARA. 8.12.1 STATES "MULTIDISC, MULTIDIAPHRAGM AND NONCONVOLUTED SINGLE ELEMENT FLEXIBLE COUPLINGS DO NOT EXHIBIT UNDAMPED VIBRATION RESPONSE."

| REV | DESCRIPTION | ECNA | SIG. | DATE |
|---|---|---|---|---|
| E | SPACER, BALANCE CLAMP CHANGED. HUBS REMOVED. MASS UPDATED | 10560 | EDM | 09-OCT-2014 |
| D | TRIM BAL HOLES - BAL. BANDS ADDED. | 7746 | EDM | 16-JULY-2013 |
| C | Ø45 x 15 SPIGOT AND 4 M3 HOLES ADDED TO EACH HUB | 7682 | ARI | 11-JUNE-2013 |
| B | BALANCE CLAMPS NOW AN ASSEMBLY. ITEM 13 WAS M316HS. SPACER LENGTH INCREASED AFTER FEA FOR 1st LATERAL SPEED. | 7634 | EDM | 08-MAY-2013 |
| A | ORIGINAL ISSUE | - | EDM | 26-APR-2013 |

DO NOT SCALE IF IN DOUBT ASK
THIRD ANGLE PROJECTION
UNLESS OTHERWISE STATED, ALL DIMENSIONS IN MILLIMETRES, BS, ISO & DIN STANDARDS ARE AT LATEST ISSUE

Bibby Transmissions
CANNON WAY, MILL ST WEST, DEWSBURY, WF13 1EH
TEL. 01924 460801 FAX. 01924 457668

| | |
|---|---|
| CUSTOMER | SIEMENS/LINCOLN UNIVERSITY |
| CUSTOMER ORDER No. | 3096330 |
| BIBBY ORDER No. | 1038686 |
| DRAWN BY | EDM |
| CHECKED BY | - |
| SCALE | 1:1 |
| PAPER SIZE | A3 |

# GENERAL ARRANGEMENT

TF0027L100/BAL/GS/WH/BK
ARRANGEMENT DRAWING

DRG No: 10625SHT1 REV: E